HARVARD
Kenneth C. Griffin

GRADUATE SCHOOL
OF ARTS AND SCIENCES

THESIS ACCEPTANCE CERTIFICATE

The undersigned, appointed by the

Harvard John A. Paulson School of Engineering and Applied Sciences
have examined a dissertation entitled:

"Geometric Control for High-Fidelity Entanglement of Individual Ultracold Molecules"

presented by: Scarlett Seejia Yu

Signature _____
Typed name: Professor John Doyle

Signature _____
Typed name: Professor Evelyn Hu

Signature _____
Typed name: Professor Giulia Semeghini

Signature _____
Typed name: Professor Kang-Kuen Ni

Date: July 6, 2026

Geometric Control for High-Fidelity Entanglement of Individual Ultracold Molecules

a dissertation presented
by
Scarlett Seejia Yu
to
Harvard John A. Paulson School of Engineering and Applied Sciences (SEAS)

in partial fulfillment of the requirements
for the degree of
Doctor of Philosophy
in the subject of
Applied Physics

Harvard University
Cambridge, Massachusetts
July 2026

©2026 Scarlett Seejia Yu
all rights reserved.

Thesis advisor: John M. Doyle Scarlett Seejia Yu

Geometric Control for High-Fidelity Entanglement of Individual Ultracold Molecules

Abstract

Ultracold polar molecules provide a powerful platform for quantum science because they combine long-lived rotational states, rich internal structure, and strong electric dipole-dipole interactions. Optical tweezer arrays provide a pristine way of controlling these molecules at single-particle level, in which molecules can be individually trapped, rearranged into programmable geometries, coherently manipulated by optical and microwave fields, and entangled through their native dipolar interactions. This dissertation describes the development of geometric control as a resource for improving interaction coherence and high fidelity of quantum entanglement between directly laser-cooled calcium monofluoride (CaF) molecules in optical tweezers.

A central challenge in molecular tweezer systems is that dipolar interactions are intrinsically sensitive to the relative position of the molecules. Thermal motion in the traps, especially along the weakly confined axial direction, causes molecules to sample a distribution of intermolecular separations, degrading dipolar coherence and limiting entanglement fidelity. We show in this work that the interaction itself can be made robust by controlling its geometry.

The experimental work begins with improvements to the production and optical trapping of dense CaF samples. We realize a blue-detuned “conveyor-belt" magneto-optical trap (MOT) that compresses laser-cooled CaF to a mean cloud radius of 64(5) μm and a peak density of $3.6(5) \times 10^{10}$ cm^{-3}, a 600-fold density increase over conventional red-detuned CaF MOTs. Loading from this compressed source into an optical dipole trap yields up to 2.6×10^4 trapped molecules at 14(2) μK, with a peak phase-space density of approximately 2.4×10^{-6}. This high-density source improves the transfer of laser-cooled molecules into conservative optical traps and provides the starting point for loading and manipulating single molecules in a hybrid SLM-AOD optical tweezer array. Using this platform, we prepare CaF molecules in

selected rotational and hyperfine states to encode a rotational qubit. We show how to preserve the single-qubit coherence with a combination of techniques, including “magic" polarization condition and microwave dynamical decoupling, as well as reduce motional quantum state of the trapped molecule with Raman sideband cooling. We then characterize coherent dipolar spin exchange between pairs of molecules and identify thermal motion and relative trap-center offsets as dominant sources of interaction dephasing. To suppress these effects, we engineer the three-dimensional interaction geometry between two individually trapped molecules. More specifically, we show that one can tune the *static* geometric of the dipolar interaction to configurations where sensitivity to thermal fluctuations is strongly reduced while retaining a finite interaction strength. Furthermore, we show that a molecule can be moved during the interaction while preserving the coherence of ongoing entangling operations. We leverage programmable molecular motion to refocus dephasing arising from relative positional jitter of the optical tweezers.

Combining static geometric insensitivity, programmable molecular motion, and partial Raman sideband cooling, we generate two-molecule entanglement with a Bell-state fidelity of $\mathcal{F} = 0.976^{+0.008}_{-0.011}$ in directly laser-cooled molecules. Crucially, the high-fidelity molecular entanglement here is performed without ground-state preparation. Rather than relying on stringent cooling or species-specific trapping conditions, as in prior work, the methods demonstrated here are instead based on dynamic and static geometric control of interacting molecules and are therefore broadly applicable across molecular platforms. These results extend moving optical tweezers beyond assembly and rearrangement, opening routes to robust two-qubit gates, many-body dynamics, and dynamically programmable networks of interaction.

Table of Contents

Title page . . . i
Copyright . . . ii
Abstract . . . iii
Table of Contents . . . v
List of Figures . . . ix
List of Tables . . . xiv
Dedication . . . xv
Acknowledgments . . . xvi
Citations to Previously Published Work . . . xxii

1 Introduction **1**
1.1 Overview of Laser-cooled Polar Molecules . . . 1
1.2 Polar Molecules for Quantum Information Science . . . 2
1.3 This Work: Geometric Control of Dipolar Interactions of CaF Molecules in Optical Tweezers . . . 3
1.4 Organization of This Dissertation . . . 5

2 Ultracold Polar Molecules for Quantum Science **9**
2.1 Interactions Between Molecules . . . 9
2.2 Dipolar Quantum Simulation and Hamiltonian Engineering . . . 12
2.3 Quantum Information Science . . . 15
2.3.1 Molecular Tweezer Array Platform for Quantum Information . . . 17
2.4 State-resolved Ultracold Chemistry and Collisions . . . 19
2.5 Dipolar Quantum Matter . . . 20
2.6 Precision Measurements and Fundamental Physics . . . 22

3 Molecular Properties and Quantum States of CaF **24**
3.1 Overview of CaF and its Amenability to Laser Cooling . . . 24
3.2 Electronic Ground State of CaF ($X^2\Sigma$) . . . 27
3.2.1 Molecular Constants and Energy Scales . . . 28
3.2.2 Field-free Hamiltonian of $X^2\Sigma$ State . . . 29
3.2.3 X-State Zeeman Hamiltonian . . . 31
3.2.4 X-State DC Stark Hamiltonian . . . 33
3.3 Low-lying Excited electronic States: $A\,^2\Pi$ and $B\,^2\Sigma^+$ . . . 36
3.3.1 Excited $A^2\Pi$ State . . . 37
3.3.2 Zeeman Interaction in the $A^2\Pi$ State . . . 39
3.3.3 DC Stark Interaction in the $A^2\Pi$ . . . 39
3.3.4 Excited $B^2\Sigma^+$ State . . . 41
3.4 Laser Slowing and Trapping Schemes . . . 43
3.4.1 Photon Budgets and Repumps . . . 45
3.4.1.1 Off-resonant Scattering . . . 47

3.4.2 Laser Slowing . . . 48
3.4.3 Laser Trapping . . . 49
3.5 AC Stark Shifts and Polarizability of CaF in Optical Traps . . . 50
3.5.1 Scalar Stark Shift . . . 53
3.5.2 Tensor Stark Shift . . . 53
3.6 Transition dipole moment of between rotational states . . . 55
3.7 Blackbody Radiation . . . 57

4 Experimental Apparatus and Developments 59
4.1 Overview . . . 59
4.2 Generation of Two-dimensional Tweezer Array . . . 61
4.2.1 Detection Path . . . 63
4.2.1.1 Monitoring and Feedback for SLM-AOD Alignment . . . 63
4.2.2 SLM Stability . . . 65
4.3 Glass Cell and Microscope Objective Characterization . . . 67
4.3.1 Interferometric Optical Testing . . . 67
4.3.2 Objective Wavefront and Point Spread Function . . . 70
4.4 Passive and Active Stabilization of Stray Fields . . . 72
4.4.1 Electric Fields . . . 72
4.4.2 Magnetic Fields . . . 74
4.5 Laser Systems . . . 76
4.5.0.1 Agile Laser Locking and Frequency Jumping . . . 76
4.5.0.2 Slowing Beams . . . 78
4.5.1 606 nm for $X - A$ Transition . . . 80
4.5.1.1 Frequency Control and Hyperfine Components . . . 83

5 Magneto-optical Trapping and Cooling of CaF 84
5.1 Magneto-Optical Trapping of CaF . . . 85
5.2 Blue-detuned Conveyor-Belt MOT . . . 87
5.2.1 Introduction and Development of Blue-detuned MOTs . . . 87
5.2.2 The Conveyor MOT Trapping Mechanism . . . 89
5.2.3 Conveyor MOT of CaF . . . 91
5.2.3.1 RF – DC MOT coil switching . . . 92
5.2.3.2 Magnetic field ramp optimization . . . 93
5.2.4 Compression of molecular cloud . . . 95
5.2.5 Conveyor-Belt MOT lifetime and scattering rate . . . 99
5.2.6 Temperature of molecules in conveyor MOT . . . 100
5.3 Loading into Optical Dipole Trap . . . 100
5.3.1 Loading dynamics and efficiency . . . 101
5.3.2 Losses during ODT loading . . . 102
5.3.3 ODT trap depth and alignment . . . 103
5.4 Characterization of Optical Tweezer Traps . . . 105
5.4.1 Trap Frequency Measurements . . . 106
5.4.2 Trap Waist, Intensity, and Depth . . . 106
5.4.3 Tweezer Lifetime . . . 108
5.4.4 Minimum Separation between Two Optically Trapped Molecules . . . 109

5.5 Homogenization of Tweezer Arrays . . . 109
5.5.1 Trap Depth . . . 110
5.5.2 SLM Trap Aberrations . . . 113
5.5.3 SLM-AOD Transfer Fidelity . . . 113
5.5.4 Technical Heating . . . 117

6 Single Molecule Quantum Control and Cooling to Motional Ground State 118
6.1 Rotational Qubit States and Sensitivities . . . 119
6.2 State Preparation . . . 121
6.2.1 Choice of Optical Pumping Stretched State . . . 122
6.2.2 Optical Pumping Light . . . 124
6.2.3 Microwave Transfers . . . 125
6.3 Single-Qubit Coherence . . . 125
6.3.1 Magic Condition for Suppressing Light Shifts . . . 126
6.3.2 Dynamical Decoupling Microwave Pulses . . . 128
6.3.3 Rotational Coherence Time Measurements . . . 131
6.4 Cooling to Motional Ground State: Raman Sideband Cooling (RSC) . . . 133
6.4.1 Theory of Raman Sideband cooling . . . 133
6.4.1.1 Raman Transition in Three-level System . . . 133
6.4.1.2 Resolved Sideband . . . 136
6.4.1.3 Raman Sideband Cooling Cycle and Limit . . . 138
6.4.2 RSC Implementation for Motional Ground-State Preparation . . . 139
6.4.3 Improved RSC Implementation for Molecule Survival . . . 144
6.4.3.1 Partial Raman Sideband Cooling . . . 150

7 Geometric Engineering of Dipolar Interactions 153
7.1 Overview . . . 153
7.2 Dipolar Spin-Exchange in 1D Array of CaF . . . 154
7.2.1 Procedure and Experimental Sequence . . . 154
7.2.2 Experimental Characterization of Dipolar Interactions . . . 158
7.2.3 Site-Resolved Initial-State Preparation . . . 162
7.3 Limitation on Dipolar Coherence . . . 164
7.4 Tuning Motional Sensitivity of Dipolar Coupling in 3D . . . 164
7.4.1 2D Case: “Magic” Angle . . . 164
7.4.2 3D case: “Magic” Configuration . . . 167
7.5 Experimental Control of Interaction Geometry . . . 167
7.5.1 Experimental Control and Coordinates . . . 168
7.5.2 Measurement Procedure . . . 169
7.6 Static Geometric Engineering of Motional Sensitivity . . . 171
7.7 Dynamic Geometric Engineering: Position Noise and Positional Echo . . . 173
7.8 Two-molecule Dipolar Interaction Model . . . 177

8 High-Fidelity Two-Molecule Entanglement Generation 180
8.1 Bell State Fidelity Theory . . . 181
8.1.1 From Spin-exchange to Bell State Generation . . . 181
8.1.2 Bell State Fidelity . . . 183

8.1.3 Parity Oscillation Signal . . . 184
8.2 Experimental Generation of High-Fidelity Bell State . . . 185
8.3 Future Avenues for Improving Fidelity . . . 188

9 Conclusion and Outlook **191**
9.1 Concluding Remarks . . . 191
9.2 The Road Ahead . . . 192

Appendix A High-field Coil Design and Assembly **194**
A.1 Overview and Design Considerations . . . 195
A.2 Coil Simulations and Specs . . . 198
A.3 Coil Winding and Fabrication . . . 200
A.4 Thermal Performance . . . 202

Appendix B Dynamic Optical Ring Trap **204**
B.1 Motivation . . . 204
B.2 Optical Principle and Compact Layout . . . 205
B.3 Ring Size Calibration . . . 206
B.4 In-Situ Alignment using Raman Scattering and Performance . . . 207

Appendix C Indium-Seal based Cryogenic Cell **210**
C.1 Motivation . . . 210
C.2 Indium Seals and Cell Design . . . 211

References **235**

List of Figures

2.1 **Representative interacting quantum platforms for quantum simulation and quantum information.** . . . 12
2.2 **Experimental platforms for quantum simulation with atoms and molecules: quantum gas microscope (left) and optical tweezer array (right).** . . . 15

3.1 **(a)** Quantum level diagram for $X^2\Sigma(v = 0)$ state in CaF, showing hyperfine and Zeeman substates within the lowest two rotational manifolds, the energy splittings between the hyperfine states, and the g-factor [1, 2]. . . . 27
3.2 **(a)** Low-field Zeeman structure for $N = 0$ and $N = 1$ rotational manifolds in $X^2\Sigma(v = 0)$ state. . . . 33
3.3 DC Stark shifts for rotational manifolds (N=0,1,2) in the ground electronic state $X^2\Sigma(v = 0)$. . . . 34
3.4 **Relevant electronic, vibrational, rotational, fine and hyper-fine levels of CaF.** All the states used for laser cooling, slowing, repumping, and qubit state preparation in this work lie within the $X^2\Sigma^+$, $A^2\Pi$ and $B^2\Sigma^+$ electronic manifolds, with blue levels denoting the states directly participating in the main cycling transitions. . . . 36
3.5 **Laser-driven transitions for optical cycling schemes used for laser cooling and slowing of CaF.** Solid arrows denote laser-driven transitions and wavy arrows indicate spontaneous decay pathways. . . . 44
3.6 Scalar trap depth $U_0/k_B = \tilde{\alpha}^{(0)}(\lambda)I_0/k_B$ for the $X\,^2\Sigma^+(v = 0)$ state of CaF as a function of trap wavelength for given optical power and waist. . . . 52
3.7 Dynamic polarizability coefficients in the $X^2\Sigma^+(v = 0)$ state. . . . 54

4.1 Thermal population of rotational states of CaF in $X^2\Sigma^+$, $v = 0$ as a function of rotational temperature. . . . 60
4.2 Optical setup for generating the two-dimensional tweezer array. . . . 61
4.3 Monitor-camera feedback scheme for SLM array calibration and long-term stabilization. . . . 64
4.4 (a) An example image of the tweezer traps from the monitor camera showing pairs of the SLM and AOD traps. . . . 66
4.5 Optical layout of a short-coherence phase-shifting Fizeau interferometer used for glass-cell and optical-surface characterization. . . . 68
4.6 Data-processing workflow for phase-shifting interferometry. . . . 70
4.7 Fluorescent-bead measurement of the objective point-spread function. . . . 72
4.8 Schematic of the nested coil system used to stabilize slow magnetic-field drifts near the glass cell region. . . . 73
4.9 Laser locking scheme for 531 nm system used for laser slowing and optical pumping during Raman sideband cooling. . . . 77

4.10 Optical transitions **(a)** and beam delivery optics **(b)** used for slowing. 79
4.11 (a, left) "White-light" EOM, where the driven crystal is rigidly supported from the housing using Ultem, with stainless-steel fasteners and spring-loaded pogo-pin contacts to minimize stray capacitance. 80
4.12 Interior of the 606 nm SFG head. 82

5.1 Schematic of experimental stages along with typical molecular number and temperature at each stage: starting from production of CaF molecular beams and laser slowing, magneto-optical trapping (MOT) of CaF molecular gas, application of sub-Doppler cooling, to compression of the molecular cloud for loading into conservative optical traps. 85
5.2 Illustration of the working principle of a conveyor-belt blue-detuned MOT; see text. 89
5.3 Relevant level structure of CaF and laser configurations used in this work. . . 91
5.4 Conveyor MOT loss rates with different magnetic field ramp profiles. 93
5.5 Oscilloscope traces of the current and voltage programming sequence to the current supply used in the experimental sequence (magenta and blue, respectively), as well as measured output current (yellow) to the coils, and TTL signal for RF–DC MOT switching (cyan). 94
5.6 **Dependence of conveyor MOT cloud size on frequency detunings and magnetic field.** MOT radius σ as a function of two-photon detunings **(a)** δ_a, **(b)** δ_b, **(c)** single-photon detuning Δ, and **(d)** applied magnetic field gradient B'. 96
5.7 **Size and density of conveyor-belt blue MOT as a function of time**. . 97
5.8 Frequency schemes explored during experimental development. 98
5.9 Comparison of conveyor-MOT compression between two-frequency and three-frequency schemes. 98
5.10 **(a)** Number of remaining trapped molecules in the conveyor MOT as a function of holding time, with the magnetic field gradient set at 40 G/cm. 99
5.11 **ODT loading characterization.** (a) Loading efficiency as a function of conveyor MOT cloud size. 101
5.12 ODT loading efficiency versus ODT powers. 104
5.13 ODT loading efficiency versus ODT position. 104
5.14 Trap frequency measurements. 107
5.15 Survival probability for molecules held in the optimized tweezer as a function of hold time. 108
5.16 **Measurements minimum separations between two molecules in optical tweezers without loss or tunneling. (a)** Survival probability versus hold time for different trap separations, where frequency of 200, 250, 300, 350, and 400 kHz correspond approximately to separations of 1.4, 1.75, 2.1, and 2.8 μm. 110
5.17 Trap depth homogenization using Ramsey spectroscopy, before **(a)** and after **(b)** three iterations (a representative data set). 111
5.18 Trap frequency homogenization using motional sideband spectra. 112
5.19 Scans of a range of Zernike coefficients as stretched state transition frequency center is probed. 114

5.20 **Characterization of AOD to SLM transfer. (a)** Survival rate of repeated handover between pairs of traps with different AOD trap intensity ramp duration. **(b)** Survival rate of 9 rounds of handover between pair of traps as a function of the coefficients of the defocus Zernike mode Z_2^0 on SLM trap. 115
5.21 Illustration of the experimental steps used to measure motional excitations of molecules after SLM–AOD trap transfer. 116

6.1 **(a)** Relevant rotational (N), hyperfine (F) and Zeeman (m_F) states in the ground electronic state $X^2\Sigma$ and first excited state $A^2\Pi$ of CaF. 120
6.2 **(a)** Relative purity of the two stretched states versus magnetic field and trap depth. 123
6.3 **(a)** Top: calculated differential light shift $\delta\nu_{\mathrm{q}}(U)$ of the rotational qubit state at $B = 3.2\,\mathrm{G}$, where U/k_B is trap depth. 129
6.4 **(a)** Schematic of the microwave generation system, including a beat-note measurement setup. 130
6.5 (a) Top: Ramsey phase contrast measurement sorted by number of occupied nearest-neighbor sites. 132
6.6 Three level in Λ configuration. 134
6.7 **(a)** Relevant hyperfine and Zeeman states in the $X^2\Sigma(v = 0, N = 1)$ and $B^2\Sigma(v = 0, N = 0)$ states of CaF at low field. 140
6.8 **(a)** Configuration of Raman beams and optical pumping beams used in the Raman sideband cooling experiment. 141
6.9 Raman sideband thermometry spectra for radial x direction, radial y direction, and axial z direction, respectively. 143
6.10 Calculated magnetic-field dependence of branching ratio for spontaneous decay out of $|B, N' = 0, (m'_S = -1/2, m_I =' -1/2)\rangle$ into other spin manifolds in $X^2\Sigma^+(v = 0, N = 1)$. 145
6.11 Debugging de-pumping rate out of optical pumping dark state $\left|m_N = +1; (m_S = -\frac{1}{2}, m_I = -\frac{1}{2})\right\rangle$ with σ^+OP light and π OP light on separately, at different magnetic fields. 147
6.12 (a) Relevant m_N states at high field in the $(m_s = -\frac{1}{2}, m_I = \pm\frac{1}{2})$ spin manifolds of ground state $X^2\Sigma(N = 1)$. 148
6.13 The corresponding connected states and coupling involved in higher-field RSC scheme shown in low-field basis regime. 149
6.14 Histogram of simulated axial (z) motional distributions before (left) and after (right) a partial Raman sideband cooling sequence. 151
6.15 **Signatures of reduced motional excitation after Raman sideband cooling** Interaction frequency as a function of axial displacement, with and without partial sideband cooling applied. 151

7.1 Theoretical distance and angular scaling of dipolar coupling strength for CaF molecules plotted for a range of experimentally relevant spacings. 155
7.2 **Schematic of experimental procedure used for observing dipolar interaction in 1D tweezer array of CaF molecules.** The procedure for state initialization is described in Chapter 6.2. 156

7.3 **(a)** A representative schematic of the optical tweezer and coordinate system defined in this work (For visual clarity, only four sites of the realized twenty-site array are depicted). . . . 159
7.4 **(a)** Measured and Simulated $1/e$ dipolar coherence times (Top) and number of dipolar oscillation cycles (contrast decayed to $1/e$) (Bottom) at different tweezer spacings. . . . 161
7.5 **(a)** Schematic of interaction geometry used for angular measurements. . . . 162
7.6 (a) Rabi oscillation of molecules initialized in $|\downarrow\uparrow\rangle$ state. . . . 163
7.7 **(a)** Sensitivity coefficients $A_{i,2}(\theta)$ in expansion of J, showing the angular dependence. . . . 165
7.8 **(a)** Planar interaction configuration for a pair of molecules where both traps are in the same focal plane. . . . 166
7.9 **Dipolar motional sensitivity in experimentally accessible three-dimensional geometry.** Color shows the dimensionless weighted relative sensitivity $\mathcal{S}$, defined in main text, of the interaction strength to thermally-induced dephasing. . . . 168
7.10 **Illustration of the optical tweezer array and geometric coordinates used in this work.** CaF molecules are loaded into 775 nm optical tweezers projected through a 0.6 NA microscope objective into a vacuum glass cell. . . . 169
7.11 **Static geometric engineering of dipolar interactions**. . . . 172
7.12 **Positional Echo Protocol.** (a) Timing of positional echo during the interaction. 174
7.13 (a) Experimental sequence for probing dipolar interaction with applied positional echo protocol. . . . 175
7.14 **Simulated effect of reducing axial disorder**. . . . 176

8.1 **(a)** Illustration of the experimental sequence. . . . 186
8.2 (**a**) Pair population statistics, measured in the computational basis at $t = 11.2$ ms of dipolar exchange evolution, corresponding to the $\pi/2$ point of the two-particle population oscillation. . . . 187
8.3 Reported SPAM-corrected Bell state fidelity in molecular tweezer platforms, plotted against reported mean motional occupation. . . . 188
8.4 Simulated interaction quality factor Q as a function of mean motional occupation $\bar{n}$ for different rms axial position disorders σ_z. . . . 189

A.1 **High-field coils assembly surrounding the science glass cell. (a, b)** CAD model views of three orthogonal coil pairs, along with objective, glass cell and laser beam; the coordinate convention used throughout this section is indicated in (b). . . . 195
A.2 Ultra-low profile K-type thermocouples (Evosensors). . . . 197
A.3 Finished coils darkened with carbon-black coating (Aeroglaze Z306 diluted with Aeroglaze 9958 thinner). . . . 198
A.4 **(a)** Simulation of generated magnetic field by the X pair at 160 A. . . . 199
A.5 **Measured magnetic-field flatness of each of the three coil pairs.** Points show the measured field and solid curves are quadratic fit to $B(x) = B_0 + ax^2 + bx$. 200

A.6 **Coil winding setup on the lathe.** The G10 bobbin is mounted to the lathe using an aluminum adapter plate, and the hollow-core copper tubing is fed onto the bobbin as the spindle is rotated slowly. 201
A.7 **Copper adapter block for water and electrical connection for the hollow-core coils.** The adapter is machined with through holes for both the conductor and the 1/4-inch-OD water tube, together with a threaded electrical terminal. 202

B.1 **Optical layout of the dynamically tunable ring trap.** A 531 nm Gaussian beam is converted into an annular beam using an axicon, where a subsequent annular aperture mask the removes residual light in the center of the beam. . . 206
B.2 **Compact vertical assembly of the ring trap optics.** All the optics are mounted in a vertical cage system to fold the beam path without taking up too much table space, making the setup compact enough to fit above the science glass cell. 207
B.3 **(a)** Schematic of the imaging path in the in-situ transverse alignment of the ring trap. 208
B.4 **Ring-trap compression and effect on tweezer loading. (a)** Images of the projected 531 nm ring initially (left) and at the end of compression (right), showing dynamic tuning of the ring diameter from approximately 900 μm to 250 μm, respectively. 209

C.1 **CAD model of the indium-sealed cryogenic buffer-gas cell. (a,b)** Exterior views of the assembled cell, showing the front plate, target plate, snorkel with YAG window, and gas inlets. 211
C.2 **Indium sealing surfaces on the cell body and mating plates. (a)** Extruding lip machined on the main cell body. 213

List of Tables

3.1 **Frequencies, branching ratios and characteristic rates for cycling transitions**. All lower states are $X^2\Sigma^+(v, N = 1)$. Upper panel summarizes the two main cycling transitions. Middle panel lists vibrational spontaneous decay from the corresponding cycling excited states. Lower panel gives the repumping transitions used experimentally to return population from $X(v = 1, 2, 3)$ for both X–A and X–B cycling. Here, $A \equiv A^2\Pi_{1/2}(J' = 1/2, p = +)$ and $B \equiv B^2\Sigma^+(N' = 0)$. The Franck–Condon factor $q_{v'v}^{e-X}$ is the squared vibrational overlap between the indicated $e(v')$ and $X(v)$ states. The branching fraction β_i^e is the probability for spontaneous decay from the cycling excited state into $X(v)$. Recoil velocities are calculated using $v_{\mathrm{rec}} = h/(M\lambda)$ for $^{40}\mathrm{Ca}^{19}\mathrm{F}$, and Doppler temperature is defined $T_D = \hbar\Gamma/(2k_B)$. 46

6.1 Comparison of branching ratios for spontaneous decay from $B^2\Sigma^+(N' = 0)$ state spin manifold $\left|(m'_S = -\frac{1}{2}, m_I = -\frac{1}{2})\right\rangle$ to all the spin manifolds in $X^2\Sigma^+(N = 1)$ state, at 200 G and 350 G. 145

A.1 **Summary of the high-field coil specs.** Listed magnetic fields are evaluated at center of coils at 200 A, Resistance and inductance are measured values, while dissipation powers are from simulation. 199

To my mother, who made everything possible.

Acknowledgments

Many people made this PhD possible, and I have been incredibly fortunate to share this journey with those who made the hard parts easier and the good parts better.

I want to begin by thanking my advisor, Prof. John Doyle. My time in the group coincided with unusually turbulent years, including COVID-19 shutting down campus a few months after I started, and a sudden loss of federal funding. As a student, I felt nothing but reassured by John's leadership as the group navigated all of this. Thank you, John, for handling an enormous amount of behind-the-scenes work, giving us the freedom to take our time to explore and understand various experimental limits, and the care you put into our personal growth. Thank you also for the unlimited supply of coffee beans for the lab espresso machine, as well as generous offerings of epicurean delights, and dashes of wisdom and cultural references you shared along the way. The collaborative and balanced atmosphere of the group reflects the care you have put into building it.

The work in this dissertation is built on expertise, patience, and support from many labmates. Joining the CaF experiment meant keeping pace with Loïc, Sean, Yicheng, and Lawrence, a team of "udarniks", as John once put it. Together, you all set a high bar, scientifically and technically, for what it means to be a good experimentalist:

- Yicheng Bao and I started CaF Gen II together and worked side by side for five years. As the senior student, Yicheng designed much of the experimental infrastructure, and did so quickly despite the supplier delays and general chaos of the pandemic. Yicheng, your breadth of technical knowledge is remarkable, but what I also appreciated was your ability to explain complicated things with simple physical pictures. Thank you for teaching me everything I knew about the experiment, and for your patience during periods of tight deadlines.
- Loïc has been both a colleague and a collaborator throughout much of my time in the group. I first "met" Loïc as an undergraduate during DAMOP, where I went to his poster hoping to learn about molecular tweezer arrays, which had just been demonstrated for the

first time. But Loïc was swarmed a large curious crowd which I never managed to push through. I certainly did not imagine that I would later work on the same experiment and make more tweezer arrays of CaF. Loïc, working with you has been deeply valuable; I have always admired the efficiency and precision with which you debug technical problems, and I am glad to continue having you as a collaborator as you build a new CaF experiment in your own group.

- Sean Burchesky was also wonderfully easy to talk to, and had a gift for knowing the quick-and-dirty trick that make something work. Thank you, Sean, for helping whenever I had machining, optics, or general "how do I get this done quickly" questions.
- I also had the pleasure of briefly overlapping with Lawrence Cheuk, then the CaF postdoc, and came away thoroughly impressed by Lawrence's work ethic and the depth of the physics discussions.

In later years of the experiment, I was lucky to work closely with Jiaqi You and Avikar Periwal:

- Jiaqi joined us as a G1 and has been a steady force on the experiment for the past several years. Thank you to Jiaqi for your sharp questions, your efficient approach of getting to the heart of a problem, and for being a labmate I could always count on when something technical needed debugging.
- Avikar does not like compliments, but this is my Acknowledgment, so a few will have to be tolerated. Avikar has been everything one could hope for in a postdoc– joining the experiment with a broad skill set and vision, picking things up remarkably quickly, and bringing both practical improvements and different physical insights to the work. Thank you, Avikar, for continuing to expand our view of what CaF and this experiment can do. And thanks for always being so generous with offering help and being available, both in and outside the lab. We have also had plenty of banter along the way, but through all of it I have been inspired by and learned a great deal from you.

CaF is diatomic, and the number of active grad students on the experiment at a given time seems almost always constrained to be two, so I want to thank all visiting students who contributed to CaF at different stages: Chenyuan Li for building the OPLL, Zirui Liu for many Python scripts and calculations, Dongkyu Lim for helping during the conveyor MOT measurements, Youngju Cho for helping with the dipolar interaction project, and Qinshu Lyu for Raman sideband cooling simulations.

Beyond the CaF team, my lab life was enriched by many kind and talented members of the Doyle Group:

- Grace Li has been an amazingly supportive labmate in and out of the lab. Grace, talking to you always brightened my day, whether it was about molecular physics, lab shenanigans, or some joke of mine that you generously chose to find entertaining. You also improved the group's quality of life in very tangible ways, most notably by introducing the 3D printer. There were days when I started a print before heading to lab just so that, even if the experiment did not work, at least I would have something turned out nicely.
- Abdullah has somehow been both the younger brother and the older brother of the group. Thank you, Abdullah, for making the lab so lively, often through heroic levels of self-deprecation, and for being someone many of us could turn to when we needed a conversation.
- I have shared many good times in the Batcave office with Paige and Annika. Thank you both for always being willing to help, chat, and organize various group events to foster such friendly group atmosphere.
- Giseok and Jack made the office a fun place to be. Giseok, I will miss talking each other up before going to the gym, and exchanging real-time intelligence on how crowded Hemenway is, and also learning proper Korean from you. Jack has also been a great office mate, with an impressive and inexhaustible enthusiasm for yapping about $CaNH_2$.
- Thank you also to Arian for unwavering friendliness and willingness to spend serious time helping me think through physics problems and experimental mysteries.
- Christian has evolved into a juggernaut of simulations and AI tools, and I am grateful for many helpful physics and simulation-related discussions we have had.
- Thank you to all past and present group members who helped me in many different ways, including Alex, Ben, Zack, Nathaniel, Hiro, Hana, Louis, Debyan, Mingda, Jungheng, and Saif.

Outside the research group, I am grateful for generous advising and support of many collaborators, advisors, and committee members:

- I feel especially indebted to have had Prof. Wolfgang Ketterle as a co-PI. As we all know, Wolfgang has an extraordinary ability to abstract away from experimental details and elevate an idea to its essential mechanism. Thank you, Wolfgang, for all the discussions that left me with fresh perspectives and a deeper understanding of our work, and for appreciating the technical work that goes into making the science possible.

- Thank you to Prof. Kang-Kuen Ni for being a long-term collaborator on the experiment and for bringing molecular tweezer expertise and sharp questions to our meetings. I was also excited to learn, even before coming to Harvard, that we both came through UC LEADS, a small UC research program that meant a lot to me as an undergraduate. That connection made the collaboration feel special, and made Kang-Kuen a role model to me from the start.

- I also want to thank Prof. Eunmi Chae for joining our meetings every week remotely from Korea at four in the morning. Your commitment and work ethic have been truly inspiring.

- Thank you to Prof. Evelyn Hu for being such an exceptionally approachable co-advisor, always managing to respond to my emails and clear my Crimson Cart within minutes. Your kindness and attentiveness have made every meeting and administrative step so pleasant.

- Thank you to Prof. Giulia Semeghini for serving on my committee and for being so generous with your time. Your questions and comments in meetings and talks were always thoughtful and direct, and you helped make the committee process feel smooth and non-intimidating.

To all the supporting staff who make our research possible, thank you:

- Erica Mantone for heroically handling all the administrative tasks from scheduling and purchasing to reimbursements, deadlines, and the many reminders that I admittedly often needed.

- Machine shop manager, Alejandro Lopez, for making the shop such a welcoming place with your passionate teaching and bright personality. I will miss your check-ins on my español, which unfortunately hasn't progressed much.

- Steve Sansone for tirelessly keeping the waterjet alive and running, for being such a calm presence whenever something needs fixing.

- Jim MacArthur at the electronics shop for your patient help with anything electronics-related, including helping me solder the tiniest things on my laptop motherboard which saved the laptop. Many parts of our lab would not have worked nearly as smoothly without you, and your help has been, quite literally, instrumental.

- Lisa Frazier Zezze, SEAS PhD academic coordinator, for all your timely reminders and prompt replies that keep so many of us on track.

Beyond research, I want to acknowledge Harvard Taekwondo (HTKD) and, outside of Harvard, CW Taekwondo, both of which have been essential to my mental and physical health during grad school. Thank you to everyone I have practiced and trained with, and to Master Jang and Coach Kathy at HTKD, and to people at CW for creating such wonderful spaces where people could come together and have a great time while working out hard together. The lessons I learned there will carry far beyond the mat.

I have been extremely lucky to have a tight group of friends who became pillars of my life in Boston. Thank you all for keeping me sane and grounded, reminding me that life existed beyond blinking lasers and pulse tube hissing.

- Enid has been my best friend since we met at the CUA retreat during G1. So, to future students: go to the retreat. You probably won't remember what you learned at the science talks, but you might gain a friendship to keep forever. Enid, thank you for being with me through the ups and downs, picking me up at various bus stops and subways stations because I have no sense of directions, for all the warm meals we shared and the irresistible cakes you made. Thank you also for igniting my insatiable passion for baseball and for many trips to Fenway.
- Greg, thank you for being such a reliable friend and a constant source of questionable wisdom. You carried me through many p-sets, and I cherish all the time we spent working together in that windowless room in Pierce, hyping each other up and goofing around. Whether over a warm cup of tea at dawn or a drink and good music late at night, you have made life feel just a bit more manageable.
- I feel deeply obliged to Caroline and Derrick, both of whom I first met through the Doyle group. Caroline, thank you for being one of the most selfless friends I know, always willing to go out of your way to help, and for bringing such steady optimism into my life. Derrick, thank you for your kindness, humor, and for being someone I could turn to in lab about anything. I still remember calling you on a Sunday night because I could not lift a heavy shield, and you came all the way from home to help. You made my time in the Doyle group much better, and I am very glad we have remained friends.

I want to extend my sincere thanks for friends who supported me from farther away. Yijin has been a close friend since high school and has witnessed many stages of my life. Thank you for years of support and friendship across distance. Kayla and Grant have been wonderful friends since undergrad, and somehow both of you also ventured into experimental AMO without

my influence. Speaking of AMO, I found my way into this field in large part because of the wonderful mentors I had as an undergraduate. Thank you to Prof. Wes Campbell, Xueping Long, and Tony Ransford for patiently teaching me when I knew very little, and for showing me the kind of scientific atmosphere I hoped to find in graduate school.

I am deeply grateful to my partner, Jing, for walking with me through these years with such patience and love. I have learned so much from you, both as a brilliant scientist and as a wonderful person. You bring a chemist's care and precision to everything, especially cooking, where you measure ingredients on a scale and I go by order of magnitude. Thank you for taking such good care of me, for the joy you brought, the delicious meals, the travel adventures, and for sharing my love of deep-sea fishing. Your passion for your work, focus, efficiency, and thoughtfulness with time have all been such positive influences on me. I cannot imagine this journey without you.

Lastly, I want to thank my family. Thank you, dad, for providing me the best life possible you could and your constant optimism. I also want to honor my stepdad, James, who passed away during my G3 year. Our time together in this world was far too short. I wish you could be here, and I know you would be proud. I am also thankful for the kindness of James's family, and for all the warm gatherings that filled the house with joy.

Most of all, I want to thank my mom – the single most important person in my life, and the most wholesome person I know. She raised and supported me largely on her own, and every part of who I am is built on her love, sacrifice, and resilience. In fact, my earliest memory of the concept of a dissertation came from watching my mom write her MBA thesis late at night on a ThinkPad. I remember thinking, from the comfort of bed, that I was very glad I would never have to go through that. Clearly, that did not age well. More than twenty years later, here I am writing this, also on a ThinkPad. Mom, I aspire to be even a fraction of the person you are. This dissertation, and everything it represents, belongs to you as much as it belongs to me.

Citations to Previously Published Work

Parts of this dissertation or the results described herein have been reported in the following articles:

1. S. S. Yu, A. Periwal, J. You, Z. Liu, Q. Lyu, Y. Cho, L. Anderegg, E. Chae, and J. M. Doyle, "High-fidelity entanglement of polar molecules by dynamic geometric control," arXiv preprint arXiv:2607.13008 (2026).

2. J. You, J. M. Doyle, Z. Liu, S. S. Yu, and A. Periwal, "Control of dipolar dynamics by geometrical programming," *Phys. Rev. Lett.* **135** (25), 253002 (2025).

3. S. S. Yu, J. You, Y. Bao, L. Anderegg, C. Hallas, G. K. Li, D. Lim, E. Chae, W. Ketterle, K.-K. Ni, *et al.*, "A conveyor-belt magneto-optical trap of CaF," *Nature Communications* **17** (1), 1175 (2026).

4. Y. Bao, S. S. Yu, J. You, L. Anderegg, E. Chae, W. Ketterle, K.-K. Ni, and J. M. Doyle, "Raman sideband cooling of molecules in an optical tweezer array to the 3D motional ground state," *Phys. Rev. X* **14** (3), 031002 (2024).

5. Y. Bao, S. S. Yu, L. Anderegg, E. Chae, W. Ketterle, K.-K. Ni, and J. M. Doyle, "Dipolar spin-exchange and entanglement between molecules in an optical tweezer array," *Science* **382** (6675), 1138–1143 (2023).

6. Y. Bao, S. S. Yu, L. Anderegg, S. Burchesky, D. Gonzalez-Acevedo, E. Chae, W. Ketterle, K.-K. Ni, and J. M. Doyle, "Fast optical transport of ultracold molecules over long distances," *New J. Phys.* **24** (9), 093028 (2022).

7. S. Burchesky, L. Anderegg, Y. Bao, S. S. Yu, E. Chae, W. Ketterle, K.-K. Ni, and J. M. Doyle, "Rotational coherence times of polar molecules in optical tweezers," *Phys. Rev. Lett.* **127** (12), 123202 (2021). doi:10.1103/PhysRevLett.127.123202

For us, there is only the trying. The rest is not our business.

T. S. Eliot, *Four Quartets: East Coker*

1 Introduction

1.1 Overview of Laser-cooled Polar Molecules

Polar molecules occupy a distinctive place in quantum science as they offer a compelling combination of quantum resources, including long-lived rotational transitions [3–6], large internal-state manifolds for multilevel encoding and synthetic dimensions [6–8], and permanent electric dipole moments that enable long-range entangling interactions [9–12] that can be tuned with microwave and dc electric fields [13–16]. These capabilities suggest new routes to quantum simulation of many-body spin dynamics [16–24], quantum information processing [7, 25–29], precision laboratory searches for dark matter [30, 31], and new CP-violating particles in the > 10 TeV range [32–35].

Turning these polar molecules into controllable quantum systems requires capability to control both their internal states and their motion. Over the past decade, laser cooling and manipulation of molecules on the quantum level has enabled researchers to obtain molecular

samples at μK or sub-μK temperatures. So far, two complementary approaches have been developed to bring molecules into the ultracold regime: coherent assembly from laser-cooled atoms [36–38], and direct cooling of molecules produced in a beam [39, 40]. The latter method is used in this work to produce ultracold gas of calcium monofluoride (CaF) [41].

Direct laser cooling of molecules requires an optical transition that can scatter many photons while keeping population within a small set of internal states. The difficult of applying this to molecules comes from the additional internal vibrational and rotational structure that can scatter population into many unaddressed dark states [42]. Nevertheless, for a growing class of species with highly diagonal Franck–Condon factors, a finite set of repumping lasers can close the optical cycle sufficiently to scatter the thousands to tens of thousands of photons required for slowing, trapping, and cooling. Beginning with direct laser cooling of an SrF beam [39], the technique has progressed rapidly, leading to three-dimensional magneto-optical traps (MOTs) of several diatomic species, including SrF [40], CaF [41], YO [43], BaF [44], and CaH [45], and, more recently, of the polyatomic molecules CaOH [46] and SrOH [47]. The MOT has become a starting point in experiments, where subsequent transfer from MOT into conservative optical dipole traps and tweezer arrays extend our control to individual molecules. [48, 49]

1.2 Polar Molecules for Quantum Information Science

A defining requirement for pursing both quantum simulation and quantum information processing is the ability to generate high-fidelity entanglement through controlled interactions. This has been demonstrated across quantum platforms ranging from resonant dipole-dipole exchange in Rydberg atom arrays [50, 51] to exchange-based gates in silicon quantum dots [52]. Polar molecules naturally provide us with a mechanism to realize quantum entanglement between particles through their electric dipole-dipole interaction. The long-lived rotational states can be used to encode an effective spin-1/2 degree of freedom, and the transition dipole moments mediate resonant exchange of rotational excitation.

Long-range spin exchange dynamics (equivalently the isotropic XY or XX Hamiltonian),

has been explored in several atomic platforms, including resonant dipole-dipole exchange between Rydberg atoms in optical tweezer arrays [50, 53, 54] and tunable XXZ dynamics with atoms in optical lattices [55]. In molecules, dipolar spin exchange was first observed with rotational states of KRb molecules pinned in a three-dimensional optical lattice [19], and dipolar-exchange physics has since been explored in layer-resolved and quantum-gas-microscope platforms [22, 56]. More recently, tweezer arrays of individually controlled molecules have realized rotational-state spin exchange at the single-molecule level, enabling deterministic two-molecule entanglement [9–11], including the CaF tweezer experiment described in parts of Chapter 7 and 8, and with Floquet engineering, programmable many-body XXZ and XYZ spin models [16]. Together, these developments place molecular systems in a practical regime for quantum simulation of interacting spin models and entangling operations for digital quantum information processing.

However, dipolar interactions are highly sensitive to the relative position of the molecules. For molecules in optical tweezers, thermal occupation of many motional states leads to a distribution of effective interaction strengths, degrading the interaction coherence and thereby limit the entanglement fidelity. This motional sensitivity had been a central limitation in molecular tweezer systems.

The effect is especially severe because optical tweezers are strongly anisotropic. The weak confinement along the longer tweezer beam axis makes the molecular positional wave packet more largely spread, so the axial thermal motion is the dominant contribution to dephasing. Previous demonstrations of molecular entanglement were fundamentally limited, at least in part, by a even few quanta motional excitation [9–11].

1.3 This Work: Geometric Control of Dipolar Interactions of CaF Molecules in Optical Tweezers

In this work, we demonstrate that this limitation can be overcome by controlling the geometry of the interaction between two molecules: by placing two laser-cooled CaF molecules at certain

relative geometries, the interaction can be tuned to become minimally sensitive to thermal motion while preserving a finite entangling interaction. We characterize several geometries that suppress sensitivity to thermal fluctuations.

Furthermore, we show that a molecule can be moved during the interaction without erasing the entanglement operation. This capability takes advantage of different timescales in molecular tweezers: the dipolar exchange is slow enough that the interaction geometry can be reconfigured during the entangling operation, yet fast enough compared with rotational coherence times. We use this programmable, coherence-preserving molecular motion to refocus dephasing arising from relative positional jitter of the optical tweezers, which is relevant even on the 10 nm scale. Controlled motion thereby becomes not just a tool for assembly and rearrangement, but a corrective resource during the interaction. This places molecular tweezer arrays within a broader family of quantum processors in which motion is a coherent control resource. In trapped ions and neutral atoms, for example, transport has enabled reconfigurable connectivity while simply preserving quantum information [57–59].

Using these methods, we generate a Bell state with fidelity of $F = 0.976^{+0.008}_{-0.011}$. This is, to our knowledge, the highest fidelity reported for directly laser-cooled molecules and is on par with the best demonstrations in assembled molecular tweezer platforms. Importantly, this performance does not require near-ground-state motional preparation. In prior approaches, residual motional excitation remained a fundamental limitation, and high fidelity relied on stringent cooling or species-specific trapping conditions. The methods demonstrated here are instead based on the relative geometry of the interacting molecules, and are therefore broadly applicable across molecular species and tweezer platforms.

Looking forward, when geometry can be programmed on timescales that are short compared with the entangling dynamics, spatial control can be used as part of Hamiltonian engineering [60], complementary to the static analog simulation based on fixed geometries [54, 61–63], and gate-based digital approaches [57, 64, 65]. This opens routes to robust two-qubit gates [66, 67], geometry-echo-protected many-body dynamics [68], and programmable molecular systems in which the network of effective couplings [69, 70] can be dynamically engineered during coherent

evolution.

1.4 Organization of This Dissertation

This dissertation develops the control of dipolar interactions between individually trapped CaF molecules in optical tweezers, with the central goal of making molecular entanglement robust against the motional and technical positional noise that inevitable arise in microscopic optical traps. The first part of the thesis introduces the molecular platform and the experimental methods required to prepare single CaF molecules in a programmable tweezer array. The later chapters then use this single-state quantum control to engineer the geometry of the dipole-dipole interaction, generating high-fidelity two-molecule entanglement by static and dynamic geometric control.

Chapter 2 introduces ultracold polar molecules as a resource for quantum science. We first discuss the nature and origin of dipolar interactions and the ways in which their long range, anisotropy, and tunability distinguish molecules from neutral atoms. The chapter then surveys the major scientific directions enabled by these features, including dipolar quantum simulation, Hamiltonian engineering, quantum information processing, state-resolved collisions, dipolar quantum matter, and precision measurements. This chapter sets the broad motivation for the thesis: polar molecules are not merely atoms with stronger interactions, but quantum objects whose internal structure and spatially programmable interactions provide a qualitatively different control toolbox.

Chapter 3 reviews the molecular structure of CaF relevant to laser cooling, trapping, and coherent manipulation. We describe the electronic ground state $X^2\Sigma^+$, its rotational and hyperfine structure, and the Zeeman and DC Stark interactions that define the molecular eigenstates in external fields. We then discuss the relevant low-lying $A^2\Pi$ and $B^2\Sigma^+$ excited states, followed by the AC Stark shifts and polarizability structure that determine the behavior of the quantum states of CaF in optical traps. The chapter ends by introducing the microwave transition dipole moment between rotational states and the role of blackbody radiation, both

of which set important scales for coherent dipolar experiments.

Chapter 4 describes the experimental apparatus and the technical developments essential for realizing a stable molecular tweezer platform. The chapter begins with the generation of two-dimensional (2D) optical tweezer arrays using SLM and AOD, including the detection path and feedback methods used to monitor relative SLM-AOD alignment. We then describe the characterization of the science glass cell and microscope objective, including interferometric optical testing, wavefront quality, and point-spread-function measurements. The chapter also covers passive and active stabilization of stray electric and magnetic fields, and the relevant laser systems. Together, these sections establish the optical, magnetic, and mechanical infrastructure required for coherent geometric control.

Chapter 5 follows the experimental sequence used to cool, trap, transport, and load CaF molecules into optical tweezers. After a brief review of RF MOT capture and sub-Doppler cooling, the chapter focuses on the blue-detuned conveyor MOT, which compresses the molecular cloud before ODT loading. We then describe the loading from the conveyor MOT into the ODT, transport into the science glass cell, and characterization of the optical tweezer traps. The final sections describe homogenization of the 2D hybrid array, including SLM aberration compensation, SLM-AOD transfer fidelity, and technical heating. These measurements provide the practical foundation for producing reproducible, well-characterized single-molecule arrays.

Chapter 6 develops single-molecule quantum control. We introduce the rotational qubit states used throughout the interaction and entanglement experiments and discuss their relevant sensitivities to magnetic fields, electric fields, and trap light, as well as methods to reduce these sensitivities. The chapter then describes state preparation by hyperfine optical pumping and microwave transfer, followed by measurements of single-qubit rotational coherence under magic trapping conditions and dynamical decoupling. The final part of the chapter presents Raman sideband cooling of CaF molecules in optical tweezers, including the theory of resolved sideband cooling, its molecular implementation, and later improvements that trade full ground-state preparation for higher molecule survival. This partial cooling sequence becomes important in Chapter 7, where it suppresses residual higher-order motional dephasing during Bell-state

generation.

Chapters 7 and 8 form the core result of the thesis. Chapter 7 introduces geometric engineering of the dipolar interaction. We first describe coherent spin-exchange interactions in a 1D array of CaF molecules and show how the dipolar coupling can be characterized experimentally. From these early results, we identify the central limitation of interaction coherence: the interaction strength J depends sensitively on the relative position and orientation of the molecules, so thermal motion and relative trap-center shifts convert spatial uncertainty into interaction dephasing. This motivates ways to suppress dephasing via engineering of interaction geometry.

The chapter then develops the idea of tuning the motional sensitivity of J in three dimensions, beginning with the planar magic angle and extending to a full three-dimensional magic configuration. In the experiment, the AOD controls the in-plane separation and angle, while the SLM controls the relative axial displacement, giving access to a three-dimensional interaction geometry. This geometry is then used to suppress sensitivity to thermal motion while preserving a finite dipolar interaction. The chapter further introduces dynamic geometric engineering through a positional echo, in which one molecule is moved during the interaction to refocus dephasing from quasi-static relative position noise. In summary, static geometry suppresses the dominant motional broadening, while dynamic geometry cancels first-order sensitivity to slow position offsets. We report that this positional echo improves dipolar coherence by about a factor of three and reaches $Q = 6.03(97)$ at an optimized three-dimensional geometry.

Chapter 8 converts the geometric-control tools of Chapter 7 into a high-fidelity entangling operation. I first review how spin-exchange dynamics generates Bell states and how Bell-state fidelity is extracted from pair populations and parity oscillations. The experimental sequence then combines several ingredients developed throughout the thesis: single-molecule state preparation, SLM-to-AOD handover, partial Raman sideband cooling, geometric positioning, XY8 dynamical decoupling, positional echo, and state-resolved readout. At the optimal configuration, the interaction produces coherent two-particle oscillations with $Q = 7.23(81)$; at the $\pi/2$ interaction time, the measured pair populations and parity oscillation give a Bell-state fidelity of $F = 0.976^{+0.008}_{-0.011}$. This result demonstrates that high-fidelity entanglement can

be achieved in directly laser-cooled molecules without relying on full motional ground-state preparation. We conclude the chapter with future avenues for improving fidelity.

...a gigantic minuscule game...

Primo Levi, *The Periodic Table*

2

Ultracold Polar Molecules for Quantum Science

2.1 Interactions Between Molecules

Two molecules interact with one another through fundamental electrostatic Coulomb potentials. At large intermolecular separation, this potential can be expanded in terms of multipole potentials, with decreasing interaction range scaling as $1/R^n$ where $n = 1, 2, ...$ is the multipole order [71]. For *neutral* polar molecules, the leading term is the dipole term (associated with separation of positive and negative charge distributions). Since the permanent electric dipole moment of a polar molecule is defined in the body-frame, in absence of an external electric field, the molecule's dipole moment is not oriented, so the averaged dipole moment in the lab frame is zero. As a result, the first-order dipole-dipole interaction vanishes for a pair of molecules in

the same parity rotational eigenstates. However, opposite-parity rotational states differing by one rotational quanta ($\Delta N = \pm 1$) are connected by a nonzero transition dipole matrix element.

For two molecules i and j separated by a vector $\mathbf{R}_{ij} = R_{ij}\hat{\mathbf{R}}_{ij}$, their electric dipole-dipole interaction is

$$\hat{H}_{dd} = \frac{1}{4\pi\epsilon_0} \frac{\hat{\mathbf{d}}_\mathbf{i} \cdot \hat{\mathbf{d}}_\mathbf{j} - 3(\hat{\mathbf{d}}_\mathbf{i} \cdot \hat{\mathbf{R}}_\mathbf{ij})(\hat{\mathbf{d}}_\mathbf{j} \cdot \hat{\mathbf{R}}_{ij})}{R_{ij}^3}. \tag{2.1}$$

Here, $\hat{\mathbf{d}}_\mathbf{i}$ is the dipole moment operator for molecule i and $\mathbf{R}_\mathbf{ij} = \hat{\mathbf{R}}_\mathbf{ij} R_{ij}$ is the vector connecting the center-of-mass positions of the two molecules. The interaction is long-ranged, state-dependent, and anisotropic –the interaction depends on orientation of the intermolecular axis relative to the quantization axis.

Equivalently, dipole-dipole interaction can be written as a scalar product of rank-2 spherical tensors [72–74]:

$$\hat{H}_{\mathrm{dd}} = \frac{\sqrt{6}}{4\pi\epsilon_0 R^3} \sum_{q=-2}^{2} (-1)^q C^2_{-q}(\theta,\phi)[\hat{\mathbf{d}}_1 \otimes \hat{\mathbf{d}}_2]^2_q, \tag{2.2}$$

This decomposition elucidates more of the physical structure of the interaction, separating the spatial term $C^k_q(\theta,\phi) = \sqrt{4\pi/(2k+1)}Y_{kq}(\theta,\phi)$ which describes the orientation of the intermolecular axis relative to the quantization axis, with the term that acts on the internal molecular states formed by coupling the two rank-1 dipole tensors of the two molecules: $[\hat{\mathbf{d}}_1 \otimes \hat{\mathbf{d}}_2]^2_q = \sum_{p_1,p_2} \langle 1p_1; 1p_2|2q\rangle \hat{d}_{1,p_1}\hat{d}_{2,p_2}$, where p_1 and p_2 label the spherical components of the dipole operators on molecules 1 and 2, respectively, with $p_i = -1, 0, +1$; the Clebsch-Gordan coefficient $\langle 1p_1; 1p_2|2q\rangle$ requires $p_1 + p_2 = q$. In optical tweezers or deep optical lattices, the molecules are highly localized compared with the intermolecular separation, so ${\mathcal{C}_\Pi}^{(2)}$ is typically treated as a geometry-dependent coupling evaluated at the mean trap centers, while the dipole operators remain as quantum operators acting on the internal-state manifold. Note that in the actual experiment, however, there is residual thermal motion that changes R_{ij}, θ_{ij}, and ϕ_{ij} each shot. This thermal motion-induced interaction disorder has been a central limit on coherent dipolar dynamics in molecular tweezer arrays and in later part, we will show methods to overcome this.

Projecting the dipole-dipole interaction H_{dd} into a two-state manifold maps our system

onto effective spin-1/2 models that are widely used in quantum simulation and quantum information [17, 18]. In the simplest case, one can encode an effective spin$-1/2$ degree of freedom in two lowest opposite-parity rotational states $|\uparrow\rangle$ and $|\downarrow\rangle$, connected by a transition dipole matrix element $d_{\uparrow\downarrow}$, and the electric dipolar interaction will lead to resonant exchange of rotational excitation between two molecules, which naturally realizes an XX spin-exchange Hamiltonian:

$$\hat{H}_{XX} = \hbar \sum_{i<j} J_{ij}^{\perp} \left(\hat{S}_i^x \hat{S}_j^x + \hat{S}_i^y \hat{S}_j^y \right) = \frac{\hbar}{2} \sum_{i<j} J_{ij}^{\perp} \left(\hat{S}_i^+ \hat{S}_j^- + \hat{S}_i^- \hat{S}_j^+ \right), \tag{2.3}$$

where

$$J_{ij}^{\perp} = \frac{|d_{\uparrow\downarrow}|^2}{4\pi\epsilon_0 \hbar R_{ij}^3} \left(1 - 3\cos^2\theta_{ij} \right). \tag{2.4}$$

Here the coupling strength $J_{ij}^{\perp}$ is set by the transition dipole matrix element $d_{\uparrow\downarrow}$, the intermolecular separation R_{ij}, and the orientation of the molecular pair relative to the quantization axis θ_{ij}. Note that the Hamiltonian in Eq. 2.3 conserves the total number of spin excitations.

Now, to get a more concrete picture of what it means to have "exchange of a rotational excitation", consider two molecules i and j, each prepared in either one of two rotational states $|\uparrow\rangle$ and $|\downarrow\rangle$ that differ by one quantum of rotational energy. In both of the anti-ferromagnetic states $|\uparrow_i\downarrow_j\rangle$ and $|\downarrow_i\uparrow_j\rangle$, the two-molecule system contains one unit of excitation. These two states are degenerate in absence of inter-molecule interaction. When the molecules are brought close together, the dipole-dipole interaction adds an off-diagonal coupling between them. The eigenstates of the two-molecule system are now the symmetric and anti-symmetric superpositions $\frac{|\uparrow_i\downarrow_j\rangle \pm |\downarrow_i\uparrow_j\rangle}{\sqrt{2}}$, and the interaction has a nonzero off-diagonal matrix element between these states $\langle\downarrow_i\uparrow_j | \hat{H}_{dd} | \uparrow_i\downarrow_j\rangle$. So, during time evolution under this Hamiltonian, the excitation de-localizes and coherently oscillates between the two molecules. In this sense, the rotational excitation is exchanged between the molecules. This dynamics is what is measured in our two-molecule Ramsey experiment for observing dipole-dipole interaction, as detailed in Chapter 7. We can either put two molecules in superposition state containing the degenerate single-excitation

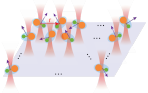
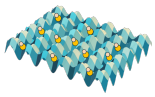
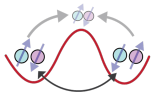
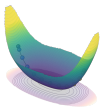
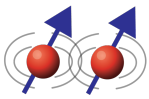
	 Polar molecules in tweezer arrays	 Polar molecules in optical lattice	 Rydberg atoms	 Ground-state neutral atoms	 Trapped ions	 Magnetic atoms
Interaction mechanism	Electric dipole-dipole	Electric dipole-dipole	Van der Waals; Resonant dipole-dipole	Contact interaction; Superexchange	Coulomb interaction	Magnetic dipole-dipole
Spatial form	$(1-3\cos^2\theta)/r^3$	$(1-3\cos^2\theta)/r^3$	$1/r^6$ or $(1-3\cos^2\theta)/r^3$	Mostly nearest-neighbor exchange	$1/r^\alpha$ $(0<\alpha<3)$	$(1-3\cos^2\theta)/r^3$
Native or accessible spin couplings	(J_x, J_y, J_z)	(J_x, J_y, J_z)	$(0,0,J_z)$ or (J_x, J_y, J_z)	(J_x, J_y, J_z)	$(0,0,J_z)$ or $(J_x, J_y, 0)$	$(J_x, J_y, J_z;\ -2J_z)$
Coupling Strength (Hz)	$J \sim 10$ - 10^2	$J \sim 10$ -10^4	$J \sim 10^4$ -10^9	$J \sim 1$-10^3	$J \sim 10^2$ - 10^4	$J \sim 10$ - 10^3
Relevant Coherence (s)	$\tau \sim 10^{-1}$ - 1	$\tau \sim 10^{-2}$ - 10^{-1}	$\tau \sim 10^{-6}$ - 10^{-4}	$\tau \sim 10^{-2}$ - 1	$\tau \sim 10^{-3}$	$\tau \sim 10^{-1}$ - 10^3
Present scale	$N \sim 10 - 10^2$	$N \sim 10^3 - 10^5$	$N \sim 10^2 - 10^3$	$N \sim 10 - 10^4$	$N \sim 10$ - 10^2	$N \sim 10^4 - 10^5$

Figure 2.1: Representative interacting quantum platforms for quantum simulation and quantum information. Relevant properties (interaction mechanism, spatial dependence, accessible spin couplings, characteristic coupling strengths, and coherent-evolution timescales) of several representative interacting quantum platforms have been studied experimentally for quantum simulation and quantum information processing in the context of our discussion. The quoted ranges are order-of-magnitude values from representative experiments.

component $|\uparrow_i\downarrow_j\rangle + |\downarrow_i\uparrow_j\rangle$, or directly initialize them in anti-ferromagnetic states $|\uparrow_i\downarrow_j\rangle$ (or $|\downarrow_i\uparrow_j\rangle$), and let the state evolve under $H_{\rm dd}$ for spin-exchange of rotational excitation. The physics can also be viewed in terms of a near-field resonant energy transfer, analogous to the concept of virtual photon used in molecular quantum electrodynamics and Förster-type energy transfer [75, 76].

2.2 Dipolar Quantum Simulation and Hamiltonian Engineering

The ability to trap and coherently manipulate ultracold polar molecules has opened a route to many-body systems governed by long-range and anisotropic interactions [17, 18, 29, 77]. We have introduced the simplest spin-1/2 XX model above, which naturally arises from the resonant dipole-dipole interaction between molecules. By adding or engineering an Ising term to the XX (or XY) spin model, one can obtain more general family of spin Hamiltonians, known

as the XXZ Hamiltonian.

$$\hat{H}_{XXZ} \sum_{i<j} = \left[J_{ij}^{\perp} \left(\hat{S}_i^x \hat{S}_j^x + \hat{S}_i^y \hat{S}_j^y \right) + J_{ij}^z \hat{S}_i^z \hat{S}_j^z \right]. \tag{2.5}$$

Here $J_{ij}^{\perp}$ is set by the transition dipole matrix element while J_{ij}^z, the Ising interaction strength, can be implemented using DC electric field dressing or microwaves to induce lab-frame dipole moments by mixing opposite-parity rotational states, as proposed in Ref. [17, 18]. If the two spin states acquire different lab-frame dipole moments, then the energy of a molecular pair can depend on whether the molecules occupy $|\uparrow\uparrow\rangle, |\uparrow\downarrow\rangle, |\uparrow\downarrow\rangle$, or $|\downarrow\downarrow\rangle$. In that case, the dipole-dipole interaction produces state-dependent energy shifts in addition to exchange, and these shifts appear as an Ising interaction $\hat{S}_i^z \hat{S}_j^z$ after projection into the spin-1/2 manifold. This has been realized with KRb molecules loaded in an optical lattice, where electric fields tune both spin-exchange and Ising interactions [14]; by tuning the ratio $J_{ij}^z / J_{ij}^{\perp}$, the model moves continuously between the XY-exchange limit and the Ising-dominated limit. Alternatively, an effective XXZ Hamiltonian can be synthesized dynamically, using microwave pulse sequences to periodically rotate the spin basis during native XY interaction, so that the time-averaged Hamiltonian contains an effective Ising component. This is explained in more details below.

An even more general anisotropic spin model is the XYZ Hamiltonian:

$$\hat{H}_{XYZ} = \sum_{i<j} \left(J_{ij}^x \hat{S}_i^x \hat{S}_j^x + J_{ij}^y \hat{S}_i^y \hat{S}_j^y + J_{ij}^z \hat{S}_i^z \hat{S}_j^z \right). \tag{2.6}$$

When $J_{ij}^x = J_{ij}^y$, the transverse part reduces to nominal XY exchange and conserves the total spin excitation number. When $J_{ij}^x \neq J_{ij}^y$, the Hamiltonian contains terms: $\hat{S}_i^+ \hat{S}_j^+ + \hat{S}_i^- \hat{S}_j^-$, which coherently create or annihilate pairs of spin excitations. These terms can be engineered using microwave or Floquet control. In the simplest Floquet construction, one can start from the natural spin-exchange Hamiltonian $\hat{H}_{XX}$ and apply a sequence of global microwave $\pi/2$ pulses to rotate the spin basis. In the toggling frame of the pulses, the XX+YY interaction appears as: (XX+YY), (XX+ZZ), (YY+ZZ). When the pulse period is short compared with

the dipolar evolution time, the leading-order average Hamiltonian is a weighted sum of these toggling-frame Hamiltonians, allowing an effective XXZ or XYZ model to be engineered by choosing the time spent in each frame. Recent molecular experiments have begun to access this regime using Floquet-engineered XXZ and XYZ dynamics in KRb in optical lattices [15], as well as in CaF tweezer arrays to generate tunable XXZ and XYZ spin chains [16].

In such control schemes, the accessible couplings are set by positive duty cycles, so the coupling vector lies inside a triangle inside a restricted region of parameter space, as shown in Fig. This can be limiting for Hamiltonians requiring relative sign reversal to realize arbitrary XYZ couplings, for example, the canonical two-axis-twisting Hamiltonian, which has the form:

$$\hat{H}_{\mathrm{TAT}} \propto \hat{S}_x^2 - \hat{S}_y^2. \tag{2.7}$$

One way to extend the access more models is through dynamic geometry control with optical tweezers, which we introduce in Chapter 7 of this thesis. Analogous to time-domain Floquet control, one can engineer the Hamiltonian via spatial movement [60]. Because the interaction contains the angular factor $1 - 3\cos^2\theta_{ij}$, dynamically moving molecules relative to the quantization axis changes both the magnitude and the sign of the exchange Hamiltonian during the interaction period.

In optical lattices, molecules are allowed to tunnel and their motion couples to their internal state through dipolar interactions, leading to a different class of Hamiltonians: t-J-V-W model, a natural extension of Hubbard physics in which spin, density, and motion are coupled by long-range dipolar interactions [18, 78]. The Hamiltonians may contain tunneling t, spin exchange J, as well as density-density interactions $V_{ij}n_in_j$, and density-spin couplings of the form $W_{ij}(n_i\hat{S}_j^z + n_j\hat{S}_i^z)$. These models all simulations of itinerant magnetism, spin-motion coupling, correlated transport, generalized Hubbard models, and strongly interacting dipolar matter [18, 23].

Taken together, these works show that interaction between polar molecules can be harnessed to realize a wide range of spin models for quantum simulation. The most direct projection of

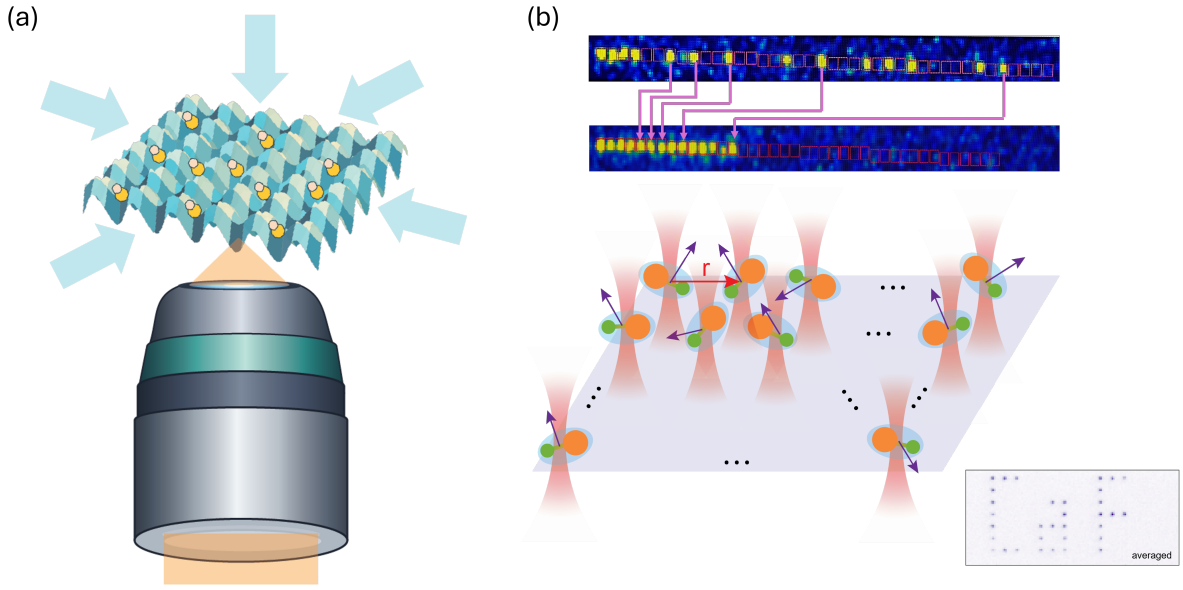


Figure 2.2: Experimental platforms for quantum simulation with atoms and molecules: quantum gas microscope (left) and optical tweezer array (right). Quantum gas microscopes use high-resolution imaging of particles in optical lattices to access site-resolved observables in extended many-body systems, while rearrangeable optical tweezer arrays assemble particles into programmable geometries by moving individually occupied traps.

the resonant rotational dipole-dipole interaction gives a long-range XX model. Dressing fields add state-dependent Ising terms and produce XXZ models, and Floquet pulse sequences extend the control to XYZ Hamiltonians and beyond.

2.3 Quantum Information Science

Molecule-based quantum information platforms are still at an early but rapidly advancing stage. Recent experimental progress has established that ultracold molecules can now be prepared and manipulated with high fidelity in bulk gases, three-dimensional optical lattices, and individually addressed tweezer or lattice sites [3, 22, 79]. In the span of four years, the field has moved from proposals of dipolar gates to first experimental demonstrations of two-molecule entanglement and iSWAP gates, and to high-fidelity entanglement approaching the 0.99 level [12, 80]. Progress in quantum information science across diverse quantum architectures, including superconducting circuits, trapped ions, semiconductor spins, neutral atoms, and

molecules, is driven by improving a common set of hardware capabilities [81–83]. Grounded in the foundational DiVincenzo criteria [84], which states that a useful quantum-computing platform needs scalable, well-characterized qubits; reliable initialization; long coherence times compared with gate operations; a universal gate set; and qubit-specific readout, these universal benchmarks translate to quantitative requirements on state preparation, readout, single-qubit gates, and two-qubit entangling operations. Neutral-atom arrays have developed this paradigm using programmable optical tweezers and Rydberg-mediated interactions [62, 85]. As discussed below, molecular tweezer arrays inherit the same programmability as atomic arrays, while offering distinct features and opportunities.

The earliest proposal in 2002 for quantum computation with molecules envisioned individual diatomic molecules trapped in a one-dimensional array, with qubits encoded in molecular states whose dipoles are oriented by the dc electric field and coupled by electric dipole-dipole interaction [25]. A subsequent proposal [26] took advantage of the switchable dipolar interaction: quantum information can be stored in weakly interacting molecular states, while interactions are turned on by selectively coupling one of the qubit states to an auxiliary state with a substantially larger dipole moment. Evolution under the $\hat{H}_{XX}$ Hamiltonian implements an iSWAP-type operation; The iSWAP gate, together with arbitrary single-qubit rotation gates, forms a gate set that is sufficient for universal quantum computation.

A complementary scheme uses state-dependent permanent or induced dipoles to generate controlled-phase gates. In this case, the pair energy depends on the two internal states occupied by the molecules, producing an Ising-like interaction instead of resonant exchange [25–27]. Such schemes are natural for molecules whose rotational or parity-doublet structure allows interactions to be switched by coupling weakly interacting storage states to strongly polarized auxiliary states [25, 26, 86, 87]. Compared with exchange gates, controlled-phase gates place somewhat different demands on the experiment, since the desired conditional phase is accumulated only when the relevant population is mapped into the interacting manifold. The experiment must therefore return population to the computational basis with low leakage, while calibrating or refocusing single-particle phases from differential AC stark or dc field-induced shifts.

2.3.1 Molecular Tweezer Array Platform for Quantum Information

Programmable optical tweezers provide exquisite control over single molecules for implementing these ideas, due to their scalability and individual site addressability [49, 88–92]. In particular, since the dipolar coupling strength scales as $1/r^3$, separations $\lesssim$ few micrometers are needed for the interaction to be appreciable for typical dipolar molecules ($\sim$ tens of Hz to kHz). Dynamic tweezer control allows molecules to be rearranged, brought close together for interaction, and separated again for storage or readout.

Experimentally, like any other physical qubits, molecular qubits inadvertently are coupled to lab environment. Therefore, before molecular qubits could be useful, one must ensure the single-qubit coherence time –the duration for which a qubit coherently stores the quantum information– of individual molecules can be preserved over a timescale that is much longer than the quantum gate operation time. However, with the tightly confining optical tweezer traps come larger induced differential light shifts, causing the qubit transition frequency to vary across the trap depending on the thermal trajectory of the molecule. Pioneering work in our group by [3] first identified pairs of states in the lowest two rotational manifolds and experimentally showed the existence of a “magic condition", where a certain combinations of trap intensity, applied magnetic field strength (which sets the quantization axis), and the angle of linear trap polarizations with respect to the quantization axis, can suppress first order differential light shifts. This leads to a measured rotational coherence time of 470(40) ms (with a spin-echo), establishing that rotational coherence of molecules trapped in tweezers can be preserved for times far longer than typical dipolar interaction times.

With this single-particle control in place, the coherent dipolar exchange between pairs of molecules was first realized in 2023 in our work[9], and concurrently in [10], between individual laser-cooled CaF molecules. Rotational states are used to encode an effective spin$-1/2$ XY Hamiltonian, which generated Bell states with SPAM-corrected fidelity of 0.89(6) [9]. This is followed by implementation of an universal iSWAP gate between hyperfine-state molecular qubits in tweezer array of NaCs molecules [11]. In the NaCs experiment, “magic" trap ellipticity

is used to suppress differential tensor light shifts between rotational states: in the high magnetic-field regime of the NaCs experiment, the rotational eigenstates are strongly affected by the trap polarization, and tuning the ellipticity of the tweezer light cancels the first-order differential light shift between the relevant rotational states, enabling a measured coherence time up to 250(40) ms, and a 94(3)% Bell state fidelity [11]. Around the same time, work with RbCs in magic-wavelength tweezers produced long-lived two-molecule entanglement, reporting SPAM-corrected Bell-state fidelity $0.976^{+0.014}_{-0.016}$, with no measurable entanglement decay over 0.5 s [12].

These early results also made clear the technical limits to molecular entanglement fidelity. Dipolar interactions depends sensitively on the relative positions between two molecules. But molecules in an optical trap are never perfectly pinned at trap potential center due to thermal motion, especially along the weakly confined trap beam axis. The thermal motion makes molecules sample different distances and angles across experiment shots, and the decoherence can be understood as a distribution of effective interaction strengths across shots. For pure fluctuations in $\mathbf{r}$, the leading fractional change is $|\delta J/J| \simeq 3|\delta r/r|$, in addition to changes in the dipolar angle. Improving dipolar coherence is therefore directly on the critical path to realistic high-fidelity molecular entanglement. A main part of this thesis work addresses this limitation by developing two complementary techniques based on both static and dynamic control of the interaction geometry, as detailed in Chapters 7 and 8.

Scalable quantum information processing also requires high-fidelity preparation and readout. Additional challenges are faced by molecular systems as population can leak into many uncoupled dark states. This complexity, however, can also be a resource: looking beyond two-qubit gates, molecules provide natural qudit encoding and multi-level quantum registers [7]. Rotational and hyperfine manifolds contain many long-lived, microwave-addressable states, so more broadly, a $d = 2^n$ multilevel system, or in some encodings, several virtual qubits can be encoded within one molecule [7]. Multilevel encodings can make some algorithms more compact, as operations internal to one molecule can replace operations that would otherwise require multiple two-level systems and entangling gates, although the advantage is algorithm- and

hardware-dependent [7, 93–95].

The internal complexity of molecules has also motivated more ambitious and unique forms of error protection based on rotational degrees of freedom, and designed to be robust against certain physical errors [96]. Proposals for molecular rotor codes and absorption–emission codes explore how logical information might be encoded and distributed over rotational states to address noise channels native to molecular platforms, including spontaneous photon emission, absorption, or small changes in angular momentum [96–98]. Although these ideas are still theoretical, they highlight a potential route to protecting quantum information in molecules, where some of the redundancy needed for quantum error correction may eventually be stored inside one molecule's large Hilbert space rather than across several separate particles.

2.4 State-resolved Ultracold Chemistry and Collisions

Ultracold polar molecules constitute an exceptional system for controlled quantum chemistry. At room temperatures, chemical reactions typically average over many internal states of the reactants. At ultracold temperatures (typically $\sim 1\mu$K and below), molecules can be populated in a small number of quantum states, or even in single quantum states. In this regime, the thermal de Broglie wavelength far exceeds the range of interaction potential, so molecule-molecule collisions occur in the quantum threshold regime where only a few partial waves contribute, and reaction or loss rates can depend sensitively on quantum statistics, long-range interactions, external fields, and the prepared internal states of the molecules [99–102]. Understanding and controlling collisions are important for many practical applications of ultracold molecules, such as achieving dense molecular gases, evaporative cooling, quantum-degenerate dipolar matter, and loading a large-scale molecule array. At the same time, having molecules at ultracold temperatures inspires one to ask microscopic chemical questions: Can reaction rates or pathways be tuned by preparing the molecules in certain internal states? Can product-state distributions be measured or controlled? Experiments with bulk gas of ultracold KRb have shown that quantum statistics and internal-state preparation can strongly affect reaction rates [101], that

reactants, intermediate complexes, and products can be directly observed in a bimolecular reaction [103], and that nuclear-spin conservation can enable state-to-state control over reaction products [104, 105].

Optical tweezers of molecules are a particularly pristine way to control and study ultracold chemistry in a few-body limit: Individual molecules can be separately trapped and state-prepared, merged into the same tweezer and allowed to collide, and detected with single-particle sensitivity [106, 107]. This capability was first demonstrated in our CaF tweezer experiment in Doyle group to observe collisions between exactly two ultracold CaF molecules [106], where both molecules are prepared in either the absolute ground state or in selected excited hyperfine and rotational states. This level of control also makes it possible to approach chemistry in a bottom-up way where chemical reactions begin with known number of molecules in known internal states.

2.5 Dipolar Quantum Matter

Another active research frontier is creating dense, stable, quantum-degenerate gases of polar molecules. These degenerate molecular gases open routes to phases that are difficult to access with magnetic atoms or contact-interacting atomic gases. In this regime, instead of using molecules for simulating a target Hamiltonian as in analog quantum simulation [63], the electric dipolar interactions of the molecular gas itself can govern the equilibrium phases and collective dynamics of the system.

The first milestone was the realization of a degenerate Fermi gas of ground-state KRb molecules [108], where Fermi statistics suppresses short-range reactive collisions, providing a long-lived quantum degenerate sample. Subsequent work evaporatively cooled the reactive KRb molecules to below the Fermi temperature, using tunable dipolar interactions to enhance elastic collisions while suppressing short-range loss [109]. Nevertheless, evaporative cooling of dense, interacting molecular gases remained broadly challenging. The difficulty is that at short intermolecular range, molecules can undergo chemical reactions or form long-lived collision

complexes because of their dense rovibrational structure [107, 110, 111]. These processes can lead to rapid loss even for chemically stable species.

A powerful method that has been developed in the past decade to solve this problem is collisional shielding. The idea is to use either microwave or DC electric fields to engineer a repulsive potential that prevents molecules from reaching short range while preserving large elastic collision rates [112–115]. Microwave shielding, in particular, dresses rotational states with a near-resonant microwave field to create an effective long-range repulsive barrier. This mechanism was first demonstrated experimentally in our work with laser-cooled CaF in optical tweezers [116] and has subsequently enabled evaporative cooling of microwave-shielded fermionic NaK molecules to well below the Fermi temperature [117]. The bosonic counterpart followed the first molecular Bose-Einstein condensate of dipolar NaCs in 2024 [118]. More recently, microwave-dressed NaCs condensates have been used to create self-bound molecular droplets and droplet arrays, demonstrating that dipolar interactions can drive qualitatively new phases of quantum matter [119].

In fermionic systems, the long-range and anisotropic feature of the dipolar interaction can favor unconventional odd-parity pairing, and it is predicted that polarized dipolar fermions can undergo superfluid pairing with an anisotropic order parameter [120, 121]. In 2D gas, with microwave dressing, fermonic polar molecules have been proposed as a way to obtain topological $p_x + ip_y$ superfluid phase, as the dressed interaction provides an attractive $1/r^3$ tail to support p-wave pairing [122]. But obtaining such phase requires exceptionally low entropy (with estimates for microwave-shielded NaK suggesting $T/T_F \lesssim 0.14$)), long lifetimes (on the order of seconds) at two-dimensional densities near $10^9, \mathrm{cm}^{-2}$, and precise control of microwave dressing. On the other hand, bosonic dipolar molecules provide a complementary route to strongly correlated matter. Dipolar molecules in optical lattices naturally realize extended Bose-Hubbard models, in which off-site density–density interactions compete with tunneling and on-site interactions, supporting richer phase diagram than the contact-interaction Bose–Hubbard model [17, 123, 124].

2.6 Precision Measurements and Fundamental Physics

Precision measurement is one of the most distinctive applications of ultracold molecules. Certain polar molecules possess features that can amplify small symmetry-violating or beyond-Standard-Model effects [125–127]. In general, this class of application has quite different experimental requirements from molecular quantum simulation or quantum information processing. Precision measurement experiments typically benefit from large molecule number in bulk, long interrogation time, exceptional control of electric and magnetic fields (order of) and all gradients, and systematic-error rejection through field reversals or internal co-magnetometer states. Laser cooling and trapping can improve these measurements by increasing coherence time, reducing systematics, and enabling high-fidelity preparation in selected quantum states.

Searches for eEDM. A quintessential example is the search for the electron electric dipole moment (eEDM). An electron having a nonzero permanent EDM would constitute direct evidence of time-reversal symmetry violation, and, assuming CPT symmetry, would also imply $\mathcal{CP}$-violation beyond the Standard Model. Such new $\mathcal{CP}$-violating phases are strongly motivated by the observed matter-antimatter asymmetry of the Universe [126, 127]. The experimental observable for an eEDM is an energy shift: $\Delta E_{\mathrm{EDM}} \propto -d_e \cdot E_{\mathrm{eff}}$, where E_{eff} is the effective electric field experienced by the electron. A nonzero observable effect arises from relativistic electronic structure, especially near heavy nuclei, where the eEDM interaction mixes electronic wavefunctions of opposite parity. This relativistic enhancement grows rapidly with nuclear charge and makes heavy atoms and molecules especially sensitive probes [128]. The current best experimental limit $|d_e| < 4.1 \times 10^{-30}\, e\,\mathrm{cm}$ was set using trapped HfF^+ molecular ions at JILA [129]. Complementary measurements using a cryogenic ThO beam by the ACME collaboration provide independent and different systematics [130].

Polyatomic molecules offer additional advantages for next-generation eEDM and other moments searches. Heavy polyatomic molecules such as YbOH, RaOH, SrOH, BaOH, $ThOH^+$ and $RaOH^+$, are especially promising because they combine laser-coolability, polarizability, long coherence times, with their parity-doublet or bending-mode structure useful for

fundamental-symmetry tests [125, 126, 129]. In linear triatomic molecules, bending modes create closely spaced opposite-parity states, allowing the molecule to be polarized in modest electric fields, and can provide internal co-magnetometer states, enabling suppression of systematic errors [30, 35]. This has been demonstrated with optically trapped CaOH as a proof-of-principle experiment [131]. Heavier molecules provide larger eEDM enhancement factor [132–134]. In particular, RaOH is a candidate uniquely sensitive to both eEDM and $\mathcal{P},\mathcal{T}$-violation searches [132, 135]: radium-containing molecules are expected to have large effective electric fields ($\sim$55 GV/cm) for eEDM searches, and the octupole-deformed ^{225}Ra nucleus can enhance sensitivity to hadronic CP-violating moments such as nuclear Schiff moments [132, 135, 136].

Variation of fundamental constants and ultralight dark matter. Beyond eEDM searches, certain molecular spectra are also sensitive to possible temporal or spatial variation of the fundamental constants, in particular the fine-structure constant α and the proton-to-electron mass ratio $\mu \equiv m_p/m_e$. This is because transitions between near-degenerate levels have large fractional sensitivity to variations in these constants [137, 138]. In a related direction, ultralight dark matter fields would manifest as oscillating transition frequencies, and laser-cooled SrOH has been proposed as a platform with strongly enhanced sensitivity to ultralight bosonic dark matter through its coupling to $\partial_t \mu$, enabled by nearly degenerate vibrational levels [30]

Nuclear spin-dependent parity violation. Molecules are also sensitive probes of nuclear spin-dependent parity violation, which arises from weak electron-nucleon interactions and nuclear anapole moments, as the the near-degenerate opposite-parity rotational states can amplify the otherwise tiny mixing [139].

Twice two makes five is sometimes a very charming thing too.

Fyodor Dostoyevsky, *Notes from Underground*

3

Molecular Properties and Quantum States of CaF

The general theory of diatomic molecular structure, and its application to CaF, has been discussed extensively in several previous CaF theses, including Refs. [140–142]. Here we focus on state specific structure in CaF that is essential for the studies in this thesis. This includes the effective Hamiltonians, angular-momentum bases, spectroscopic constants, and field-dependent Zeeman and Stark shifts for the electronic ground state, as well as for the low-lying and excited states. We also discuss the optical polarizability relevant to optical trapping.

3.1 Overview of CaF and its Amenability to Laser Cooling

Direct laser cooling of molecules requires an optical transition that can scatter many photons while keeping population within a small set of internal states. In other words, each absorption–

emission cycle must return the molecule to states that are either part of the cooling cycle or can be efficiently repumped. In practice, three ingredients are especially important. First, the molecule must have an electronically allowed transition with a sufficiently large scattering rate. Second, spontaneous emission from the excited electronic state must return predominantly to a small number of vibrational levels. Third, leakage into long-lived electronic, vibrational, or rotational manifolds not addressed by the cooling light must be negligible or experimentally manageable [42, 143].

The vibrational part of this requirement is usually expressed in terms of Franck–Condon factors (FCF). Physically, since electronic excitation is much faster than nuclear motion, the nuclei can be approximated as stationary during the electronic transition. This is referred to as the Born–Oppenheimer approximation. In a potential energy diagram, each electronic state defines an effective potential energy curve $V_e(R)$ for the nuclear motion, where R is the internuclear separation of the two atoms. The probability for spontaneous emission from an excited vibrational level ν' to a ground-state vibrational level ν is then governed, to leading order, by the squared overlap of the nuclear wavefunctions, $q_{\nu'\nu} = |\langle\chi_\nu|\chi_{\nu'}\rangle|^2$. A "diagonal" FCF matrix therefore means that q_{00} is close to unity and the off-diagonal overlaps q_{01}, q_{02}, *etc.* are small. Laser cooling favors highly diagonal FCFs where most decay returns to the same vibrational level, while the small residual leakage can be recovered with a finite number of repump lasers. Rotational branching must also be closed, usually by choosing a transition whose angular-momentum and parity selection rules force spontaneous emission back into the desired rotational manifold.

For a generic molecule, this is difficult. Electronic excitation can change the equilibrium bond length, the curvature of the molecular potential, and sometimes even the character of the chemical bond. The emitted photon then scatters the molecule into many possible vibrational and rotational states, rapidly leaking population outside the addressed cycle.

Alkaline-earth monohalide radicals such as CaF, SrF, and BaF, commonly written as M-X, where M is an alkaline-earth metal and X is a halogen, greatly reduce these difficulties. The bonding in these molecules can be viewed as strongly ionic, in which one valence electron

is transferred from the alkaline-earth atom to the halogen, leaving a closed-shell ionic core together with one unpaired electron localized mainly on the metal end.

In CaF, this picture is roughly Ca^+F^-, or equivalently a $Ca^{2+}F^-$ core plus a Ca-centered valence electron. Because the optically active electron is largely localized away from the bond, electronic excitation changes the nuclear potential only modestly. The ground and excited vibrational wavefunctions therefore have large overlap, giving the diagonal Franck–Condon structure needed for photon cycling. The unpaired valence electron in CaF gives the molecule electronic spin $S = 1/2$ and produces a $^2\Sigma^+$ electronic ground state. Taking the molecular axis to define $\hat{z}$, the Ca-centered $4s$ orbital and the $4p_z$ orbital both have σ symmetry, meaning that the projection of electronic orbital angular momentum onto the molecular axis is $\Lambda = 0$. The anisotropic electrostatic potential of the nearby F^- ion mixes orbitals of the same molecular symmetry, so the Ca-centered valence orbital is not a pure atomic $4s$ state. This s-p_z admixture polarizes the electronic density along the molecular axis and contributes to the large body-frame permanent electric dipole moment of CaF, approximately 3.07 D.

This electronic localization also explains the relatively simple hyperfine structure. We use $^{40}Ca^{19}F$, where ^{40}Ca has nuclear spin $I_{Ca} = 0$, so the nuclear spin comes entirely from ^{19}F, with $I_F = 1/2$. Since the unpaired electron is concentrated near Ca, the Fermi-contact interaction with the fluorine nucleus is weak compared with typical alkali-atom hyperfine splittings, although it is still large enough to resolve the ground-state hyperfine components. The resulting structure is well described by an effective $X^2\Sigma^+$ Hamiltonian containing rotational, spin-rotation, and hyperfine terms.

In this chapter, we will discuss in detail the ground and first two lowest lying electronic states of CaF relevant to this work, the laser schemes involved, and the behavior of these states in external electric and magnetic fields.

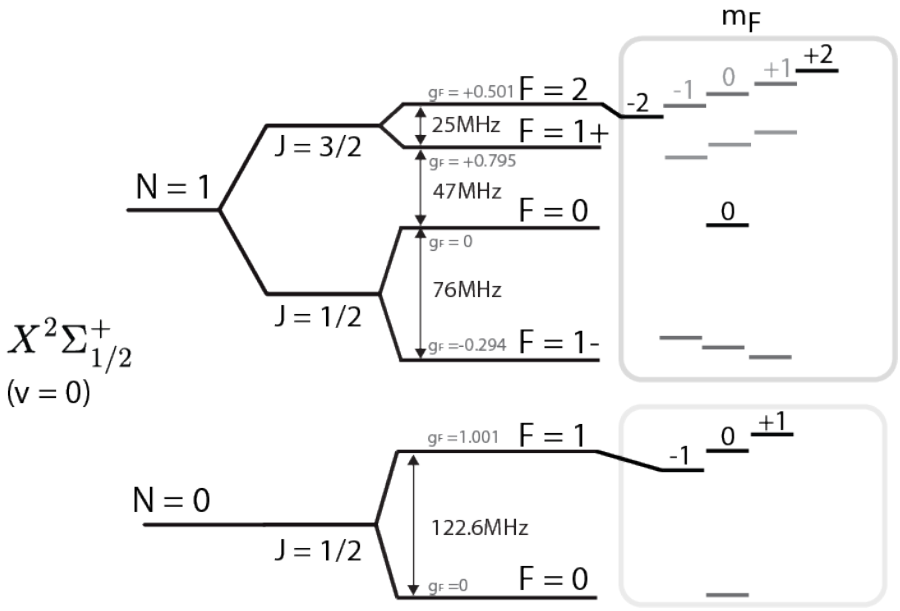


Figure 3.1: (a) Quantum level diagram for $X^2\Sigma(v = 0)$ state in CaF, showing hyperfine and Zeeman substates within the lowest two rotational manifolds, the energy splittings between the hyperfine states, and the g-factor [1, 2].

3.2 Electronic Ground State of CaF ($X^2\Sigma$)

The electronic ground state of $^{40}Ca^{19}F$ is $X\,^2\Sigma^+$ (or abbreviated to "X"). Some of the most important features and symmetries are encoded in this term symbol: the label X denotes the lowest electronic state. The superscript 2 gives the spin multiplicity $2S+1 = 2$, so the electronic spin is $S = 1/2$. The symbol Σ means that the projection of the electronic orbital angular momentum onto the internuclear axis is $\Lambda = 0$. The superscript $+$ denotes the symmetry of the electronic wavefunction under reflection in a plane containing the internuclear axis.

The X state internal structure is set by a small number of angular momenta: the rotation of the nuclei, the spin of the unpaired electron, and the nuclear spin of fluorine. The effective Hamiltonian for this state describes how these angular momenta couple to one another and how the resulting levels shift in applied electric and magnetic fields. Because $\Lambda = 0$, the electronic orbital angular momentum is not strongly coupled to the molecular axis, and there is no first-order spin-orbit splitting within the $X\,^2\Sigma^+$ state. The largest internal energy scale is set by the end-over-end rotation of the nuclei (molecular rotation), described by the angular

momentum $\mathbf{N}$ of the nuclei about the center of mass. This rotation couples weakly to the electron spin $\mathbf{S}$ through the spin-rotation interaction. The resulting angular momentum $\mathbf{J}$ then couples to the nuclear spin $\mathbf{I}$ to form the total angular momentum $\mathbf{F}$, where the only nuclear spin in $^{40}Ca^{19}F$ is the fluorine ^{19}F spin with $I = 1/2$, : $\mathbf{J} = \mathbf{N} + \mathbf{S}, \quad \mathbf{F} = \mathbf{J} + \mathbf{I}$.

The most natural basis for a low-lying $^2\Sigma$ state to use is the Hund's case (b) basis [74]. At low magnetic and electric fields, where the hyperfine eigenstates are good quantum states, we use the coupled basis:

$$|\Lambda = 0, N, S = 1/2, J, I = 1/2, F, m_F\rangle \equiv |N, J, F, m_F\rangle \tag{3.1}$$

Here N labels the rotational manifold, J includes electron spin, F includes nuclear spin, and m_F is the projection of $\mathbf{F}$ onto the laboratory quantization axis. For each $N > 0$ state, the allowed values of J and F follow directly from angular-momentum addition. The spin-rotation coupling splits the rotational level into $J = N \pm 1/2$. Hyperfine coupling to $I = 1/2$ further splits each J level into $F = J \pm 1/2$. Thus the $N = 0$ manifold contains $F = 0, 1$, while the $N = 1$ manifold contains four hyperfine branches, commonly labeled $F = 1^-$, $F = 0$, $F = 1^+$, and $F = 2$, where the sign on $F = 1^\pm$ distinguishes the $J = 1/2$ and $J = 3/2$ branches.

3.2.1 Molecular Constants and Energy Scales

Throughout the thesis, note that we often write the internal Hamiltonian in frequency units when spectroscopic constants are quoted in Hz. For $X\,^2\Sigma^+(v = 0)$, the relevant molecular constants are

Constant	Value	meaning
B_0	10267.5387 MHz	Rotational constant
D_0	0.014060 MHz	Centrifugal distortion
γ	39.65891 MHz	Spin-rotation coupling
b	109.1839 MHz	Isotropic Frosch-Foley hyperfine constant
c	40.1190 MHz	Anisotropic hyperfine constant
C_I	0.02876 MHz	Nuclear spin-rotation constant
d_0	3.07 D	Permanent body-frame electric dipole moment

The rotational spacing is set by $2B_0 \simeq 20.535$ GHz, which is much larger than the fine and hyperfine splittings.

3.2.2 Field-free Hamiltonian of $X^2\Sigma$ State

The field-free Hamiltonian describes the internal structure of CaF in the absence of applied electric or magnetic fields. The electronic and vibrational motion mainly set an overall energy, and so within a single vibrational level of the $X, {}^2\Sigma^+$ state, the internal structure is determined by molecular rotation and by the couplings among $\mathbf{N}$, $\mathbf{S}$, and $\mathbf{I}$. Since $\Lambda = 0$, there is no first-order electronic orbital angular momentum in the Hamiltonian, and the field-free state structure can be well described by an effective ${}^2\Sigma$ Hamiltonian [74]:

$$\begin{aligned} H_X/h &= B_0\mathbf{N}^2 - D_0\mathbf{N}^4 + \gamma\,\mathbf{N}\cdot\mathbf{S} + b\,\mathbf{I}\cdot\mathbf{S} + c\,(\mathbf{I}\cdot\hat{\mathbf{n}})(\mathbf{S}\cdot\hat{\mathbf{n}}) + C_I\,\mathbf{I}\cdot\mathbf{N} \\ &= B_0\mathbf{N}^2 - D_0\mathbf{N}^4 + \gamma\,\mathbf{N}\cdot\mathbf{S} + b_F\,\mathbf{I}\cdot\mathbf{S} + \frac{c}{3}\sqrt{6}\,T^{(2)}(C)\cdot T^{(2)}(\mathbf{I},\mathbf{S}) + C_I\,\mathbf{I}\cdot\mathbf{N}. \end{aligned} \tag{3.2}$$

Here B_0 is the rotational constant and D_0 is the centrifugal distortion constant. The first term gives the rigid-rotor energy, while the second accounts for the stretching of the bond at higher rotational angular momentum. The constant γ describes the spin-rotation interaction, which couples the electron spin $\mathbf{S}$ to the rotating molecular frame. The constants b and c describe the electron-nuclear hyperfine interaction with the fluorine nucleus, where b gives the isotropic Fermi-contact interaction, and c gives the anisotropic dipolar part. $\hat{\mathbf{n}}$ is the internuclear axis

unit vector. The last term, with coefficient C_I, is the nuclear spin-rotation interaction. The form in the second line is written in irreducible tensor form, separating the scalar hyperfine interaction, proportional to $\mathbf{I} \cdot \mathbf{S}$, from the rank-2 tensor hyperfine interaction. $T^{(2)}(C)$ is the rank-2 rotational tensor of normalized spherical harmonics $C_q^{(2)}(\theta, \phi)$, and $T^{(2)}(\mathbf{I}, \mathbf{S})$ is the rank-2 tensor product of the nuclear and electron spin operators. The b_F constant is the effective scalar hyperfine constant in this tensor form. The tensor notation can be very convenient because the matrix elements follow angular momentum algebra nicely.

Here we will go over the matrix elements of each of the terms to elucidate the different physical interaction and couplings.

The rotational and spin-rotation terms are diagonal in $|N, J, F, m_F\rangle$, so we have:

$$\begin{aligned} \langle i'|H_{\text{rot}}/h|i\rangle &= [B_0 N(N+1) - D_0 N^2 (N+1)^2]\delta_{N'N}\delta_{J'J}\delta_{F'F}\delta_{m'_F m_F}, \\ \langle i'|H_{\text{sr}}/h|i\rangle &= \frac{\gamma}{2}[J(J+1) - N(N+1) - S(S+1)]\delta_{N'N}\delta_{J'J}\delta_{F'F}\delta_{m'_F m_F}. \end{aligned} \tag{3.3}$$

The second expression follows from $\mathbf{N} \cdot \mathbf{S} = (\mathbf{J}^2 - \mathbf{N}^2 - \mathbf{S}^2)/2$. Since spin-rotation coupling splits each rotational manifold with $N > 0$ into the two fine-structure components $J = N \pm 1/2$. For $N = 0$, only $J = 1/2$ exists, so there is no spin-rotation shift.

The scalar hyperfine interaction mixes states with the same N, F, and m_F, but it can also couple different J components within a rotational manifold. The scalar hyperfine matrix element is [74]

$$\begin{aligned} &\langle N'SJ'IF'm'_F|\mathbf{I}\cdot\mathbf{S}|NSJIFm_F\rangle \\ &= (-1)^{F+I+N+S+2J'+1}\delta_{N'N}\delta_{F'F}\delta_{m'_F m_F}\sqrt{(2J'+1)(2J+1)}\sqrt{S(S+1)(2S+1)}\sqrt{I(I+1)(2I+1)} \\ &\quad \times \begin{Bmatrix} I & J & F \\ J' & I & 1 \end{Bmatrix} \begin{Bmatrix} S & J & N \\ J' & S & 1 \end{Bmatrix}. \end{aligned} \tag{3.4}$$

Physically, this term is the magnetic interaction between the fluorine nuclear spin and the unpaired electron spin. In the $N = 0$ manifold it gives the dominant splitting between the $F = 0$ and $F = 1$ hyperfine states. For $N > 0$, it also contributes to the mixing between states

with the same F that arise from different fine-structure components.

Finally, for the anisotropic term. The anisotropic hyperfine interaction depends on the orientation of the internuclear axis relative to the two spins. The matrix element is

$$\begin{aligned}
&\langle N'SJ'IF'm'_F|H_{\text{tens}}/h|NSJIFm_F\rangle \\
&= c\sqrt{10}\,(-1)^{J'+F+N+S}\delta_{F'F}\delta_{m'_F m_F}\sqrt{(2N'+1)(2N+1)(2J'+1)(2J+1)} \\
&\quad\times \begin{Bmatrix} F & I & J \\ 1 & J' & I \end{Bmatrix} \begin{Bmatrix} J & J' & 1 \\ S & 3/2 & N \end{Bmatrix} \begin{Bmatrix} N & N' & 2 \\ S & 3/2 & J \end{Bmatrix} \begin{pmatrix} N' & 2 & N \\ 0 & 0 & 0 \end{pmatrix},
\end{aligned} \tag{3.5}$$

The $3j$ symbol at the end of the expression above imposes the rotational selection rule $\Delta N = 0, \pm 2$ and requires the same rotational parity. For the low-lying manifolds this term mainly changes the hyperfine eigenvectors and splittings, and does not really produce a large rotational admixture. The last $3j$ term imposes the rotational selection rule $\Delta N = 0, \pm 2$ and requires the same rotational parity.

Taken together, these terms define the zero-field eigenstates, which we use as the starting point for the Zeeman and Stark shifts in later sections. The diagonal rotational energy sets overall spacing between different N manifolds, spin-rotation coupling resolves the fine structure, and the scalar and tensor hyperfine interactions produce the MHz scale splittings observed within each rotational manifold.

3.2.3 X-State Zeeman Hamiltonian

A magnetic field shifts the $X^2\Sigma^+$ levels by coupling to the magnetic moments associated with electron spin, nuclear spin, and molecular rotation. Since, again, $\Lambda = 0$ is X state, there is no first-order orbital magnetic moment. The dominant contribution then comes from the unpaired electron spin, and its magnetic moment is larger than the nuclear magnetic moment by the factor $\mu_B/\mu_N \simeq 1836$.

For a magnetic field $\mathbf{B}$, the effective Zeeman Hamiltonian is

$$H_Z = g_S \mu_B \, \mathbf{S} \cdot \mathbf{B} - g_I \mu_N \, \mathbf{I} \cdot \mathbf{B} - g_r \mu_B \, \mathbf{N} \cdot \mathbf{B} + g_l \mu_B [\mathbf{S} \cdot \mathbf{B} - (\mathbf{S} \cdot \hat{\mathbf{n}})(\mathbf{B} \cdot \hat{\mathbf{n}})]. \tag{3.6}$$

Here g_S is the electron-spin g factor, g_I is the fluorine nuclear g factor, g_r is the rotational g factor, and g_l is a small anisotropic correction caused by mixing with electronically excited states.

The first term is usually the leading term, because of the large ratio of μ_B/μ_N. The g_l anisotropic terms is small, which can be ignored in most low-field cases. For a bias field along the z axis, $\mathbf{B} = B_z \hat{\mathbf{z}}$, the dominant electron-spin matrix element in the coupled Hund's case (b) basis [74] is

$$\begin{aligned}
&\langle N' S J' I F' m'_F | g_S \mu_B B_z S_0 | N S J I F m_F \rangle \\
&= g_S \mu_B B_z (-1)^{F'-m'_F} \begin{pmatrix} F' & 1 & F \\ -m'_F & 0 & m_F \end{pmatrix} (-1)^{F'+J+1+I} \sqrt{(2F'+1)(2F+1)} \\
&\quad \times (-1)^{J'+N+1+S} \sqrt{(2J'+1)(2J+1)} \sqrt{S(S+1)(2S+1)} \begin{Bmatrix} F & J & I \\ J' & F' & 1 \end{Bmatrix} \begin{Bmatrix} J & S & N \\ S & J' & 1 \end{Bmatrix}.
\end{aligned} \tag{3.7}$$

where S_0 is the $q = 0$ spherical component of $\mathbf{S}$. The $3j$ symbol forces $\Delta m_F = 0$ for a field in z. The electron spin operator leaves N unchanged.

In weak magnetic fields, the Zeeman interaction is small compared with the hyperfine splittings. The eigenstates are then still well described by $|N, J, F, m_F\rangle$, and the leading shift is

$$\Delta E_Z \simeq h \, g_F \frac{\mu_B}{h} m_F B_z. \tag{3.8}$$

For $m_F = 0$ states, this first-order term vanishes, and the leading magnetic sensitivity is second order because the field admixes nearby hyperfine levels. Figure 3.2 (a) shows the Zeeman energy structure in the $N = 0$ and $N = 1$ rotational states around low fields. Note that $m_F = 0$ states have no first-order Zeeman shift, and shift mainly through hyperfine mixing.

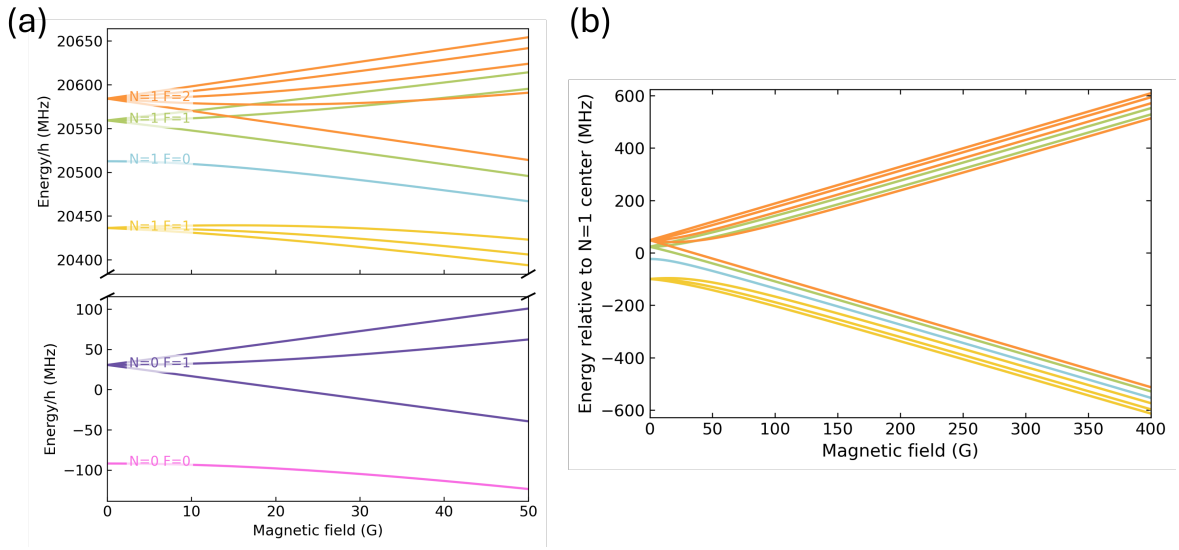


Figure 3.2: (a) Low-field Zeeman structure for $N = 0$ and $N = 1$ rotational manifolds in $X^2\Sigma(v = 0)$ state. In this regime$F$ and m_F are good quantum numbers. **(b)** Zeeman structure of the $X^2\Sigma^+(v = 0, N = 1)$ manifold over a wider field range.

At higher magnetic fields (Paschen-Back regime), the field decouples **S** and **I** from **N**, and Zeeman interaction becomes comparable to the hyperfine interaction. So the coupled quantum numbers F and J are then no longer good labels, and we turn to uncoupled basis: $|N, m_N\rangle\,|S, m_s\rangle\,|I, m_I\rangle$. In this high field limit, the leading Zeeman shift is $\Delta E_Z \simeq g_S \mu_B m_S B_z$. This is the regime for our high-field Raman sideband cooling (see Sec. 6.4.2), where the states are grouped by spin manifolds m_S and m_I. Figure 3.2 (b) shows the Zeeman energy structure in $X^2\Sigma(v = 0, N = 1)$ from low to high fields of several hundred gauss. At high field, the Zeeman interaction is comparable to or larger than the hyperfine splittings.

3.2.4 X-State DC Stark Hamiltonian

The permanent electric dipole moment of CaF is defined in the body-fixed frame, along the internuclear axis. In the lab frame, a rotational eigenstate at zero field has no average dipole moment. Static electric fields can still shift the energy by mixing rotational states of opposite parity. Therefore, for the $X^2\Sigma^+$ state, the DC Stark effect is quadratic at weak fields.

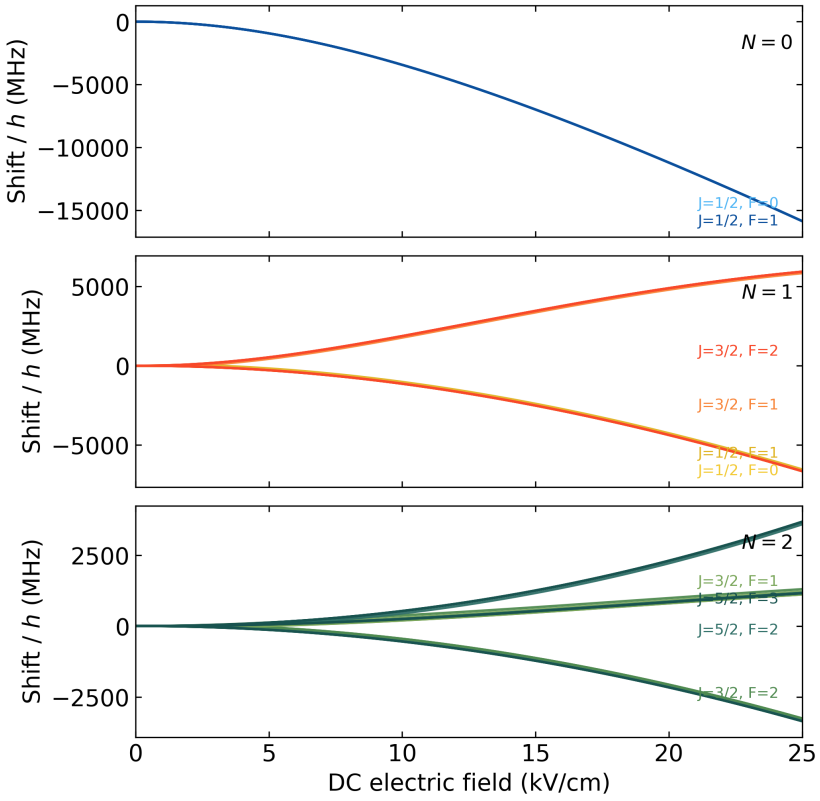


Figure 3.3: DC Stark shifts for rotational manifolds (N=0,1,2) in the ground electronic state $X^2\Sigma(v = 0)$. The energy plotted is referenced to the corresponding state at zero field. Calculated by diagonalizing $H_X + H_{\rm dc}$ in the coupled basis $|N, J, F, m_F\rangle$, with basis states up to $N \leq 4$.

The Stark interaction Hamiltonian is

$$H_{\rm dc} = -\mathbf{d} \cdot \mathbf{E}_{\rm dc} = -d_0 \sum_{q=-1}^{1} (-1)^q E_q C^{(1)}_{-q}(\theta, \phi). \tag{3.9}$$

where d_0 is the body-frame permanent electric dipole moment, E_q are the spherical components of the applied electric field, and $C^{(1)}_q(\theta, \phi)$ is the rank-1 rotational tensor that describes the orientation of the molecular axis relative to lab quantization axis [74].

For an electric field along z: $\mathbf{E}_{\rm dc} = E_z\hat{\mathbf{z}}$, the matrix element in Hunds (b) state basis is

$$\begin{aligned}
&\langle N'SJ'IF'm'_F|H_{\rm dc}|NSJIFm_F\rangle \\
&= -d_0E_z(-1)^{F'-m'_F}\begin{pmatrix} F' & 1 & F \\ -m'_F & 0 & m_F \end{pmatrix}(-1)^{F'+J+1+I}\sqrt{(2F'+1)(2F+1)}\begin{Bmatrix} J' & F' & I \\ F & J & 1 \end{Bmatrix} \\
&\quad\times(-1)^{J'+N+1+S}\sqrt{(2J'+1)(2J+1)}\begin{Bmatrix} N' & J' & S \\ J & N & 1 \end{Bmatrix}(-1)^{N'}\sqrt{(2N'+1)(2N+1)}\begin{pmatrix} N' & 1 & N \\ 0 & 0 & 0 \end{pmatrix}.
\end{aligned} \tag{3.10}$$

The last $3j$ terms gives us the opposite-parity rotational selection rule of $\Delta N = \pm 1$. For fields in z, the additional selection rule is $\Delta m_F = 0$.

In weak electric fields, the Stark shift of an eigenstate $|i\rangle$ from standard second-order perturbation theory is simply:

$$\Delta E_i^{(2)} = \sum_{j\neq i}\frac{|\langle j|H_{\rm dc}|i\rangle|^2}{E_i - E_j}. \tag{3.11}$$

Note that since the sign of the shift is set by the energy difference in denominator, the $N = 0$ manifold couples mainly to the higher-lying $N = 1$ manifold, so its Stark shift is negative.

For a simple rigid rotor without spin or hyperfine structure, the $N = 0, m_N = 0$ state couples only to $N = 1, m_N = 0$ and the shift of $N = 0$ is about $\Delta E^{(2)}_{N=0} \simeq -\frac{d_0^2E^2}{6B_0}$. Using the CaF dipole moment and rotational constant gives a Stark coefficient (i.e. differential DC Stark sensitivity) of order 40 Hz/(V/cm)^2 for low fields, which is actually very close to the values obtained after considering all the hyperfine states. Figure 3.3 shows the DC stark shifts of the lowest few rotational states in $X(v = 0)$ for CaF, where at low fields the shifts are quadratic as expected, since the shifts come from mixing of nearby opposite-parity rotational states by the electric field.

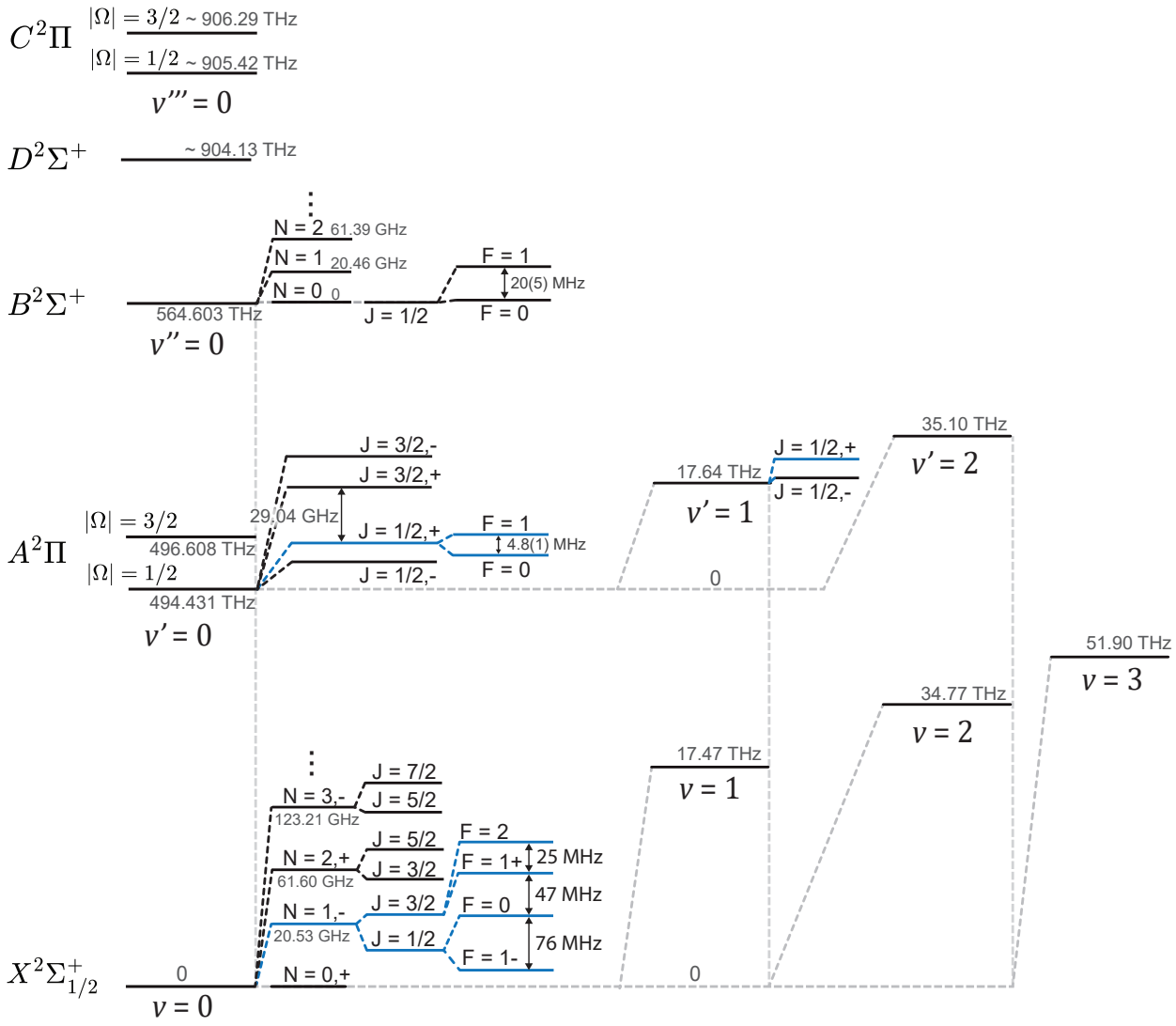


Figure 3.4: Relevant electronic, vibrational, rotational, fine and hyper-fine levels of CaF. All the states used for laser cooling, slowing, repumping, and qubit state preparation in this work lie within the $X^2\Sigma^+$, $A^2\Pi$ and $B^2\Sigma^+$ electronic manifolds, with blue levels denoting the states directly participating in the main cycling transitions. Energies are referenced to the $X\,^2\Sigma^+(v = 0)$ ground-state manifold, with relevant vibrational spacings, rotational, spin-orbit/parity, and hyperfine splittings. The higher-lying $C^2\Pi$ and $D^2\Sigma^+$ are also included to provide spectroscopic context. The diagram is schematic and energies not to scale.

3.3 Low-lying Excited electronic States: $A\,^2\Pi$ and $B\,^2\Sigma^+$

The overall energy level structure of CaF is schematically depicted in Fig. 3.4. The low-lying electronically excited states most relevant for this work are $A\,^2\Pi$ and $B\,^2\Sigma^+$.

3.3.1 Excited $A^2\Pi$ State

The first low-lying electronically excited state in caF called an A state. The molecular orbital is a Π state, mainly composed of the Ca^+ 4p orbital. In this state the electronic orbital angular momentum has a nonzero projection on the internuclear axis, $|\Lambda| = 1$. The molecule also has one unpaired electron, so $S = 1/2$. The spin-orbit interaction couples the electron spin projection Σ to Λ, giving the total electronic projection $\Omega = \Lambda + \Sigma$. For a $^2\Pi$ state, the possible values are $|\Omega| = 1/2$ and $|\Omega| = 3/2$, corresponding to the two spin-orbit manifolds $A, ^2\Pi_{1/2}$ and $A, ^2\Pi_{3/2}$. We use the lower $A^2\Pi_{1/2}$ manifold for all optical transition.

Since Λ, Σ, and Ω are all coupled to the internuclear axis, the natural basis to use here is Hund's case (a):

$$|A, v, \Lambda, S, \Sigma, J, \Omega, I, F, m_F\rangle \quad \Omega = \Lambda + \Sigma, \quad \mathbf{F} = \mathbf{J} + \mathbf{I}. \tag{3.12}$$

Here v is the vibrational quantum number, F is the total angular momentum including nuclear spin, and m_F is the projection of $\mathbf{F}$ on the lab quantization axis. The two electronic components with $\Lambda = +1$ and $\Lambda = -1$ are nearly degenerate. Small rotational electronic interactions can mix them and form opposite parity states from superpositions of opposite projections:

$$|J, |\Omega|, p, F, m_F\rangle = \frac{1}{\sqrt{2}}[|\Lambda, \Sigma, J, \Omega, I, F, m_F\rangle + p(-1)^{J-S}\,|-\Lambda, -\Sigma, J, -\Omega, I, F, m_F\rangle], \tag{3.13}$$

where $p = \pm 1$ labels the two opposite-parity components.

The field-free Hamiltonian for within a vibrational level in A state is:

$$H_A = H_{\text{ev}} + H_{\text{so}} + H_{\text{rot}} + H_\Lambda + H_{\text{hfs}}, \tag{3.14}$$

the first $H_{\text{ev}} = hcT_A$ (T_A is electronic-vibrational energy constant) sets the optical energy of the $A(v =)$ relative to the ground state, and so it does not affect internal state spitting. Below, we will go over the each of the terms.

First, the spin-orbit interaction is $H_{\rm so} = hcA_A\Lambda\Sigma$, where A_A is spin-orbit constant. For the manifold $A^2\Pi_{1/2}$ we use, $\Lambda = 1$, $\Sigma = -1/2$, and $\Omega = 1/2$, giving

$$\frac{E(A\,^2\Pi_{1/2})}{hc} \simeq T_A - \frac{A_A}{2} = 494.39 \text{ THz}. \tag{3.15}$$

The $A\,^2\Pi_{3/2}$ manifold lies higher by approximately $A_A = 2.14$ THz.

Next, the rotational Hamiltonian is

$$H_{\rm rot} \approx hc[B_A\mathbf{N}^2 - D_A\mathbf{N}^4], \quad \mathbf{N} = \mathbf{J} - \mathbf{S}. \tag{3.16}$$

Here B_A is the rotational constant, D_A is the centrifugal distortion constant. The term $J(J+1) - \Omega^2$ is the part of the angular momentum associated with rotation of the nuclei perpendicular to the molecular axis. In Hunds (a) basis, $\mathbf{N}^2$ has diagonal part and a spin-uncoupling part, the matrix element is

$$\begin{aligned}
&\langle\Lambda'\Sigma'J'\Omega'IF'm_F'|\mathbf{N}^2|\Lambda\Sigma J\Omega IFm_F\rangle \\
&= [J(J+1) + S(S+1) - 2\Omega\Sigma - \Lambda^2]\delta_{\Sigma'\Sigma}\delta_{\Omega'\Omega}\delta_{\Lambda'\Lambda}\delta_{J'J}\delta_{F'F}\delta_{m_F'm_F} \\
&\quad - 2(-1)^{J-\Omega+S-\Sigma}\sqrt{J(J+1)(2J+1)S(S+1)(2S+1)} \\
&\quad \times \sum_{r=\pm1} \begin{pmatrix} J & 1 & J \\ -\Omega & r & \Omega' \end{pmatrix} \begin{pmatrix} S & 1 & S \\ -\Sigma & r & \Sigma' \end{pmatrix} \delta_{\Lambda'\Lambda}\delta_{J'J}\delta_{F'F}\delta_{m_F'm_F}.
\end{aligned} \tag{3.17}$$

The first term here is the rigid-rotor energy. The second term couples $\Sigma = +1/2$ and $\Sigma = -1/2$ at the same J and is the leading correction to the pure Hunds (a) state.

The hyperfine interaction in $A^2\Pi$ is much smaller than the spin-orbit, rotational, and Λ-doubling energies. In fact, in $A^2\Pi_{1/2}, J = 1/2$ state, the hyperfine splitting is only a few megahertz [140, 142], comparable to or smaller than the natural linewidth, and not resolved in the experiment. Nonetheless, the Hamiltonian is

$$H_{\rm hfs} = a_A I_{\hat{n}} L_{\hat{n}} + b_{F,A}\,\mathbf{I}\cdot\mathbf{S} + \frac{c_A}{3}(3I_{\hat{n}}S_{\hat{n}} - \mathbf{I}\cdot\mathbf{S}), \tag{3.18}$$

where $\hat{n}$ is the internuclear-axis direction, a_A describes the coupling of the fluorine nuclear spin to the electronic orbital angular momentum, $b_{F,A}$ is the scalar Fermi-contact interaction, and c_A is the anisotropic electron-nuclear dipolar interaction.

3.3.2 Zeeman Interaction in the $A^2\Pi$ State

The magnetic response of $A^2\Pi$ is different from that of the $X^2\Sigma^+$ ground state because the excited state has electronic orbital angular momentum. The dominant Zeeman Hamiltonian is

$$H_{Z,A} = \mu_B(g_L\mathbf{L} + g_S\mathbf{S}) \cdot \mathbf{B} - g_I\mu_N\mathbf{I} \cdot \mathbf{B} + H_Z^{\text{rot}}. \tag{3.19}$$

$g_L \simeq 1$ is the orbital g factor, $g_S \simeq 2.0023$ is the electron spin g factor, and H_Z^{rot} denotes smaller rotational contributions.

In weak fields, F and m_F are good quantum numbers, and the first-order Zeeman shift is

$$\Delta E_Z^{(1)} = g_F\mu_B m_F B, \tag{3.20}$$

where hyperfine Lande factor is $g_F = g_J\frac{F(F+1)+J(J+1)-I(I+1)}{2F(F+1)}$, and $g_J \simeq \frac{\Omega}{J(J+1)}(g_L\Lambda + g_S\Sigma)$ (for pure Hunds (a) basis).

For $A\,^2\Pi_{1/2}$, $\Lambda = 1$ and $\Sigma = -1/2$, so $g_L\Lambda + g_S\Sigma \approx 1 - 1.001 \approx 0$, so the orbital and spin magnetic moments basically cancel and thus A state has a small magnetic moment. In consideration of magneto-optical trapping where magnetic field varies with position, the position-dependent force is linearly proportional to the magnetic moment (following Eq. 3.20). Consequently, for MOT operating on X–A transition, the magneto-optical force is dominated by the ground state Zeeman structure.

3.3.3 DC Stark Interaction in the $A^2\Pi$

The DC Stark effect in $A^2\Pi$ is important because the state contains a pair of nearly degenerate opposite-parity states. The electric dipole operator is odd under parity, so a static electric field

couples the two components of the Λ doublet. The Stark Hamiltonian is [74]

$$H_{\mathrm{S},A} = -\mathbf{d}_A \cdot \boldsymbol{\mathcal{E}} = -d_A \sum_{p=-1}^{1} (-1)^p \mathcal{E}_p C^{(1)}_{-p}(\theta,\phi), \tag{3.21}$$

where d_A is the body-frame electric dipole moment of A state. $\boldsymbol{\mathcal{E}}$ is the applied electric field, and $C^{(1)}_q(\theta,\phi)$ is a spherical harmonic that rotates the body fixed dipole into the lab frame [74], where

$$\begin{aligned}
&\langle A,\Lambda,\Sigma,J,\Omega,I,F,m_F|C^{(1)}_p|A,\Lambda,\Sigma,J',\Omega',I,F',m'_F\rangle \\
&= (-1)^{F-m_F}\begin{pmatrix} F & 1 & F' \\ -m_F & p & m'_F \end{pmatrix}(-1)^{J+I+F'+1}\sqrt{(2F+1)(2F'+1)}\begin{Bmatrix} J & F & I \\ F' & J' & 1 \end{Bmatrix} \\
&\quad\times (-1)^{J-\Omega}\sqrt{(2J+1)(2J'+1)}\begin{pmatrix} J & 1 & J' \\ -\Omega & 0 & \Omega' \end{pmatrix}.
\end{aligned} \tag{3.22}$$

For a field along the z axis, the interaction couples opposite-parity states with the same J, F, and m_F to leading order.

For a single parity doublet, the Stark Hamiltonian reduces to the two-level form

$$H_{\mathrm{doublet}} = \begin{pmatrix} h\Delta_\Lambda/2 & -d_A\eta_{Fm_F}\mathcal{E} \\ -d_A\eta_{Fm_F}\mathcal{E} & -h\Delta_\Lambda/2 \end{pmatrix}. \tag{3.23}$$

where Δ_Λ is the Λ-doublet splitting at zero-field, and η_{Fm_F} is a dimensionless angular factor describing how strongly the molecular dipole projects onto the applied electric field for that hyperfine state. The eigenvalues or the Stark-shifted energies are

$$E_\pm = \pm\sqrt{(\frac{h\Delta_\Lambda}{2})^2 + d_A^2\eta_{Fm_F}^2\mathcal{E}^2} \tag{3.24}$$

At weak electric field, where $d_A|\eta_{Fm_F}|\mathcal{E} \ll h\Delta_\Lambda$, the shifts are quadratic: $\delta E_\pm \approx \pm\frac{d_A^2\eta_{Fm_F}^2\mathcal{E}^2}{h\Delta_\Lambda}$, and the admixture of the opposite-parity state is about $\frac{|d_A\eta_{Fm_F}\mathcal{E}|}{h\Delta_\Lambda}$.

At higher electric field, the opposite-parity states become more strongly mixed and the energy

becomes approximately linear in $\mathcal{E}$. SinceΔ_Λ/h is only about 1.3 GHz for $A^2\Pi_{1/2}, J = 1/2$ level, a modest strength of applied electric fields can cause parity mixing. This effect is seen in RF MOTs (see Sec. 5.1), where electric fields on the order of tens of V/cm can admix the opposite-parity excited state and open decay channels to rotationally dark $X(N = 0, 2)$ states [48].

3.3.4 Excited $B^2\Sigma^+$ State

Like the ground X state, the excited B state is a $^2\Sigma^+$ state with $\Lambda = 0$, $S = 1/2$, and there is no first-order electronic orbital angular momentum along the internuclear axis. Therefore, the angular-momentum structure is also described by the same Hund's case (b) coupling scheme used for the $X^2\Sigma^+$ state [74]: $\mathbf{J} = \mathbf{N} + \mathbf{S} \quad \mathbf{F} = \mathbf{J} + \mathbf{I}$, with basis $|B, v, N, S = 1/2, J, I = 1/2, F, m_F\rangle$. $\mathbf{N}$ is the rotational angular momentum excluding electron spin, $\mathbf{S}$ is the electron spin, and $\mathbf{I}$ is the fluorine nuclear spin.

Since B state uses the same coupling scheme as X state which is elaborated in the previous section, we will focus more on the different energy scales here. The $B(v = 0)$ term origin is near $18840\,\mathrm{cm}^{-1}$, corresponding to the $B - X$ transition wavelength near 531nm. The rotational constant is $B_B = 10.263\,\mathrm{GHz}$, and the permanent dipole moment is smaller than in the X state, with $|d_B| \simeq 2.06\,\mathrm{D}$. The natural linewidth is $\Gamma_B/2\pi \simeq 6.3\,\mathrm{MHz}$, corresponding to a lifetime of about 25 ns [48, 140, 142, 144].

The field-free Hamiltonian of B state is (using frequency units for the constant):

$$\begin{aligned} H_B/h = \nu_B, \mathbf{1} + B_B\mathbf{N}^2 - D_B\mathbf{N}^4 + \gamma_B, \mathbf{N}\cdot\mathbf{S} + b_{F,B}, \mathbf{I}\cdot\mathbf{S} \\ + \frac{c_B}{3}\sqrt{6}, T^{(2)}(C)\cdot T^{(2)}(\mathbf{I},\mathbf{S}) + C_{I,B}, \mathbf{I}\cdot\mathbf{N}. \end{aligned} \tag{3.25}$$

The first term $\nu_B = cT_B$, like the constant T_A for A state, fixes the optical transition energy, and it does not affect the internal splittings. The next two terms give us the rotational ladder states and centrifugal distortion. The remaining terms are similar to those in the X state: spin-rotation coupling, scalar hyperfine coupling, tensor hyperfine coupling, and nuclear

spin-rotation coupling.

An important difference from the X state to note here is the size of the spin-rotation interaction. In the B state, $\gamma_B \simeq -1.37\text{GHz}$. For $N > 0$, this splits the rotational level into $J = N \pm 1/2$ components, with energies $E_{\text{SR}}/h = \gamma_B/2[J(J+1) - N(N+1) - S(S+1)]$. For example, in the $N = 1$ manifold the two fine-structure components are separated by $\Delta_{\text{sr}}(N = 1) = \frac{3}{2}|\gamma_B| \approx 2.06$ GHz.

The lowest rotational level $B(v = 0, N = 0)$, which we use for laser slowing and Raman sideband cooling (see Sec.6.4.2), has only $J = 1/2$. Spin-rotation coupling vanishes for $N = 0$, so the dominant internal splitting is the scalar hyperfine interaction. The two hyperfine levels are $F = 0, 1$, with a splitting of $E_{F=1} - E_{F=0} \sim hb_{F,B} \approx h \times 20$ MHz. This splitting is larger than the natural linewidth by a factor of a few, so the $B(N = 0)$ hyperfine structure is experimentally resolvable and needed to be addressed separately.

The Zeeman interaction has the same form as for any $^2\Sigma$ state. Since $\Lambda = 0$, the dominant magnetic moment is the electron spin:

$$H_{Z,B} \simeq g_S \mu_B \mathbf{S} \cdot \mathbf{B} \tag{3.26}$$

where the nuclear, rotational, and anisotropic corrections are much smaller and can be neglected. In weak fields, the good basis is labeled by $|N, J, F, m_F\rangle$, and the leading order shift is $\Delta E_Z^{(1)} = g_F \mu_B m_F B$. For the $B(v = 0, N = 0, F = 1)$ state, g_F is close to unity, while the $F = 0$ state has no first-order Zeeman shift.

In the high field limit, once $g_S \mu_B B/h$ becomes comparable to the ~ 20 MHz hyperfine splitting, the eigenstates cross over toward the uncoupled basis $|N, m_N\rangle |I, m_I\rangle |S, m_S\rangle$, just like the case for X state. In this regime, the Zeeman energy shift is linear in applied B: $\Delta E_Z \simeq g_S \mu_B m_S B$.

The DC Stark effect in the B state is also similar in the X state. Since $B^2\Sigma^+$ has definite rotational parity and no nearby Λ doublet, there is no first-order DC Stark shift at weak field.

The second order Stark shift is

$$\Delta E_i^{(2)} = \sum_{j \neq i} \frac{|\langle j|H_{S,B}|i\rangle|^2}{E_i^{(0)} - E_j^{(0)}}. \tag{3.27}$$

For the $N = 0$ level, ignoring spin and hyperfine structure, the dominant coupling is to $N = 1$, giving $\Delta E^{(2)}_{N=0}/h \simeq -\frac{d_B^2 \mathcal{E}^2}{6h^2 B_B}$.. Using $|d_B| = 2.06\,\mathrm{D}$ and $B_B = 10.26\,\mathrm{GHz}$, we have $\Delta E^{(2)}_{N=0}/h \approx -17.5\,\mathrm{Hz}(\frac{\mathcal{E}}{\mathrm{V/cm}})^2$. Thus the B state is much less sensitive to weak DC electric fields than the $A^2\Pi_{1/2}$, where there is strong mixing between nearby Λ doublet states.

3.4 Laser Slowing and Trapping Schemes

As discussed in Sec. 3.1, the consideration about suitability of an optical transition for laser slowing and trapping revolve around two quantities: the number of photons that can be scattered before population is lost from the optical cycle, and the rate at which those photons can be scattered. The former is set by vibrational and rotational closure, while the latter depends on excited state linewidth, light intensity and the multi-level structures. The two workhorse transitions used in this work are from the ground electronic state to the first two lowest lying electronic states: $X\,^2\Sigma^+(v = 0, N = 1) - A\,^2\Pi_{1/2}(v' = 0, J' = 1/2, p = +)$ and $X\,^2\Sigma^+(v = 0, N = 1) - B\,^2\Sigma^+(v' = 0, N' = 0)$. Fig. 3.5 illustrates the relevant energy level structure, driven transitions, and spontaneous decay paths during laser slowing and trapping.

Rotational closure follows from electric-dipole angular-momentum and parity selection rules [74]. For the X–A cycle, spontaneous emission from $A(J' = 1/2, p = +)$ must change parity and can reach only $J = 1/2$ or $3/2$. In $X\,^2\Sigma^+$, the only negative-parity rotational manifold containing these values of J is $N = 1$. For the X–B cycle, $B(N' = 0, p = +) \to X$ obeys the Σ–Σ rotational selection rule $\Delta N = \pm 1$, so spontaneous emission likewise returns to $N = 1$. Therefore, the ground state for both transition is $X\,^2\Sigma^+(v, N = 1)$, as $N = 1$ is lowest rotational manifold from which one can drive an electric-dipole transition to a low-J excited state and have rotational closure.

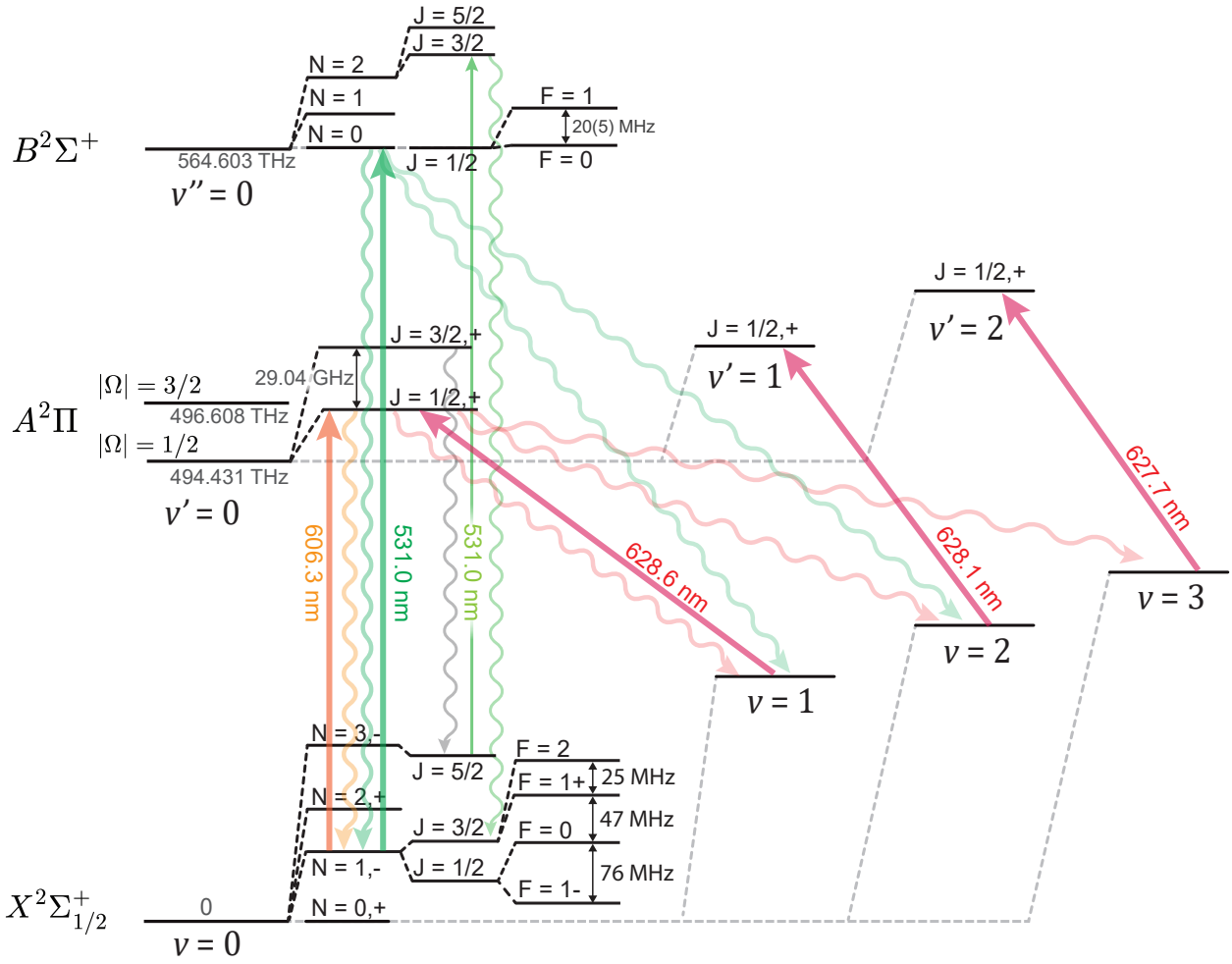


Figure 3.5: Laser-driven transitions for optical cycling schemes used for laser cooling and slowing of CaF. Solid arrows denote laser-driven transitions and wavy arrows indicate spontaneous decay pathways. The main X–A cycling transition near 606.3 nm addresses $X(v = 0, N = 1) \rightarrow A(v' = 0, J' = 1/2, p = +)$, while vibrational leakage into $X(v = 1, 2, 3)$ is returned through the corresponding X–A repump transitions near 628!nm. Radiative slowing is driven on the X–B transition near 531 nm. Additionally, population that accumulates in the $A^2\Pi(v' = 0, J' = 3/2, +)$ state due to off-resonant excitation is returned to main X–Acycle through another repump around 531 nm, going through $X(N = 3)$ and $B(N = 2)$ state.

As for vibrational states, there are no selection rules to enforce vibrational closure. Instead, the amount of vibrational leakage is mainly determined by the overlap of the vibrational wavefunctions in the two electronic potentials. i.e. the Franck–Condon factor (FCF):

$$q_{v'v}^{e-X} = \left| \int \chi_{e,v'}^{*}(R)\, \chi_{X,v}(R)\, dR \right|^2, \tag{3.28}$$

where $\chi_{e,v'}(R)$ and $\chi_{g,v}(R)$ are normalized vibrational wavefunctions for the ground and electronic potentials, respectively. Electronic states with similar equilibrium bond lengths and potential curvature have more closely matched vibrational wavefunctions, resulting highly diagonal Franck–Condon factor, $q_{v'v} \approx \delta_{v'v}$. The goal then is to choose an excited state with such properties as the ground state. Both the A–X and B–X systems of CaF have this favorable structure, and small off-diagonal overlaps ultimately determine our vibrational repumping requirements. Since FCF in itself does not inform the spontaneous decay branching fraction, we also use β_i^e for probability of spontaneous decaying from the cycling state $e(v' = 0)$ into $X(v = i)$, as defined and discussed in the following section.

3.4.1 Photon Budgets and Repumps

To more directly characterize the photon budget, we define the spontaneous branching fraction from an excited vibrational state $e(v')$ into a ground-state vibrational state $X(v)$ as

$$\beta_v^{(e,v')} = \frac{A_{e,v'\to X,v}}{\Gamma_{e,v'}} = \frac{A_{e,v'\to X,v}}{\sum_f A_{e,v'\to f}}, \tag{3.29}$$

where the sum runs over all accessible final states, and $A_{e,v'\to g,v}$ is the Einstein A-coefficient for decay to $g(v)$. Within the Condon approximation, the Einstein A-coefficient scales as

$$A_{v'v} \propto \omega_{v'v}^3 \left|\mu_{\mathrm{el}}\right|^2 q_{v'v}, \tag{3.30}$$

Table 3.1 summarizes the transition frequencies, vibrational branching ratios and characteristic rate constants for the laser-driven transitions relevant for laser slowing and cooling. $\beta_i^A \equiv \beta_i^{(A,v'=0)}$ denotes decay from $A(v' = 0)$ to $X(v = i)$, and similarly for $\beta_i^B \equiv \beta_i^{(B,v'=0)}$.

The total photon budget can then be estimated from the total branching fraction into levels that are not addressed. For a simple cycling transition with a total probability ℓ per scattering event of decaying into an unaddressed state, the survival probability after N_γ scattering cycles

Main electronic transitions

Cycle	Driven transition	Wavelength / frequency	FCF	Rate constants and characteristics
X–A	$X(v=0) \leftrightarrow A(v'=0)$	$\lambda \simeq 606.3$ nm [145] $\nu_0 \simeq 494.4$ THz [145]	$q_{00}^{A-X} = 0.987^{+0.013}_{-0.019}$ [146]	$\tau_A = 19.2(7)$ ns [146] $\Gamma_A/2\pi \simeq 8.3$ MHz [146] $v_{\mathrm{rec}} = 1.12$ cm/s $T_D \simeq 200$ μK
X–B	$X(v=0) \leftrightarrow B(v'=0)$	$\lambda \simeq 531.0$ nm [145] $\nu_0 \simeq 564.6$ THz [145]	$q_{00}^{B-X} = 0.998$ [41]	$\tau_B = 25.1(4)$ ns [147] $\Gamma_B/2\pi \simeq 6.3$ MHz [147] $v_{\mathrm{rec}} = 1.27$ cm/s $T_D \simeq 150$ μK

Vibrational leakage

	Decay path	Leakage path's FCF	Branching fraction
X–A	$A(v'=0) \to X(v=1)$	$q_{01}^{A-X} = 2.04 \times 10^{-2}$ [148]	$\beta_1^A \simeq 2.1 \times 10^{-2}$ [149]
	$A(v'=0) \to X(v=2)$	$q_{02}^{A-X} = 8.74 \times 10^{-4}$ [149]	$\beta_2^A = 7.84 \times 10^{-4}$ [150]
	$A(v'=0) \to X(v=3)$	$q_{03}^{A-X} = 3.59 \times 10^{-5}$ [41]	$\beta_3^A \simeq 2.6 \times 10^{-5}$ [149]
X–B	$B(v'=0) \to X(v=1)$	$q_{01}^{B-X} = 1.3 \times 10^{-3}$ [41]	$\beta_1^B \simeq 4.4 \times 10^{-4}$ [41]
	$B(v'=0) \to X(v=2)$	$q_{02}^{B-X} = 3.81 \times 10^{-5}$ [149]	$\beta_2^B = 1.5(3) \times 10^{-5}$ [151]
	$B(v'=0) \to X(v=3)$	$q_{03}^{B-X} = 9.834 \times 10^{-8}$ [149]	$\beta_3^B \simeq 7 \times 10^{-8}$ [149]
	$B(v'=0) \to A$	—	$\beta_{B-A} \sim 1.2 \times 10^{-4}$ [149]

Addressed vibrational repumps

Repump name	Driven transition	Wavelength/frequency	Repump-transition's FCF
$v=1$	$X(v=1) \to A(v'=0)$	$\lambda \simeq 628.6$ nm [145] $\nu_0 \simeq 476.9$ THz [145]	$q_{01}^{A-X} = 0.0204$ [148]
$v=2$	$X(v=2) \to A(v'=1)$	$\lambda \simeq 628.1$ nm [145] $\nu_0 \simeq 477.3$ THz [145]	$q_{12}^{A-X} = 0.0386$ [148]
$v=3$	$X(v=3) \to A(v'=2)$	$\lambda \simeq 627.7$ nm [145] $\nu_0 \simeq 477.6$ THz [145]	$q_{23}^{A-X} = 0.0548$ [148]

Table 3.1: Frequencies, branching ratios and characteristic rates for cycling transitions. All lower states are $X^2\Sigma^+(v, N=1)$. Upper panel summarizes the two main cycling transitions. Middle panel lists vibrational spontaneous decay from the corresponding cycling excited states. Lower panel gives the repumping transitions used experimentally to return population from $X(v=1,2,3)$ for both X–A and X–B cycling. Here, $A \equiv A^2\Pi_{1/2}(J'=1/2, p=+)$ and $B \equiv B^2\Sigma^+(N'=0)$. The Franck–Condon factor $q_{v'v}^{e-X}$ is the squared vibrational overlap between the indicated $e(v')$ and $X(v)$ states. The branching fraction β_i^e is the probability for spontaneous decay from the cycling excited state into $X(v)$. Recoil velocities are calculated using $v_{\mathrm{rec}} = h/(M\lambda)$ for ^{40}Ca^{19}F, and Doppler temperature is defined $T_D = \hbar\Gamma/(2k_B)$.

is:

$$p(N_\gamma) = (1-\ell)^{N_\gamma} \simeq e^{-\ell N_\gamma} \qquad \langle N_\gamma \rangle_{\text{loss}} \simeq \ell^{-1}. \tag{3.31}$$

For X–A cycle with only $X(v=0)$ addressed, $\beta_0^A \approx q_{00} = 0.987$ corresponds to only about 80 photons before vibrational loss. Adding $v = 1, 2, 3$ repumps reduces the vibrational leakage to order of 10^{-5} –10^{-6} level, or 10^5 photons. For X–B, with only the main transition $X(v=0, N=1) \to B(v'=0, N'=0)$ addressed, the cycle can scatter order of $1/\beta_1^B \sim 1000$ photons before population accumulates in $X(v=1)$. That is, the B-state cycle is much more diagonal compared to the A-state. After just adding the first 628 nm $X(v=1) \to A(v'=0)$ repump, the photon budget becomes $\sim 3 \times 10^4$ [41].

3.4.1.1 Off-resonant Scattering

A rotational loss channel we need to account for in X–A cycling arises from off-resonant excitation to nearby $A^2\Pi(v'=0, J'=3/2)$, which lies about 29 GHz away from the cycling state $A^2\Pi(v'=0, J'=1/2)$. This small off-resonant scattering rate can introduce population loss that is non-negligible, especially in high-fidelity single-molecule imaging using X-A. Population that goes to $A^2\Pi(v'=0, J'=3/2)$ (lifetime ~ 19 ns) can decay to $X^2\Sigma^+(v=0, N=3, J=5/2)$ ("N=3" state), which is outside of the rotationally closed cycle and needs to be returned through $X(v=0, N=3) - B(v'=0, N'=2)$ rotational repump ("N=3 repump"). The decay pathway and repump transitions are schematically indicated in Fig. 3.5.

We can estimate this loss, i.e. fraction of population that ends up accumulating in the dark $N=3$, by first calculating the rate of molecules getting off-resonantly excited from $X^2\Sigma(v=0, N=1)$ to $A^2\Pi(J'=3/2)$. This can be obtained by taking Lorentzian excitation factor suppressed by detuning $(\frac{\Gamma_A}{2\Delta})^2$, multiplied by the usual resonant photon scattering rate and saturation parameter:

$$R_{3/2} = \frac{\Gamma_A}{2} s_{3/2} \left(\frac{\Gamma_A}{2\Delta}\right)^2, \tag{3.32}$$

where $s_{3/2} = \mathcal{R}\frac{I_{\text{tot}}}{I_{\text{sat}}}$ is the saturation parameter for the transition, and $\mathcal{R}$ accounts for the relative rotational line strength ratio between transitions $X(N=1) \to A(J'=3/2)$ and

$X(N=1) \rightarrow\ A(J'=1/2)$. Here, $\Delta = 29\,\mathrm{GHz}$ [140] and $\Gamma_{\mathrm{A}} = 8.3\,\mathrm{MHz}$ (Table 3.1). $\mathcal{R} = 7/5$ can be calculated using detailed balance with population averaged over entire $X(N=1)$ manifold.

Next, we estimate the probability of decaying from $A^2\Pi(J'=3/2)$ to $N=3$ state, which is determined by the branching ratio $\beta_{\mathrm{N=3}}$,

$$\beta_3 = q_{00}^{X-A}\frac{3}{10} \approx 0.3, \tag{3.33}$$

where where $q_{00}^{X-A} = 0.987$, and $\frac{3}{10}$ is the Hönl-London rotational branching factor [74] from $A(J'3/2)$ to $N=3$ state.

For typical tweezer Λ-imaging intensity of about 60 mW/cm^2 in each beam, with three imaging beams and each retro-reflected, then $I_{\mathrm{tot}} = 360$ mW/cm^2. I_{sat} can be approximated by taking the ideal two-level saturation intensity $I_{\mathrm{sat}}^{\text{2-level}} = \pi hc/3\lambda^3 \approx 4.9$ mW/cm^2 and scaling over the corresponding molecular manifolds for multilevel $I_{\mathrm{sat}} \sim 3_{\mathrm{sat}}^{\text{2-level}}/q_{00}^{X-A} \sim 14.8$ mW/cm^2. During a $t_{\mathrm{img}} = 20$ ms image, without "N=3 repump", this would result in population loss of

$$P_{N=3} \approx 1 - e^{-R_{3/2}\beta_3 t_{\mathrm{img}}} = 7.4\%. \tag{3.34}$$

3.4.2 Laser Slowing

In radiative slowing, each photon absorption from a counter-propagating beam removes a directed momentum $\hbar k$. The number of scattered photon required to decelerate a cryogenic beam of CaF molecules (59 amu) is then:

$$N_\gamma = \frac{M\Delta v}{\hbar k} = \frac{\Delta v}{v_{\mathrm{rec}}}. \tag{3.35}$$

The recoil velocity is $v_{\mathrm{rec}} = 1.27$ cm/s at 531 nm and $v_{\mathrm{rec}} = 1.12$ cm/s at 606 nm, so decelerating mean forward velocity of ~ 150m/s to ~ 10m/s MOT capture velocity requires about 1.1×10^4 photons on the X–B transition, or 1.3×10^4 photons on the X–A transition.

Experimentally, we perform the laser slowing on X-B, driving $X(v=0, N=1) \rightarrow B(v'=0, N'=0)$ at 531 nm, while population that leaks into excited vibrational levels of X is returned through the $A^2\Pi_{1/2}$ state. The reason for this is that as the B–X FCF is very diagonal, this means the off-diagonal repumping transitions that put population back to $B(v'=0)$ are much weaker. For comparison, for the first repump, $q_{01}^{B-X} \simeq 0.00134$, whereas $q_{01}^{A-X} \simeq 0.0344$ for $X(v=1) \rightarrow A(v'=0)$. So the X–A repump is roughly 25 times stronger in FCF, and practically, this makes the 628 nm X–A repump remove population from $v=1$ much faster for a given optical power.

3.4.3 Laser Trapping

For magneto-optical trapping, the minimum number of scattered photon required is set by the small momentum that needs to be removed relative to the single photon recoil. At 606 nm, $v_{\mathrm{rec}} = 1.12$ cm/s, so damping a 10 m/s velocity requires $\sim 9 \times 10^2$ directed recoils. However, the actual number of scattered photons depends on the full position- and velocity-dependent multilevel MOT force, beam geometry, and momentum diffusion. For example, a recent stochastic-Schrödinger-equation Monte Carlo simulation that include all 28 states of the $X(v=0)$, $X(v=1)$ and $A(v'=0)$ manifolds reproduces the observed dependence of MOT loading on several experimental parameters, and show that the MOT capture cannot generally be inferred from a two-level scattering-rate model [152].

In principle, both X–A and X–B cycling transitions can support magneto-optical trapping. The $B^2\Sigma^+(N'=0, F'=1)$ state has a magnetic g-factor of $g_F = 1.022$ and Zeeman shift of ~ 1.43 MHz/G, which is roughly fifty times larger than that of $A(F'=1)$, since magnetic moment of $A^2\Pi_{1/2}$ is small (see Sec. 3.3.2). At 10 G, the B state Zeeman shift is then 14.3 MHz, more than twice the B-state linewidth ($\Gamma_B/2\pi \simeq 6.3$ MHz). Thus the large excited-state Zeeman effect means an X–B MOT can generate substantial Zeeman restoring force.

MOT operating X–A transition forms a type-II system, with ground-state 12 Zeeman states and only 4 excited-state Zeeman states. Moreover, the $A^2\Pi_{1/2}$ state has a very small magnetic moment, so conventional Zeeman MOT on X–A provides very weak restoring force. One can

nonetheless obtain a strong restoring force in a type-II MOT by using dual-frequency trapping mechanisms in a DC MOT or operating an RF MOT, which exploit ground state Zeeman structure and optical pumping.

Briefly, in a dual-frequency MOT, two optical components, one red-detuned and blue-detuned, of opposite polarization address the same hyperfine state to maintain restoring radiation force as the molecules get optically pumped among the Zeeman sublevels. This way, regardless of which Zeeman state is populated, there is always a component that preferentially pushes the molecule toward the zero field center [153]. In an RF MOT, which is what our experiment employs, the magnetic-field gradient and optical polarizations are synchronously reversed on the optical-pumping timescale, continually de-stabilizing the Zeeman dark states (see Sec. 5.1 for experimental implementation).

Early calculations comparing the X–B and X–A schemes have found similar peak restoring forces but a substantially broader velocity range for X–A MOT, because in B state, the nearby $F' = 0$ and $F' = 1$ hyperfine components could produce unwanted excitation and anti-damping at finite velocity, reducing the calculated X–B MOT capture velocity [154]. However, later global optimization of detunings, polarizations, intensities, beam sizes, and magnetic-field gradient shows comparable simulated capture velocities for both transitions [155]. Our present scheme follows the historically established implementation [9, 49], operating MOT on the 606 nm X–A transition with three vibrational repumps as listed in Table 3.1 and indicated in Fig. 3.5, but an X–B MOT is also a viable option in principle.

3.5 AC Stark Shifts and Polarizability of CaF in Optical Traps

For molecules (and atoms), the optical trapping potential arises from the AC Stark shift effect. In contrast to how a DC electric field can orient a polar molecule by mixing opposite-parity rotational states, an optical field oscillates rapidly and induces an oscillating dipole moment. The time-averaged interaction between this induced dipole in the molecules and the light field shifts the molecular energy levels. This shift can be described by the dynamic polarizability,

which depends on the trap wavelength, polarization, and molecular quantum states.

For an optical field expressed classically as $\mathbf{E}(\mathbf{r},t) = \frac{E_0(\mathbf{r})}{2}[\boldsymbol{\epsilon}e^{-i\omega_L t} + \boldsymbol{\epsilon}^* e^{i\omega_L t}]$, the time-averaged intensity is $I(\mathbf{r}) = \frac{1}{2}c\epsilon_0 E_0^2(\mathbf{r})$, where $\boldsymbol{\epsilon}$ is the complex polarization vector and ω_L is the angular frequency of trap light.

The AC Stark Hamiltonian for molecule in the ground state, for example, within the $X^2\Sigma^+(v = 0)$ rotational and hyperfine manifolds, can be estimated from second-order perturbation theory:

$$\langle i|H_{\mathrm{ac}}|i'\rangle = -\frac{E_0^2}{4}\sum_{j\notin X}\left[\frac{\langle i|\mathbf{d}\cdot\boldsymbol{\epsilon}^*|j\rangle\langle j|\mathbf{d}\cdot\boldsymbol{\epsilon}|i'\rangle}{\hbar(\omega_{ji}-\omega_L)} + \frac{\langle i|\mathbf{d}\cdot\boldsymbol{\epsilon}|j\rangle\langle j|\mathbf{d}\cdot\boldsymbol{\epsilon}^*|i'\rangle}{\hbar(\omega_{ji}+\omega_L)}\right]. \tag{3.36}$$

The first denominator is the resonant (or rotating-wave) contribution. The second is the counter-rotating contribution. $|i\rangle$ and $|i'\rangle$ are two molecular states in the manifold, while $|e\rangle$ in principal runs over all excited states that are allowed by dipole transitions. In practice, the sum includes electronic, vibrational, rotational, and hyperfine levels, with the transition energies and dipole matrix elements determining the size and sign of each contribution, and we usually include the few intermediate states in calculations.

The expression above shows that the optical field produces an effective Hamiltonian inside the ground state manifold through coupling to other excited electronic states. The magnitude of light shift is proportional to the optical field intensity and depends on the molecular states through a sum over dipole coupled excited states. For CaF molecules in X, the dominant contributions come from dipole-allowed transitions to the low-lying A and B states, with higher electronic states giving additional corrections. For convenience, instead of wrtitng out this sum explicitly, one can absorb it into a so-called dynamic polarizability. This polarizability is "dynamic" because it depends on the trap frequency ω_L. Furthermore, it is a matrix because the light can shift and mix different internal states within a manifold of interest. Therefore, we let

$$\langle i|H_{\mathrm{ac}}|i'\rangle = -\frac{E_0^2}{4}\alpha_{ii'}(\omega_L,\boldsymbol{\epsilon}) = -\frac{I(\mathbf{r})}{2\epsilon_0 c}\alpha_{ii'}(\omega_L,\boldsymbol{\epsilon}), \tag{3.37}$$

where $I(\mathbf{r})$ is the trap intensity, ω_L is the trap light frequency, and polarizability $\alpha_{ii'}$ now

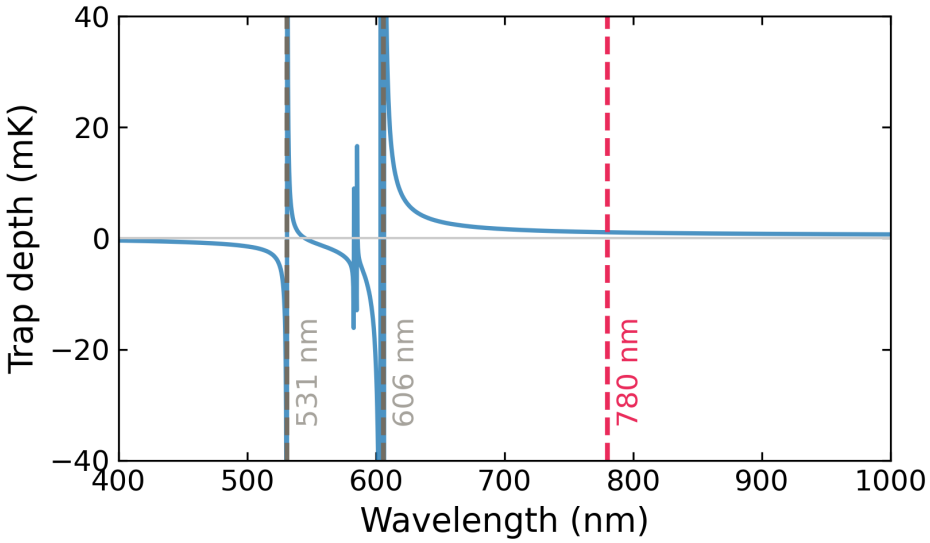


Figure 3.6: Scalar trap depth $U_0/k_B = \tilde{\alpha}^{(0)}(\lambda) I_0/k_B$ for the $X\,^2\Sigma^+(v=0)$ state of CaF as a function of trap wavelength for given optical power and waist. The calculation here includes only $X - A$ and $X - B$ transitions, and uses Gaussian beam with $P = 24$ mW and $w_0 = 970$ nm, corresponding to $U_0/k_B \simeq 1.05$ mK at 780 nm, which is marked by the vertical dashed line. The dispersive features at optical resonances with $B^2\Sigma^+$ and $A^2\Pi$ states are marked

contains the full sum over intermediate excited states, including the transition dipole moments, detunings, and polarization selection rules. The diagonal element of α_{ii} give the light shifts of the states $|i\rangle$, while the off-diagonal elements describe light induced mixing between internal states $|i\rangle$ and $|i'\rangle$. Note that the polarizability $\alpha_{ii'}$ is generally a complex matrix. In real molecules, each excited state $|e\rangle$ has finite decay rate Γ_e, and thus a finite probability that a molecule coupled to that excited state will scatter a photon. This means that the induced dipole response is not perfectly in phase with the applied optical field, and it is this dissipative part of the response that gives the polarizability a imaginary part. It is also useful to decompose this matrix into scalar, vector, and tensor contributions,

$$H_{\rm ac} = -I(\mathbf{r})[\tilde{\alpha}^{(0)} + \tilde{\alpha}^{(1)} + \tilde{\alpha}^{(2)}], \tag{3.38}$$

where we absorb the factor $1/(2\epsilon_0 c)$ in $\tilde{\alpha}^{(K)}$ to intensity directly into energy. The scalar term $K = 0$ gives the trap depth common to all states in the manifold, the vector term $K = 1$ acts like a polarization-dependent fictitious magnetic field, and the tensor term $K = 2$ gives

state-dependent shifts that depend on the orientation of the molecule relative to the light polarization. When the optical field is far detuned and the off-diagonal couplings are negligible, the AC Stark shift of state $|i\rangle$ is simply:

$$U_i(\mathbf{r}) = -\frac{I(\mathbf{r})}{2\epsilon_0 c}\mathrm{Re}[\alpha_{ii}(\omega_L, \boldsymbol{\epsilon})]. \tag{3.39}$$

For CaF in optical trap at $\lambda_{\mathrm{tw}} \simeq 780$ nm, these light shift coefficients are: $\tilde{\alpha}_0/h \approx 1.4 \times 10^{-3}$ Hz/(W/m^2); $\tilde{\alpha}_1/h \approx 3 \times 10^{-5}$; $\tilde{\alpha}_2/h \approx -8 \times 10^{-4}$. Figure. 3.7 shows the dynamic polarizability components of CaF in the $X^2\Sigma^+$ state, where at a given trap wavelength, the scalar component $\tilde{\alpha}^{(0)}$ sets the trap depth, and tensor components produce state-dependent light shifts.

3.5.1 Scalar Stark Shift

For red-detuned tweezer light, the scalar AC Stark shift lowers the molecular energy at the intensity maximum. The trap depth U_0 (positive) is defined as the magnitude of the scalar Stark shift at the peak intensity I_0 is $U_0 = \tilde{\alpha}^{(0)} I_0$. For a Gaussian trap with power P and waist w_0, the intensity is then $I_0 = \frac{2P}{\pi w_0^2}$. The trap depth, commonly expressed in frequency $U_{0,i}/h$, or in a temperature unit $U_{0,i}/k_B$ is then

$$U_0/h = \frac{\tilde{\alpha}^{(0)}}{h}\frac{2P}{\pi w_0^2} \quad \Rightarrow U_0/k_B = \frac{h}{k_B}\frac{\tilde{\alpha}^{(0)}}{h}\frac{2P}{\pi w_0^2} \tag{3.40}$$

In Figure 3.6, we show the scalar trap depth in temperature unit for CaF over trap light wavelength, where the depth follows from the scalar light-shift coefficient through $U_0 = \tilde{\alpha}^{(0)} I_0$.

3.5.2 Tensor Stark Shift

In addition to the scalar part of light shift that supplies the trapping potential, we are also interested in state-dependent tensor part, as it is important for coherence between two states. Here we focus on the tensor light shift in the $X^2\Sigma^+(v = 0)$ ground state. As discussed earlier,

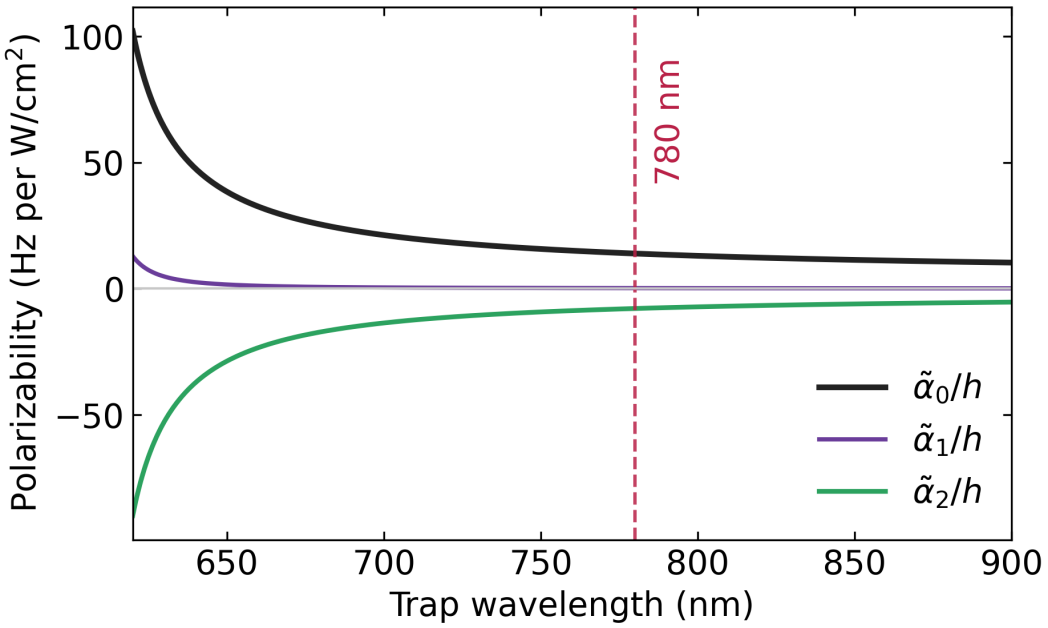


Figure 3.7: Dynamic polarizability coefficients in the $X^2\Sigma^+(v = 0)$ state. The plot show the scalar, vector, and tensor components $\tilde{\alpha}^{(0)}$, $\tilde{\alpha}^{(1)}$, and $\tilde{\alpha}^{(2)}$, plotted as $\tilde{\alpha}^{(K)}/h$ in units of $\mathrm{Hz}/(\mathrm{W}/\mathrm{cm}^2)$. The dashed vertical line marks the 780 nm tweezer wavelength used in the experiment. At this wavelength the scalar coefficient sets the trap depth, and tensor coefficient sets the scale of state-dependent differential light shifts.

the states in this manifold are expressed in basis $|N, J, F, m_F\rangle$.

For ideal linearly polarized tweezer light, the vector light shift vanishes. The AC Stark Hamiltonian can then be schematically written as

$$H_{\mathrm{ac}} \propto -I[\tilde{\alpha}^{(0)}\mathbf{1} + \tilde{\alpha}^{(2)}\hat{Q}^{(2)}(\beta)], \tag{3.41}$$

where I is the trap intensity, $\tilde{\alpha}^{(0)}$ is the scalar light-shift coefficient, $\tilde{\alpha}^{(2)}$ is the tensor light-shift coefficient, and $\hat{Q}^{(2)}(\beta)$ is a dimensionless rank-2 operator that describes the anisotropic part of the polarizability. The angle β is the angle between the trap light polarization and the lab quantization axis, which in our experiment is set by an applied bias magnetic field $\mathbf{B}$. For a given applied magnetic field B, tweezer intensity I, and polarization angle β, we diagonalize

$$H_{\mathrm{tot}} = H_X + H_Z(B) + H_{\mathrm{ac}}(I, \beta). \tag{3.42}$$

where $H_{\rm ac}$ is evaluated as a matrix in the $X^2\Sigma^+(v=0)$ basis $|N, J, F, m_F\rangle$.

Let us denote the energy of state $|i\rangle$ in the optical trap as $E_i(I, \beta, B)$, where I is the local trap intensity, β is the angle between the linear tweezer polarization and the quantization axis, and B is the bias magnetic field. The corresponding zero-light energy at the same magnetic field is $E_i(0, B)$.

For a transition $|a\rangle \to |b\rangle$, the trap induced differential AC Stark shift is

$$\Delta\nu_{ba}^{\rm ac} = \frac{[E_b(I,\beta,B) - E_a(I,\beta,B)] - [E_b(0,B) - E_a(0,B)]}{h}. \tag{3.43}$$

To isolate the state-dependent tensor part in a plot of individual levels, we subtract the common scalar trap shift $U_0 = \tilde{\alpha}^{(0)} I$, then the scalar subtracted shift of state $|i\rangle$ is

$$\delta\nu_i^{\rm tens} = \frac{E_i(I,\beta,B) - E_i(0,B)}{h} + \frac{U_0}{h}. \tag{3.44}$$

The differential tensor light shift of the transition is then

$$\Delta\nu_{ba}^{\rm tens} = \delta\nu_b^{\rm tens} - \delta\nu_a^{\rm tens}. \tag{3.45}$$

To give a physical scale for CaF, for a trap intensity of $I = 15\,\mathrm{GW/m^2}$, which is equivalently a scalar trap depth of about 1mK, the tensor light-shift scale is $\frac{|\tilde{\alpha}^{(2)}|I}{h} \simeq 12$ MHz.

3.6 Transition dipole moment of between rotational states

For a CaF rotational qubit, we let $|\uparrow\rangle = |N=1, J=1/2, F=0, m_F=0\rangle$ and $|\downarrow\rangle = |N=0, J=1/2, F=1, m_F=0\rangle$. The dipole operator acts only on the spatial part of the molecular wavefunction, while the spin degrees of freedom enter through angular-momentum recoupling.

Using the Wigner-Eckart theorem for a Hund's case (b) molecule,

$$\langle\uparrow|\hat{d}_0|\downarrow\rangle = d_0 \underbrace{(1)}_{N \text{ reduced}} \underbrace{\left(\sqrt{\frac{2}{3}}\right)}_{N,S\to J} \underbrace{\left(\frac{1}{\sqrt{2}}\right)}_{J,I\to F} \underbrace{\left(-\frac{1}{\sqrt{3}}\right)}_{m_F} = -\frac{d_0}{3}. \tag{3.46}$$

Here the four factors come from the rotational matrix element, the $N, S \to J$ recoupling, the $J, I \to F$ recoupling, and the m_F Clebsch-Gordan factor, respectively. Therefore the effective transition dipole moment is $d_{\text{eff}} = |\langle\uparrow|\hat{d}_0|\downarrow\rangle| = d_0/3 \simeq 1.02$ D, with $d_0 = 3.07$ D for CaF (Ref. [156] reports the direct experimental measurement of this).

Note 1 *For a spherical tensor operator $\hat{T}^k_q$, the matrix element between angular momentum states is*

$$\langle j'm'|\hat{T}^k_q|jm\rangle = (-1)^{j'-m'} \begin{pmatrix} j' & k & j \\ -m' & q & m \end{pmatrix} \langle j'||\hat{T}^k||j\rangle. \tag{3.47}$$

For CaF, the state quantum numbers are constructed by angular momentum coupling: $\mathbf{J} = \mathbf{N} + \mathbf{S}$, *and* $\mathbf{F} = \mathbf{J} + \mathbf{I}$, *so the electric dipole operator is rank-1 that only acts on the rotational coordinate, and we can "peel off" or reduce the angular momentum couplings in layers. First getting rid of m_F:*

$$\langle F'm'_F|\hat{d}_p|Fm_F\rangle = (-1)^{F'-m'_F} \begin{pmatrix} F' & 1 & F \\ -m'_F & p & m_F \end{pmatrix} \langle F'||\hat{d}||F\rangle. \tag{3.48}$$

For $F' = 0, m'_F = 0$, $F = 1, m_F = 0$, $p = 0$,

$$\begin{pmatrix} 0 & 1 & 1 \\ 0 & 0 & 0 \end{pmatrix} = -\frac{1}{\sqrt{3}}. \tag{3.49}$$

Then recouple from F to J using the $6j$ symbol:

$$\langle F'||\hat{d}||F\rangle = (-1)^{F'+J+1+I}\sqrt{(2F'+1)(2F+1)} \begin{Bmatrix} J' & F' & I \\ F & J & 1 \end{Bmatrix} \langle J'||\hat{d}||J\rangle. \tag{3.50}$$

For $J' = J = 1/2$, $F' = 0$, $F = 1$, $I = 1/2$, this factor evaluates to $\frac{1}{\sqrt{2}}$. Then recouple from J to N:

$$\langle J'||\hat{d}||J\rangle = (-1)^{J'+N+1+S}\sqrt{(2J'+1)(2J+1)}\begin{Bmatrix} N' & J' & S \\ J & N & 1 \end{Bmatrix}\langle N'||\hat{d}||N\rangle. \tag{3.51}$$

For $N' = 1$, $N = 0$, $J' = J = 1/2$, $S = 1/2$, this gives $\sqrt{\frac{2}{3}}$. Finally the pure rotational reduced matrix element is

$$\langle N'||\hat{d}||N\rangle = d_0(-1)^{N'}\sqrt{(2N'+1)(2N+1)}\begin{pmatrix} N' & 1 & N \\ 0 & 0 & 0 \end{pmatrix}. \tag{3.52}$$

For $N' = 1$, $N = 0$, this is just $\langle N' = 1||\hat{d}||N = 0\rangle = d_0$.

Multiplying everything:

$$\langle\uparrow|\hat{d}_0|\downarrow\rangle = d_0(1)\left(\sqrt{\frac{2}{3}}\right)\left(\frac{1}{\sqrt{2}}\right)\left(-\frac{1}{\sqrt{3}}\right) = -\frac{d_0}{3}. \tag{3.53}$$

In short, coupling N with electron spin S reduces d_0 by $\sqrt{2/3}$. Coupling J with nuclear spin I gives another factor $1/\sqrt{2}$. The $m_F = 0 \to m'_F = 0$ component gives $-1/\sqrt{3}$.

3.7 Blackbody Radiation

For molecules in the ground state $X(v = 0)$, blackbody radiation can drive vibrational excitation to $v = 1$. The blackbody excitation rate out of $v = 0$ is related to the spontaneous decay rate of the transition $v = 1$ *rightarrow*$v = 0$ by

$$\Gamma_{\mathrm{BBR}}(0 \to 1) = \Gamma_{\mathrm{sp}}(1 \to 0)\bar{n}_{\mathrm{th}}(\omega_{01}, T), \tag{3.54}$$

where the thermal photon occupation for a vibrational transition with angular frequency ω_{01} is

$$\bar{n}_{\text{th}}(\omega_{01}, T) = \frac{1}{\exp(\hbar\omega_{01}/k_B T) - 1}. \tag{3.55}$$

and

$$\Gamma_{\text{sp}}(1 \to 0) = \frac{\omega_{01}^3 |d_{10}|^2}{3\pi\epsilon_0 \hbar c^3}. \tag{3.56}$$

For CaF, $\omega_{01}/2\pi$ is about 17.6 THz, so at $T = 300$ K, $\bar{n}_{\text{th}} \simeq 6.3 \times 10^{-2}$.

The spontaneous lifetime of $v = 1 \to v = 0$ is [157, 158]: $\Gamma_{01}^{-1} = \frac{1}{4.65\ \text{s}^{-1}} \simeq 0.22$ s. Plugging this into Eq. (3.54) gives us

$$\tau_{\text{BBR}} = \Gamma_{\text{BBR}}^{-1} \simeq \frac{1}{(0.23\ \text{s})^{-1}(6.3 \times 10^{-2})} \simeq 3.6\ \text{s}, \tag{3.57}$$

which explains that observed ~ 3.5 s lifetime of optically trapped CaF in $X(v = 0)$ in Fig. 5.15 is black-body limited.

"I don't care about what anything was designed to do, I care about what it can do"

Apollo 13 (1995 film)

4

Experimental Apparatus and Developments

The experimental machine used in this work is the second-generation CaF apparatus, and retains much of its architecture from earlier CaF work: cryogenic buffer-gas beam source, radiative slowing, RF MOT, Λ-enhanced gray molasses, optical trapping, and loading of a 1D tweezer array of molecules and control are described quite comprehensively in the thesis in Ref. [159]. Many of the laser cooling and trapping techniques are first developed in the first-generation experiment, detailed in the thesis in Ref. [141]. Here we summarize most of these parts only to the extent needed to orient the discussion or to add more detailed description, and focus on the parts of the apparatus and modifications used in the present work.

4.1 Overview

In this section, for a clear overview of the apparatus involved, let us follow a CaF molecule along that path in the experiment, from the moment it is chemically synthesized in a cryogenic

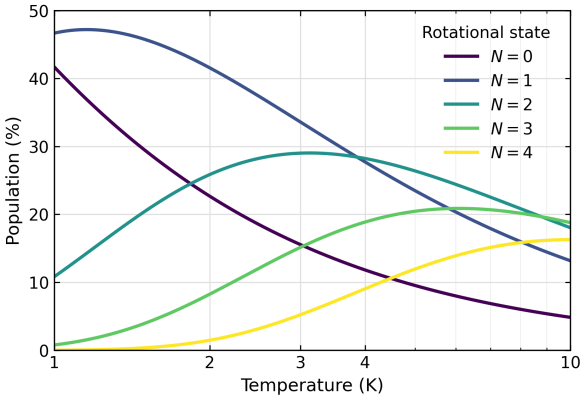


Figure 4.1: Thermal population of rotational states of CaF in $X^2\Sigma^+$, $v = 0$ as a function of rotational temperature. Calculated using Boltzmann weight of linear rotor: $(2N + 1)\exp[-E_N/(k_B T_{\mathrm{rot}})]$ with centrifugal distortion included in the calculation of E_N.

source to the when it is trap in an optical tweezer.

The experimental sequence begins in the "beambox" with production of a pulsed beam of CaF molecules from a cryogenic buffer-gas source (CBGB). The molecules are produced by laser-ablating a solid calcium target into a flow of sulfur hexafluoride (SF_6) gas inside the cell held at around 2.3 K by a closed cycle liquid helium pot. The produced molecules thermalize with cold helium buffer gas inside the cryogenic cell before being entrained into a molecular beam and exiting the cell. At this point, most of these molecules are in the $N = 1$ rotational states of $X^2\Sigma(v = 0)$ (see Fig. 4.1)

Our UHV system consists of a MOT chamber and a science glass cell, separated by a pumping manifold.

In the "MOT region", the molecular beam is radiatively slowed by a counter-propagating, frequency-chirped laser beam resonant on $X - B$ transition (531 nm), captured in an RF magneto-optical trap (MOT) which drives the main $X^2\Sigma^+ - A^2\Pi_{1/2}$ transition near 606 nm [41], then cooled by Λ-enhanced gray molasses [160] to $\sim 10\,\mu$K. A blue-detuned "conveyor-belt MOT" (described in Sec. 5.2) compresses it to high density to improve the subsequent transfer into a conservative optical dipole trap (ODT) far detuned at 1064 nm [161]. After this initial preparation stage, the cold gas of trapped CaF molecules is transported from the MOT region into a separate glass cell over a distance of 45 cm, by a one-dimensional optical lattice formed

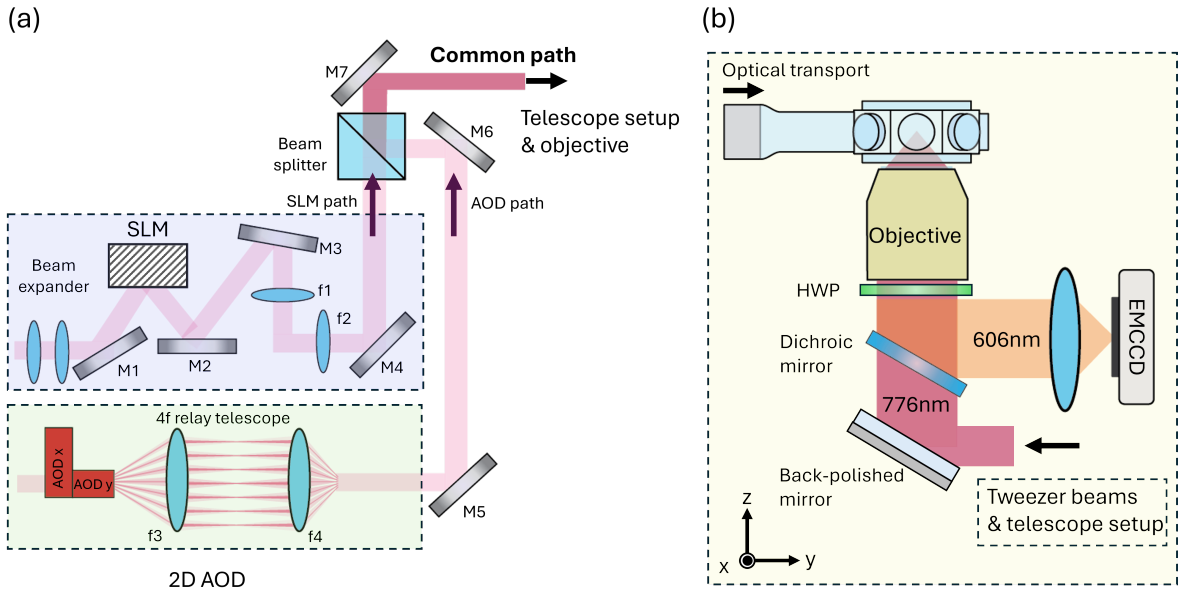


Figure 4.2: Optical setup for generating the two-dimensional tweezer array. Two independent 776-nm tweezer paths are combined before a common telescope setup and the microscope objective, through which they project trap light into a vacuum glass cell. The SLM path holographically generates a static array of traps, while the crossed-AOD path produces dynamically movable tweezers

by two counter-propagating 1064 nm beams.

Finally, in the "science region", the large optical access of the glass cell allows the use of a custom high-NA microscope objective to focus and project diffraction-limited optical tweezer traps at 776 nm. The microscope objective, imaging path, and basic trap characterization are described in Sec. 4 of Ref. [159]. The tightly focused optical tweezers provide single-molecule trapping, site-resolved detection and addressing, ability to perform rearrangement, and flexible control of the intermolecular separation.

4.2 Generation of Two-dimensional Tweezer Array

The tweezer array is generated by combining two complementary optical controls: a spatial light modulator (SLM, Exulus HD3HP) produces a static two-dimensional (2D) array of traps and defines trap position in the axial direction, while a pair of acousto-optic deflectors (AODs, AA Opto-Electronic) in a crossed configuration generate dynamically movable traps in lateral

directions. This hybrid architecture, already explored in many neutral-atom experiments [50, 57], is well suited for geometric control of relative positions between individually trapped molecules. During dipolar interaction experiments, one trap of an interacting pair of molecules is generated by the SLM and the other by the AODs.

Although crossed, multi-tone AODs can generate a static two-dimensional array, they cannot independently move individual tweezers in two dimensions and thus do not support arbitrary 2D rearrangement. Multi-tone RF driving also introduces several technical complications. Each trap generated by an AOD has an optical frequency shifted by its driving RF tone. When we bring many AOD-generated traps close together, their optical fields can overlap and beat at the RF frequency difference [88]. If the beatnote frequency falls close to twice the trap frequencies, it can result in intensity modulation and lead to parametric heating of molecules. In addition, for multi-tone driving waveforms into an AOD, especially for larger arrays, one needs to be careful about phases of the RF tones as they could sum up to cause large instantaneous peaks, which can saturate the RF amplifier and produce nonuniform trap depths and inter-modulation, as seen in many experiments [88, 162]. These problems become especially constraining for our dipolar interaction experiments with CaF, where the intermolecular spacings need to be a few micrometers. There are, of course, techniques to mitigate these technical inconveniences, for example, by using spectral engineering, but we opted to use the hybrid array to avoid them.

Figure. 4.2 shows the optical setup for generating the tweezer traps. The array is formed from two beam paths derived from the same laser: in one path, the light is reflected by a 2D phase-only SLM, while in the other path, the beam is diffracted by two crossed AODs to create a set of dynamic tweezers. In the SLM path, the array is generated holographically: a phase pattern is imprinted onto the incident light wavefront as it reflects off the SLM, and the microscope objective Fourier transforms that phase into intensity pattern at its focal plane. The hologram used for the SLM is computed iteratively using a weighted Gerchberg–Saxton-type algorithm that equalizes spot intensities [163, 164], and later optimized experimentally to equalize trap depths and correct residual wavefront errors (see Sec. 5.5). A 4f relay (f_1, f_2) between the SLM and the common path images the SLM plane onto the objective pupil.

In the 2D-AOD beam path, the AOD deflection plane is placed at a Fourier plane of the lens f_3, and a telescope relays this plane to the back focal plane of the objective. This converts transverse momentum to position control in the objective's focal plane (transverse plane). A single AOD provides steering in one direction, so for 2D control, two AODs are crossed with orthogonal acoustic axes. The two AODs are independently driven by programmed RF waveforms from an arbitrary-waveform generator (AWG).

The two beams are combined at a beamsplitter to a common beam path, which is subsequently expanded through a telescope setup to and sent through the objective for diffraction-limited projection in the glass cell.

4.2.1 Detection Path

A dichroic before the objective back pupil transmits 776 nm trapping light and reflects the molecular fluorescence at 606 nm for detection. The emitted fluorescence is imaged by a $f = 400$ mm tube lens and relayed through a $1:1$ telescope formed by two $f = 150$ mm lenses. There are interference filters and dichroic optics in the imaging path to filter leaked trapping and cooling light before the fluorescence is imaged onto an EMCCD camera (Andor iXon Ultra 897).

With an effective objective focal length of 18 mm, the imaging magnification is set primarily by the tube lens, giving a magnification factor of $M = f_{\text{tube}}/f_{\text{obj}} \simeq 400/18 = 22.2$, and thus object-plane pixel size of 16 μm$/22.2 \simeq 0.72$ μm per camera pixel, or equivalently 1 μm $\simeq 1.39$ pixels. In practice, the final pixel calibration is checked experimentally using the known tweezer spacing, as there can be small deviations arising from relay alignment.

4.2.1.1 Monitoring and Feedback for SLM-AOD Alignment

The SLM and AOD tweezer arrays have separate optical path lengths (differing by $\sim$ 1m) before being combined at the beamsplitter. Their differential beam path, and thus the relative alignment between the two sets of arrays, can slowly drift due to thermal gradient or mechanical

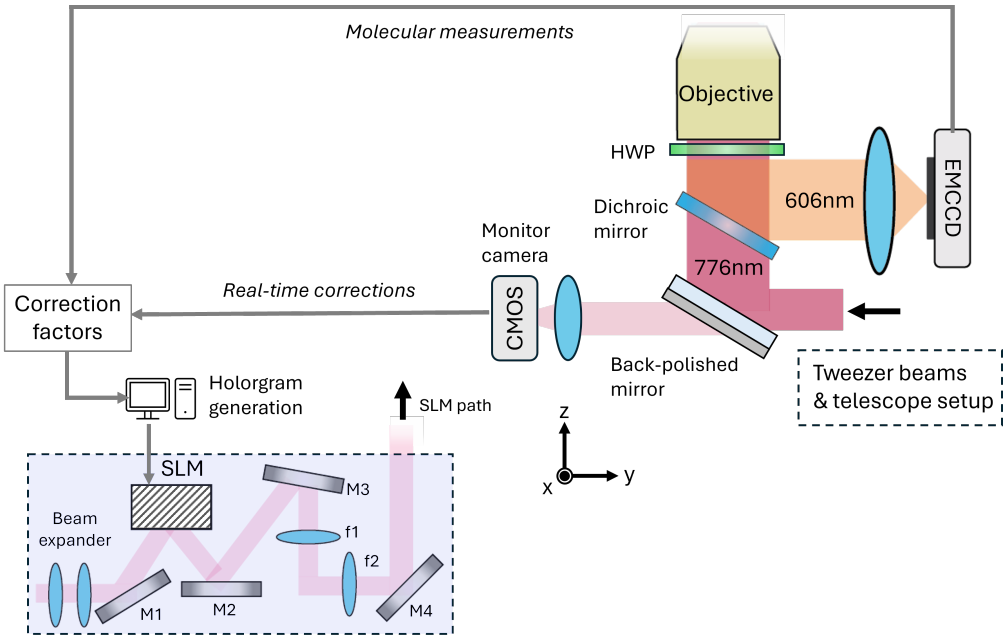


Figure 4.3: Monitor-camera feedback scheme for SLM array calibration and long-term stabilization. Leakage 776 nm tweezer light is imaged onto a CMOS monitor camera, providing real-time monitor of the projecting traps. The measured trap positions are used to update correction factors in the hologram-generation algorithm, providing feedback for SLM position and intensity uniformization. Further calibration is performed with in-situ molecular signals from the 606 nm fluorescence collected on the EMCCD.

creeps. To monitor the transverse overlap between the two sets of arrays, we collect the leaked light from a back-polished dichroic mirror before the objective and image the tweezer light onto a CMOS camera running at $\sim 160\,\mathrm{Hz/fps}$ with 170 μs exposure. The resultant image provides the site-resolved positions of the SLM and AOD tweezers in the x-y plane. In this way, the monitor camera gives us real-time, in-situ non-destructive diagnostic of the relative alignment during experimental sequence, and we update the feedback corrections approximately every 2 minutes with experiment repetition rate at 1 Hz.

We first use this image to individually position each SLM tweezer in the $x-y$ plane with respect to the AOD array. We fit the measured spots on the monitor camera, and extract the centers in $x-y$ plane. The correction factors to SLM phase pattern and site weights are obtained through iterations with a weighted Gerchberg–Saxton algorithm [163]. Once this per-site SLM calibration is done, it is then held fixed during data taking. and is stable over the course of weeks. We also verify the transverse alignment by optimizing the molecule handoff

independently between the SLM and AOD tweezers; within our measurement precision, the handoff optimum agrees with the camera-based calibration.

The SLM calibration can be strongly affected by changes in the thermal load on SLM. For example, we have observed that turning the tweezer incident light on and off can change the horizontal scaling of the SLM array relative to the unaffected AOD array. The monitor camera therefore also provides a long-term feedback signal for correcting slow differential drifts between the two beam paths. The camera records the tweezer images at every experimental shot, and an analysis program extracts the sub-pixel centroid of each trap, from which we can also obtain each pair's separation vector in the $x - y$ plane, as well as the mean relative displacement between two arrays by taking the average of all the pair-wise offsets. This information monitors the positional disorder in pair separation and global drift over time, and is converted into correction factors applied to the SLM hologram. The slow feedback is updated at a rate of a few Hz, with correction size at each step bounded to prevent large jumps.

With the feedback and compensation in place, we can maintain the overlap between the AOD and SLM arrays to within 100 nm. Note that the monitor camera does not detect any relative axial offset. To compensate for that, we turn to molecular measurement signals described in Sec. 5.4.

4.2.2 SLM Stability

Beside the obvious effect of thermal load causing changes in trap pattern generated by SLM, we also observe that water-cooling circulation on the SLM can induce fast mechanical vibrations. These vibrations are roughly from tens of hertz to hundreds of hertz, which is too fast to be compensated by the feedback or the positional echo protocol (see Chap. 7), but slow enough to affect millisecond-scale dipolar evolution in CaF molecules.

We characterize this mechanical noise using the monitor camera described above in a high-frame-rate mode. The camera records the SLM and AOD tweezer spots at more than 200 fps, and each frame is fit to extract the individual trap centers. From these, we can obtain the time-dependent separation of each SLM-AOD trap pair. We apply Fourier transform to

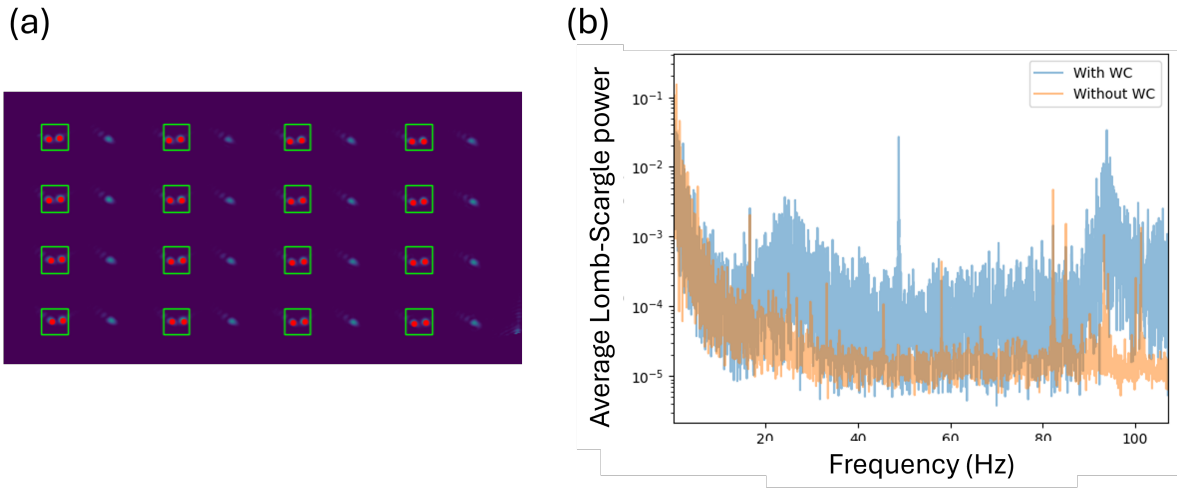


Figure 4.4: (a) An example image of the tweezer traps from the monitor camera showing pairs of the SLM and AOD traps. (b) Fourier transform of the time-dependent relative pair separations measured with SLM water cooling (WC) system enabled and disabled. Water cooling unit introduces broadband position noise and narrow mechanical lines, most prominently near 50 Hz and 95 Hz, while turning off water cooling substantially reduces the mid-frequency relative positional jitter.

convert the measured trap-separation time trace into a frequency spectrum, where peaks in the spectrum identify periodic vibration, while the broadband background measures non-periodic jitter spread over many frequencies. Figure 4.4 shows the measured Lomb–Scargle periodogram with the circulating water cooling on and off, revealing that with water cooling, there is broadband noise from 10 Hz to over 100 Hz with a narrow peak around 50 Hz (consistent with the water pump rotation speed) and a large bump near 95 Hz.

Turning off water cooling reduces fast mechanical vibrations, but we measure that the uncontrolled SLM temperature drifts by more than 1°C over the timescale of hours. This corresponds to an observed RMS relative motion of about 42 nm. A useful scale to put this into context is the molecular wavepacket width. In our tweezers, the CaF motional ground-state size is approximately 46 nm in the radial directions and 114 nm along the axial direction. So this drift is comparable to the radial ground-state wavefunction size.

4.3 Glass Cell and Microscope Objective Characterization

The science region in our experiment is built around a UHV-compatible octagonal fused-silica glass cell (Precision Glassblowing) with nano-textured anti-reflection coatings on the visible optical surfaces. The glass cell provides large optical access for high-NA tweezer projection and fluorescence collection, and is part of the imaging system as our the microscope objective is designed to operate through the specified fused-silica window thickness.

Therefore, for diffraction-limited performance, we performing testing and characterization to ensure (1) the glass cell windows meet specified design flatness and thickness, and that the window flatness does not deform beyond spec range when pumped under vacuum; (2) the objective is diffraction-limited both for projecting trap light and for imaging emitted CaF fluorescence. To do so, we build a phase-shifting interferometer to measure the flatness and thickness of optical surfaces, as well as perform direct point-spread-function measurement.

4.3.1 Interferometric Optical Testing

The glass cell has two large primary windows fused to a fused-silica frame, each with a specified thickness of 0.25 in (or 6.35 mm). These windows along the objective axis are the most important because any surface figure error will causes wavefront distortion of incident light (which is near normal), and thickness variations will cause additional path lengths in glass. For scale, with a glass index refraction of $n \approx 1.46$, a quarter wave of surface figure error is $\sim 0.11\lambda$ of transmitted wavefront error (TWE).

Interferometry is a non-contact technique widely used to quantify surface topology with high precision, where an interferogram of recorded fringes can show what kinds of aberrations are in the optical system under test. For our glass cell, we are interested in the four parallel optical surfaces of the primary windows. However, since surfaces have comparable reflectivity, a conventional long-coherence interferometer would produce overlapping fringe patterns from several surfaces at once. We therefore build a short-coherence phase-shifting Fizeau interferometer to isolate the desired surface. Schematic of the full optical setup is shown

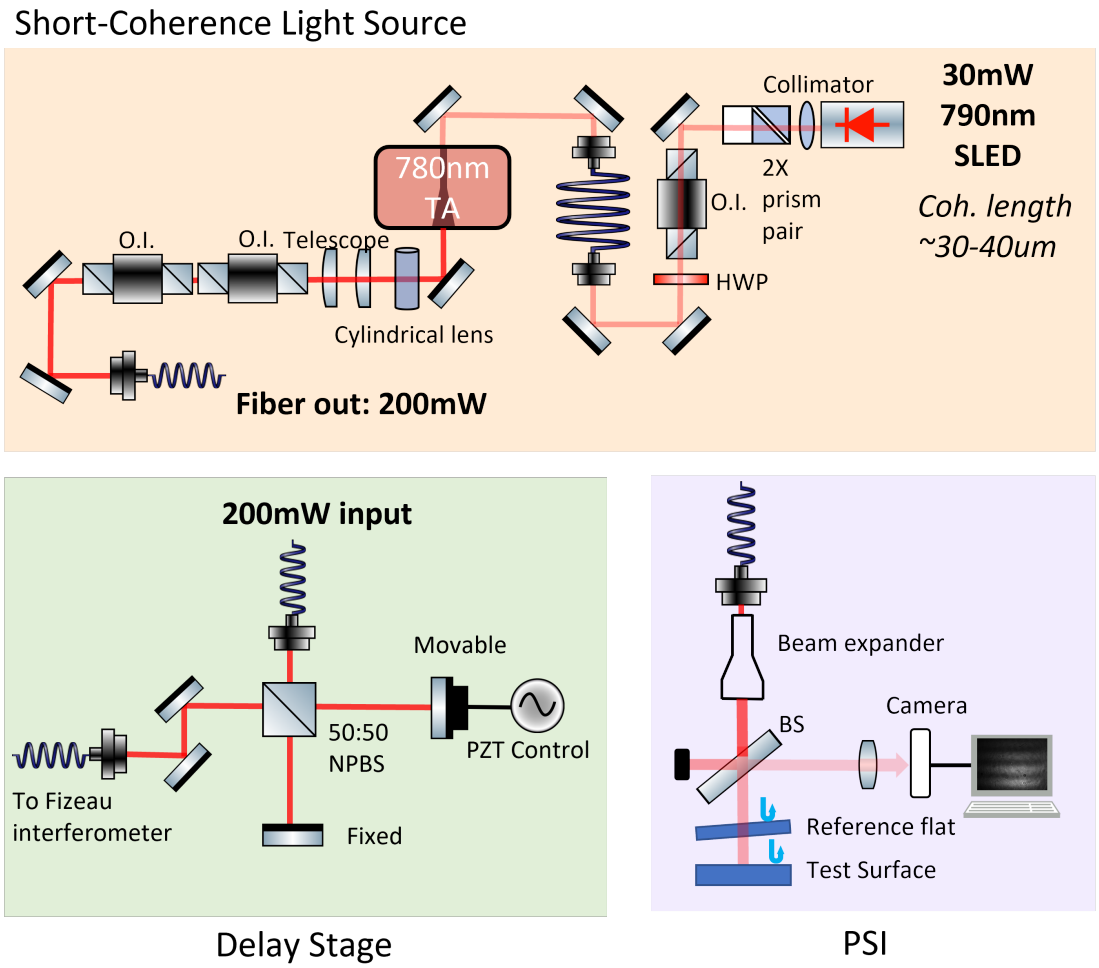


Figure 4.5: Optical layout of a short-coherence phase-shifting Fizeau interferometer used for glass-cell and optical-surface characterization. An SLED amplified by a tapered amplifier provides a high-power, short-coherence source. A delay stage is used to select the desired reflecting surface by tuning the optical path length, while a piezo-mounted mirror provides the phase scan for PSI. The expanded beam interferes the reference-flat reflection with the test-surface reflection, and the resulting interferogram is imaged on a camera.

in Figure 4.5.

The setup consists of a short-coherence light source, a delay stage, and the phase-shifting interferometer (PSI). The light source comes from a 790 nm superluminescent diode (SLED) amplified by a tapered amplifier (TA). The output power after TA is about 200 mW, enough to see fringe contrasts from two weakly reflecting AR-coated window surfaces. The SLED has a short coherence length of $l_c = \lambda^2/\Delta\lambda \approx 45\,\mu$mm where $\Delta\lambda = 13.9$ is the laser line width and $\lambda = 790$ nm, and because l_c is shorter than any surface spacing (the glass cell window

thickness is 6.35 mm), the surfaces are well separated to suppress unwanted interferences from other surfaces along the optical path.

A variable delay line allows us to select the surface under test. The delay stage is essentially a a fiber-coupled Michelson delay line, with a 50:50 non-polarizing beamsplitter splitting the input light into fixed arm and a piezo-actuated movable arm to produce two copies of the wavefront, and a piezo provides the scanning of the phase shift used for phase-shifting interferometry. Finally, the light is sent through polarization-maintaining fiber to a Fizeau cavity formed by a $\lambda/20$ reference flat and the surface under test.

For each measurement, we recorded a video of the interferogram while scanning the piezo to produces a phase shift $\phi(t)$. We then select four frames separated by approximately $\pi/2$ in phase and analyze with a four-step PSI algorithm. The measured intensity of the interferometer is

$$I(\phi) = I_1 + I_2 + 2\sqrt{I_1 I_2}\cos(\Delta\phi + \phi). \tag{4.1}$$

By taking four images separately at $\phi = 0, \pi/2, \pi, 3\pi/2$, we can obtain the phase

$$\tan(\Delta\phi) = \frac{I(3\pi/2) - I(\pi/2)}{I(0) - I(\pi)}. \tag{4.2}$$

We then use algorithm to unwrap the phase and subtract a best-fit plane, which removes the tilt from any residual non-parallelism, to get the surface error map. Figure 4.6 shows the measurement data processing workflow of obtaining a surface error map of a surface. A single data set gives the figure of all four surfaces, each window thickness, and the inter-window parallelism.

This procedure is applied to measure all four surfaces of the glass cell windows, both before and after pumpdown. Before pumpdown, the central ~ 1 inch region of the primary windows is consistent with approximately $\lambda/4$ flatness. After pumpdown, the center of the window curved inward under atmospheric pressure, increasing the measured surface curvature. The measured deformation is qualitatively consistent with the COMSOL simulation that the window bends in a nearly cylindrically symmetric manner. For an objective well centered on the glass cell

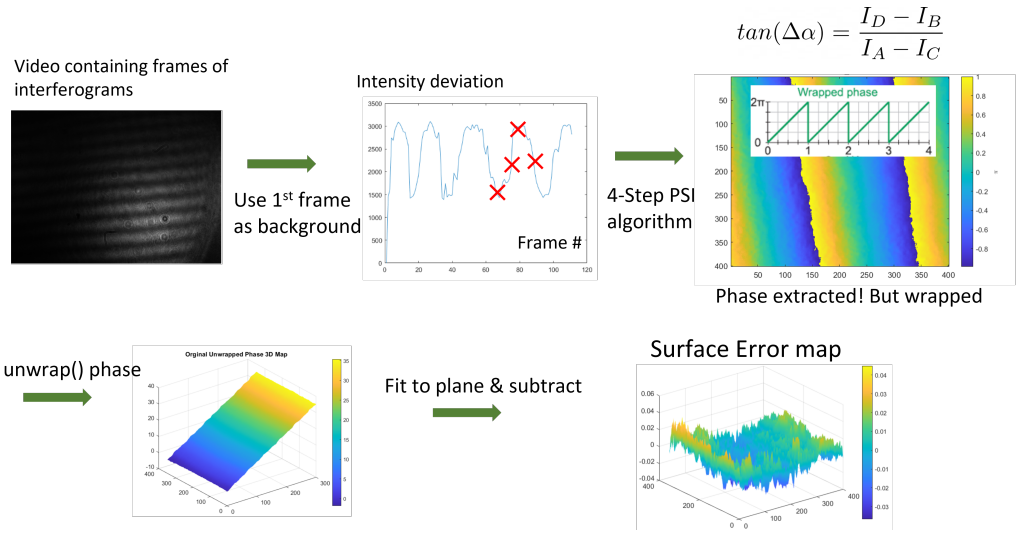


Figure 4.6: Data-processing workflow for phase-shifting interferometry. A video of interferograms is recorded while the piezo-mounted mirror is scanned. The frame-to-frame intensity deviation is used to select four interferograms separated by approximately $\pi/2$ in phase. A four-step PSI algorithm extracts the wrapped phase, which is then unwrapped, fit to a plane, and tilt-subtracted to obtain the residual surface error map.

window, this low-order curvature is mostly defocus and can be compensated by refocusing the objective; the more troubling errors are higher-order surface figure terms, which we cannot remove by doing focus adjustment.

In short, the test verified that the glass cell is sufficiently flat over the central science region to the spec tolerances.

4.3.2 Objective Wavefront and Point Spread Function

Our microscope objective (Special Optics) is custom-engineered to have 0.6 NA, back aperture size of ~ 22 mm, and diffraction limited performance at 531 nm ($X - B$ transition), 606 nm ($X - A$ transition), and 780 nm (optical tweezer light wavelength) over a field of $\approx 100\,\mu$m in the center. The objective serves to both project trap potentials into the glass cell and to collect 606 nm fluorescence. For trap projection, the figure of merit is the intensity distribution near focus as the optical potential follows $U(\mathbf{r}) \propto I(\mathbf{r})$. Aberrations can increase the beam waist, distort the harmonic potential near the trap center, and even introduce site-dependent trap properties across the field of view. For imaging, the metric is the point spread function (PSF),

which sets the ability to resolve fluorescence from neighboring molecules.

With these in mind, we characterize objective using two complementary methods: an interferometric transmitted-wavefront test and a direct PSF measurement.

For the transmitted-wavefront measurement, the wavefront is measured by autocollimation. A flat reference wavefront enters the objective, and is converted into a converging spherical wave. Inside the glass cell, we place a reference sphere (a bearing ball) at the focal plane of the objective. Now the wavefront from the sphere will interfere against the flat, and the return wavefront is again analyzed by interferometry technique. The reference sphere we use is a Grade-5 silicon-carbide bearing ball, and we attach it to a 5-axis translational stage for translation, pitch, yaw, and focus control to minimize aberrations due to mis-alignment. Note that because the light passes the objective twice, the map is the round-trip wavefront error and the single-pass aberration is approximately half.

From the measurements, we obtain approximately NA $\simeq$ 0.5, and the measured RMS wavefront error is about 0.09 waves, consistent with near-diffraction-limited performance used for most tweezer operation.

Finally, we measure the imaging PSF Using sub-resolution fluorescent beads deposited on a cover glass to mimic the molecular fluorescence signal (since we cannot have molecules in there yet). These beads have size ranging from tens of nanometers up to 200 nm, which is much smaller than the airy radius $\frac{0.61\lambda}{\mathrm{NA}} \approx 0.6\,\mu$m at visible wavelengths. We dilute the beads in isopropyl alcohol, drop cast onto a thin microscope cover slip, and let them dry. We then place the coverslip at the focal plane of objective. The beads are excited optically with 574 nm light and imaged through the objective onto a camera, with a 610 nm bandpass filter selecting the bead fluorescence. As the bead diameter is well below the expected diffraction-limited spot size, the recorded image can be used to approximate the objective PSF, convolved with a small source.

Finally the measured spot is fit to an Airy model, yielding a full width at half maximum of 0.5 μm, consistent with the expected diffraction scale for visible light at NA near 0.5–0.6. The Airy first-zero radius is approximately $0.61\lambda/\mathrm{NA}$, and the intensity FWHM is approximately

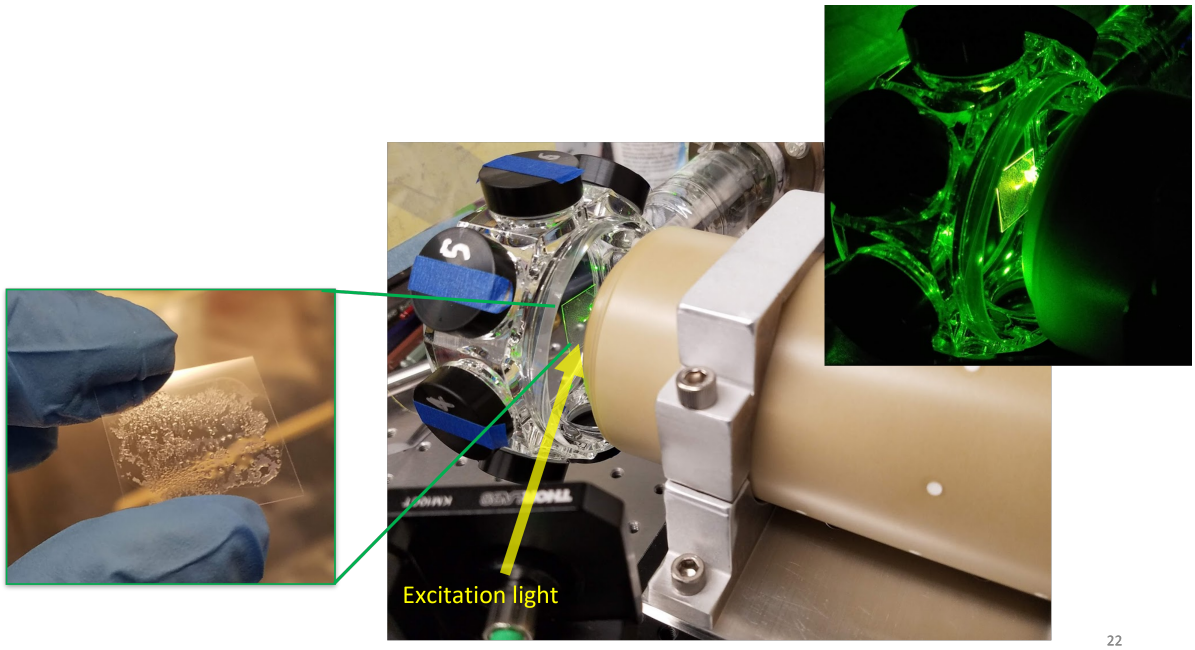


Figure 4.7: Fluorescent-bead measurement of the objective point-spread function. Sub-resolution fluorescent beads were diluted, deposited on a microscope coverslip, and placed at the objective focus. The beads are excited, and their fluorescence is collected by the objective and imaged onto the camera.

$0.51\lambda/\mathrm{NA}$. For $\lambda \simeq 606$–610 nm and $\mathrm{NA} \simeq 0.6$, these give a diffraction-limited transverse scale of order 0.5–0.6 μm.

4.4 Passive and Active Stabilization of Stray Fields

In this section, we describe the passive and active field compensation systems in place to reduce stray electric fields from charges around the glass cell, and to suppress magnetic field drifts with active field stabilization.

4.4.1 Electric Fields

Static electric fields produce a differential DC Stark shift through weak admixture of opposite-parity rotational states. The dominant source of stray DC fields is charge accumulation on insulating (dielectric) surfaces on the glass cell. Dielectric surfaces can acquire patch charges from many sources, such as optical illumination, charged particle flux, or nearby high-voltage

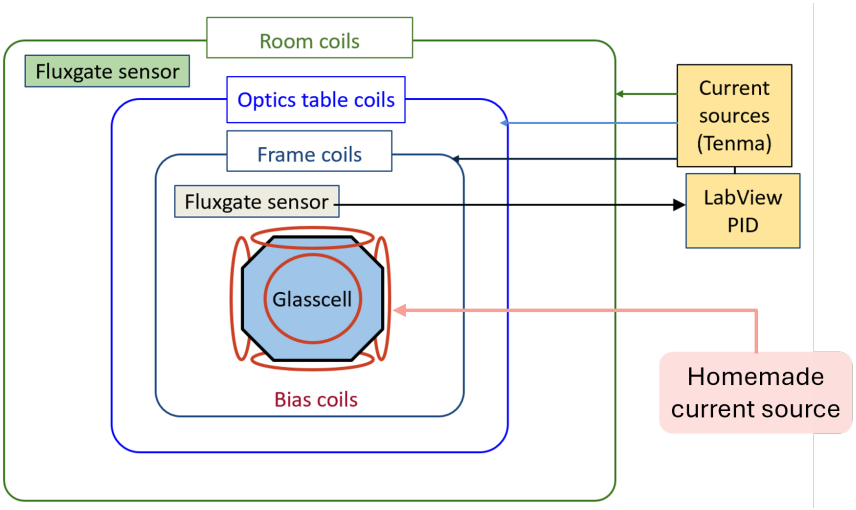


Figure 4.8: Schematic of the nested coil system used to stabilize slow magnetic-field drifts near the glass cell region. A fluxgate magnetometer measures the ambient field and feeds a LabVIEW PID loop, which drives the compensation coils through current sources. With compensation enabled, the line-cycle-averaged total field noise is reduced to the $\sim 60\ \mu$G level, compared with ~ 200 mG without compensation.

switching. These charges can produce large, slowly drifting electric fields that are difficult to trace. To neutralize charge on external dielectric surfaces, a commercial cleanroom ionizing bar (Terra Universal) containing titanium corona emitters that produce a balanced flux of positive and negative ions, is mounted directly beneath the HEPA fan-filter unit, so that the airflow carries the charges on to the optics table. In addition, since these ions cannot reach charges on the interior of glass cell, we illuminate the glass cell with a high-power 365 nm UV LED (Violumas). This technique follows from Rydberg-atom experiments in which stray fields from surface charge, such as adsorbed atoms or electrons bound to the glass cell wall, are shown to be reduced by light-induced desorption and redistribution of the charge layer [165, 166]. Lastly, the largest stray time-varying electric fields in lab comes from the 60 Hz mains. We trigger the experimental sequence at a fixed phase of the 60 Hz power line so that the start of each experimental shot is phase-locked to the power line cycle.

4.4.2 Magnetic Fields

For the rotational qubit used in this work (see Sec. 6.3), the states carry a small differential magnetic moment, and at finite magnetic field, the transition frequency shifts roughly linearly with the B field, with a slope of -309 Hz/mG at our typical $B = 3.2\,\mathrm{G}$ applied field.

Our magnetic-field coils are separated into coils for applying local fields that are not compensated, and nested sets of compensation fields. For applied fields, the bias coils and high-field coils (used only during Raman sideband cooling, see sec 6.4.2) around the glass cell provide the main quantization field used during experiment.

Around the glass cell, besides the coils used for applying the quantization B field, there is an additional set of small bias coils ($\sim 2-5\,\mathrm{G}$) around the glass cell. These coils are controlled by linear current supplies (Tenma), and used to zero residual fields at the molecules when no large external field is applied, or to provide small offsets relative to the table coils. The current to these coils are scanned, for example, to optimize Λ-cooling temperature of molecules in traps which requires zero field. When scanning for the zero-field point, the axis under test is temporarily switched to a programmable bench supply controlled over Ethernet. Similarly, a separate set of table frame coils (14 AWG magnet wire wound on a machined aluminum U-channel) that go around entire optics table (including glass cell "science" region and MOT region, see Sec. 4.1) provide the initial zeroing at the MOT chamber. Finally, the room coils cover the entire lab room, and are used to compensate far-field noise. These coils are multi-core cables routed around the ceiling, with the lower wall runs replaced by thin copper coil, reaching 10

,A on the X and Y axes for roughly 20 mG and 5 mG, respectively.

The two dominant sources of magnetic field noise are the nearby MBTA subway trains, and the 60 Hz power line and its harmonics. To mitigate our sensitivity to fluctuating fields due to the subway trains, we employ an active, multi-axis magnetic-field stabilization on the room coils with a feedback loop. A three-axis fluxgate magnetometer (Bartington Mag-13MS100) is positioned as close to the glass cell as the geometry allows us to sense variations in the magnetic

fields at the molecules. The fluxgate's output signal is digitized synchronously with the 60 Hz line by an 18-bit input card (NI PXI-6289), with acquisition triggered on the line zero-crossing and averaged over each line cycle ($\approx 16.7\,\mathrm{ms}$), and fed into a LabVIEW PID controller. The digital PID output is converted back to an analog control voltage (by a 16-bit output card, NI PXI-6733).The bias coils are driven by a homemade bipolar, voltage-controlled current source (see Ref.[159] for design details). This current source uses four OPA549 high-power operational amplifiers (op-amp) connected in parallel, each through a $0.1\,\mathrm{m}\Omega$ ballast resistor for load-balancing. The output current is measured with a low-drift current-sensing resistor, amplified with instrumentation amplifier (AD8228), and compared against an external analog set-point to form an error signal; an analog PI stage then regulates the current, with proportional and integral terms tuned separately, supplying a low-noise current for the large room coils. Note that the compensation axes are not perfectly orthogonal, so the correction intended to cancel one component can project onto another component. The multi-axis control allows us to independently tune all three directions to minimize the total field vector.

This active loop suppresses slow, random magnetic-field drifts, but it does not remove magnetic-field noise within a single 60 Hz cycle. The 60 Hz and its harmonics are taken care of by synchronizing the experiment to the power line. Since the 60 Hz component and its 180 Hz harmonic are stable in phase and amplitude, each experimental shot samples nearly the same waveform. This means the line-synchronous field appears mostly as a repeatable phase shift.

One other complication is that, during the experimental sequence, applied magnetic fields for setting quantization axis and other magnetically activated components nearby such as tunable lens can saturate the fluxgate sensor. To handle this, we hold the PID output for the duration of each shot and update it between sequence runs.

The active feedback, together with the line-triggering, reduces the residual field seen on the experiment to below $\sim 40\,\mu$G along the nosier axis affected by the subway line, and $\sim 35\,\mu$G RMS in the remaining two axes, or a total magnetic field noise of $\sim 70\,\mu$G.

4.5 Laser Systems

The 531nm laser (Precilasers, 10W) drives the $B^2\Sigma^+(v'=0) \rightarrow X^2\Sigma^+(v=0)$ transition. The laser source is based on a single-frequency 1062 nm DBR seeding a Yb-doped fiber amplifier in which the infrared light is frequency-doubled through MgO:PPSLT crystal, producing about 10 W at 531 nm. The beam exiting from the laser doubling head is only ~ 0.5 mm in diameter, so handling this requires some care in the few downstream optics. In particular, we used a telescope immediately after to expand the beam, and replaced optics components susceptible to thermal lensing with high-power ones, including optically contacted fused-silica PBS and a quartz AOM.

The laser is primarily used during radiative slowing of molecular beam for which several watts of optical power is required and frequency is swept over 400 MHz. The light source is frequency-jumped and reused in the experimental sequence for optical pumping during Raman sideband cooling (RSC) described in 6.4, where much lower power is required. To get robust sub-millisecond frequency hopping over GHz range from laser slowing to RSC optical pumping within the experimental sequence time, we implement an offset-lock of the laser seed to a separate 1062 nm reference laser using an optical phase-locked loop (OPLL) described below.

4.5.0.1 Agile Laser Locking and Frequency Jumping

The OPLL locking scheme is shown in Fig. 4.9. A low-power, low-noise, narrow-linewidth 1062 nm laser (NKT Photonics) serves as the frequency reference, where part of the light is frequency-doubled in a waveguide PPKTP crystal to visible 531 nm in order for it to be locked to the wavemeter through software servo. The rest of the 1062 nm reference light is then combined in fiber with the experimental 1062 nm seed light (Photodigm DBR) used by the high-power 531 nm to produce an optical beat note signal at ~ 2.57 GHz detected by a fast photodiode. The OPLL converts this beat note from optical frequency to an error signal to within the operating RF frequency range of the phase-frequency detector (ADF4002). The frequency division in the setup makes it possible to deal with the high-frequency optical beat

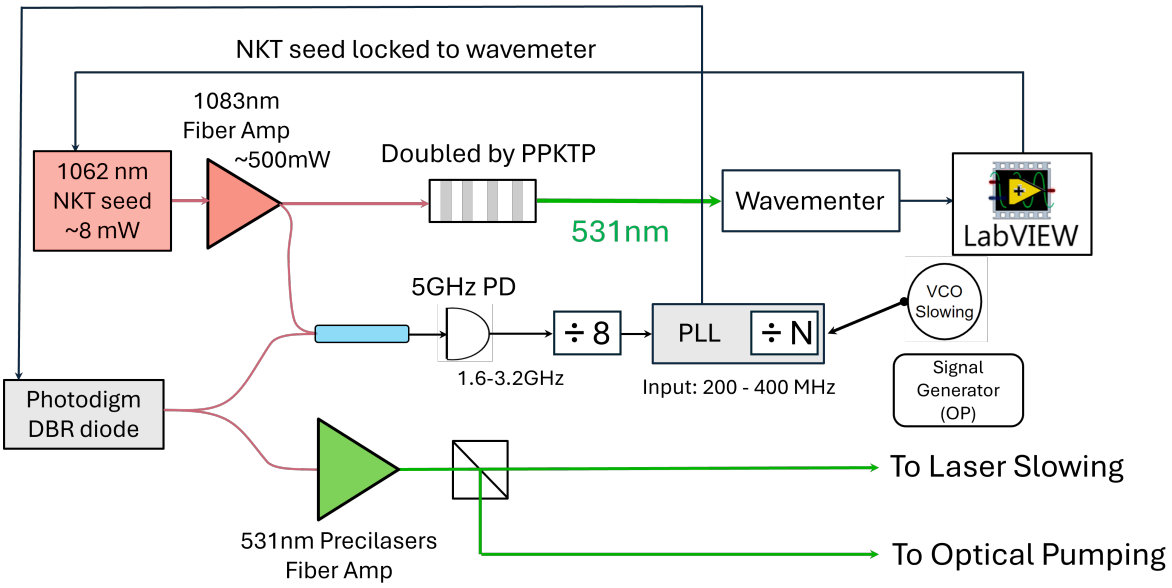


Figure 4.9: Laser locking scheme for 531 nm system used for laser slowing and optical pumping during Raman sideband cooling.

note electronically. More specifically, we use an RF pre-scalar to divide the optical signal's frequency by 8 and further dividing the signal by programmable N counter of the ADF4002. Lowering the division ratio can improve the phase-noise suppression, but the main goal for our application is to have reliable, rapid jumps of frequency offset. The resultant signal is compared against an external RF reference near 65 MHz set by either the chirp slowing VCO or RSC optical pumping signal generator. Finally, the charge-pump output of ADF4002 is passed through a loop filter and fed back to current control of the DBR diode driver. In bench tests of the setup, where a $\sim$ 16 GHz optical beat and an overall divide-by-64 RF prescaler were used, the lock settled in about 10 μs with a capture range of about 1.6 GHz.

During laser slowing, as the molecules decelerate, their Doppler shift spans over hundreds of MHz. To cover this range, we chirp the center frequency of the laser to approximately follow the Doppler shift seen by the molecules in the beam, with a chirp rate proportional to the photon-scattering rate. As each photon scattering transfers momentum of $\hbar k = h/\lambda$, with a scattering rate of R_{sc}, the average radiative force is $F = \hbar k R_{\mathrm{sc}}$. For molecules counter-propagating the slowing beam, the Doppler shift the laser frequency in molecule's frame is $f_D = v/\lambda$, the rate

of frequency shift is then $|\frac{df_D}{dt}| = \frac{1}{\lambda}|\frac{dv}{dt}| = \frac{h}{m\lambda^2}R_{\mathrm{sc}}$. Decelerating CaF from ~ 160 m/s to the 10 m/s MOT capture velocity requires about 1.2×10^4 photon recoils. Over a 4.5 ms slowing duration, this corresponds to a time-averaged $R_{\mathrm{sc}} \sim 2.6 \times 10^6$ s^{-1}. The frequency reference during the chirp is provided by a VCO (voltage-controlled Oscillator), and we tune the control voltage of the VCO to set the OPLL frequency offset, generating the chirp without taking laser out of lock. In the experiment, a typical sweep starts about 450 MHz below the resonance of $B(v = 0, N = 0) \rightarrow X(v = 0, N = 1)$ and ends on resonance.

The method used to implement the frequency locking also evolved during development of the apparatus. In early implementation where this laser source was used only for slowing, we locked the frequency to wavemeter and used a simple Fabry-Pérot cavity for fast frequency reference, where a small pick-off beam is modulated at 15 MHz. The demodulated signal is then detected after the cavity at a photodiode to produce error signal that was fed back to the frequency-control input of the 1062 nm seed. The cavity resonance is swept by adding Cicero-generated chirp waveform to the piezo control voltage, and an LF398-based sample-and-hold circuit held the wavemeter correction fixed during the chirp.

4.5.0.2 Slowing Beams

The optical transitions and beam delivery optics for slowing are shown in Fig. 4.10. The main radiative slowing force comes from photon cycling on the $X^2\Sigma^+(v = 0, N = 1) \rightarrow B^2\Sigma^+(v'' = 0, N'' = 0)$ transition at 531 nm, where population leakage into higher vibrational levels of the X state is repumped through two X-A transitions near 628 nm: $X^2\Sigma^+(v = 1, N = 1) \rightarrow A^2\Pi_{1/2}(v' = 0, J' = 1/2, +)$ and $X(v = 2, N = 1) \rightarrow A(v' = 1, J' = 1/2, +)$, conventionally referred to as $v = 1$ and $v = 2$ repumps, respectively. The 531 nm X-B light is frequency chirped, and is passed through a resonant EOM at 25 MHz that generates the sidebands to address to all four hyperfine components of the $X(N = 1)$ state. Note that more recently, a programmable spectral synthesis is used to generate the sidebands using high-bandwidth fiber phase modulator [167], where a computed time-dependent phase waveform is applied to the 1062 nm seed such that after phase modulation, amplification, and frequency doubling, the

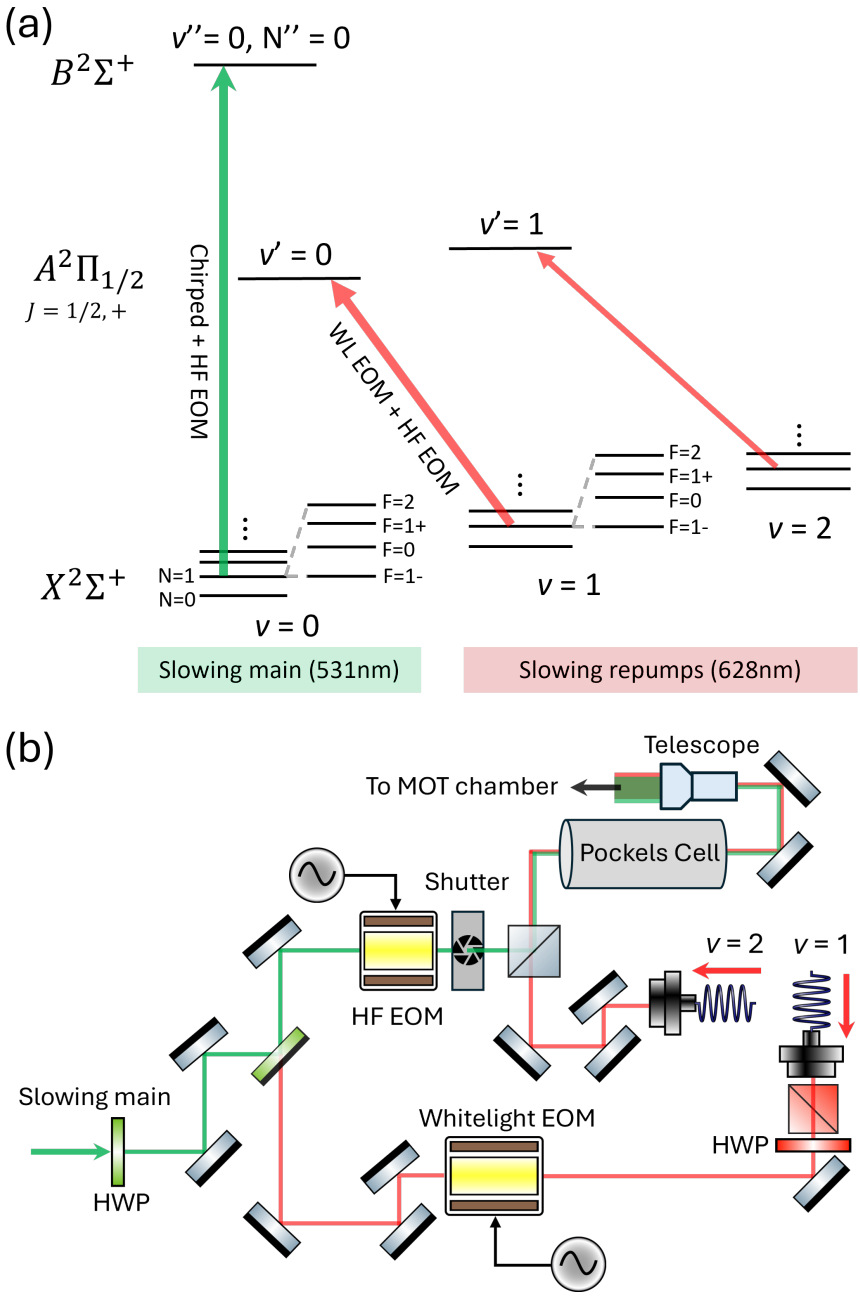


Figure 4.10: Optical transitions **(a)** and beam delivery optics **(b)** used for slowing. Main slowing transition $X^2\Sigma^+(v=0, N=1) \rightarrow B^2\Sigma^+(v'=0, N'=0)$ at 531 nm is frequency chirped and passed through a hyper EOM to address $X(N=1)$ hyperfine states. The $v=1$ repump is broadened using a white-light EOM and also contains the hyperfine components. Both $v=1$ and $v=2$ repump beams are combined with the main 531 nm light and sent through a Pockels cell that switches the polarization to remix Zeeman dark states before being sent into the MOT chamber counter-propagating to the molecular beam. The 531 nm system and optics are also described in [9].

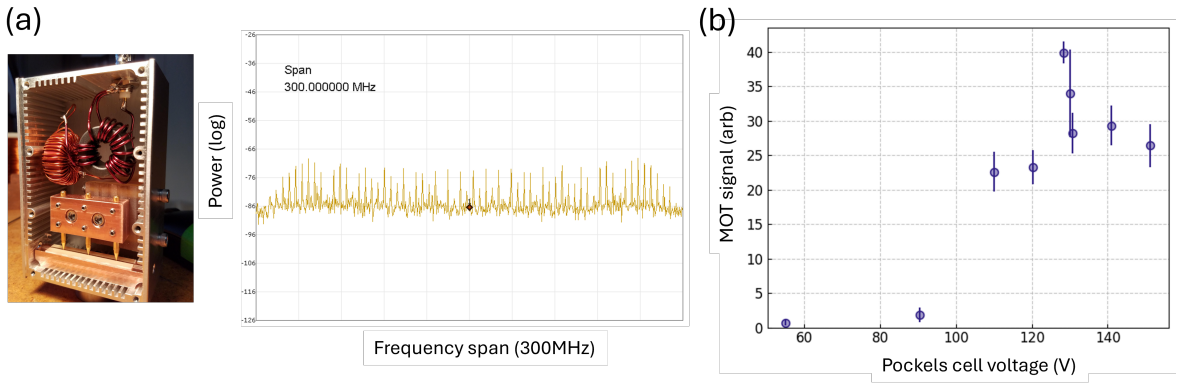


Figure 4.11: (a, left) "White-light" EOM, where the driven crystal is rigidly supported from the housing using Ultem, with stainless-steel fasteners and spring-loaded pogo-pin contacts to minimize stray capacitance. The resonant circuit is impedance matched to the 50 Ω RF source with a transformer and is driven through a RF amplifier (Mini Circuits ZHL-5W-1+) with approximately 44 dB gain. (a, right) Measured spectrum produced by the White-light EOM, which is driven at 5 MHz and has a measured resonance width of ~ 50 kHz, corresponding to $Q \sim 100$. The EOM generates closely spaced sidebands over a bandwidth of 250–300 MHz. (b) MOT signal versus Pockels-cell drive voltage. The applied voltage controls the electro-optic retardance, and hence the polarization of the slowing light. The homemade Pockels-cell driver takes in a 1 MHz TTL input and converts it into control signals for a GaN half-bridge, which rapidly switches the externally supplied high-voltage DC bus to generate the high-voltage square waveform drive that modulates the crystal birefringence and thus changing polarization of the input light.

optical spectrum approximates our desired sideband frequencies and powers. The $v = 1$ slowing repump light (460 mW out of the fiber) is white-light broadened with a spectrum of roughly 250 MHz bandwidth using a homemade EOM (more technical details are described in Appendix C of [9]), and also contains the four $X(N = 1)$ hyperfine components. The main 531 nm light, $v = 1$ and $v = 2$ beams are combined before going through a Pockels cell (Conoptics 350-80) oriented at 45° and driven to switch the polarization to de-stabilize the Zeeman dark states. The combined beam is sent into the MOT chamber counter-propagating to molecular beam, and weakly focused with ~ 18 mm beam diameter at the MOT center and 6 mm at the cryogenic cell aperture. Fig. 4.9(b) shows the effect of polarization switching from the Pockels-cell on the MOT signal.

4.5.1 606 nm for $X - A$ Transition

The beginning of our trust issue with Precilasers...

The 606 nm main light drives the $X^2\Sigma \rightarrow A^2\Pi_{1/2}$ cycling transition in CaF and is used for

laser cooling in the MOT and optical traps, as well as detection, and state preparation. Initially, this light was generated by a commercial Raman fiber amplifier (RFA) from Precilasers, seeded at 1212 nm external-cavity diode seed, amplified in the Raman gain fiber and frequency-doubled in a pair of MgO:PPLN crystals to 606 nm, producing up to 4 W of output (also see Ref. [159]). After roughly four years of continuous service, the output power degraded substantially over time, with a failure mode consistent with dead pump diodes inside the amplifier. Unfortunately, due to certain regulations, a replacement RFA is off the table.

To replace this, we turn to custom sum-frequency-generation (SFG) system, by combining high-power infrared light near 977.5 nm and 1597 nm:

1. The 977 nm system is seeded by hybrid external-cavity laser (HECL) diode from IPS with > 100 mW, in a homemade free-space seed box containing the diode driver, optical isolation and fiber coupling, and amplified by a ytterbium-doped fiber amplifier (YDFA, Precilasers) to ~ 6 W.
2. The 1597 nm arm consists of a DFB seed amplified by an EDFA; both the seed and amplifiers for 1597 nm come from Precilasers.

The two beams are combined and mixed inside a pre-built Precilasers SFG head, and the system is specified to output up to 5.2 W laser power at 606 nm. Note that for the 977 nm seed box, a free-space setup is preferred over a fiber-coupled butterfly package, because for an external-cavity seed, back-reflections can destabilize the cavity and produce mode hops. The free-space layout allows us to place isolators before the fiber coupler and to control the seed polarization before injection into the amplifier. Another technical note is that the seed must have clean, linear polarization (PER >20 dB), and launched into the correct axis of the a polarization-maintaining fiber. This is because fiber amplifiers are polarization sensitive and are designed to amplify the field polarized along the specified axis of the polarization-maintaining fiber, typically the slow axis.

After optimizing the 977.5 nm seed polarization, we obtained stable overnight operation. With approximately 6 W of 977 nm light and 8 W of 1596 nm light, the SFG system produced an average 606 nm output power of 5.27 W, with 1.6% RMS fluctuations. The only problem

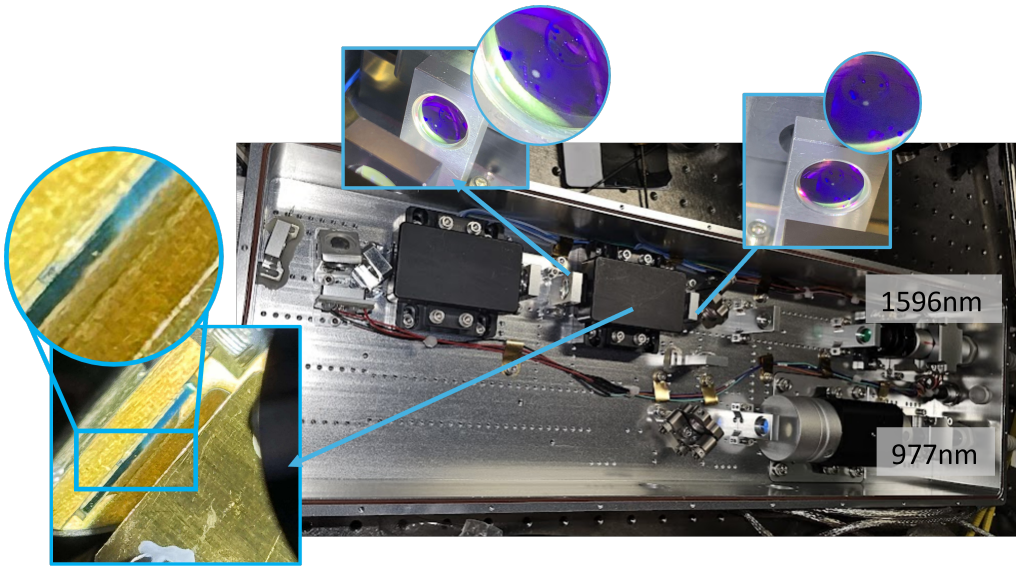


Figure 4.12: Interior of the 606 nm SFG head. The two black enclosures house the temperature-stabilized SFG crystals. The insets show damages on multiple optical surfaces along the beam path.

is that this performance lasted a grand total of one night. After the system was turned off and restarted the following day, the 606 nm output dropped dramatically and could not be recovered by normal tuning. Upon opening the sealed SFG head, we found multiple burn marks throughout on several internal optics, including one of the SFG crystal, see Fig. 4.12. Some marks were due to removable contamination, while others appeared to be permanent coating damage. The exact cause of this remains unclear, but it could be due to small amounts of burned dust that led to this cascade of optical damages and it was suggested epoxy outgassing could have been helpful.

Repairing the system by ourselves required replacing and re-aligning the internal lenses and SFG crystals. This was a delicate and laborious task, because the SFG module in the laser head is designed for factory alignment: the lenses and crystals have very limited adjustment range, there is no translation stage available for crystal alignment, and perhaps the worst of all, it requires careful hand tuning of the heated crystal while it is at the phase-matching temperatures of 60°C–80°C.

The repaired SFG system now produces approximately 4 W of 606 nm. The 606 nm power delivered to the molecules is actively intensity-stabilized. A small fraction of the output power

is picked off and detected by a photodiode, where the analog voltage is then digitized by a Red Pitaya and processed using the Linien PID servo software. The PID output is then fed back to the RF amplitude control of the 606 nm AOM.

4.5.1.1 Frequency Control and Hyperfine Components

Before being delivered and distributed onto the experiment, the 606 nm light passes through a frequency control stage that sets the overall single-photon detuning for the $X^2\Sigma^+(v = 0, N = 1) \rightarrow A^2\Pi_{1/2}(v' = 0, J' = 1/2, +)$ transition. This global frequency tuning is used for setting the different single-photon detuning during MOT, Λ-cooling, and tweezer imaging. In the original implementation, the global frequency shift was set through a double-pass AOD. This has been later upgraded to a cavity-referenced offset lock, in which sideband on the 606 nm light generated by a fiber EOM is locked to an optical cavity referenced to the wavemeter. This enables access to wider tuning range of the single-photon to expand from ~ 50 MHz to over 100 MHz, and is found to improve tweezer loading and imaging.

After the global frequency control, the light is then coupled into a downstream “hyperfine board" which generates the individual frequency components to address the four hyperfine states within $X(v = 0, N = 1)$, as described in [9]. On this board, the 606 nm light is combined with the 628 nm $v = 1$ repump light using dichroic optics. The light is polarization switched with a Pockels cell and then divided into four optical paths. AOMs on these paths independently set the frequency and power required to address the $F = 0$, $F = 1-$, $F = 1+$, and $F = 2$ hyperfine components of $X(v = 0, N = 1)$. The four components are finally recombined using a 4×4 polarization-maintaining fiber coupler (Evanescent). On the experiment, three outputs form the three orthogonal MOT beams, while the fourth is subsequently split to provide the smaller beams used for imaging in the science glass cell.

Gotta Catch 'Em All!

Pokemon

5

Magneto-optical Trapping and Cooling of CaF

This chapter describes the experimental methods used to laser cool, compress, optically trap, transport, and finally load individual CaF molecules into optical tweezers. The main experimental sequence proceeds through six stages: (1) radiative slowing and trapping in a red-detuned RF MOT, (2) sub-Doppler cooling, (3) conveyor-belt MOT compression, (4) loading into an optical dipole trap (ODT), (5) transport of the trapped molecules to the glass cell, and (6) loading into optical tweezers.

Much of the early-stage laser cooling sequence follows techniques developed in earlier generations of the CaF apparatus: radiative slowing of a cryogenic molecular beam, capture in a red-detuned RF magneto-optical trap, and subsequent sub-Doppler cooling by gray molasses and Λ-enhanced cooling [9, 48]. Here, we begin with a summary of these established stages,

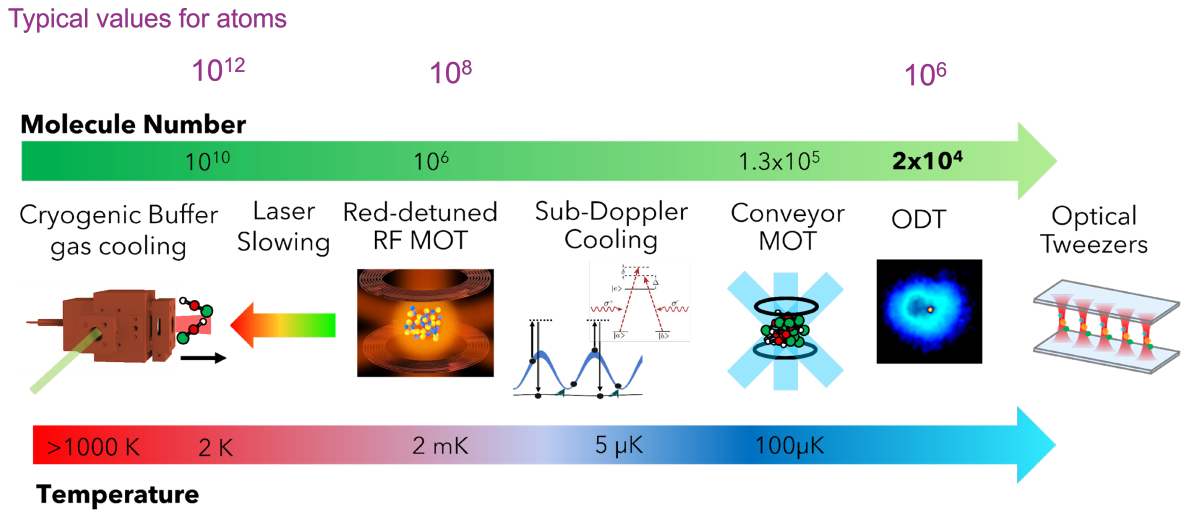


Figure 5.1: Schematic of experimental stages along with typical molecular number and temperature at each stage: starting from production of CaF molecular beams and laser slowing, magneto-optical trapping (MOT) of CaF molecular gas, application of sub-Doppler cooling, to compression of the molecular cloud for loading into conservative optical traps.

emphasizing the experimental choices relevant for the present apparatus. Then we describe and demonstrate a new blue-detuned MOT technique ("conveyor-belt MOT") that compresses the relatively large RF-MOT cloud into a much smaller, denser sample whose size is better matched to the optical dipole trap. This compression step is the key improve for subsequent efficient loading into the conservative optical traps downstream. Lastly, we detail the hybrid two-dimensional tweezer array used in this work, including characterization and homogenization of the tweezers.

5.1 Magneto-Optical Trapping of CaF

Once CaF molecules are extracted as a beam from a cryogenic source (see Sec. 4.1), the molecular beam is radiatively slowed by a counter-propagating frequency chirped laser pulse resonating with the X–B transition (see Sec. 4.5), with the linear polarization of the slowing light rapidly switched between two orthogonal polarization states using a Pockels cell to destabilize dark states during the slowing. $v = 1$ and $v = 2$ vibrational repump beams (see Sec. 3.4.3) are sent together along the X–B laser into the MOT chamber.

The slowed molecules are captured in a radio-frequency red-detuned MOT operating on the $X(\nu = 0, N = 1) - A(\nu' = 0, J' = 1/2)$ cooling transition at 606 nm. The MOT light consists of three orthogonal beam pairs, with frequency components addressing the four hyperfine levels in the $N = 1$ rotational manifold. These components are generated with acousto-optic modulators, with independent control for the intensity, detuning, and polarization of the different hyperfine components. The magnetic fields in the MOT are generated by pair of in-vacuum magnetic coils, each of which forms a resonant tank circuit that is individually driven by a homemade 1 kW RF amplifier at 1 MHz for RF operation.

Since we operate the MOT X–A transition, which is a type-II system, there are Zeeman dark states that can reduce the MOT trapping force. To avoid population accumulation in these dark states, we synchronously switch the MOT's magnetic-field gradient and the light polarization at $\approx 1\,\mathrm{MHz}$, forming an RF MOT. The rapid switching of the circular polarization of the MOT beams is enabled by a Pockels cell driven by a signal generator, while the frequency of the magnetic field switching is set on a separate signal generation. The signal generators for Pockels cell and MOT coils are frequency- synchronized by sharing a common clock. Note that the phase between electrical outputs of the two signal generators can pick up relative shift due to going through RF circuits, cables, etc., and experimentally what is relevant is the relative phase between the field gradient and polarization seen by the molecules. Therefore, we determine the operating phase empirically by scanning one of the signal generator and measuring the MOT signal.

For the initial RF-MOT loading stage, we use a relatively large capture volume and high scattering rate. More specifically, we begin with a magnetic field gradient of $B^{'} = 20$ G/cm RMS and a total intensity of $I_o = 30$ mW/cm^2 per MOT beam including 16 mW/cm^2 of $v = 1$ repump, at a detuning of $\Delta = 2\pi \times -8$ MHz and load the MOT for 5 ms.

The intensity is then reduced to $I_o/4$ in 5 ms and the magnetic field gradient is ramped to $B' = 50$ G/cm RMS, compressing the molecular cloud to $\sigma \sim 600$ μm, with 2×10^5 trapped molecules, corresponding to $n_o^{\mathrm{red}} \approx\ 5.8 \times 10^7$ cm^{-3}.

After RF-MOT compression, in the next 5 ms, the RF magnetic field and polarization

switching are turned off. We jump the laser intensity and detuning to the free-space Λ-cooling parameters[48, 160], with a single-photon detuning of $\Delta = +34$ MHz. A 5-ms sub-Doppler cooling pulse reduces the temperature of the molecular cloud to 18(5) μK while retaining $\sim 80\%$ of the initially captured molecules. This produces a cold molecular sample with a characteristic size of order several hundred micrometers, suitable as the starting point for sub-Doppler cooling but still much larger than the optical traps used later in the sequence. This leads us to introduce an additional blue-detuned compression technique described in the following section.

5.2 Blue-detuned Conveyor-Belt MOT

In this section, we detail the working principle and experimental implementation of a blue-detuned "conveyor-belt" MOT for CaF. This is initially motivated by overcoming the large discrepancy between the spatial extends of the MOT and ODT, which has led to a low ODT loading efficiency. With the conveyor-belt MOT, we are able to obtain a highly-compressed cloud, with a mean radius of 64(5) μm and a peak number density of $3.6(5) \times 10^{10}$ cm^{-3}, a 600-fold increase over the conventional red-detuned MOTs of CaF. Subsequent loading of these molecules into an optical dipole trap yields up to 2.6×10^4 trapped molecules at a temperature of 14(2) μK with a peak phase-space density of $\sim 2.4 \times 10^{-6}$.

Work in this Section, including portions of the text and figures, has been distributed as publication [161].

5.2.1 Introduction and Development of Blue-detuned MOTs

The magneto-optical trap is a pivotal technique for generating cold, dense samples of atomic gases, and has now been progressively extended to diatomic [40, 41, 43, 44, 145, 168] and polyatomic molecular gases [46, 47]. It serves as an essential starting point for further cooling and subsequent transfer into conservative optical potentials [49, 169]. MOTs are conventionally formed using red-detuned light ("red MOT"), where the trapping light is tuned below the transition resonance. For molecules, these red MOTs typically contain $10^4 - 10^5$ molecules,

with a peak number density of $\sim 10^5 - 10^7$ cm^{-3} [41, 43, 143, 170–172].

Despite this progress, the densities and phase-space densities of these molecular gases are roughly five orders of magnitude lower than those routinely reached in atomic MOTs, and far from the what's required to reach bulk quantum degeneracy. More generally, achieving high-density samples of laser-cooled molecules is a critical step toward advancing applications in precision measurements, ultracold chemistry and quantum science.

Laser cooling of alkali atoms is typically realized on type-I transitions with $F' > F$, where $F(F')$ is the quantum number of total angular momentum of ground (excited) electronic state. In contrast, all laser cooling of molecules to date operates on type-II transitions ($F' \leq F$) to ensure rotational closure for effective optical cycling [43, 173–175]. Studies [173] have shown that type-II red MOTs experience sub-Doppler heating at low velocities, resulting in a higher temperature and lower density cloud that has a limited overlap volume with the tightly-confined optical dipole trap (ODT). This, combined with molecular laser slowing limitations, lower photon scattering rate, and lower capture velocity of molecular MOTs compared to atomic MOTs in general, results in only a few thousands of trapped molecules in the optical dipole trap (ODT) and a phase-space density prohibitively low to realize many potential applications [49, 169, 176].

However, numerical simulations [177] have revealed that for a type-II system in a 3D molasses, the sub-Doppler Sisyphus-type force near zero velocity persists over the range of magnetic fields typically seen in the MOT. This finding motivated the introduction of a blue-detuned MOT ("blue MOT") stage, utilizing sub-Doppler processes in the presence of a magnetic field and implemented after the red MOT to increase compression and, consequently, phase-space density. This approach, first demonstrated with Rb atoms [177], has since been successfully implemented on several laser-cooled diatomic molecules, consistently producing substantially colder and denser samples [178–180] with peak number densities of $n_o \approx 10^7 - 10^8$ cm^{-3} and phase-space density of $\rho \approx 10^{-9}$. The reported cloud mean radii were $\gtrsim 150$ μm, limited by position-dependent trapping forces.

These limitations prompted the recent development of a blue MOT [181, 182] using a

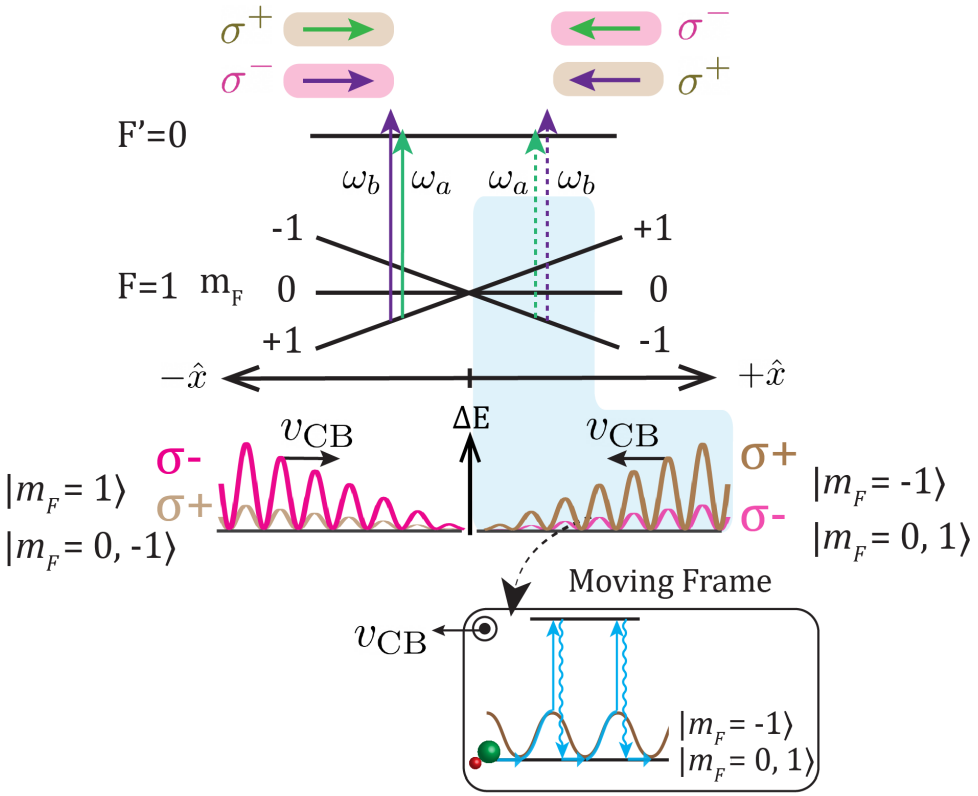


Figure 5.2: Illustration of the working principle of a conveyor-belt blue-detuned MOT; see text. The energy scale is shown for illustration purposes only. (b) Relevant level structure of CaF and laser configurations used in this work. J and F label the hyperfine states, where J the total angular momentum without nuclear spin and F is the total angular momentum.

frequency scheme that produces an additional physical effect, generating significantly more effective compression than the previously demonstrated blue MOTs. The improvement in the trapping force is attributed to Sisyphus-type blue-detuned cooling in the presence of a magnetic field gradient occurring in combination with a slowly-moving optical molasses [181, 182]. This "conveyor-belt" effect shuttles the molecules towards the center region of the MOT and deposits them there.

5.2.2 The Conveyor MOT Trapping Mechanism

The underlying working principle of the conveyor-belt MOT, as supported by numerical simulations [180], is illustrated in Fig. 5.2.

Consider a MOT beam containing two closely-spaced frequency components, ω_a and ω_b, each

with opposite circular polarizations (σ^+ and σ^-, respectively). As in the conventional MOT configuration, the beams are directed towards the MOT center along, say, the $\hat{x}$ direction, and retro-reflected, with the retro-reflected beam containing the same frequency components but flipped polarizations. When two counter-propagating beams of the same polarization interfere, they form a standing wave. If these beams have a relative detuning δ, the resultant wave will move along $\hat{x}$ in the lab frame, creating the conveyor belt effect, much like a moving lattice. Here, the ω_a (σ^+) light traveling towards the $+\hat{x}$ and the ω_b (σ^+) towards $-\hat{x}$ will form a "σ^+ conveyor belt" that slowly travels along $-\hat{x}$ direction at a velocity $v_{\mathrm{CB}} \approx \frac{\delta}{2\omega_a} c$ where $\delta = \omega_b - \omega_a$. Similarly, a "$\sigma^-$ conveyor belt" moving in $+\hat{x}$ is formed by ω_a (σ^-) traveling towards $-\hat{x}$ and ω_b (σ^-) in $+\hat{x}$.

Now consider a type-II transition between hyperfine levels $F = 1 \leftrightarrow F' = 0$, where the ground-state has a nonzero g-factor g_F (assume, without loss of generality, that $g_F > 0$). The presence of magnetic field gradients creates a position-dependent interaction strength between the molecule with either the σ^+ or σ^- conveyor belt, depending on the sign of g_F. If ω_a and ω_b in the MOT beam are blue-detuned from the transition, in the $B > 0$ region the $|F = 1, m_F = -1\rangle$ magnetic substate is Zeeman-shifted closer to resonance and thus molecules preferentially interact with the σ^+ conveyor belt.

In the conveyor belt's moving frame, the σ^+ light appears to the molecules as a stationary wave, setting up a spatially periodic light shift potential to facilitate Sisyphus-type cooling [173]. Here, a molecule experiences maximum optical pumping rate as it traverses across the intensity maxima, before spontaneously decaying to the $|F = 1, m_F = 0, 1\rangle$ dark states. The molecule subsequently returns to the $|F = 1, m_F = -1\rangle$ bright state primarily through orthogonal MOT beams and the transverse magnetic field, thereby completing the Sisyphus cooling cycle.

In the lab frame, the molecules get accelerated towards $\sim v_{\mathrm{CB}}$ and transported towards the MOT center by the moving σ^+ conveyor belt. On the other side of the MOT, in the $B < 0$ region, the molecules preferentially interact with the σ^- conveyor belt while experiencing Sisyphus cooling in the σ^- conveyor belt's moving frame. Near the MOT center where the magnetic field is weak, the preferential interaction with the $\sigma^\pm$ conveyor belts diminishes. At

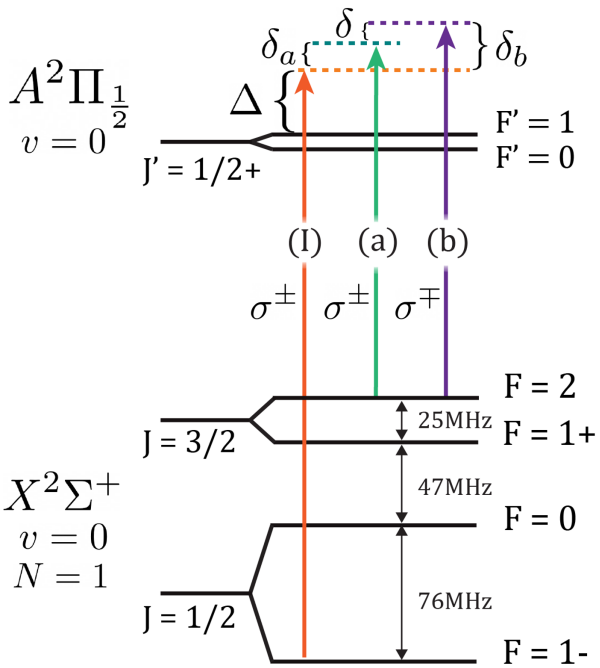


Figure 5.3: Relevant level structure of CaF and laser configurations used in this work. J and F label the hyperfine states, where J the total angular momentum without nuclear spin and F is the total angular momentum.

the center, the dominant cooling is provided by gray-molasses cooling in the lab frame with Λ-systems forming between the hyperfine levels. This, in part, effectively prevents the molecules from being over-transported out of the MOT center region.

In summary, in a conveyor MOT, molecules away from the MOT center on either side selectively interact with one of the $\sigma^{\pm}$ conveyor belts, in which they are cooled into the moving frame of the conveyor belt and slowed to near zero velocity as they approach the center, resulting in a large number of near zero-velocity molecules piled up in the MOT center.

5.2.3 Conveyor MOT of CaF

In this section, we describe how we experimentally apply the conveyor-belt trapping mechanisms to CaF molecules. The goal here is to load the CaF molecules from RF red MOT (Sec. 5.1) after Λ-cooling into a DC conveyor MOT. The switch from RF to DC MOT is realized by employing high-impedance inductors and back-to-back solid-state relays (See Sec. 5.2.3.1).

Starting from red MOT, we simply need to introduce one additional frequency component to form the conveyor MOT. The frequency scheme is shown in Fig. 5.3. In this configuration, the frequency ω_I, addressing the $|F = 1-\rangle$ hyperfine state, is blue-detuned with a single-photon detuning Δ. The other two frequency components, ω_a and ω_b, both addressing the $|F = 2\rangle$ state, have opposite circular polarizations and detunings of $\Delta + \delta_a$ and $\Delta + \delta_b$, respectively.

These two closely-spaced components with a slight relative detuning of $\delta = \delta_b - \delta_a$ create the conveyor-belt effect and consequently an enhanced trapping force on the $|F = 2\rangle$ state, while ω_I mainly functions as a repumper to prevent population loss to dark states and facilitates lab-frame cooling at the MOT center. We then gradually increase the DC magnetic field using an optimized profile that minimizes molecular loss (see Sec. 5.2.3.2 for more detail). Finally, to detect and measure the spatial profile of the molecular cloud, we collect in-situ fluorescence onto a camera.

5.2.3.1 RF – DC MOT coil switching

The RF-to-DC switching circuit is designed to isolate the RF and DC paths of the MOT coils' tank circuits while maintaining RF resonance. Our MOT coils consist of a pair of in-vacuum magnetic coils, forming a resonant tank circuits with variable capacitors and are driven near 1 MHz by custom-built 1 kW RF amplifiers. During RF MOT operation, the peak-to-peak RF voltage across the coils reach ~ 4 kV. Isolation is critical here because the high voltages in the RF side can couple into the DC current supply ground, causing interference and instability; proper isolation ensures the integrity of both the RF and DC systems. While mechanical relays are capable of handling high voltages, they have limited lifetimes and slower switching times. In contrast, solid-state relays offer longer lifetimes and faster switching but are limited by their lower working voltage range.

To overcome this, we use homemade high-impedance inductors (Z_L) acting as RF chokes to isolate the RF from the DC circuit. At the RF drive frequency, these inductors have impedance $Z_L = 10,668\ \Omega$, while the RF-bypass capacitor on the DC side has impedance $Z_C \simeq 1\ \Omega$. DC current is thus applied to the $Z_C \simeq 1\ \Omega$ capacitor with self-resonance frequency greater than

1 MHz, and connected to the MOT coil through the high-impedance inductor. The DC path is switched using back-to-back solid-state relays, which block current in both directions. To reduce switching time, a damping resistor is placed in parallel with Z_C. This forms a large RF voltage divider, reducing the RF voltage seen by the DC switching electronics by roughly four orders of magnitude, ensuring efficient switching and reliable operation during the transition from RF to DC operation.

5.2.3.2 Magnetic field ramp optimization

As mentioned above, we use an empirically optimized profile for the DC magnetic field that minimizes molecular loss. Initially, we used a simple smooth ramp, increasing the control voltage into the current supply. In Fig. 5.4, we show the loss rates of the compression at different magnetic field gradients (orange, green, and purple data). We have observed that higher magnetic field gradient compresses the cloud more but the process is very lossy, with less than 20% of molecules at the end of the compression. Most of the loss occurs in first 30 ms.

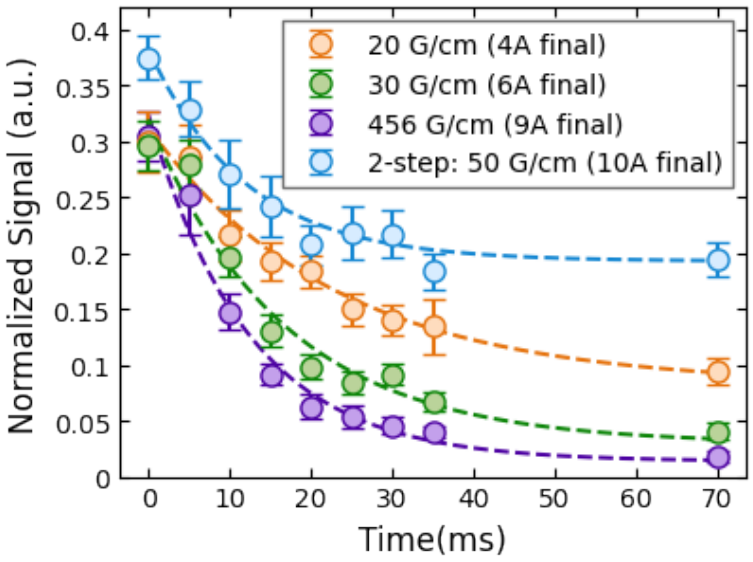


Figure 5.4: Conveyor MOT loss rates with different magnetic field ramp profiles. The orange, green, and purple data are for simple ramps to different final magnetic-field gradients. The blue data show the optimized two-step ramp with reduced loss.

This has prompted us to look into the the ramp profile and dynamics. We have found that,

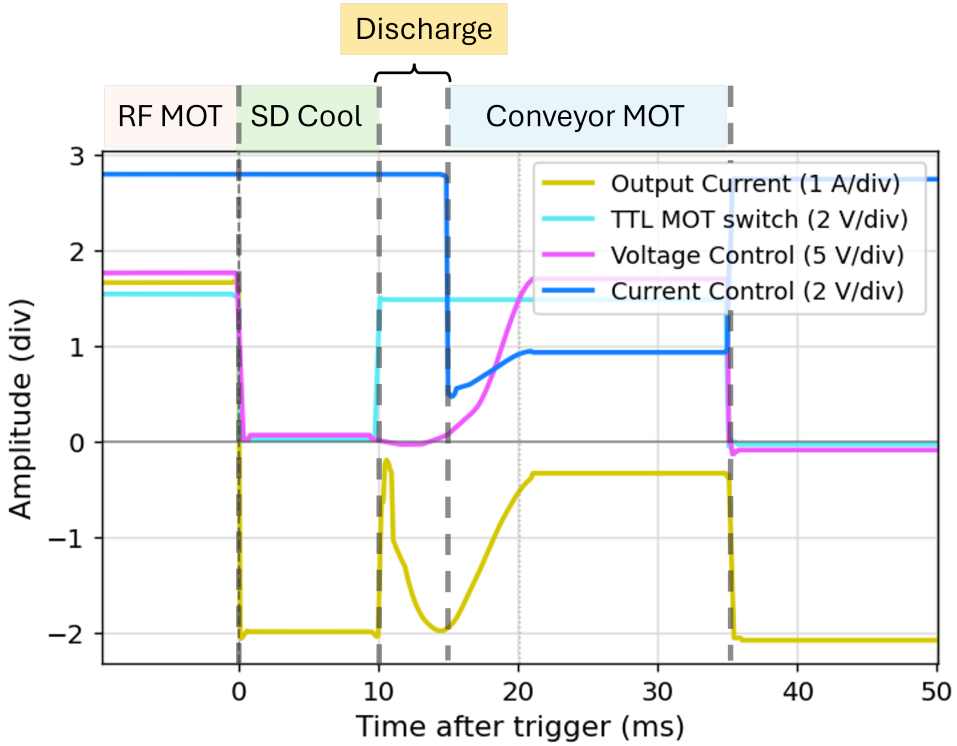


Figure 5.5: Oscilloscope traces of the current and voltage programming sequence to the current supply used in the experimental sequence (magenta and blue, respectively), as well as measured output current (yellow) to the coils, and TTL signal for RF–DC MOT switching (cyan).

in practice, one needs to be careful that the magnetic field ramp might not solely determined by the programmed current setpoints, but both the control current and voltage. In our case, the current supply used (Delta Elektronica) has a large internal output capacitance ($\sim 325\mu$F), so residual coil current and stored energy in the coupling circuit can persist, causing the output current to have transient spikes that can lead to molecular loss. Fig. 5.5 shows the oscilloscope traces of the control current and voltage to the current supply, the measured output current, and the experimental TTL signal.

After sub-Doppler cooling, before turning on DC conveyor MOT, we need to wait a duration of $\sim$ 6 ms for the about 4 A of current (10 V across) through the capacitor to discharge. During this time, the sub-Doppler cooled molecules are in free expansion mode, since we cannot effectively apply Λ-cooling as the magnetic field current is changing.

Ideally, we want to discharge the capacitor rapidly but charge up slowly, since a slow charging

makes the magnetic field ramp smoother. This means that during "discharge" in Fig. 5.5, control current is set high while the voltage is kept low. This because discharge rate is driven by the voltage potential between initial voltage across the capacitor and final voltage to which it is discharging. By maintaining a high discharge current, we allow the capacitor to dump its stored charge rapidly.

After the discharge, we then slowly increase up the control voltage in an experimentally-optimized two-step ramp, where we start with slowly ramping the magnetic field to 20 G/cm in the first 10 ms, then to the full 50 G/cm (about 10 A) for the next 20 ms. The blue trace in Fig. 5.4 shows a measured loss curve for this optimized ramp process for 4 A final current, where we see that it helps to retain $\sim 58\%$ of molecules at the end of the 30 ms compression. The actual final magnetic field gradient used in the experiment is slightly lower, retaining about 65% of the initial molecules (see Fig. 5.6).

5.2.4 Compression of molecular cloud

To maximize compression of the molecular cloud, we investigate the effect of single and two-photon detunings (Δ, δ_a and δ_b) on the mean radius σ of molecules in the conveyor MOT. Fig.5.6(a-c) show σ as a function of Δ, δ_a and δ_b. We obtain σ in each direction by fitting it to a Gaussian distribution. σ is minimized at $\delta_a = -2\pi \times 1.5$ MHz, $\delta_b = 2\pi \times 0.5$ MHz, corresponding to a conveyor belt speed of approximately $v_{\mathrm{CB}} \approx 0.6$ m/s. Physically, due to the decreasing magnetic field as the molecules are compressed towards MOT center, combined with the frictional force imparted by the opposing conveyor belt, the molecules on average do not get fully accelerated to v_{CB}. σ is relatively insensitive to Δ over the range $\Delta = 2\pi\times$ (20 MHz to 30 MHz), similar to the observations in [181]. This detuning range suggests that part of the trapping force may also originate from the $|F = 1+\rangle$ state. $\Delta = 2\pi \times 20$ MHz is used for all subsequent measurements.

In Fig. 5.6(d), a scan of $B^{'}$ reveals that $\sigma = 64(5)$ μm (with radial and axial widths of $\sigma_{\mathrm{ax}} = 58(4)$ μm and $\sigma_{\mathrm{rad}} = 68(2)$ μm, respectively) is reached at $B^{'} \approx 40$ G/cm. The light intensity used for the conveyor MOT is $\sim 2I_{\mathrm{sat}}$ and the total light power is equally distributed

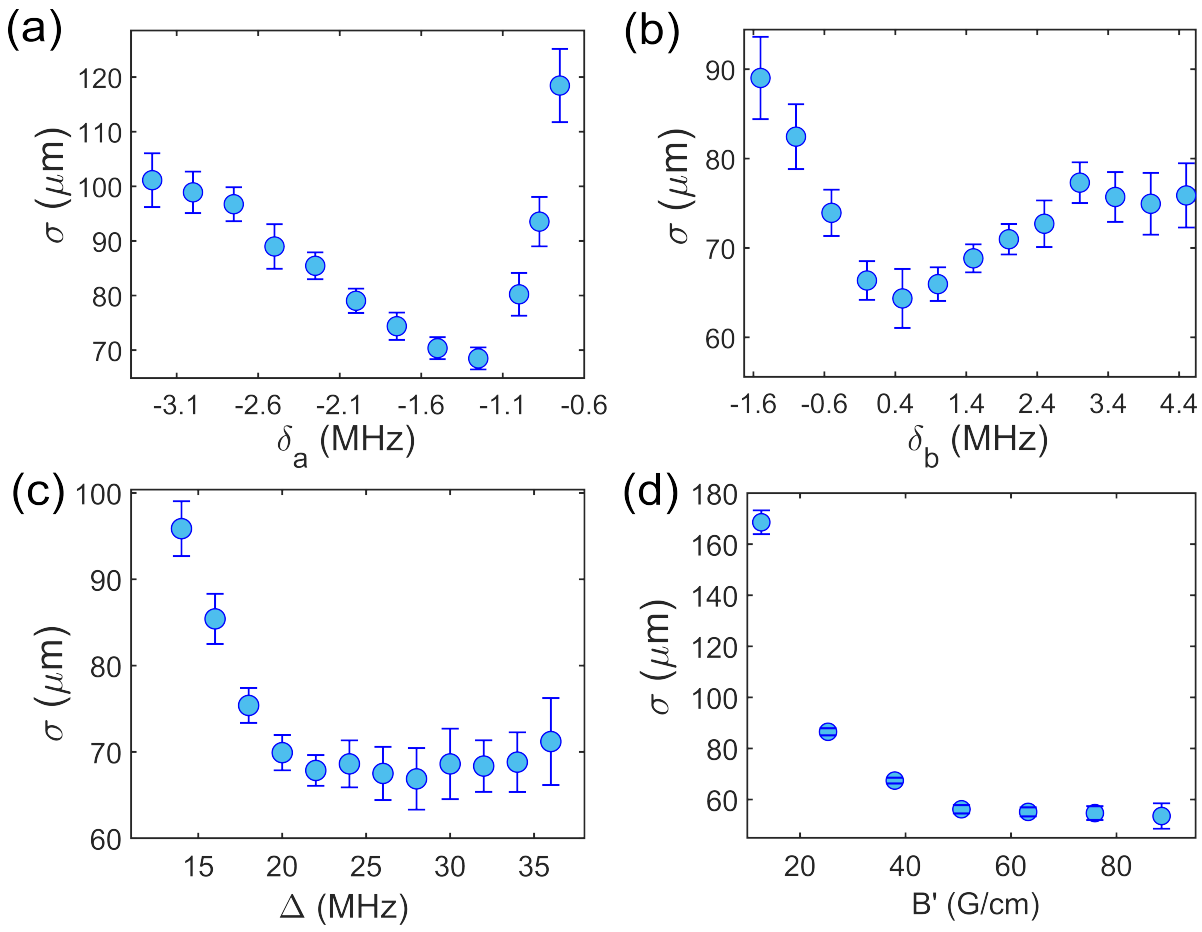


Figure 5.6: Dependence of conveyor MOT cloud size on frequency detunings and magnetic field. MOT radius σ as a function of two-photon detunings **(a)** δ_a, **(b)** δ_b, **(c)** single-photon detuning Δ, and **(d)** applied magnetic field gradient $B^{'}$. For each scan in (a-c), all other detunings and the total intensity are kept fixed. The intensity of each beam is calibrated such that it remains constant as frequency is varied. The maximum magnetic field gradient used in (a-c) is $B^{'} \approx 40$ G/cm.

among the three frequency components. We observe that the minimum σ is relatively insensitive to the ratio of power intensities for the three components. With the available laser power in our experiment, we observe an increase in the number of trapped molecules with higher power, as expected from the corresponding enhancement in both capture velocity and trap volume for gray-molasses cooling.

Fig. 5.7 presents σ and n_o as a function of conveyor MOT application time, with top images showing the in-situ fluorescence. Most of the compression takes place within the first 10 ms, during which the cloud reduces from $\sigma \gtrsim 550$ μm to $\sigma = 130$ μm as $B^{'}$ is ramped to ~ 20 G/cm.

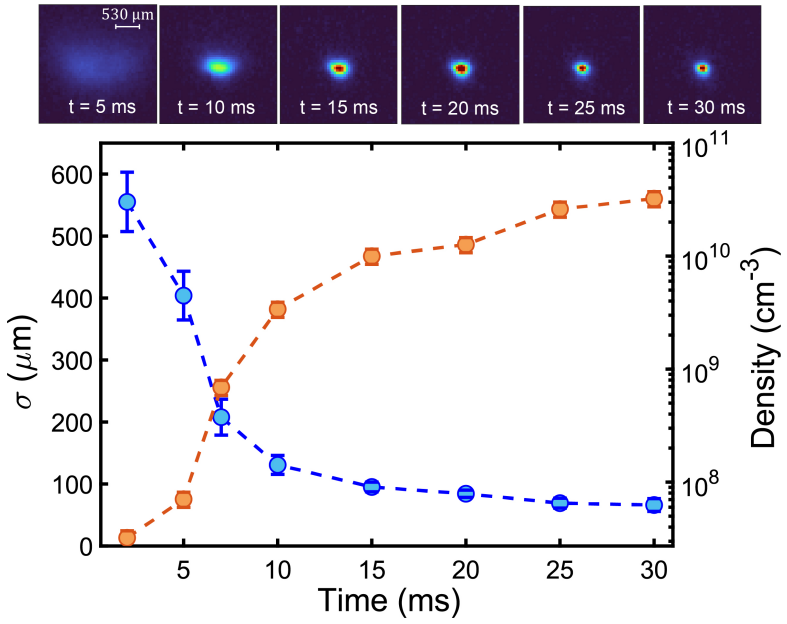


Figure 5.7: Size and density of conveyor-belt blue MOT as a function of time. Blue: fitted $1/e$ cloud radius σ (left axis). Orange: peak molecule number density n_o (right axis). Dashed lines are guides to the eye. Data are taken with frequency parameters $\Delta = 2\pi \times 20$ MHz, $\delta_a = -2\pi \times 1.5$ MHz and $\delta_b = 2\pi \times 0.5$ MHz, and a magnetic field gradient of up to $B^{'} \approx 40$ G/cm. Top: Images of the molecular cloud taken by collecting 2 ms of in-situ fluorescence following a compression time of t.

Over the next 20 ms, σ continues to decrease as $B^{'}$ reaches 40 G/cm. By the end of the compression, up to $N_{\mathrm{MOT}} \sim 1.3 \times 10^5$ molecules remain trapped, corresponding to a peak density of $n_o^{\mathrm{MOT}} = 3.6(5) \times 10^{10}$ cm^{-3}, with measured mean temperature of $T_{\mathrm{MOT}} = 141(7)$ μK. Given the relatively low measured photon scattering rate of $0.27(3) \times 10^6$ s^{-1} in the conveyor MOT (using laser parameters optimized for minimal σ) (Fig. 5.10 (b)), it may be that higher light intensity could provide larger trapping volume, but this is open for further investigation. In addition, we find that the $1/e$ lifetime of molecules in the conveyor MOT follows a single exponential decay, with a fitted $\tau = 37.2(8)$ ms measured for $B^{'} \approx 40$ G/cm (Fig. 5.10(a)), limited by the trap loss at high magnetic field.

Besides the three-frequency scheme (Fig. 5.3), which has been found to be the most effective one, we have tested two other frequency configurations, as shown in Fig. 5.8. The two-frequency version is similar to the "conventional" blue-detuned MOTs that have been demonstrated on diatomic molecules [178, 179] where there is no conveyor-belt effect. We see that although the minimal cloud size achieved is similar, the compression is much slower(Fig. 5.9) and with

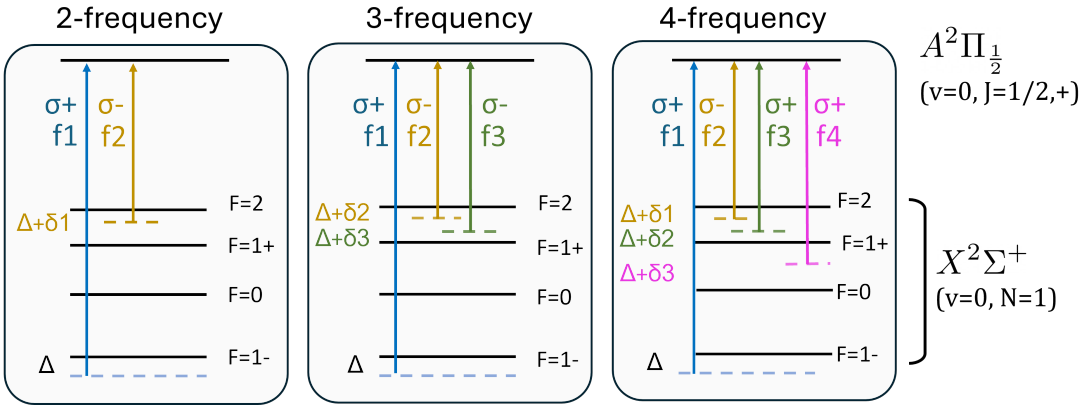


Figure 5.8: Frequency schemes explored during experimental development.

substantially more loss and higher temperatures of order 200–250 μK.

This supports our understanding that, with the conveyor belt formed by the two closely spaced components addressing $|F = 2\rangle$, there is a steeper zero crossing of the acceleration curve, i.e. a larger effective restoring force or spring constant [180], leading to faster compression. We also tested a four-frequency version by adding a component near the $|F = 1+\rangle$. After scanning the power and frequency of the fourth component, as well as total power, and both single- and two-photon detunings, we did not observe a improvement over the three-frequency configuration.

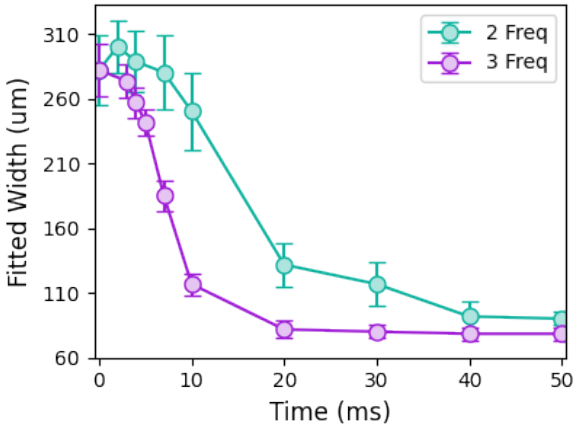


Figure 5.9: Comparison of conveyor-MOT compression between two-frequency and three-frequency schemes. The fitted cloud width is extracted from in-situ fluorescence images after at the end of conveyor MOT for a variable time.

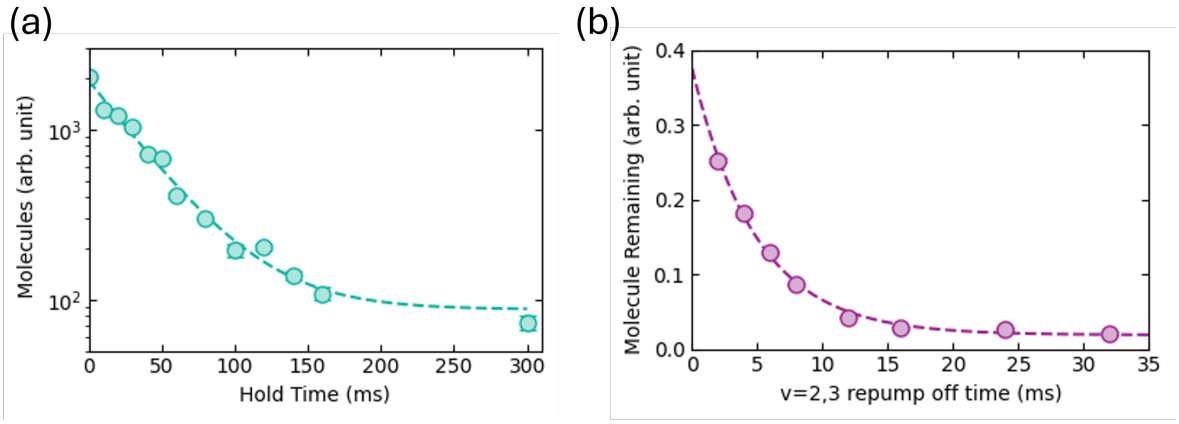


Figure 5.10: (a) Number of remaining trapped molecules in the conveyor MOT as a function of holding time, with the magnetic field gradient set at 40 G/cm. The fitted lifetime is $\tau_{\text{conveyor}} = 37(8)$ ms. **(b)** Number of remaining molecules as a function of T_{hold} during which $v = 2$ and $v = 3$ repumping lasers are turned off. The data has an exponential decay with a fitted lifetime $\tau_{\text{reduced}} = 4.9(0.6)$ ms due to finite photon budget.

5.2.5 Conveyor-Belt MOT lifetime and scattering rate

To measure the lifetime of the conveyor MOT, after the compression stage, we hold the the magnetic field at 40 G/cm for variable amount time while monitoring the remaining molecules. Figure 5.10(a) shows the decay in fluorescence signal (or the number of trapped particles) as a function of hold time. The result fits to a single exponential decay with a fitted lifetime $\tau_{\text{conveyor}} = 37(8)$ ms, consistent with the absence of light-assisted two-body collisions at this density.

When molecules are exposed to the light and scatter photons for a given time, they have a certain probability to decay to unaddressed vibrational state(s). By turning off selective repumping lasers and holding the molecules in the conveyor-belt MOT for variable amount of time, we allow the population to accumulate in unaddressed states, effectively limiting the number of photons that can be scattered. The scattering rate is then extracted from the observed lifetime and known vibrational branching ratios.

During the holding period, decay in molecular signal can occur mainly due to two mechanisms: optical pumping into unaddressed vibrational states, or trap loss. To isolate the loss due to finite photon budget, we fix the total holding time at 40 ms and vary the duration T_{off} during

which $v = 2$ and $v = 3$ vibrational repumps are turned off. This reduces the photon budget per molecule from $N_{\text{photon}} = 9 \times 10^5$ to 1350. Figure 5.10(b) shows the fluorescence decay as a function of T_{off}. An exponential fit to the molecule decay signal with $v = 2$ and $v = 3$ repumps off yields a lifetime of $\tau_{\text{reduced}} = 4.9(0.6)$ ms, and the corresponding scattering rate is calculated to be $\Gamma = N_{\text{photon}}/\tau_{\text{reduced}} = 0.27(3) \times 10^6$ s^{-1}.

5.2.6 Temperature of molecules in conveyor MOT

We use a standard time-of-flight expansion method to determine the temperature of a thermal molecular cloud, assuming a Gaussian density distribution in the conveyor MOT or ODT. By turning off all the trap light and magnetic field, we allow the molecular cloud to freely expand for variable length of time t_{TOF} and use a subsequent 1-ms resonant light pulse for imaging. As resonant imaging on the molecules can cause heating, and consequently, extra expansion, the 1 ms exposure time is chosen here as it is short compared to the expansion time and causes negligible heating. We verified that the size measurements with a 1 ms exposure were similar with those using a shorter 0.5 ms exposure. We fit the molecular image along the radial (axial) direction to a 1D Gaussian to obtain the cloud radius in radial (axial) direction, σ_{rad} (σ_{ax}), and extract the corresponding radial (axial) temperature T_{rad} (T_{ax}) from the fitted slope. The final temperature reported is the geometric mean of radial and axial temperatures: $T = T_{\text{rad}}^{2/3} T_{\text{ax}}^{1/3}$.

5.3 Loading into Optical Dipole Trap

The high molecular density obtained in the conveyor-belt MOT provides a reservoir from which we transfer molecules into a 1064 nm ODT of 57 μm beam waist and a trap depth of $U \approx k_B \times$ 174 μK. To load the ODT, we first switch off all MOT light and DC magnetic field, then immediately turn on the ODT light in the presence of Λ-cooling light for 3 ms. This sequence prevents ODT trap light from inducing significant differential Stark shifts that would influence the conveyor-belt MOT's operating parameters.

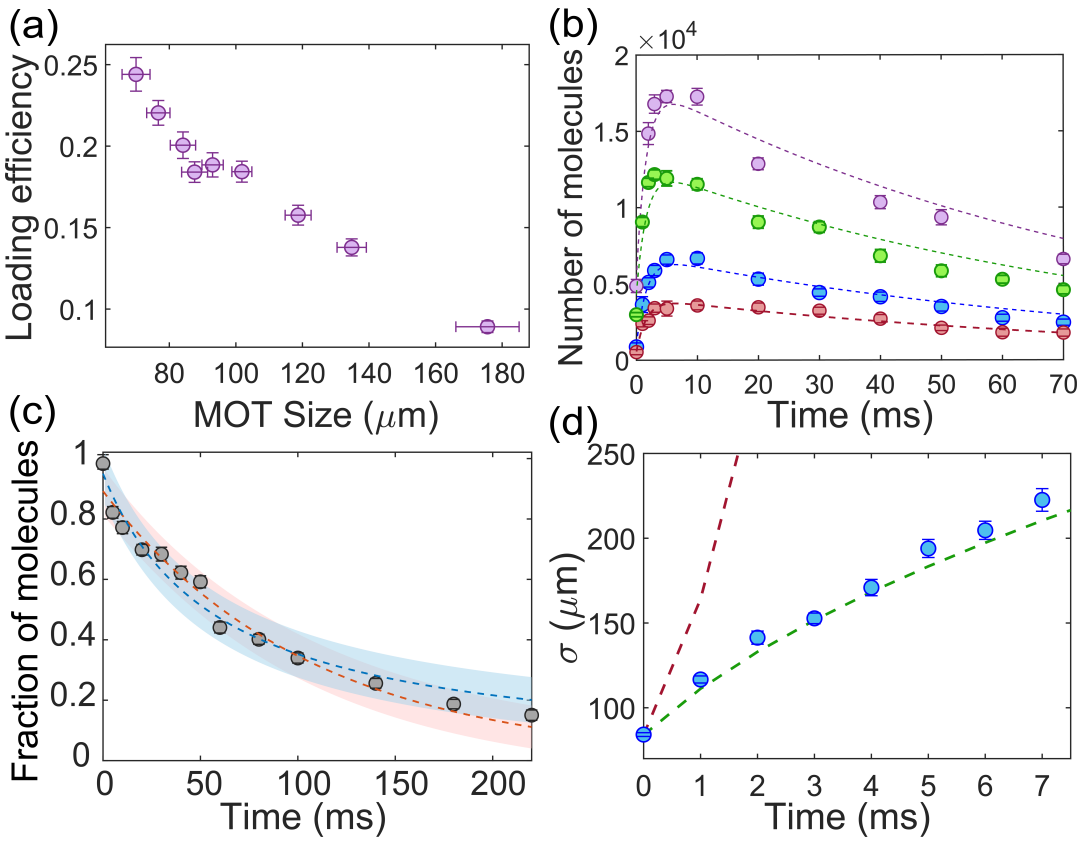


Figure 5.11: ODT loading characterization. (a) Loading efficiency as a function of conveyor MOT cloud size. (b) Number of molecules in the ODT as a function of loading time for different initial number of molecules. (c) Fraction of molecules remaining in the ODT as a function of hold time in presence of Λ-cooling light, fitted to a one-body (red, dashed) and two-body (blue, dashed) loss models. (d) Expansion of the reservoir cloud in presence of Λ-cooling as a function of time. The ballistic expansion trajectory for cloud at 147 μK is plotted as a guide (red, dashed). A diffusive model fitted to the data is shown (green, dashed).

5.3.1 Loading dynamics and efficiency

The number of molecules transferred into the ODT depends on the size (σ) of the cloud reservoir as expected, as shown in Fig. 5.11(a). The loading efficiency increases as the size of the conveyor-belt MOT cloud approaches that of the ODT, leading to better spatial mode-matching between the two. Up to 24% of the molecules from the cloud reservoir are captured into the optical trap, resulting in $N_{\mathrm{ODT}} \simeq 2.6 \times 10^4$ molecules at $T_{\mathrm{ODT}} = 14(2)$ μK with $\rho_{\mathrm{ODT}} = 2.4 \times 10^{-6}$. This corresponds to 12% of the molecules initially trapped in the red MOT ending up in the ODT, a factor of five improvement over our previous loading efficiency of $\lesssim 2\%$ using direct

transfer from the red MOT.

To understand the possible loss mechanisms during the loading process, we examine the time dependence of the molecule number during the ODT loading. Fig. 5.11(b) shows the loading curves of N_{ODT} at varying N_{MOT} in the cloud reservoir, N_{MOT}. The ODT loading dynamics are well described by a rate equation model [183] by accounting for overall molecular loss in the reservoir cloud, one-body, and two-body loss mechanisms. To investigate the potential role of two-body collisional loss in limiting the loading of molecules in the ODT, we measure the lifetime of molecules in the ODT in the presence of varying Λ-light duration [106, 116]. Fitting the data to both one-body and two-body loss models yield decay rates that are statistically indistinguishable (Fig. 5.11(c)). Additionally, the linear scaling observed between N_{ODT} and N_{MOT} suggests that current loading is far from saturation.

The results in Fig. 5.11(d) reveal that the effective ODT loading time, as seen in Fig. 5.11(b), is limited by the rapid expansion of the molecular cloud. σ increases to 153 μm in the first 3 ms in the presence of Λ-cooling light, leading to a large spatial mismatch with the ODT. With a typical Λ-cooling time of < 300 μs, the expansion quickly deviates from a ballistic trajectory that would be expected for the 147 μK conveyor MOT temperature, instead following a diffusion trajectory (dashed lines in Fig. 5.11(d)). This rapid diffusive expansion is the primary limitation on our loading efficiency, and larger optical dipole trap volume would likely improve it. In the future, the cloud expansion issue might be addressed by directly loading the ODT from the conveyor-belt MOT, provided the optical trap depth is much higher than the conveyor MOT cloud temperature.

5.3.2 Losses during ODT loading

To better understand the dominant loss mechanisms during the loading process, we examine the time dependence of the ODT loading. From the loading curves in Fig. 5.11, We find that the loading dynamics is well captured by four parameters: a loading rate $R(t)$ which depends on the reservoir cloud and its overlap with the ODT, a one-body decay rate Γ due to collisions with background gas in the chamber, and a two-body collision rate β' caused by light-assisted

collision [184, 185]. They follow a rate equation model commonly used for atoms [186].

$$\frac{dN(t)}{dt} = R(t) - \Gamma N - \beta' N^2 \tag{5.1}$$

$R(t) = R_o e^{-\gamma t}$ sets the initial increase in the loading and accounts for the total decay rate γ in the cloud reservoir arising from two processes: (1) the loss of molecules due to cloud expansion out of the ODT trapping volume, and (2) the depletion of molecules as they are successfully loaded into the ODT.

The high density of the conveyor MOT naturally raises the question of whether two-body loss play a role in the MOT lifetime or the subsequent ODT loading. To determine if two-body collisional loss plays a role in limiting the loading, we measure the lifetime (τ) of molecules in the ODT in presence of Λ-light. We first load the ODT with Λ-cooling light under optimal condition and wait for 100 ms to ensure the background cloud has fully dissipated. Then, we hold the molecules in trap for 260 ms and apply Λ-cooling for a variable length of time to induce light-assisted collisions [106, 116]. Fitting the data including the two-body loss term yields a τ that is statistically indistinguishable from that obtained using a single-body loss model (Fig. 5.11(c)), thus the two-body β' term does not dominate over Γ under the experimental conditions, indicating that two-body loss does not significantly contribute in this system.

We fit the numerical solution of Eq. 5.1 to each loading curve in Fig. 4(b), using the same cloud reservoir decay rate γ for all curves, and a fixed one-body rate constant Γ extracted from Fig. 5.11(c) measurement. The free parameters here are γ and R_o.

5.3.3 ODT trap depth and alignment

We investigate the effect of trap depth by measuring the loading efficiency at various ODT intensities. As shown in Fig. 5.12, the loading efficiency increases with intensity, suggesting further improvements are possible with a higher trap depth, though this is currently constrained by technical limitations.

We also examine how the spatial overlap between the ODT and conveyor MOT affects the

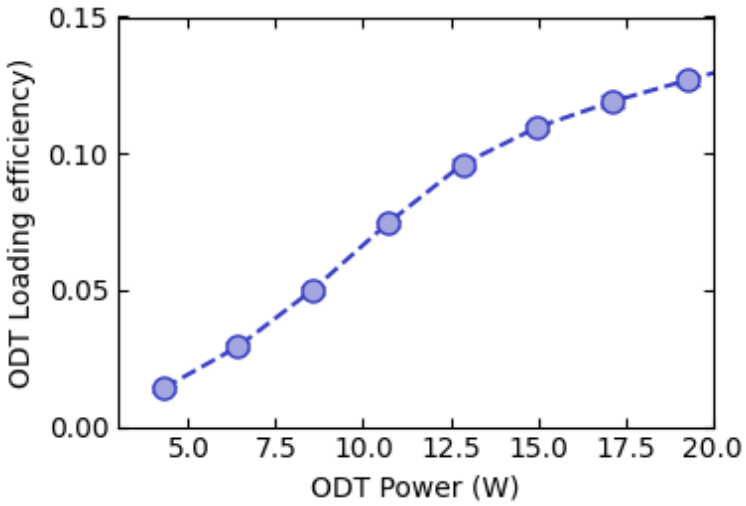


Figure 5.12: ODT loading efficiency versus ODT powers. The loading efficiency increases with higher ODT light intensities, indicating potential for further improvement by increasing the trap depth and volume.

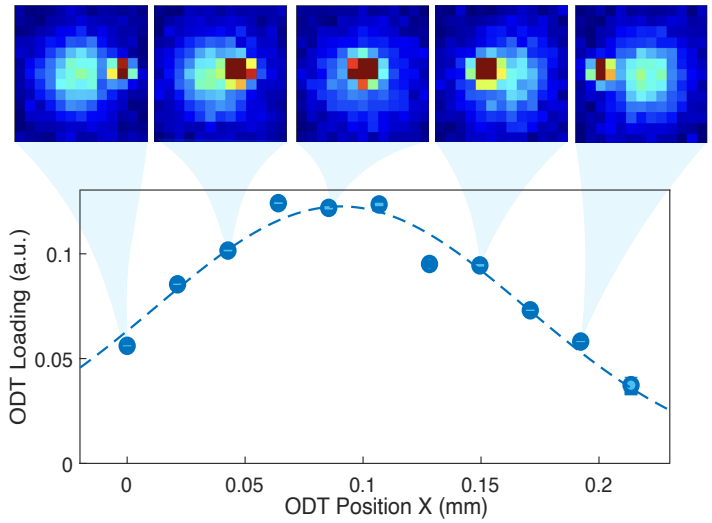


Figure 5.13: ODT loading efficiency versus ODT position. The loading efficiency is plotted against the center position of the ODT, and the data are fitted to a Gaussian distribution with a width of $\sigma_{\text{loading}} = 111(12)$ μm.

loading efficiency. We vary the ODT position while monitoring the molecular signal in the ODT. The data are fitted to a Gaussian distribution with $\sigma_{\text{loading}} = 111(12)$ μm, which is comparable to the cloud size after 1 ms of diffusive expansion,as shown in Fig. 5.13. These results are consistent with the rapid loading timescale and indicate that optimizing the spatial

overlap between the MOT and ODT is crucial for enhancing loading efficiency.

5.4 Characterization of Optical Tweezer Traps

Here we describe the some of the most important characterization of an optical trap, starting with determination of trap frequencies, and then use the Gaussian-beam model to infer effective trap waists, trap intensities, and trap depths. We also measure the lifetime of a molecule in an optical tweezer.

For a Gaussian beam propagating along z, the intensity profile is

$$I(\rho, z) = I_0(\frac{w_0}{w(z)})^2 \exp\left[-\frac{2\rho^2}{w^2(z)}\right], \qquad I_0 = \frac{2P}{\pi w_0^2}, \tag{5.2}$$

where $\rho^2 = x^2 + y^2$, P is the optical power in a single tweezer, w_0 is the $1/e^2$ intensity radius at the focus, and

$$w(z) = w_0\sqrt{1 + (\frac{z}{z_R})^2}, \qquad z_R = \frac{\pi w_0^2}{\lambda}. \tag{5.3}$$

For red-detuned light, the molecule is trapped near the intensity maximum. The trap depth U_0 is then defined as the maximin of AC Stark shift experienced by the molecule , or equivalently the magnitude of the light shift at the peak intensity. Near the center of the Gaussian trap, the potential can be expanded as a harmonic oscillator,

$$U(\rho, z) \simeq -U_0 + \frac{2U_0}{w_0^2}\rho^2 + \frac{U_0}{z_R^2}z^2. \tag{5.4}$$

For scalar polarizability $\tilde{\alpha}_0$, we have $U_0 = \tilde{\alpha}_0 I_0$. Equating the quadratic terms to a harmonic oscillator potential gives

$$\omega_r = \sqrt{\frac{4U_0}{mw_0^2}}, \qquad \omega_z = \sqrt{\frac{2U_0}{mz_R^2}}, \tag{5.5}$$

where m is the CaF molecular mass.

5.4.1 Trap Frequency Measurements

One way to measure the trap frequency is via parametric heating, where the trap depth is modulated as

$$U(t) = U_0[1 + \epsilon \cos(\omega_m t)]. \tag{5.6}$$

Heating and loss occur most strongly when the modulation frequency ω_m is near twice a trap frequency, $\omega_m \simeq 2\omega_i$, where $i \in \{x, y, z\}$. Experimentally, we modulate the tweezer power for a fixed number of cycles, lower the trap depth so that heated molecules are preferentially lost, and ramp back the intensity to image the surviving molecules in the trap. The loss feature in the scan of ω_m is then $2\omega_i$. Figure 5.14 (a) shows our trap frequency measurements using parametric heating, which shows quite broad resonances.

When the motional sidebands are spectrally resolved, the trap frequencies can be measured more directly from the sideband spacing. Figure 5.14(b) shows representative radial and axial sideband spectra, from which we extract $\Delta_r = 81.55$ kHz and $\Delta_z = 13.11$ kHz. The axial frequencies measured by the two methods agree well. The radial parametric-heating feature gives a somewhat higher value than the sideband spacing, likely because the parametric resonance is broad and sensitive to the modulation amplitude, hold time, etc. We use the resolved sideband spacing as the primary trap frequency calibration.

5.4.2 Trap Waist, Intensity, and Depth

For an ideal Gaussian tweezer, the ratio of the radial and axial trap frequencies determines an effective waist. Eliminating U_0 from Eq. (5.5) gives

$$w_0 = \frac{\lambda \omega_r}{\pi\sqrt{2}\,\omega_z} = \frac{\lambda f_r}{\pi\sqrt{2}\,f_z}, \tag{5.7}$$

Using $\lambda = 776$ nm and frequencies from the sideband spectra in Fig. 5.14 (b), $f_r = 81.55$ kHz and $f_z = 13.11$ kHz, we get an effective trap waist (which is not necessarily the "true" trap waist as measured in optical point-spread function) of $w_0 \simeq 1.09$ μm and $z_R \simeq 4.8$ μm.

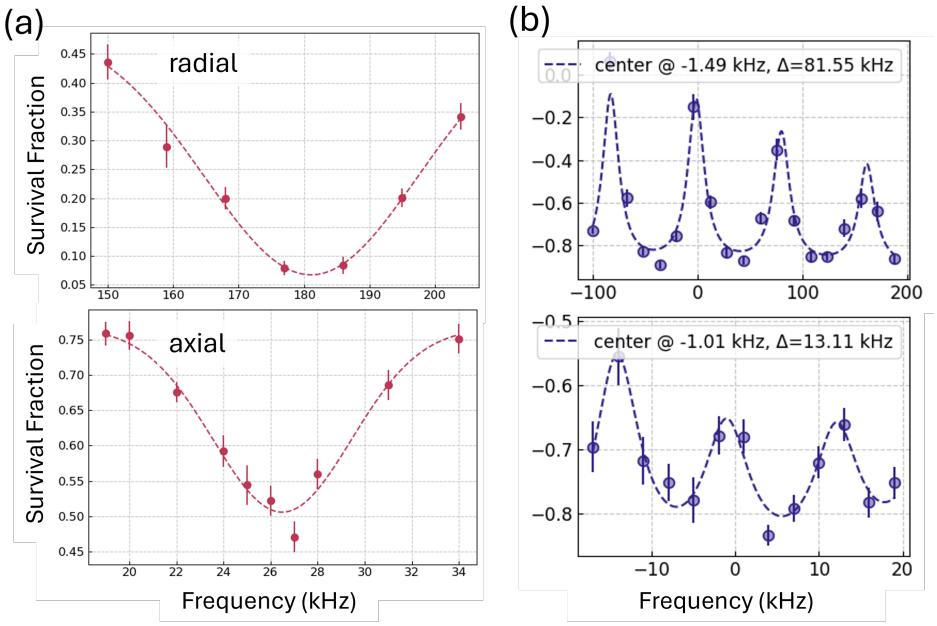


Figure 5.14: Trap frequency measurements. **(a)** Parametric heating measurements of radial (top) and axial (bottom) trap frequency. The fitted loss features occur at 181.07(54) kHz and 26.49(21) kHz, corresponding to trap frequencies $f_r = 90.54(27)$ kHz and $f_z = 13.25(11)$ kHz. **(b)** Motional sideband spectra for one radial direction (top) and axial direction (bottom), with fitted spacings of 81.55 kHz and 13.11 kHz, respectively.

With $w_0 \simeq 1.09$ μm, a typical tweezer power of $P = 24$ mW in our experiment, this corresponds to a peak intensity

$$I_0 = \frac{2P}{\pi w_0^2} \simeq 1.29 \times 10^{10} \text{ W/m}^2 = 12.9 \text{ GW/m}^2. \tag{5.8}$$

For CaF in optical trap at $\lambda \simeq 776$ nm, the scalar polarizability is about $\tilde{\alpha}_0/h \simeq 1.39 \times 10^{-3}$ Hz/(W/m^2). This means the corresponding trap depth for the peak intensity above is $U_0/h \simeq 18$ MHz, $\quad U_0/k_B \simeq 0.86$ mK.

For reference, the RMS ground-state size of a harmonic oscillator is

$$\sigma_i^{(0)} = \sqrt{\frac{\hbar}{2m\omega_i}}. \tag{5.9}$$

At trap frequencies $f_r = 81.55$ kHz and $f_z = 13.11$ kHz, this gives $\sigma_r^{(0)} \simeq 32$ nm and $\sigma_z^{(0)} \simeq 81$ nm. At the lower trap depth of $180 - 200$ μK during dipolar interaction, the axial

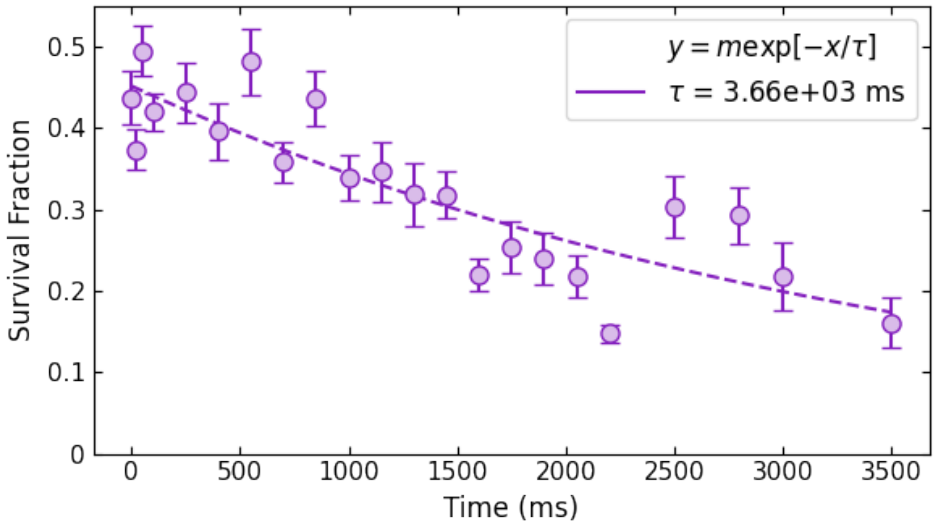


Figure 5.15: Survival probability for molecules held in the optimized tweezer as a function of hold time. A single-exponential fit gives a one-body hold lifetime of $\tau = 3.66$ s.

ground state size increases to approximately 100 nm.

5.4.3 Tweezer Lifetime

Here we characterize the single-body lifetime of CaF in the ground state $X(v = 0)$ held in individual optical tweezers. The measurement is made by loading and imaging the tweezer, holding the molecule in the dark for a variable time, and then taking a second image to determine whether the molecule remained detectable. The survival probability is described by a single exponential decay: $P(t) = P_0 e^{-t/\tau}$. Figure 5.15 shows measurement result, with a fitted lifetime of $\tau = 3.66$ s, which is comparable to the expected room-temperature blackbody-induced vibrational excitation timescale for CaF, as discussed in 3.7.

We note that the major technical limitation that had been limiting the measured lifetime was the relative intensity noise (RIN) of the 1550 nm seed laser for the 776 nm laser amplifier, which has a broad feature near 35 kHz. After second-harmonic generation and amplification to tweezer wavelength, the RIN of the tweezer light seen the by molecules had a pronounced peak near 68 kHz, which is close to twice the axial trap frequency.

5.4.4 Minimum Separation between Two Optically Trapped Molecules

For dipolar interaction experiments, it is beneficial to know the minimum separation at which two neighboring traps can be brought together without inducing loss or unwanted hopping between them.

We characterize this trap spacing limit by preparing molecules in neighboring SLM and AOD traps, moving the AOD trap towards the SLM trap at a given separation and holding it there for a variable interaction time, and then separating the traps for detection. We take this measurement for different separations by sweeping the AOD RF tones to different frequencies. We observe a sharp drop in survival when the traps are brought closer than approximately 1.75 μm, as shown in Figure 5.16 (a). Looking at the same data but separating the molecules in the SLM traps and AOD traps, as shown in Figure 5.16 (b), reveals that there is possible hopping of molecules between the two traps due to significant overlap of the trap potentials. After tuning the focusing of the AOD tweezer beams to reduce the AOD trap waist, we find that we can safely bring two molecules to around 1.5 μm.

5.5 Homogenization of Tweezer Arrays

The camera-based calibration described in Sec. 4.2 provides a coarse homogenization of the tweezer positions and intensities, but it doesn't tell us exactly the trapping potentials seen by the trapped molecules. Here we use molecular measurements as the in-situ signals to homogenize the tweezer array for both AOD- and SLM- generated traps.

The inhomogeneities that we want to correct are trap depth, global relative positions between the SLM and AOD arrays, intra-array trap spacing including axial alignment, and aberrations affecting the shapes of trapping potentials.

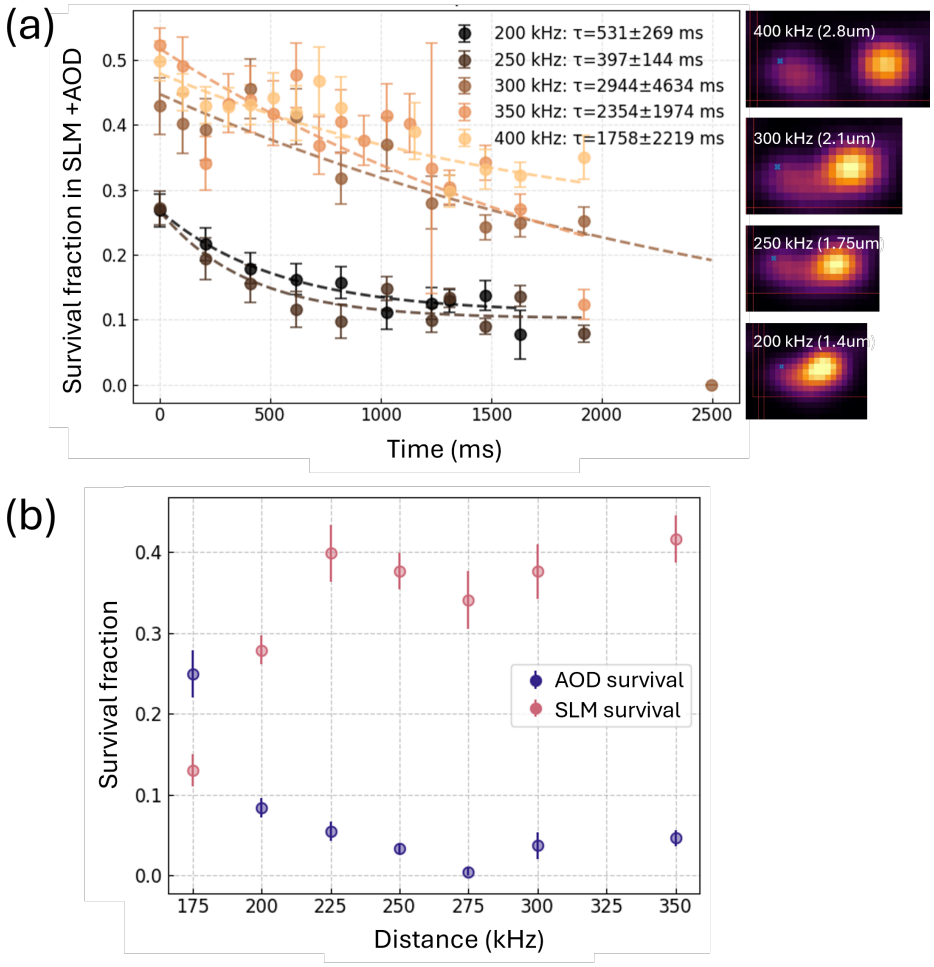


Figure 5.16: Measurements minimum separations between two molecules in optical tweezers without loss or tunneling. (a) Survival probability versus hold time for different trap separations, where frequency of 200, 250, 300, 350, and 400 kHz correspond approximately to separations of 1.4, 1.75, 2.1, and 2.8 μm. Insets show the corresponding images of projected trap at different trap separations seen on the monitor camera. Note that this is for monitoring purpose only as the images are limited in resolutions. **(b)** Analysis of the same data separating the molecule fraction detected in the AOD trap from the survival in the neighboring SLM trap. At small spacings, the fraction of molecules in AOD decreases while the SLM signal increases, indicating possible hopping of molecules between traps.

5.5.1 Trap Depth

To perform trap depth homogenization, there are different kinds of site-resolved molecular signals that one can measure, such as the loading probability and the in-trap fluorescence [187], or, most sensitively, spectroscopy of transition with sensitivity to AC stark shift [188]. We perform Ramsey spectroscopy on $|\uparrow\rangle \longleftrightarrow |\downarrow\rangle$, as the transition frequency depends on the

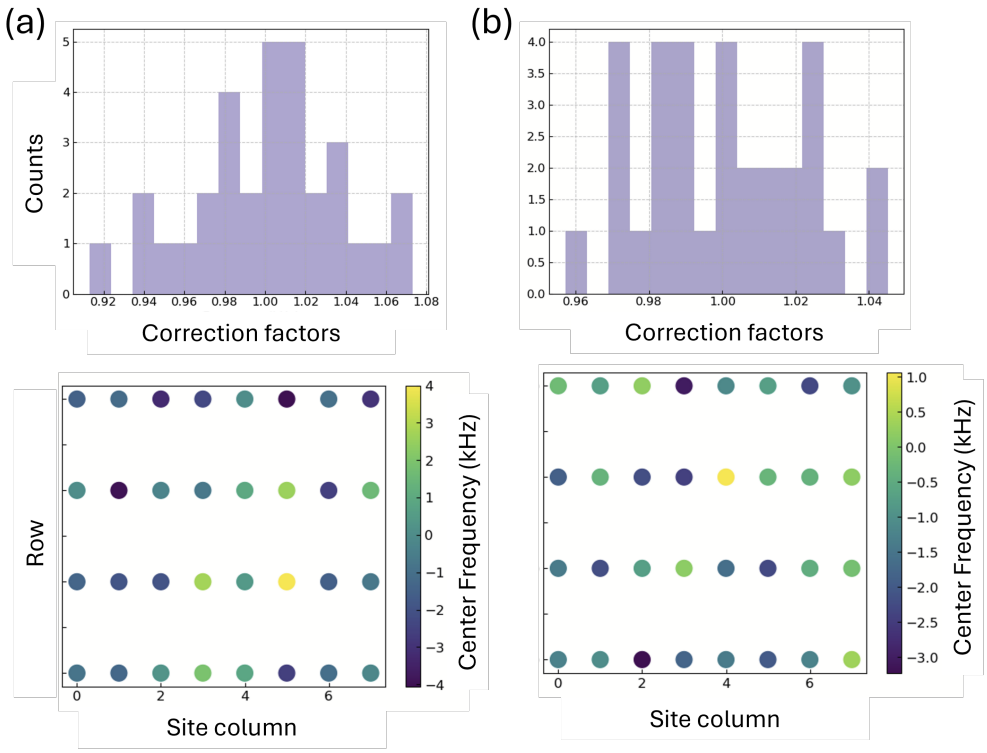


Figure 5.17: Trap depth homogenization using Ramsey spectroscopy, before **(a)** and after **(b)** three iterations (a representative data set). The fitted Ramsey center-frequency offset $\delta\nu_R$ is plotted for each site of the 4×8 SLM array before and after iterative corrections. A histogram of correction factors for initial round is shown on the top row and the measured center frequency offsets are shown on the bottom row.

trap intensity and polarization [3] Different light shifts will lead to transition frequency of the molecule at each site acquiring a slightly different detuning, giving us direct probe of the local trap intensity seen by each molecule. For the SLM array, we rearrange molecules into the SLM-generated tweezers, and the measure frequency offsets are then converted into per-site intensity correction factors, applied to corresponding hologram weights. Similarly, for the AOD array, we perform the same compensation with molecules rearranged into the AOD tweezers, and compensate the rf intensities for each row and column. Additionally, we also homogenize the trap depths by measuring and optimizing single-body coherence across the array using the $|\uparrow\rangle \longleftrightarrow |\downarrow\rangle$ rotational qubit transition. In principle, these three compensations (shifts in transverse plane, focal shifts, and intensity compensations) are independent for the SLM. However, changes in the hologram can weakly affect these different compensations. We

therefore iterate through each of these measurements and compensations. Figure. 5.17 shows a representative data of the measured Ramsey frequency offsets across the array after initial (a) and (b) three rounds of iterations.

Ramsey spectroscopy measurement tells us the carrier shifts, and traps with different waists can have the same trap depth but different trap frequencies. When the carrier frequency and sideband spacing shift together, it indicates that sites mainly differ in trap depth. If the sideband spacing changes without a corresponding carrier shift, or vice versa, the inhomogeneity is more likely associated with trap shape, or focus. To ensure the trap frequencies are uniform across the array, we measure the motional sideband spectra, obtaining the lowest three orders of motional sidebands of molecules in each site. For near harmonic traps like our tweezers, the spacing between motional sidebands give us the trap frequency. We use the fitted second- and third- order sideband spacings to be more sensitive, since the sideband order amplifies the frequency shift by approximately $\Delta m \omega_{\text{trap}}$, making site-to-site differences easier to resolve. Figure. 5.18 shows the measured lowest three orders of motional sideband spacings for molecules across the AOD array, with correction is referenced to sites that have demonstrated better Raman sideband cooling performance.

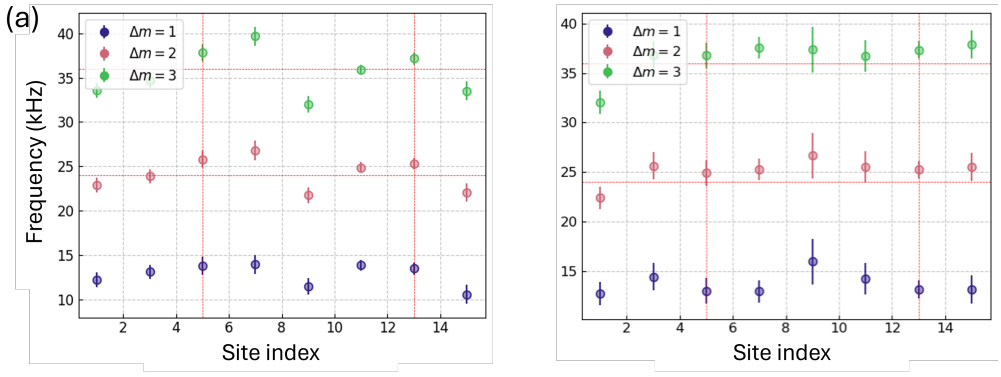


Figure 5.18: Trap frequency homogenization using motional sideband spectra. Fitted motional sideband frequencies are shown for individual tweezer sites before **(a)** and after **(b)** site-wise amplitude correction. Each color corresponds to a different sideband order Δm. Horizontal dashed lines indicate the target frequencies, and vertical lines indicate the sites that have previously shown the best Raman sideband cooling performance.

5.5.2 SLM Trap Aberrations

In the most ideal case, the SLM plane is conjugate to the back aperture of the objective, so the calculated hologram is exactly the trap pattern projected in the objective's focal. In the real optical system, aberrations from the SLM surface, relay optics and objective distorts the trap light wavefront. To correct these aberrations, we essentially use the molecules as a wavefront sensor. For each Zernike mode (orders 5 through 13, corresponding to astigmatism, coma, trefoil, spherical aberration, and so on), we scan the coefficient of the Zernike polynomial and probe the molecular response in each site –this can be Ramsey frequency of the qubit transition or AC stark shift on a stretched-state transition $|N = 1, F = 2, m_F = +2\rangle \, arrow \, |N = 0, F = 1, m_F = 1\rangle$ in $X^2\Sigma$ state, that has a large differential polarizability (see Fig 6.1 (b)). From these measurements (see Figure 5.19 for a representative data scans of applied coefficients and AC stark shifts), we identify the optimal coefficient values.

5.5.3 SLM-AOD Transfer Fidelity

In our hybrid SLM-AOD tweezer architecture, rearranging molecules for forming desired interaction geometry requires molecules to be transferred between SLM- and AOD-generated traps without minimal loss and heating. To better isolate the effect of this process on the molecules, let us make a distinguish between *handover* operation: handing the molecule from an SLM trap to the AOD trap in place, and *transfer* operation: the entire the handover followed by moving of the AOD tweezer to another position. To characterize the transfer process, we measure the loss rate as well as motional excitations after repeated handovers or transferring molecules between traps

During the handover, we adiabatically ramp up (or down) the intensity of an AOD tweezer at the position of a molecule in an SLM trap. The ramping of trap depth $\sqrt{U_0}$ changes trap frequency as $\omega_{\text{trap}} \propto \sqrt{U_0}$, and the motional state follows adiabatically if this change is slow over a trap period. As shown in Figure 5.20 (a) data, the handover loss is flat for ramp duration around 150 μs $-$ 350 μs.

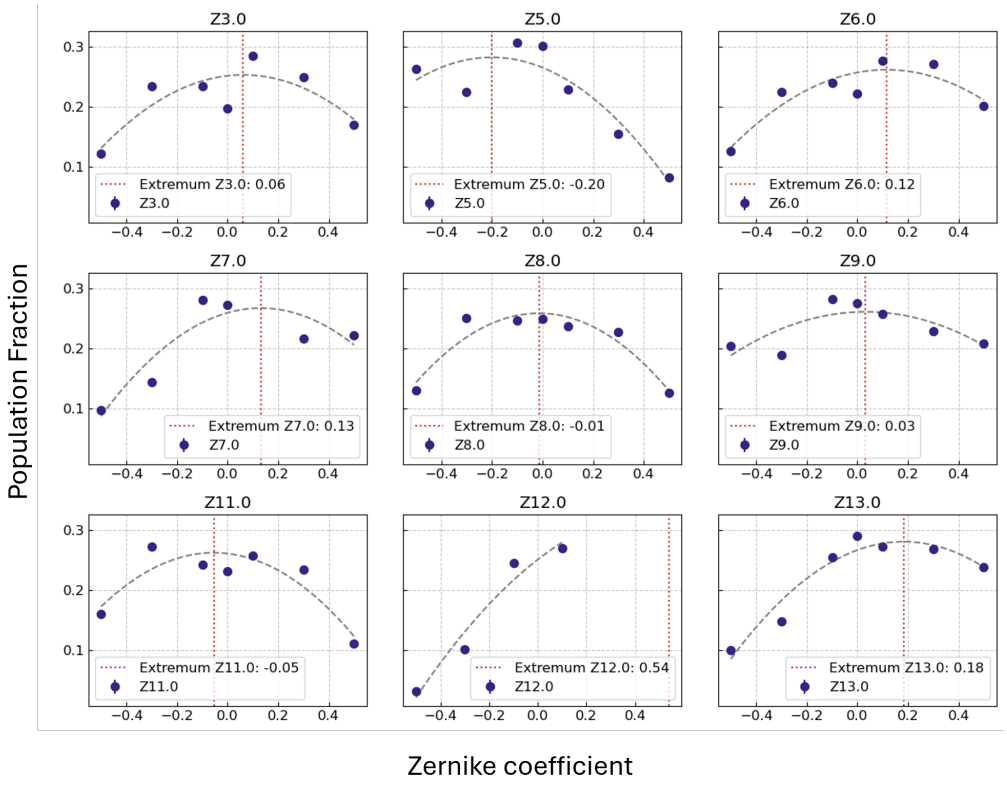


Figure 5.19: Scans of a range of Zernike coefficients as stretched state transition frequency center is probed. The dependence on the Zernike coefficient is fitted to a quadratic function, and the fitted extremum is used as optimal coefficient value.

In addition, we use handover loss rate to optimize the relative alignment between SLM array and AOD array. Without any compensation, SLM-generated tweezer arrays can exhibit site-dependent axial offsets exceeding 100 nm [189]. We calibrate these offsets by first measuring the AOD–SLM handover fidelity as a function of the defocus Zernike mode Z_2^0 (Fig. 5.20 (b)), as well as the Zernike coefficient of transverse displacement for each interacting pair. We then apply site-dependent defocus corrections to the SLM hologram, reducing the residual trap-to-trap axial disorder to less than 100 nm rms [189–191]. We further confirm this by using the dipolar interaction strength to measure the relative focal shift between a pair of SLM and AOD tweezers.

The subsequent moving of molecules by AOD traps is controlled by smooth frequency sweeps. For typical a non-interacting configuration, the molecules are separated by 7 μm. We use a fifth-order minimum-jerk trajectory [192, 193], where the velocity and acceleration

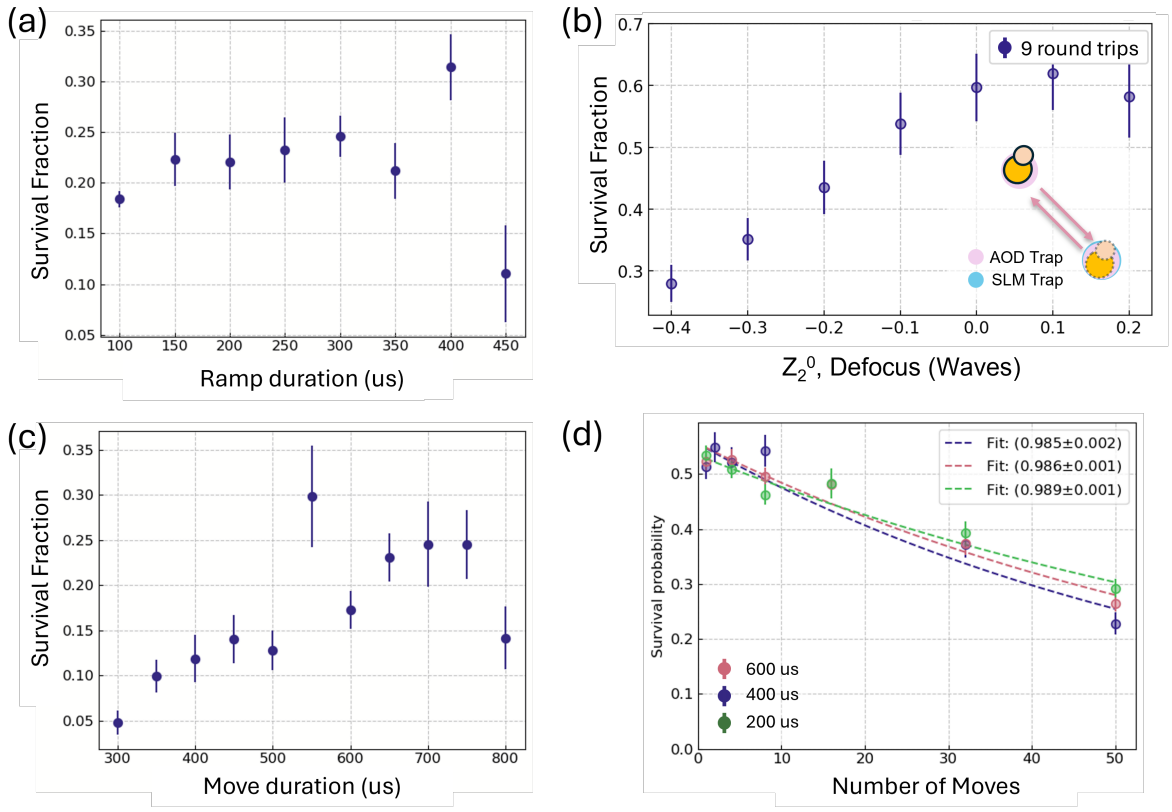


Figure 5.20: Characterization of AOD to SLM transfer. (a) Survival rate of repeated handover between pairs of traps with different AOD trap intensity ramp duration. **(b)** Survival rate of 9 rounds of handover between pair of traps as a function of the coefficients of the defocus Zernike mode Z_2^0 on SLM trap. **(c)** Survival rate (zero move refernece value is 0.5) after 50 moves, with each move of $\sim 7\mu$m, for different move durations (speeds). **(d)** Survival rate as a function of number of moves (with each move of $\sim 7\mu$m) at different move duration, where ~ 0.98 per-move survival can be obtained with $600\,\mu$s.

are zero at the endpoints to suppresses impulses at the start and end of the move. We see that experimentally, the transport loss is flat for move durations above roughly 600–700 μs, corresponding to a speed near 10 μm/ms, as shown in Fig. 5.20 (c). This is expected as the move duration is many radial and axial trap periods. From a repeated move measurements, we see an averaged single transfer fidelity around 0.98–0.99 (Fig. 5.20 (d)).

Finally, we separately check whether the handover and the transfer introduce motional heating. To do this, for each pair of molecules, which are initially all in the SLM traps, we ramp up the AOD intensity at one of the molecules, move it away into an intermediate (but non-interacting) separation for Raman sideband cooling (see Chapter 6.4), ramp down the

AOD trap intensity and perform Raman sideband thermometry on both molecules in the pair, and then move the molecule back to its initial position where the SLM trap is. The sequence is schematically shown in Figure 5.21. At the end, we compare the resolved sideband spectrum of the static molecule that is not moved to the moved molecule. We observe that the sideband spectrum of the moved molecules show clear motional excitations, which is a sign of heating.

Now the sources of this observed heating could be due to several things, including the handover, trap ramping, trap moving, or the Raman sideband cooling in AOD traps is not good to start with; as the SLM and AOD traps have slightly different trap shapes, the life Shift and trap frequencies do not match exactly, placing a limitation on hybrid array cooling performance. Eventually, after better matching the trap frequencies of AOD and SLM array, and optimizing ramping and moving, we find that the dominant contribution comes from the handover process.

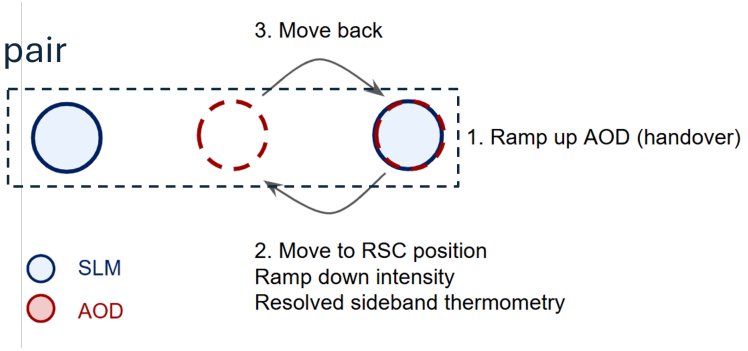


Figure 5.21: Illustration of the experimental steps used to measure motional excitations of molecules after SLM–AOD trap transfer.

This has then led us to make a change in the experimental sequence: instead of performing Raman sideband cooling on molecules initially all loaded in the SLM array and then transferring half of them into AOD array for interaction, we now first perform the SLM-AOD trap transfer to form an interleaved array, then cooling in the hybrid array, and then move into interaction geometry.

5.5.4 Technical Heating

Here we note a technical heating mechanism we have found which showed up as increased transfer loss in the AOD trapped molecules at the reduced trap intensity used for interaction. This is traced back to the way the AOD tweezer waveform is set up in the arbitrary-waveform generator (AWG). The waveform was being synthesized by AWG as a finite segment and looped with a period of about 100 μs. However, replaying a finite segment creates a periodic modulation, or a spectral component at $1/(100\,\mu\text{s}) = 10\,\text{kHz}$. If there is any discontinuity where the segment is not perfectly periodic in amplitude and phase, it can produce comb of harmonics spanning tens of kHz. With our axial trap frequency at round 13 kHz, these harmonic components would easily cause parametric heating. To fix the issue, we revised the waveform generation to avoid discontinuous looping and to keep the RF phase continuous across segments.

10^{-4} *is a thousand* 10^{-7}*'s.*

Avikar, definitely

6

Single Molecule Quantum Control and Cooling to Motional Ground State

Work in this Chapter, including portions of the text and figures, has been distributed as publications [3] and [194].

This chapter outlines the experimental framework for cooling and manipulating a single molecular qubit. We begin in Sec. 6.1 by examining the properties of the chosen rotational qubit states, particularly their susceptibility to external fields (most of the work was first developed in [3]), alongside the state preparation protocol. We then detail the techniques implemented to suppress sources that can degrade the single-qubit coherence to maximize the qubit's T_2 coherence. In the last section, we discuss the experimental development for cooling the molecules to the motional ground state via Raman sideband cooling (RSC), with Sec. 6.4.2 laying out the experimental groundwork (also see Ref. [194]) for obtaining a cooled sample with

high ground state probability, while Sec. 6.4.3 focuses on modifications to reduce loss in order to preserve more molecules after cooling.

6.1 Rotational Qubit States and Sensitivities

To realize a useful molecular qubit, we generally want it to satisfy three basic criteria [3, 7, 28, 195]. First, the qubit states should be have minimal sensitivity to ambient fluctuating field noises to maximize the T_2 coherence time, which dictates the duration of time during which the system can coherently preserve quantum information. Second, we want the qubit to be able to have strong interaction with other molecular qubits and facilitate entanglement; for polar molecules, this means retaining a large enough electric dipole moment. Third, the qubit transition frequency should be spectroscopically accessible.

This naturally points to encoding the qubit in adjacent rotational manifolds, separated by one unit of angular momentum, so that the qubits can participate in resonant dipole-dipole interaction. The simplest choice is the lowest two rotational $N = 0$ and $N = 1$ manifolds of the $X^2\Sigma^+$ electronic and vibrational ground state. The $N = 0 \leftrightarrow N = 1$ splitting of CaF is near 20.5 GHz, placing the transition in a technically convenient microwave band, and clear of any neighboring rotational lines that might be driven off-resonantly. In addition, since the rotational states have definite parity, the rotational transition has no first-order DC Stark shift. Static electric fields only induce shifts by admixing opposite-parity rotational states, so the leading sensitivity is quadratic and the energy shift is small due to the large rotational gap (differential DC Stark sensitivity is on order 40 Hz/(V/cm)^2). In practice, one still needs to be careful of charge accumulation on nearby dielectric surfaces as these can cause shifts on order of hundreds of kilohertz if fields reach the $\sim$ 100 V/cm scale.

The more restrictive considerations are the differential sensitivity to magnetic fields and trap light. First, we will investigate magnetic field sensitivity. The $N = 1$ manifold has 12 hyperfine states and $N = 0$ has 4, as shown in the state diagram in Figure 6.1, but most of the transitions between them make poor qubit candidates because the two states have

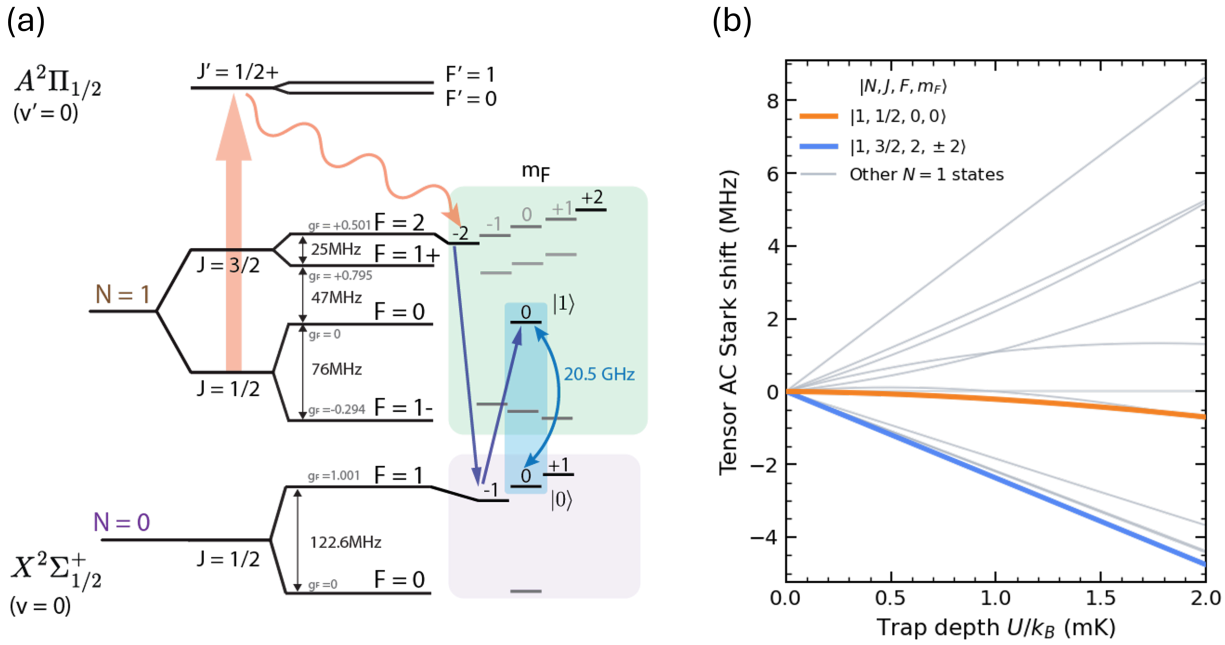


Figure 6.1: (a) Relevant rotational (N), hyperfine (F) and Zeeman (m_F) states in the ground electronic state $X^2\Sigma$ and first excited state $A^2\Pi$ of CaF. The arrows indicate pulses used in state preparation sequence: orange arrow is the optical pumping light; wavy orange line is spontaneous emission; The blue arrows are microwave transfers. **(b)** Tensor AC Stark Shifts of all $N = 1$ states versus trap depth of a 780 nm trap, with the highlighted $|N = 1, J = 1/2, F = 1, m_F = 0\rangle$ state in orange and spin-stretched state $|1, 3/2, 2, \pm 2\rangle$ in blue. Calculation assumes linear trap polarization parallel to the field.

different magnetic g-factor, and thus a differential magnetic moment on the order of a Bohr magneton ($\sim 1.4\,\mathrm{MHz/G}$); at such sensitivity, milligauss level of field drifts would produce kilohertz-level noise on the transition frequency and dephase the qubit coherence quickly. One way to avoid this is to choose a transition whose two levels share the same magnetic moment. The spin-stretched transitions are the obvious choice $|N = 1, J = 3/2, F = 2, m_F = \pm 2\rangle \leftrightarrow |N = 0, J = 1/2, F = 1, m_F = \pm 1\rangle$, as the rotational angular momentum, electron spin, and nuclear spin are nearly aligned in the same direction in these states, with residual differential sensitivity of $\sim 144\mathrm{Hz/G}$ (so an order of magnitude smaller than the full Bohr magneton). However, the stretched $N = 1$ states have large tensor AC Stark shifts in a 780 nm tweezer, about $\simeq -2.38$ MHz/mK relative to the scalar trap depth (see Fig. 6.1(b)). For a molecule that has thermal motion in the optical trap and samples different local trap intensities, this results in a large position-dependent transition frequency, and thus inhomogeneous broadening

and thermal dephasing.

Using $|N = 1, J = 1/2, F = 0, m_F = 0\rangle$ state solves part of the problem. As the $F = 0$ state is isotropic in the lab frame, it has no diagonal first-order Zeeman shift and no diagonal first-order tensor light shift at weak fields. Pairing it with an $|N = 0, J = 1/2, F = 1, m_F = 0\rangle$ state makes the leading magnetic and optical sensitivities of the transition vanish at zero field. Although the $F = 0$ state has no first-order tensor shifts at zero field, finite magnetic fields and optical light field can admix nearby hyperfine states, endowing the transition with a differential light shift. As discussed in Sec. 6.3 and [3], this shift can be mitigated by tuning the orientation of the magnetic field relative to the linear tweezer polarization, at a given magnetic field and trap intensity.

The cost of this choice of qubit states is that the transition dipole is reduced by angular-momentum projection factors, leaving us with 1/3 of the maximum dipole-dipole exchange strength available from the stretched-state transition. In practice this tradeoff is favorable when coherence is the limiting resource. Our choice for rotational qubit states used through out the rest of the work are therefore

$$|\uparrow\rangle = |N = 1, J = 1/2, F = 0, m_F = 0\rangle\,, \tag{6.1}$$

$$|\downarrow\rangle = |N = 0, J = 1/2, F = 1, m_F = 0\rangle\,. \tag{6.2}$$

6.2 State Preparation

In order to prepare the molecules in a single qubit state, we use a sequence of optical pumping and coherent microwave transfers. The relevant states and the state preparation procedure is illustrated in Figure 6.1(a).

In the experiment, once the molecules are loaded into the SLM tweezers, we take a nondestructive image using Λ-imaging [49, 160] driving $X - A$ transition and collect the fluorescence onto an EMCCD to confirm the loaded traps. Since the Λ-cooling technique relies on closed photon cycling between the $|X, N = 1\rangle$ and $|A, J = 1/2\rangle$ manifolds, only molecules

in the $|X, N = 1\rangle$ rotational manifold can be loaded into the tweezers and detected at this step. This imaging light distributes the population of molecules over all twelve hyperfine states in the $|X, N = 1\rangle$ manifold. The next task is to purify the states by the following state preparation procedure. Initially, we used a scheme that relied on using a $X - A$ beam resonant with all hyperfine levels *except* the $|\uparrow\rangle$ state, in the $N = 1$ manifold, in order to pump most of the molecules into $|\uparrow\rangle$. The optical pumping efficiency under this scheme is ~ 0.8, limited by residual population in other hyperfine states within $N = 1$. The total state preparation efficiency then, including imaging fidelity and survival rate, was $\lesssim 0.6$.

To improve on the state preparation efficiency, we replaced it with a hyperfine optical pumping scheme based on [10]. We optically pump the molecules to stretched $m_F = -2$ state with light containing σ^- and π polarization and a quantization B field applied. The advantage of optical pumping into a stretched state here is that the target state can be made dark by angular-momentum selection rules. Repeated scattering then accumulates population in this dark state. The relevant states and pulses are shown in Figure 6.1(a).

6.2.1 Choice of Optical Pumping Stretched State

In $N = 1$ manifold, the two stretched state options are

$$|2, +2\rangle \equiv |N = 1, F = 2, m_F = +2\rangle \text{ and } \quad |2, -2\rangle \equiv |N = 1, F = 2, m_F = -2\rangle .$$

In free space these states are basically identical and symmetric choices where one can optically pump into either one by choosing the opposite circular polarization. In tightly-focused tweezer trap, however, the trap light induces large tensor light shift. In the $N = 1$ manifold, the tensor shift depends on the orientation of the molecule relative to the tweezer polarization and produces state-dependent shifts among the m_F Zeeman sublevels. For an ideal linearly polarized trap light that is perfectly aligned with the B-field, the tensor Stark Hamiltonian only couples states having the same m_F, so it only shifts energies and does not causing coupling between nearby m_F levels. However, the tight focusing in an optical tweezer produces a longitudinal

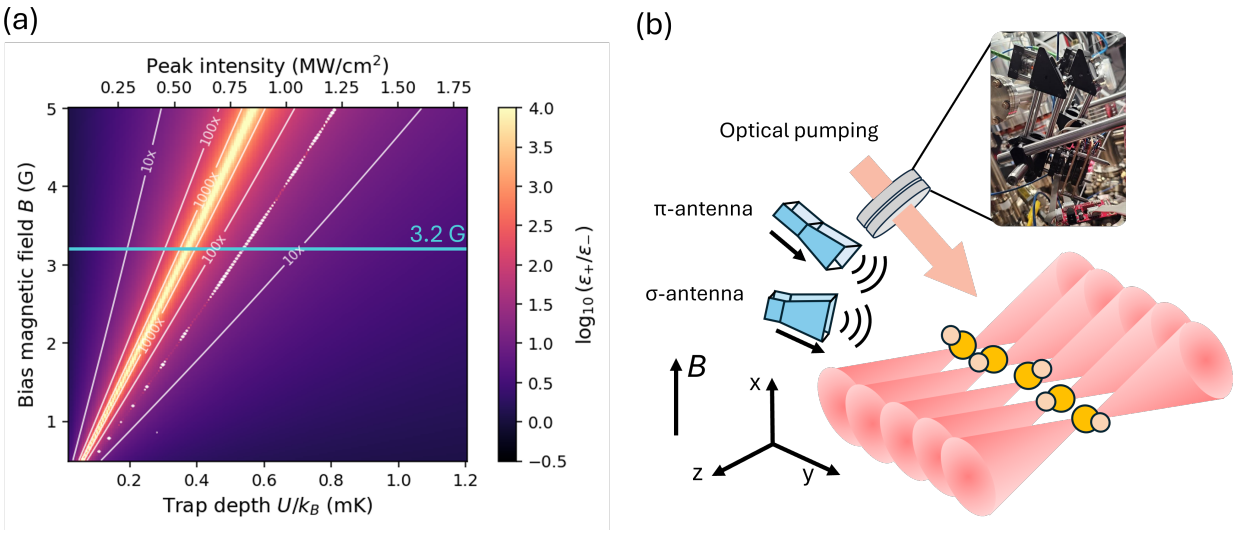


Figure 6.2: (a) Relative purity of the two stretched states versus magnetic field and trap depth. The color represents the ratio $\epsilon_{+2}/\epsilon_{-2}$, where $\epsilon_{\pm 2}$ is the population outside the corresponding free-space stretched state. Contours labeled $10\times$, $100\times$, and $1000\times$ therefore indicate how much more strongly the $m_F = +2$ state is mixed than the $m_F = -2$ state. (b) Illustration of experimental setup for state preparation.

electric field component (following from Maxwell's equation $\nabla \cdot \mathbf{E} = 0$), so away from the focus, there is spatially-varying polarization gradient [196, 197] across the molecular wave packet (eg. for molecular wave packet with rms width in radial trap direction $\sigma_x \simeq 110nm$, the longitudinal field amplitude is about 3.4% at $x = \sigma_x$). So these residual tensor components can mix our dark stretch states with other nearby bright m_F states.

We can quantify the stretch state purity by $\mathcal{P}_{\pm 2} = |\langle 2, +2|\psi_\pm\rangle|^2$, where $|\psi_\pm\rangle$ is the eigenstate at a given finite trap depth. Then the corresponding bright-state impurity is $\epsilon_{\pm 2} = 1 - \mathcal{P}_{\pm 2}$. Figure 6.2 (a) plots how the relative impurity, $\epsilon_{+2}/\epsilon_{-2}$, of the two stretched states $|2, \pm 2\rangle$ varies with magnetic field and trap depth. The feature in the plot shows the competing contribution between Zeeman and tensor AC Stark shifts. The Zeeman shifts scale approximately linearly with the applied bias field, while the tensor Stark shifts scale with the tweezer intensity. Because the tensor polarizability of CaF is negative, the light shift lowers the energy of the stretched states. For the $|2, +2\rangle$ branch this shift pushes it closer to neighboring smaller m_F states (bright states), producing avoided crossings and large admixture with those bright states. On the other hand, the $|2, +2\rangle$ branch is more isolated over the same parameter range, so its impurity is

smaller. These results motivate the use of $m_F = -2$ in our state preparation's optical pumping.

6.2.2 Optical Pumping Light

The better dark state also makes the scheme demanding in beam polarization purity and stability: any small residual σ^+ component can degrade the darkness of $mF = +2$ state. So for the stretched-state optical pumping, we want to drive only $\sigma-$ and π-transitions. Here we note several technical details needed to make the optical pumping reliable.

First, the optical-pumping beam is sent transverse to the tweezer propagation axis and oblique to the quantization axis, so that a single elliptically polarized beam can supply the desired σ^- and π components. Figure 6.2(b) shows a diagram of the experimental setup geometry. The input optical pumping light is then passed through a Glan-Taylor polarizer and coupled along the slow axis of a polarization-maintaining fiber to improve long-term stability. To generate the elliptical polarization containing the desired σ^- and π components with minimal σ^+ at the molecules, we use a motorized half-wave plate and quarter-wave plate (see Figure 6.2(b) inset). The wave-plate angles are optimized by measuring the depumping rate out of the dark state.

Lastly, to generate the hyperfine components in the optical pumping light, we replaced the previous resonant EOM, where a single EOM is driven to produce symmetric sidebands, three of which address our hyperfine splittings (see Fig. 6.1). This scheme allowed no control over relative intensities on each hyperfine components, as well as wasted optical power in unused sidebands. The spectrum was also sensitive to thermal drifts when the beam was pulsed. We therefore built a compact hyperfine board that derives the hyperfine components from the MOT light and recombines them with independent control over the relevant hyperfine frequencies and intensities. Alternatively, a more flexible method is to use either broadband EOM (or waveguide), or fiber-coupled EOM to synthesize arbitrary sideband spectra [167, 198, 199].

After optimizing the optical detuning, elliptical polarization, and tweezer trap depth during optical pumping, we reach $> 90\%$ optical pumping efficiency in state preparation, much more improved compared to the $\sim 80\%$ from previous scheme.

6.2.3 Microwave Transfers

After optical pumping light accumulates the population in the dark stretched state $|2,-2\rangle$ m_F, we use a pair of composite microwave pulses to coherently transfer the molecules into qubit $|\uparrow\rangle = |v=0, N=1, F=0, m_F=0\rangle$ state. The first microwave pulse drives $|2,-2\rangle = |N=1, F=2, m_F=-2\rangle$ to $|N=0, F=1, m_F=-1\rangle$, and a subsequently pulse drives $|\uparrow\rangle = |v=0, N=1, F=0, m_F=0\rangle$ state. Both microwave transfer require change of $\Delta m_F = +1$, that is, σ^--polarized microwave from the antenna horn. In our experimental geometry (Fig. 6.2(b)), the σ transitions are driven by an antenna horn pointing approximately along $\hat{y}$ with its short aperture axis along $\hat{z}$, emitting predominately E_z microwave electric field perpendicular to the quantization axis in $\hat{x}$.

To improve the robustness of microwave transfer, we replaced each square microwave π pulse by a Knill composite pulse [200–202], which is composed of five nominal π pulses applied with different relative phases. This cycling phase pattern causes pulse-area and small detuning errors to enter with alternating signs, such that the leading errors cancel. Experimentally this substantially improves transfer performance compared with single square pulses, reaching a transfer fidelity of (>0.99983) for each transfer and a combined efficient of ~ 0.998.

Between the two microwave pulses we also resonantly excite any remaining molecules in $|N=1\rangle$ to heat them out of the tweezer. This sequence prepares all molecules in $|\uparrow\rangle$ in the tweezer array.

6.3 Single-Qubit Coherence

Before using rotational qubits for coherent interaction or generation of quantum entanglement, it is essential to know for how long and how well a single molecule can preserve phase. For polar molecules, long single-qubit coherence, on the order of hundreds of milliseconds to seconds, is needed because the coherent interaction scales are typically tens of hertz to kilohertz depending on the molecular transition dipole moment, and trap spacing. Molecules trapped in optical

tweezers have already demonstrated long rotational and hyperfine coherence times, well beyond the expected timescales for dipole-mediated two-qubit gates [3, 203–205].

The coherence of a single rotational qubit is affected by perturbations that make the transition frequency shift during a coherent operation. The two main sources of such shifts are the trap-induced inhomogeneities and external stray fields. For polar molecules in optical traps, the trapping light generally produces different AC Stark shifts for different rotational states. A trapped molecule with thermal motion samples a distribution of intensities as it moves in the tweezer, any differential light shift is converted into fluctuations of transition frequency, leading to inhomogeneous broadening and dephasing.

A range of "magic" trapping strategies has been developed to suppress this differential shift, including magic polarization or magic-angle condition [3, 205–207], magic ellipticity in deep optical tweezers [4, 208], magic-wavelength traps [5, 209], and spin-decoupled or field-assisted magic trapping [22, 204]. Essentially, all these techniques rely on engineering conditions to make the two qubit states acquire nearly the same trap-induced light shift, or more generally so that the transition frequency has vanishing first-order sensitivity to the local trap intensity.

For our choice of qubit states $|\uparrow\rangle$ and $|\downarrow\rangle$, both states reside in the electronic and vibrational ground state, where radiative decay is negligible on experimental timescale; the lifetime limited by blackbody radiation induced vibrational excitations for CaF is $\sim 3.5\,\mathrm{s}$, see Chapter 3). So for CaF in optical tweezers, this sets a fundamental limit on the achievable T_2 time

In this section we will look into the major sources of decoherence for single CaF rotational qubits and show the experimental techniques we employ to suppress the dephasing sources and preserve coherence.

6.3.1 Magic Condition for Suppressing Light Shifts

Note that the term "magic condition" used here is used in a different context from that in Chapter 7.

In an optical tweezer, the most direct source of perturbations comes from the trap light itself. The $N = 0$ manifold that the $|\downarrow\rangle$ state belongs to is rotationally isotropic, so $|\downarrow\rangle$ state in $N = 0$

only has scalar polarizability. The $|\uparrow\rangle$ in $N = 1$, in an ideal $\mathbf{B} = 0$ environment, is also isotropic (isolated $F = 0$ state). The leading differential shift then comes from being in optical trap, where the trap light causes mixing of $|\uparrow\rangle$ with nearby hyperfine states in the $N = 1$ manifold, especially the $|N = 1, F = 2, m_F = 0\rangle$ state. This leads to the qubit transition acquiring an intensity-dependent light shift that is non-linear in intensity:

$$\delta\nu_{\mathrm{q}}(I, B = 0) \simeq -\beta I^2, \textbf{with } \beta > 0, \tag{6.3}$$

where $\delta\nu_{\mathrm{q}}$ is the differential light shift, I ([mK]) is the tweezer intensity, and β ($(\mathrm{Hz/mK^2})$) is the magnitude of quadratic light shift coefficient (also called "hyperpolarizability") of the transition. The trap light-induced differential Stark shift between the two rotational qubit states is the dominant dephasing mechanism.

To mitigate this, we employ a previously developed "magic-condition" that follows from the theory and experimental work done in previous generation of this experiment, detailed in Ref. [3]. Here we give a brief summary of the technique which is a crucial component for achieving long single-body rotational coherence time.

The idea of the magic condition for rotational coherence in CaF is that it exploits a crossover between two limiting regimes. At low trap intensity, the applied bias magnetic field $\mathbf{B}$ is the dominate perturbation that defines the quantization axis. In this regime, the Zeeman Hamiltonian H_z mixes $|\uparrow\rangle$ with nearby hyperfines, causing it to acquire small admixture of neighboring $|N = 1, F = 1^{\pm}\rangle$ branches. These admixed $F = 1$ components do have nonzero first-order tensor shift in $\mathbf{B}$, and this gives a linear differential light shift whose sign depends on the polarization angle. At high intensity, the tensor part of the light shift becomes the dominate perturbation. Overall, the differential light shift can be written in the form

$$\delta\nu_{\mathrm{q}}(I; B, \theta) \simeq a(B, \theta)I - \beta(B, \theta)I^2 + \cdots . \tag{6.4}$$

The linear term αI sets the slope of the light shift at low intensity, and it physically comes

from $\mathbf{B}$ mixing a small amount of $F = 1^{\pm}$ states into the otherwise isotropic $|\uparrow\rangle$. The quadratic term βI^2 is the Stark shift of the dressed $|\uparrow\rangle$ state, with β (defined above as the quadratic light shift coefficient or "hyperpolarizability") setting a negative curvature.

Eq. 6.4 is plotted in Figure 6.3 (a) for CaF rotational qubit states. The slope and sign of this shift is determined by the angle θ between the light polarization and $\mathbf{B}$. This means that by choosing a magnetic field magnitude $|\mathbf{B}|$ and the angle θ of the tweezer polarization, one can tune to cancel these terms in the slope at the peak intensity, resulting in a "magic" operating condition where:

$$\left.\frac{\partial \delta\nu_{\mathrm{q}}}{\partial I}\right|_{I_0} = a(B, \theta_{\mathrm{m}}) + 2\beta(B, \theta_{\mathrm{m}})I_0 = 0. \tag{6.5}$$

Because the magic condition depends jointly on the tweezer intensity, the $\mathbf{B}$ field magnitude, and the angle θ, it can be found by holding one parameter fixed and scanning the other two. For example, for measurements where a certain trap depth is desired for motional or other considerations, one can tune the bias magnetic field strength and tweezer polarization angle to maximize Ramsey coherence, or equivalently probe a transition frequency. In Figure 6.3 (b), we show corresponding magic condition for the CaF rotational qubit states with typical range of experimental values.

6.3.2 Dynamical Decoupling Microwave Pulses

With the magic condition set for suppressing the qubit's first order sensitivity to differential AC stark shift due to trap light, the other major source of decoherence comes from external field noises. In Sec 4.4, we describe the passive and active field compensation systems to either mitigate or compensate for long-term drifts in environmental fields that are slow compared to experiential times scale These measures make the qubit coherence reproducible from shot to shot, but they do not eliminate magnetic field fluctuations and technical noise on timescales shorter than the field compensation servo or not perfectly synchronized to the line cycle. To further preserve the rotational coherence, we apply an XY8 dynamical decoupling sequence. The basic idea is the same as a spin-echo pulse [210, 211], where a π pulse swaps $|\uparrow\rangle$ and $|\downarrow\rangle$,

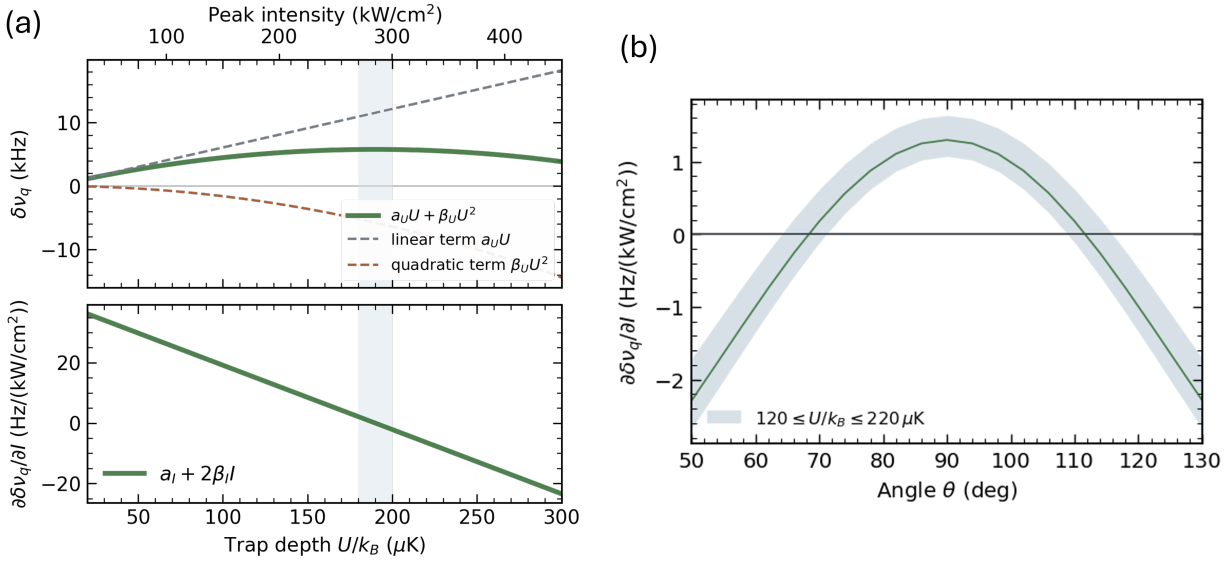


Figure 6.3: (a) Top: calculated differential light shift $\delta\nu_{\mathrm{q}}(U)$ of the rotational qubit state at $B = 3.2\,\mathrm{G}$, where U/k_B is trap depth. The gray dashed line shows the linear contribution from magnetic field mixing, and the brown dashed line shows the quadratic Tensor shift. Bottom: corresponding differential sensitivity $\frac{\partial\delta\nu_q}{\partial I} = a_I + 2\beta_I I$. Shaded region marks the typical experimental trap depth range during coherent operations (from $180\,\mu\mathrm{K}$ to $200\,\mu\mathrm{K}$. (b) Sensitivity of magic condition as a function of the polarization angle, over a range of trap depth $U/k_B = (120\,\mu\mathrm{K}, 220\,\mu\mathrm{K})$.

causing temporally varying detuning errors to contribute with opposite signs before and after the pulse. The XY8 sequence improves on a single echo by using a periodic pattern of π pulses with alternating microwave phases, making the decoupling more robust to pulse-area and phase errors [200, 201, 212–215].

In our implementation of XY8 pulse sequence, the interpulse time is $200\,\mu\mathrm{s}$, and each π pulse has a Blackman amplitude envelope [216, 217] with an $8.5\,\mu\mathrm{s}$ pulse duration. The microwave horn is aligned to maximize the π-polarized component in order to suppress coupling to unwanted states. The XY8 decoupling sequence mitigates dephasing from magnetic field fluctuations, measured to be $70\,\mu\mathrm{G}$, and from fluctuations and drifts in the tweezer light intensity.

The resonant microwave pulses used to drive the rotational qubit transition are generated by mixing of 2 sources (more details can be found in Ref. [159]): A high-speed arbitrary waveform generator (AWG) with synchronized digital outputs is used to generate the baseband signal and the blanking signal. The digital blanking signal is used to control two fast microwave switches in tandem, providing 160 dB suppression of microwave power when the microwaves are turned

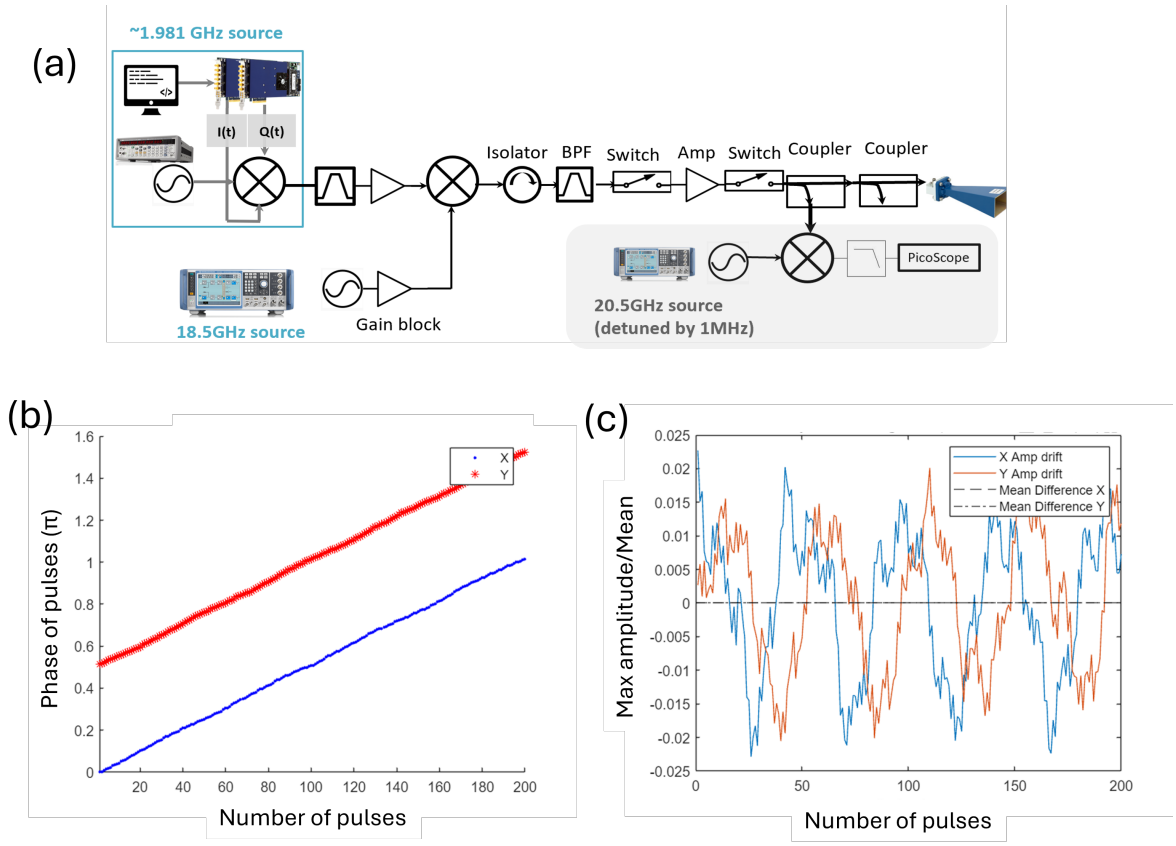


Figure 6.4: **(a)** Schematic of the microwave generation system, including a beat-note measurement setup. **(b)** Measurement of pulse to pulse phase extracted from a 1 MHz beat-note measurement. **(c)** Relative microwave pulse amplitude extracted from the same beat-note measurement.

off. The two analog channel outputs produce the analog $I(t)$ and $Q(t)$ waveforms, which set the envelope, phase, and intermediate frequency of each microwave pulse. These waveforms modulate a $\sim$ 1981 MHz source, which is then mixed with an 18.5 GHz source to produce radiation resonant with the 20.5 GHz qubit transition.

We note that for XY8 sequence containing hundreds of pulses, one important technical consideration is phase tracking between pulses because the microwave rotation axis is set by the phase of the baseband waveform at the start of each pulse. If the I/Q waveform is restarted or timed incorrectly, the microwave phase at the beginning of a pulse can jump by an unintended amount. Such phase jumps are especially detrimental in XY8, where the sequence relies on precise alternation microwave rotation axes. We have had issues with coherence because of this. We diagnosed it by beating the microwave pulse train against another stable source and

extracting the phase of each pulse. After this debugging, we use an I/Q modulation frequency and pulse timing so that the baseband phase was well defined at every pulse boundary. For example, a 10 MHz I/Q frequency has a 100 ns period. This means the phase of the waveform repeats every 100 ns, making it straightforward to choose π pulse durations (i.e. 10 μs) such that the pulse spans exactly integer number of (i.e 100) cycles every 100 ns. Figure 6.4 shows results of a beat-note measurement. In Fig. 6.4 (a) the extracted phase between pulses evolves smoothly across the XY8 pulse sequence, and the absence of abrupt jumps indicates that the programmed phases remain continuous between pulse blocks. Fig. 6.4 (b) shows the corresponding relative amplitude of the pulses, which remain within approximately 1% over the sequence.

6.3.3 Rotational Coherence Time Measurements

The single-body coherence is typically measured using a Ramsey interferometry sequence, where we prepare a superposition of two rotational states and observe the decay of Ramsey contrast over time. With the magic light-shift condition, field stabilization, and the dynamical decoupling sequence in place, we set out to measure and optimize single-body coherence time of the rotational qubit. In doing so, we found an otherwise useful source of decoherence – dipolar interaction between neighboring molecules. For this measurement, we initially loaded molecules into a one-dimensional 40-site tweezer array with 5 μm spacing, the same nominal "interaction-off" spacing used in the early characterization of dipolar spin exchange in Sec. 7.2.2 (also see Ref. [9]). Even at this separation, neighboring molecules can interact at $J/h \sim 1.5$ Hz level, causing occupation-dependent phase shifts observed in the Ramsey contrast. Figure 6.5 (a, top) shows the neighbor-induced dephasing in the single-body rotational coherence measurement, where one can see molecules with one or two occupied neighbors show reduced contrast compared with molecules with no occupied neighbors, hinting that dipolar interaction is at play. Furthermore, this effect can also been observed in Figure 6.5 (a, bottom) where molecules in a rearranged, ordered array have higher probability of having occupied neighboring sites and therefore shows lower contrast due to interaction, compared to the not-rearranged array is likely to contain more isolated molecules.

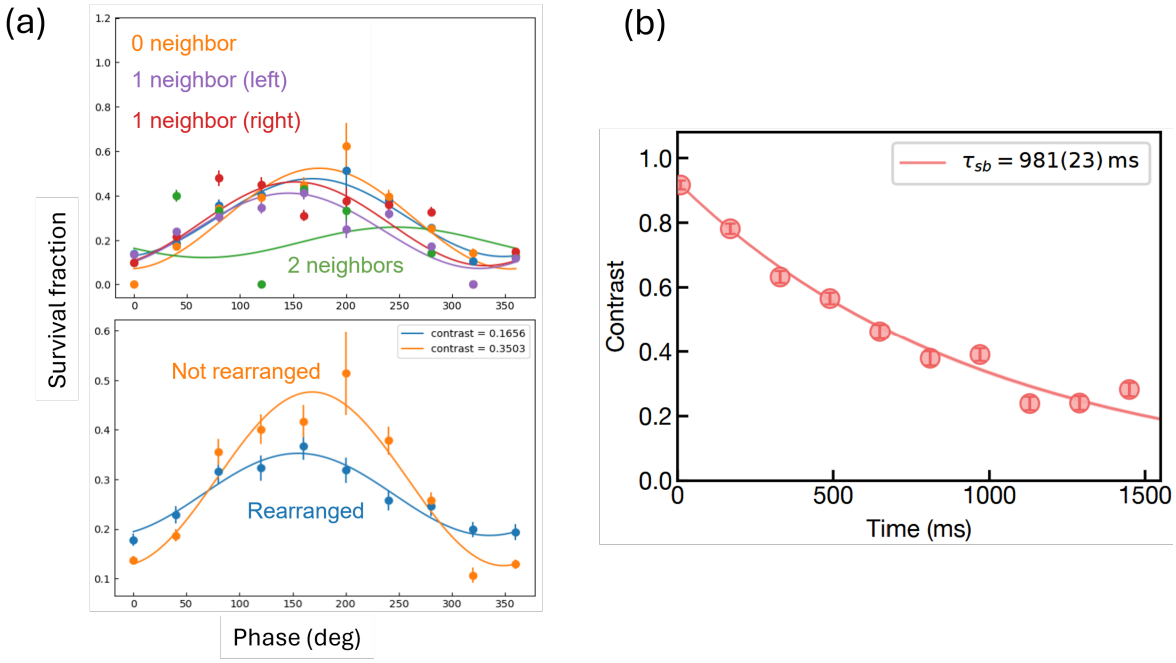


Figure 6.5: (a) Top: Ramsey phase contrast measurement sorted by number of occupied nearest-neighbor sites. Bottom: Comparison of Ramsey contrast between a stochastically loaded array and a re-arragnged defect-free array. (b) Extracted Ramsey contrast is shown as a function of interrogation time with an XY8 dynamical decoupling sequence. Solid curve shows an exponential decay fit $e^{-t/\tau_{sb}}$, giving single-body coherence $\tau_{sb} = 0.981(23)$ s.

To mitigate this effect, we rearrange molecules into an interleaved trap configuration, alternating between occupied and empty sites, effectively increasing the separation with neighboring molecules, while preserving the ability to take data with many molecules in parallel. This significantly reduces the interaction-induced dephasing. As shown in Figure 6.5 (b), the single-body rotational coherence time improves approximately from 0.6 s to 1.1 s. In the two-dimensional hybrid tweezer array, we measure a single-body coherence time T_2 of $\tau_{sb} = 0.981(23)$ s under the same XY8 decoupling protocol. This time is comparable for both the AOD and SLM tweezers.

The measured coherence time is approaching the few-second lifetime scale expected from room-temperature blackbody-radiation-induced vibrational excitation out of $v = 0$ [153, 218, 219], estimated to be $tau^{\mathrm{vib}}_{\mathrm{BBR}} \sim 3.5$ s for our system.

6.4 Cooling to Motional Ground State: Raman Sideband Cooling (RSC)

In the past two decades, Raman sideband cooling (RSC) techniques have been used to cool ions in traps [220] and neutral atoms in optical lattices and optical tweezers [221–225]. It is, however, generally challenging to cool a molecule in an optical trap in the absence of a narrow-line transition, as is the case with most (but not all [226]) laser coolable molecules.

In this section, we will show the RSC scheme we employ to bring CaF molecules in an optical tweezer array down to the motional quantum ground state: the lowest possible temperature in such molecular system.

6.4.1 Theory of Raman Sideband cooling

In many free-space laser cooling schemes, such as Doppler cooling, Sisyphus cooling, and gray molasses, the cooling force and the recoil heating both arise in the same optical cycle. Raman sideband cooling in optical traps takes a slightly different approach in that the cooling process is separated into a coherent step and a dissipative step. In a sufficiently tight trap, the motion of the trapped particle is quantized and can be spectrally resolved. A two-photon Raman transition is used to coherently lower the motional state while also changing the internal state. Spontaneous emission enters only afterward, during optical pumping which resets the internal state without changing the motional state, leaving the particle in the same internal state but with lower motional quanta. More specifically, Raman sideband cooling can be thought as an amalgamation of two processes: Raman transition in a three-level system and resolved sideband cooling (first demonstrated in ions [220]). Here we will go over these important ingredients.

6.4.1.1 Raman Transition in Three-level System

Consider the three-level Λ system in Fig. 6.6: two long-lived ground states $|1\rangle$ and $|2\rangle$; these could be hyperfine or Zeeman states of an electronic ground state), where each is coupled

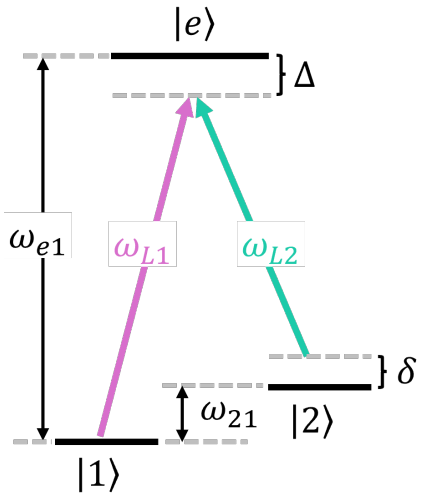


Figure 6.6: Three level in Λ configuration. Two states $|1\rangle$ and $|2\rangle$ separated by an energy $\hbar\omega_{21}$, and each is coupled by a laser field to a common excited state $|e\rangle$.

by a laser field to a common excited state $|e\rangle$. Field 1 (2), of frequency ω_{L1} (ω_{L2}) and wavevector $\mathbf{k_1}(\mathbf{k_=2})$, drives $|1\rangle \leftrightarrow |e\rangle$ ($|2\rangle \leftrightarrow |e\rangle$) with resonant Rabi frequency Ω_1 (Ω_2). Let the single-photon detuning from the excited state be Δ and the two-photon detuning between the laser difference frequency and the ground-state splitting be δ:

$$\Delta \equiv \omega_{L1} - \omega_{e1}, \qquad \delta \equiv (\omega_{L1} - \omega_{L2}) - \omega_{21},$$

and we work in the regime of large single-photon detuning, $|\Delta| \gg \Omega_1, \Omega_2, \Gamma, |\delta|$, where Γ is the natural linewidth of $|e\rangle$. With rotating-wave approximation (RWA) in the rotating frame of optical frequencies, the excited state can be adiabatically eliminated. The three-level system $|\psi\rangle = c_1 |1\rangle + c_2 |2\rangle + c_e |e\rangle$ can then described by an effective two-level Raman Hamiltonian,

$$\frac{H_{\text{eff}}}{\hbar} = \frac{\Omega_1^2}{4\Delta} |1\rangle\langle 1| + (-\delta + \frac{\Omega_2^2}{4\Delta}) |2\rangle\langle 2| + \frac{\Omega_{\text{R}}}{2} e^{i(\Delta\mathbf{kr}+\phi)} (|1\rangle\langle 2| + |2\rangle\langle 1|) \tag{6.6}$$

where $\mathbf{k} = \mathbf{k_1} - \mathbf{k_2}$ and $e^{i(\Delta\mathbf{kr})}$ is the spatial phase. This expression contains all the important pieces for the coherent step of RSC. First we have the two-photon effective Rabi frequency $\Omega_{\text{R}} = \frac{\Omega_1\Omega_2}{2\Delta}$, which sets the rate at which population coherently flops between $|1\rangle$ and $|2\rangle$. Second is the two differential AC Start (light) shift $\Omega_1^2/4\Delta$ and $\Omega_2^2/4\Delta$, which can shift the

two ground states differently, displacing the two-photon resonance to $\delta_{\text{eff}} = \delta - (\Omega_2^2 - \Omega_1^2)/4\Delta$. Lastly, we have spontaneous emission scaling at $1/\Delta^2$, since the excited state retains a small population $|c_e|^2 \sim (\Omega/2\Delta)^2$, the molecule scatters photons at a rate $\Gamma_{\text{sc}} \sim \Gamma\,\Omega^2/4\Delta^2$.

The relative scaling of these is what is crucial. The coherent coupling grows as $\Omega_{\text{R}} \propto \Omega^2/\Delta$, whereas the incoherent scattering falls as $\Gamma_{\text{sc}} \propto \Omega^2/\Delta^2$. The number of coherent Rabi cycles completed before a single photon is scattered is therefore [220]

$$\frac{\Omega_{\text{R}}}{\Gamma_{\text{sc}}} \sim \frac{\Delta}{\Gamma} \gg 1 \tag{6.7}$$

So practically, by increasing detuning and laser power together, one can retain a the Raman Rabi frequency while suppressing spontaneous emission during the coherent transfer. Equivalently, the effective linewidth of the two-photon transition is no longer the natural linewidth Γ of the transition, as it is now set by the Raman coupling and the interrogation time. This decoupling of the spectroscopic resolution from Γ is the feature that, in the next section, enables us to resolve motional structure on optical transitions whose linewidth vastly exceeds the trap frequency [227].

It is also worth noting that the two-photon coherence between long-lived states is a cornerstone technique on which a family of cooling mechanisms is built on, and that RSC is the part of this family adapted to a trapped particle. For example, velocity-selective coherent population trapping (VSCPT) builds a velocity-dependent dark superposition of ground states and accumulates population there, reaching sub-recoil temperatures without scattering at zero velocity [228, 229]. Gray-molasses and Λ-enhanced cooling also exploit this coherent dark states under a blue two-photon detuning to cool well below the Doppler limit, which is also the scheme we use for cooling CaF in traps. Raman cooling in free space, finally, uses velocity-selective two-photon transitions to remove momentum in discrete kicks [228].

.

6.4.1.2 Resolved Sideband

Now we consider putting a particle with that three-level system in a harmonic trap potential. Along each trap axis, the motion of a trapped particle is quantized into a ladder of harmonic oscillator states $|n\rangle$ with energies $E_n = \hbar\omega_t\,(n + \frac{1}{2})$, evenly spaced by the trap frequency ω_t. With this, the complete description of the quantum system now contains both internal and motional degrees of freedom, in form of product states $|i\rangle \otimes |n\rangle$ where $i = (1, 2, e)$ here. Therefore, when the internal transition $|g\rangle \to |e\rangle$ (or, for a Raman process, $|1\rangle \to |2\rangle$) is driven, the spectrum will have carrier at the transition frequency ω_0, flanked by motional sidebands displaced by integer multiples of ω_t: the red sidebands at $\omega_0 - \Delta k\,\omega_t$ lower the motional quantum number, the blue sidebands at $\omega_0 + \Delta k\,\omega_t$ raise it.

What couples the different motional states is the photon momentum. A transition is driven by light of effective wavevector Δk. This is the spatial phase carried in Raman transition in previous section, where $\Delta k = \mathbf{k}_1 - \mathbf{k}_2$. Experimentally this difference is set by two beam wavevectors projected onto the trap axis. Expressing the position operator in terms of ladder operators, $\hat{z} = z_0(a + a^\dagger)$ with $z_0 = \sqrt{\hbar/2M\omega_t}$, this phase becomes $e^{i\eta(a+a^\dagger)}$, where the Lamb–Dicke parameter,

$$\eta \equiv \Delta k\, z_0 = \Delta k \sqrt{\frac{\hbar}{2M\omega_t}} = \sqrt{\frac{E_{\mathrm{rec}}}{\hbar\omega_t}}, \qquad E_{\mathrm{rec}} = \frac{\hbar^2\Delta k^2}{2M}, \tag{6.8}$$

is defined as the ratio of the photon recoil energy associated with the Raman momentum transfer, E_{rec}, to the trap spacing $\hbar\omega_t$ [230]. Physically, it measures how strongly a photon kick changes the motional wavefunction, or equivalently, the recoil energy to the trap level spacing.

The strength of each sideband is determined by the matrix element $\langle m|\, e^{i\eta(a+a^\dagger)}\, |n\rangle$. For $\eta\sqrt{2n+1} \ll 1$ (the Lamb–Dicke regime), one can expand $e^{i\eta(a+a^\dagger)} \approx 1 + i\eta(a + a^\dagger) - \frac{\eta^2}{2}(a + a^\dagger)^2 + \cdots$, where first order terms give us three familiar transitions $|1, n\rangle \to |2, n\rangle$ (carrier), $|1, n\rangle \to |2, n-1\rangle$ (red sideband), and $|1, n\rangle \to |2, n+1\rangle$ (blue sideband), with corresponding Rabi frequencies:

$$\Omega_{n,n} \simeq \Omega_{\mathrm{R}}\big[1 - \eta^2(n + \tfrac{1}{2})\big] \quad \text{(carrier)}$$

$$\Omega_{n,n-1} = \Omega_{\mathrm{R}}\,\eta\sqrt{n} \;\; \text{(red sideband)}$$

$$\Omega_{n,n+1} = \Omega_{\mathrm{R}}\,\eta\sqrt{n+1} \;\; \text{(blue sideband).}$$

There are two important features to note here. First, all the n-changing transitions are suppressed by a factor of η relative to the carrier. This means that in Lamb–Dicke regime (ie. low temperature), transition that does not change the motional quantum number is much more favorable. This is what makes the dissipative step (i.e. optical pumping) of the cooling (discussed later) mostly preserving of n. Second, the red sideband transition carries a factor $\sqrt{n}$, and therefore it vanishes at $n = 0$, making the motional ground state the dark state.

For an initial thermal distribution starting outside of the Lamb–Dicke regime[231, 232], which is the case for our RSC cooling of CaF molecules as the molecules are hot ($\sim$ tens of μK), we need to include the full matrix element [227]:

$$\langle m|\, e^{i\eta(a+a^\dagger)}\, |n\rangle = e^{-\eta^2/2}(i\eta)^{|m-n|}\sqrt{\frac{n_<!}{n_>!}}L_{n_<}^{|m-n|}(\eta^2), \tag{6.9}$$

where $n_<$ ($n_>$) is the lesser (greater) of n and n', and L_n^α is a generalized Laguerre polynomial. Physically, the factor $e^{-\eta^2/2}$ and the Laguerre polynomial encode the full overlap of the displaced oscillator wavefunctions, so they are what allow higher-order sidebands ($|n - n'| > 1$) to be driven with appreciable strength, a fact we exploit in our cooling of CaF to remove several quanta per cycle since the molecules start warm.

Eq. 6.9 is also the basis of Raman sideband thermometry that is used to estimate the molecular temperature from the sideband spectrum. Since the red- and blue- sideband matrix elements scales $\Omega_{n,n-1}(n) \propto n$ and $\Omega_{n,n+1}(n) \propto n + 1$, respectively, in the sideband spectrum for a thermal distribution with mean motional occupation $\bar{n}$, the ratio of red-sideband peak to the first blue-sideband strengths is then:

$$\alpha = \frac{P_{\mathrm{red}}}{P_{\mathrm{blue}}} = e^{-\hbar\omega/k_BT} = \frac{\bar{n}}{\bar{n}+1}, \qquad \Rightarrow \bar{n} = \frac{\alpha}{1-\alpha}. \tag{6.10}$$

This gives us the mean motional occupation of the system along a trap direction. For three motional axes that are approximately separable and thermal, the three-dimensional ground-state probability is therefore:

$$P_{3\mathrm{D}} = P_{0,x}P_{0,y}P_{0,z} = \prod_i \frac{1}{1+\bar{n}_i} \tag{6.11}$$

Lastly, we will discuss the condition for resolving sidebands for effective cooling. To address an individual sideband we need to tell it apart from the carrier. Naturally, this means that the transition linewidth must be narrower than the sideband spacing set by the trap frequency ω_t. For a single-photon transition this is just the natural linewidth Γ, and the condition $\Gamma \ll \omega_t$ is found only by exceptionally narrow optical transitions, such as the forbidden quadrupole lines of trapped ions on which sideband cooling was first demonstrated [233]. As mentioned at the start of this Chapter, most laser-coolable molecules, including CaF do not have narrow-line optical transitions (see Ref. [226] for an exception). The broader transitions in molecules have the natural linewidth are of several megahertz, while optical trap frequencies are tens to hundreds of kilohertz. So how does one get around this impasse? We come back to the stimulated Raman transition elaborated in Sec 6.4.1.1. The effective linewidth in the Raman transition is set to the two-photon coupling and the off-resonant scattering rate $\Gamma_{\mathrm{sc}} \sim \Gamma\,\Omega^2/4\Delta^2$, which can be made arbitrarily small. This means one can resolve motional sidebands at $\omega_t \ll \Gamma$ on an otherwise broad transition simply by detuning the Raman lasers far enough [227].

6.4.1.3 Raman Sideband Cooling Cycle and Limit

A Raman sideband cooling cycle typically consists of two key steps. First, in the coherent step, motional-sideband-resolved two-photon Raman transition is driven. The Raman beams are tuned to a red motional sideband reducing the motional quantum number $|n\rangle$ by driving: $|1,n\rangle \rightarrow |2,n-1\rangle$.

This step alone does not do much because it is reversible, driving essentially a Rabi oscillation of the population. Cooling requires dissipation, and this is supplied by the next step: optical pumping: $|2,n-1\rangle \rightarrow |1,n-1\rangle$, which restores the original internal state while entropy is

carried away by the spontaneously emitted photon. Repeating the cycle ratchets the molecule down the motional ladder until it reaches $|1, n = 0\rangle$ which is dark, as the matrix element that couples it is $\sqrt{n}$ becomes zero.

The Raman sideband cooling does not reach $n = 0$ exactly. There is recoil heating of motion that accompanies every scattered photon during optical pumping, and also off-resonant excitation of the carrier and the blue sideband [230, 231]. In the resolved-sideband, Lamb–Dicke limit this minimum mean phonon number, to leading order, $\bar{n}_{\min} \approx (\frac{\Gamma}{2\omega_t})^2 \ll 1$. So if the sidebands are well resolved the ground state is occupied with high probability [220].

6.4.2 RSC Implementation for Motional Ground-State Preparation

Starting from molecules prepared in a single internal state, we apply Raman sideband cooling to reduce their motion to near the three-dimensional ground state of the tweezer trap. The basic cooling cycle follows the standard demonstrated resolved-sideband cooling technique explained above: a Raman transition first coherently transfers population between two ground states differing in motional state $\Delta n < 0$ to remove motional energy, and an optical-pumping step dissipatively returns the molecule to the initial internal state. Repeating this cycle accumulates population in a motional dark state, at which point (ie. $n = 0$) coupling matrix element to the red sideband drive is zero.

Applying this to molecules in optical traps is complicated by the large number of internal states and differential Stark shifts induced by trap light. As there are a large number of ground states in molecules, and RSC cycle is repeated many times, spontaneous emission during optical pumping can populate molecules into multiple ground states. Even small leakage out of the cycle into unaddressed states can accumulate into appreciable loss. In addition, many photons are required to be scatted during optical pumping, and each additional scattered photon contributes to recoil heating. Furthermore, differential AC Stark shifts in the tweezer can also broaden the Raman transition enough to obscure the motional sidebands.

Our experimental approach follows the strategy proposed in Ref. [234] and our initial experimental results have been elaborated in Ref. [194]. The idea is to work at a large magnetic

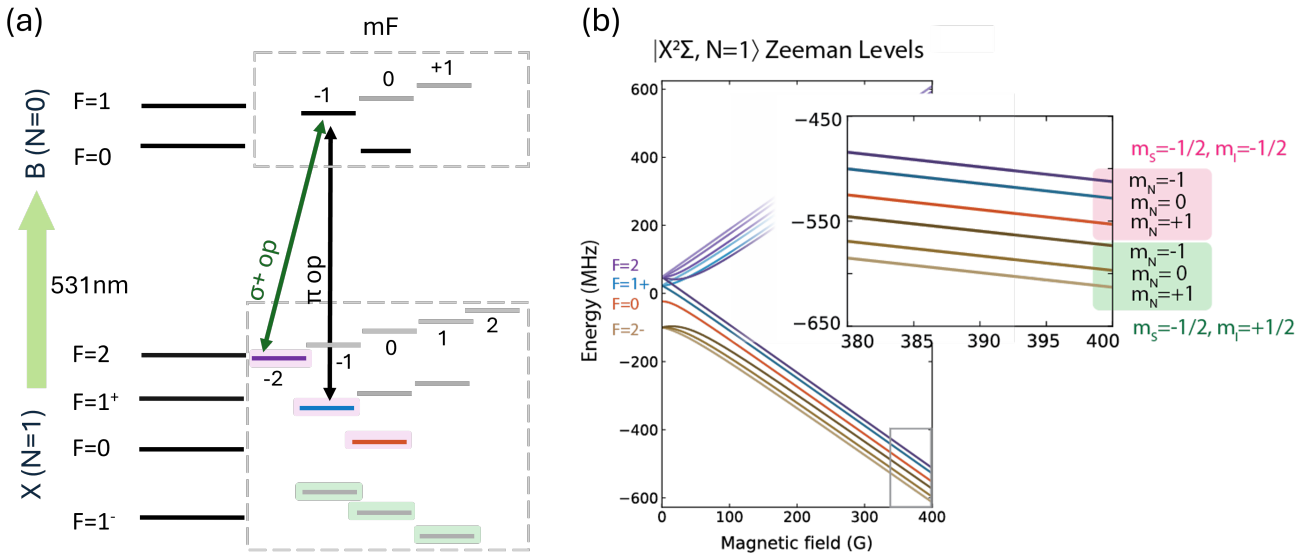


Figure 6.7: (a) Relevant hyperfine and Zeeman states in the $X^2\Sigma(v=0, N=1)$ and $B^2\Sigma(v=0, N=0)$ states of CaF at low field. **(b)** Zeeman energy levels in $X^2\Sigma(v=0, N=1)$ manifold as a function of magnetic field strength. The relevant spin manifolds for Raman sideband cooling are highlighted in red and green.

field, on the order of several hundred Gauss, to decouple the electron spin S and nuclear spin I from the molecular rotational angular momentum N, and choose a pair of states with nearly matched light shifts. In the high-field limit, the states can be approximately described using the uncoupled basis $|S, m_S\rangle |I, m_I\rangle |N, m_N\rangle$ (or $|m_N, m_S, m_I\rangle$ for short), and optical transitions that change m_I or m_S are strongly suppressed. This significantly reduces the number of states involved and confines us primarily to one of the two spin manifolds $|m_S = -1/2, m_I = \pm 1/2\rangle$ in $X^2\Sigma(v=0, N=1)$, leaving only the three rotational-projection states $m_N = 0, \pm 1$ as the relevant ground states. Figure 6.7 (a) shows all twelve of the hyperfine and Zeeman states in $X^2\Sigma(v=0, N=1)$, where (F, m_F) quantum numbers are good at low field. The Zeeman energy levels of these states at higher magnetic fields are shown in Figure 6.7 (b), with the two relevant spin subspaces used in our RSC scheme highlighted.

For linearly polarized trap light, the tensor Stark shift depends on m_N^2, scaling as $\propto \alpha_2 \left(3m_N^2 - N(N+1)\right)$. The two ground states we choose to use in Raman transition are $|m_N = \pm 1\rangle$ in the $(m_S = -1/2, m_I = -1/2)$ manifold; at low field, there are the $|F = 1+, mF = -1\rangle$ and $|F = 2, m_F = -2\rangle$ states, respectively. This pair of states has nearly matched light shifts, as

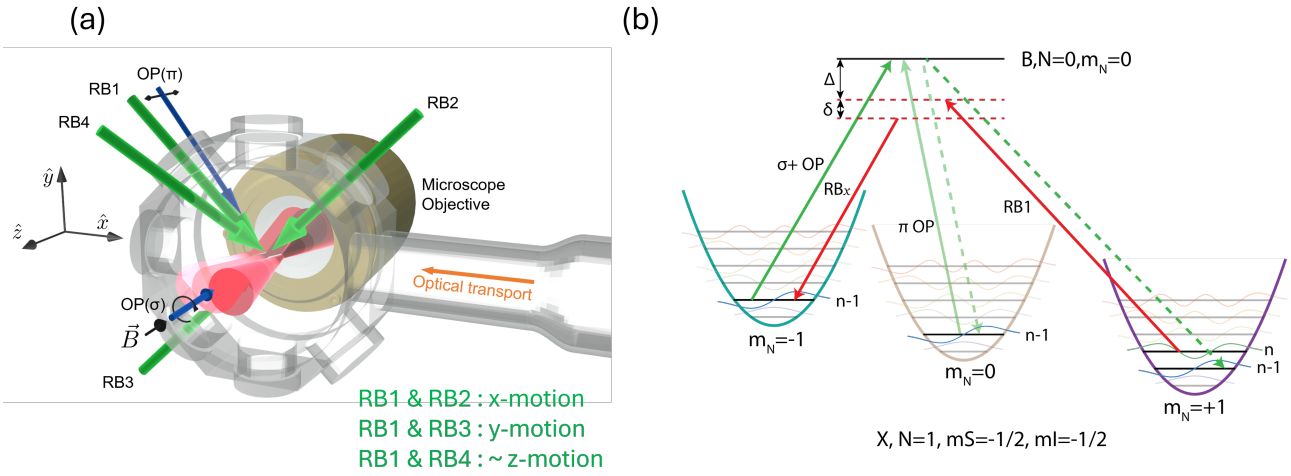


Figure 6.8: (a) Configuration of Raman beams and optical pumping beams used in the Raman sideband cooling experiment. RB1 and RB2 address the radial motion in x-direction, RB1 and RB3 address the radial motion in y-direction and RB1 and RB4 mainly address the axial motion in z-direction. RB1 path is also be employed to drive a motion-insensitive Raman π pulse for population swapping between $|m_N = \pm 1\rangle$ states. **(b)** Motional eigenstates $|n\rangle$ in a harmonic trap. Red arrows labeled RB1 and RBx ($x = 2, 3$ or 4) represent the Raman transition driven to lower the motional quantum number n by 1 for a specific trap axis and the green arrows labeled OP represent the $\sigma+$ and π optical pumping transitions and the dashed green arrow indicates the spontaneous emission (decay to $m_N = -1$ not shown). Note the negative sign in front of the Raman two-photon detuning δ, indicating cooling sidebands have a negative δ value.

they share the same m_S and m_I, and their tensor Stark shifts are equal to leading order because they have the same $|m_N|$. The excited state use is the $|m_N = 0\rangle$ in $(m_S = -1/2, m_I = -1/2)$ manifold of $B^2\Sigma$ electronic state. We use the $X-B$ optical transition because the Franck-Condon factors of the transitions between the $X^2\Sigma$ and $B^2\Sigma$ for CaF are highly diagonal (around 0.998), so the loss into excited vibrational states is minimal.

To begin the cooling, we use the state preparation procedure elaborated in Sec. 6.2 to initialize the molecules in $|\uparrow\rangle$. We then ramp the trap depth from $\sim k_B \times 1.3\,\mathrm{mK}$ to $\sim k_B \times 220\,\mu\mathrm{K}$, adiabatically bringing the molecules from $\sim 60\,\mu\mathrm{K}$ to $\sim 30\,\mu\mathrm{K}$. Then we reduce the applied bias field to zero, and simultaneously ramp on a high magnetic field $B_{\mathbf{RSC}}$ along $\hat{z}$ to adiabatically rotate the quantization axis. The $|\uparrow\rangle = |X; N = 0, F = 0, m_F = 0\rangle$ in low field now becomes the RSC dark state $|m_N = +1\rangle$ in $(m_S = -1/2, m_I = -1/2)$ spin manifold (see Fig.6.7 (b)).

Raman beams detuned from the $X^2\Sigma(v = 0, N = 1) \rightarrow B^2\Sigma(v = 0, N = 0)$ transition then drive a two-photon transition between $|m_N = +1\rangle$) and $|m_N = -1\rangle$, as indicated by the RSC

cycle shown in Figure 6.8 (b). By setting the two-photon detuning to a red motional sideband, this pulse transfers

$$|m_N = +1, n\rangle \rightarrow |m_N = -1, n - \Delta n\rangle\,, \tag{6.12}$$

where $\Delta n > 0$ is chosen according to the sideband being addressed. The RSC mechanism fundamentally relies on the momentum kick imparted in the Raman transition step, which lies in the direction defined by the difference of the **k**-vectors between two Raman beams. The difference **k** of the Raman beams therefore picks out the motional axis to be cooled. In our experimental beam geometry, we use three pairs of laser beams separated by special angles, as schematically shown in Figure 6.8 (a), where different Raman-beam pairs address the two radial directions and the weak axial direction of the harmonic potential. Four beams in total are employed (indicated as RB$1-4$), where combination of (RB1 & RBx, $x = \{2, 3, 4\}$) address the three orthogonal motional axes of the trap.

In the initial implementation, we use a magnetic field of $B_{\mathrm{RSC}} \approx 200$ G, set mainly by the 100 A current rating of the high-current solid-state relay (SSR,D1D100, Crydom) used to switch the high-field coils. This field corresponds to a coil drive current of approximately 90 A). All beams are set to have a single photon detuning of $\Delta \approx 2\pi \times 44\,\mathrm{GHz}$, red-detuned from the $|X^2\Sigma, N = 1\rangle$ to $|B^2\Sigma, N = 0\rangle$ transition, and each is separately prepared with an acousto-optical modulator (AOM) to define both its frequency and intensity. The two arms of each pair of beams are set with a frequency difference $\sim 41\,\mathrm{MHz}$ (defined as the carrier frequency), chosen to match the energy difference between the RSC ground states, $|m_N = \pm 1\rangle$, at B_{RSC}. All the Raman pulses in the RSC sequence are later programmed to have Blackman amplitude profile, which helps to reduce off-resonant driving and helps to resolve closely spaced sidebands.

In the optical-pumping step, two beams resonant with the $X^2\Sigma(v = 0, N = 1) \rightarrow B^2\Sigma(v = 0, N = 0)$ transition are applied, one with σ^+ polarization and the other with π polarization. The π polarized transition is driven to prevent accumulation of population in the $|X^2\Sigma, N = 1, m_N = 0\rangle$ state during OP. These beams pump population from $m_N = -1$ and

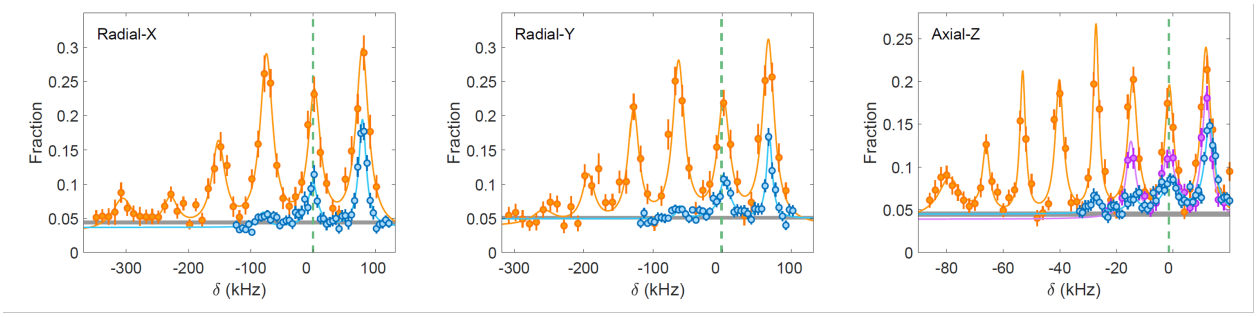


Figure 6.9: Raman sideband thermometry spectra for radial x direction, radial y direction, and axial z direction, respectively. Blue curves are the spectra obtained after RSC, orange curves are the spectra obtained before RSC. For the axial z direction, an additional purple curve represents the spectrum obtained without the last step of RSC applied (partial cooling). Green dashed line indicates the carrier frequency for each spectrum. Gray bands indicate the baseline for the spectra measured at far detuned limit.

$m_N = 0$ back into the dark state $|m_N = +1\rangle$, while ideally preserving the motional quantum number.

We characterize the motional state using Raman sideband thermometry (RST), based on the same Raman transitions used for cooling. A Raman pulse of fixed duration transfers population from $|m_N = +1\rangle$ to $|m_N = -1\rangle$, after which the transferred population is measured with state-sensitive detection. By scanning the two-photon detuning δ, we obtain a sideband spectrum containing a carrier peak at $\Delta n = 0$, together with cooling sidebands at lower frequency ($\Delta n < 0$) and heating sidebands at higher frequency ($\Delta n > 0$). For a thermal distribution, the mean motional occupation can be extracted from the asymmetry between the first cooling and heating sidebands. Defining α as the ratio of the first cooling-sideband amplitude to the first heating-sideband amplitude, $\bar{n} = \alpha/(1-\alpha)$ (see Sec. 6.4.1.2 for derivation). This means that strong suppression of the cooling sideband relative to the heating sideband is the good signature of a near ground state.

We record the RST spectra before and after applying RSC, and the results are presented in Figure 6.9. Motional sidebands are resolved along all three trap axes (Fig. 6.9, orange data), allowing us to determine the trap frequencies used in the cooling sequence: $\omega_x = 2\pi \times 75(1)$ kHz, $\omega_y = 2\pi \times 65(2)$ kHz, and $\omega_z = 2\pi \times 13.6(3)$ kHz. Note that the carrier transition has a magnetic-field sensitivity of approximately 10 kHz/G, so with a measured current noise of

24 m A rms corresponding to $\sim$ 50 mG RMS field noise, there is about 500 $\mathrm{Hz_{rms}}$ carrier frequency noise.

The spectra contain cooling sidebands up to $\Delta n = -4$ in the radial directions and $\Delta n = -6$ along the axial direction. Experimentally, with molecules starting at $\sim 30\,\mu$K, the cooling begins far outside the Lamb-Dicke regime, especially along the axial direction. So the sequence first addresses higher-order red sidebands to remove several motional quanta per optical pumping step. Once the distribution is colder, the sequence switches to lower-order sidebands to finish the cooling. The complete RSC sequence can be found in the supplementary material of Ref. [194].

After the RSC sequence, the sideband spectra show a strong suppression of the cooling sidebands relative to the heating sidebands along all three directions (Fig. 6.9, blue data). From the sideband asymmetry, we extract mean motional occupations of $\bar{n}_x = 0.16(12)$, $\bar{n}_y = 0.17(17)$, and $\bar{n}_z = 0.22(16)$, corresponding to a three-dimensional motional ground-state probability of $54 \pm 18\%$ for the molecules that survive the cooling sequence.

6.4.3 Improved RSC Implementation for Molecule Survival

The experimental groundwork above was developed for molecules trapped in a 1D tweezer array generated by a single AOD, where the main focus was to demonstrate a high ground state preparation fraction. For coherent interaction experiments discussed later in Chap. 7 and 8, the relevant figure of merit is interaction coherence, rather than to maximize remaining population in the motional ground state alone.

For flexible geometric engineering of the interaction, molecules are now trapped in a hybrid 2D array generated from two independently propagated beam paths. The relative focal alignment of the two traps in an interacting pair can drifts on a timescale much slower than an interaction period. Having a low number of surviving molecules after sideband cooling leads to longer data-taking time needed for each interaction measurement, over which a wider range of differential focal shifts is sampled, resulting in unwanted dephasing in the measured coherence. By preserving more molecules after cooling, we reduce the acquisition time required for a given statistical precision. With this consideration, we look into ways to reduce loss by reducing

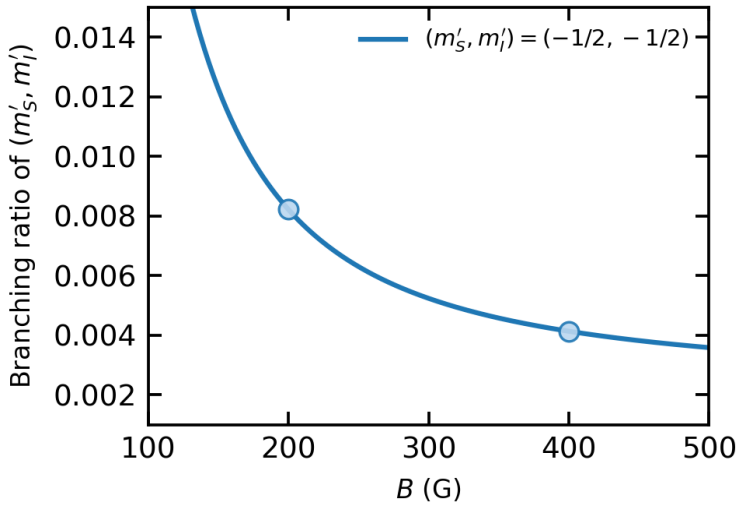


Figure 6.10: Calculated magnetic-field dependence of branching ratio for spontaneous decay out of $|B, N' = 0, (m_S' = -1/2, m_I =' -1/2)\rangle$ into other spin manifolds in $X^2\Sigma^+(v = 0, N = 1)$. At each magnetic field, the X and B state Hamiltonian are diagonalized with eigenstates labeled by (m_S', m_I'). The branching ratio is then calculated by summing the electric-dipole strengths over photon polarizations and over all $X, N = 1$ states with (m_S, m_I) different from the initial state, normalized by the total decay strength to $X, N = 1$. Calculated following Ref. [234].

spontaneous decay loss during optical pumping and optimizing RSC pulse sequence.

	200 G	350 G
$\lvert X, N = 0; (m_S, m_I)\rangle$	$b_{200\mathrm{G}}$	$b_{350\mathrm{G}}$
(Target) $(-1/2, -1/2)$	0.99178	0.99542
$(-1/2, +1/2)$	6.81×10^{-3}	4.07×10^{-3}
$(+1/2, -1/2)$	1.33×10^{-3}	4.89×10^{-4}
$(+1/2, +1/2)$	7.26×10^{-5}	1.85×10^{-5}
Total branching ratio	8.22×10^{-3}	4.58×10^{-3}

Table 6.1: Comparison of branching ratios for spontaneous decay from $B^2\Sigma^+(N' = 0)$ state spin manifold $\left|(m_S' = -\frac{1}{2}, m_I = -\frac{1}{2})\right\rangle$ to all the spin manifolds in $X^2\Sigma^+(N = 1)$ state, at 200 G and 350 G.

In the initial implementation at $B_{\mathrm{RSC}} \approx 200$ G, nearly half of the molecules are lost after full RSC due to accumulated population leakage during repeated optical pumping. In each RSC cycle, optical pumping (OP) scatters photons as population returns from the $\left|m_S' = -\frac{1}{2}, m_I' = -\frac{1}{2}\right\rangle$ manifold in $B^2\Sigma^+(v' = 0, N' = 0)$ to the $\left|m_N = +1; (m_S = -\frac{1}{2}, m_I = -\frac{1}{2})\right\rangle$, the optical pumping dark state, in $X^2\Sigma^+(v = 0, N = 1)$. In the ideal case at high-field, the scattering would conserve m_S and m_I. But as we are working with real molecules, residual hyperfine

mixing gives the monomial eigenstates small admixtures of other spin manifolds. Figure 6.10 shows the probability for spontaneous decay from excited state in $|m'_S = -1/2, m'_I = -1/2\rangle$ to different spin manifolds in $X^2\Sigma^+(v = 0, N = 1)$. At $B_{\mathrm{RSC}} \approx 200$ G, the leakage out of $|m'_S = -1/2, m'_I = -1/2\rangle$ is $b_{200\mathrm{G}} \simeq 8.2 \times 10^{-3}$ per spontaneous decay. Including the $X - B$ Franck-Condon factor of $f_{00}^{X-B} \sim 0.998$ gives a total loss probability of order $1 - f_{00}^{X-B}(1 - b) \sim 10^{-2}$ per scattered photon. The total loss due to OP can be estimated by the number of photons scattered, $N_{\mathrm{sc}} = N_{\mathrm{OP}}\bar{n}_{\mathrm{sc}}$, where N_{OP} is the number of applied OP pulse and $\bar{n}_{\mathrm{sc}}$ is the mean number of scattered photons per OP pulse. A completed OP step scatters on average three photons (assuming equal branching of the $B^2\Sigma(N' = 0)$ excited state into three $|m_N = 0, \pm 1\rangle$ states), with each applied pulse scattering $\bar{n}_{\mathrm{sc}} \approx 0.2$ photon. This means, in our case, a full sequence containing on the order of $N_{\mathrm{OP}} \approx 300$ OP pulses scatter total of $N_{\mathrm{sc}} \sim 60$ photons, incurring $\sim 1 - (1 - 0.01)^{(90\times 0.3)} = 45\%$ loss. Most of these leaked molecules end in the $\left|(m'_S = -\frac{1}{2}, m_I = +\frac{1}{2})\right\rangle$, as shown in Table 6.1.

To reduce this loss, we decided to operate at a higher $B_{\mathrm{RSC}} \approx 350\,\mathrm{G}$, where the predicted leakage to other (m_I, m_S) subspaces is smaller by a factor of 2 (see Table 6.1). What to do with the 100 A-rated SSR for the coils that was limiting the B_{RSC} to 200 G in the first place? We accidentally set it on fire so we have to just bypass it. With (or rather without) that, the high field is easily accessible as our magnetic coil pair is designed to reach fields up to approximately 420 G with a 200 A current supply. However, upon increasing the magnetic field experimentally, we found the optical-pumping dark state $|m_N = +1\rangle$ became substantially less stable. To better isolate the origin of this effect, we measured the state darkness separately with the two optical-pumping beams. The state darkness with σ^+ beam on shows no obvious dependence on the B_{RSC} strength, while the π beam leads to a strong field-dependent de-pumping, as shown in the data in Figure 6.11.

We first investigated potential technique effects that might arise at higher fields, such as birefringence along the optical-pumping beam path. To compensate any arbitrary, unknown polarization rotation introduced by birefringence on the glasscell chamber, we use a combination of polarizing elements: polarizer–QWP–HWP–QWP, with the last two waveplates mounted

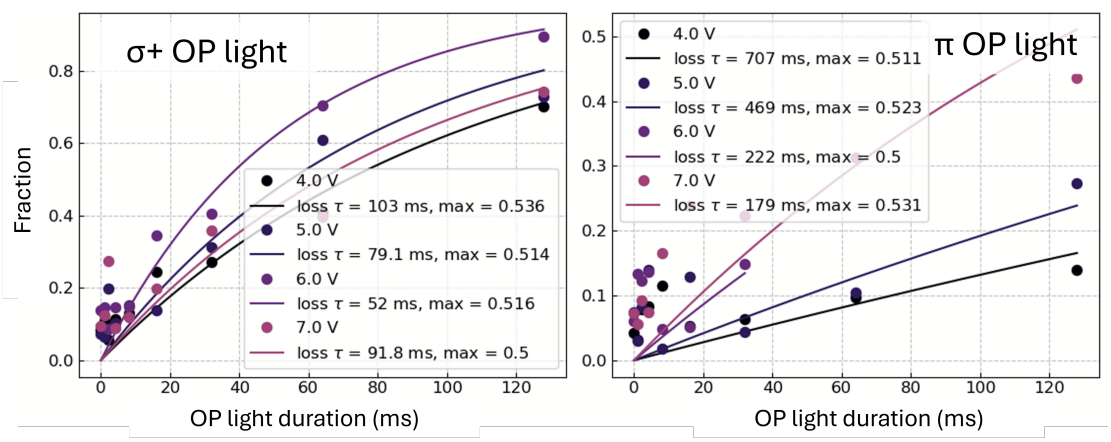


Figure 6.11: Debugging de-pumping rate out of optical pumping dark state $|m_N = +1; (m_S = -\frac{1}{2}, m_I = -\frac{1}{2})\rangle$ with σ^+OP light and π OP light on separately, at different magnetic fields. Here 4V corresponds to 200G and 7V is 350G. The stark darkness is strongly dependent on magnetic field strength with π OP on.

on motorized waveplates; this combination can be implemented for any SO(3) rotations of polarization state on the Poincare sphere. Alas, the effort with extensive polarization control was futile. We further tested the sensitivity to small transverse magnetic field that might have become appreciable at higher field, as well as checked field gradients, ramp-induced transients, and other magnetic-field-induced birefringence. None of these effects helped to restore the target state darkness.

The origin of this was traced to the molecular structure. The π-polarized optical pumping light is intended to drive population out of $m_N = 0$ to prevent molecules accumulating there during cooling cycle. At higher field, the coupling between the the nominal OP dark state $|m_N = +1\rangle$ to the a state in the neighboring spin manifold $|m_N = -1; (m_S = -1/2, m_I = 1/2)\rangle$ becomes appreciable, such that it can be weakly coupled by the π-polarized light, pumping molecules out of our target dark state. Fig. 6.12 (a) schematically shows the connected states, and Fig. 6.12 (b) shows the coupling strength between these two states as a function of magnetic field strength. We can clearly see that the coupling is highly suppressed around 200 G, but much larger at 350 G; so being unaware of this we happened to hit a lucky spot previously. This coupling can be made immediately evident by going back to looking at the states at low field, as shown in Fig. 6.13.

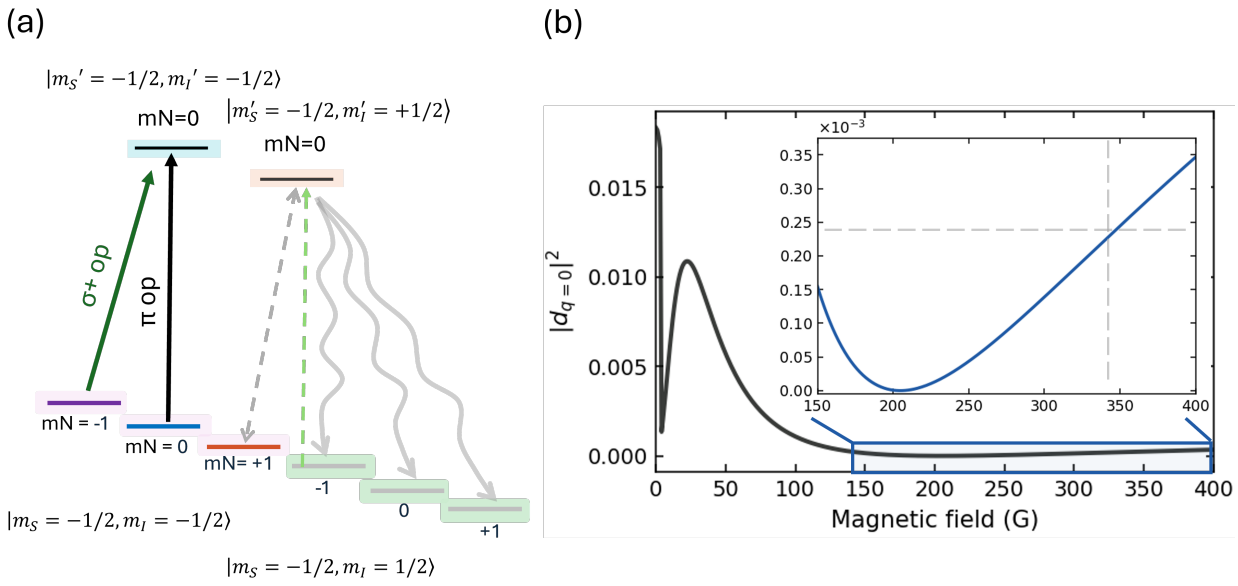


Figure 6.12: (a) Relevant m_N states at high field in the $(m_s = -\frac{1}{2}, m_I = \pm\frac{1}{2})$ spin manifolds of ground state $X^2\Sigma(N = 1)$. The solid arrows connect the transitions intended to be driven by optical pumping light. The gray dashed arrow indicates the weak coupling induced by π OP light, and wavy arrow indicates spontaneous decay. The dashed green arrows indicate the states affected by the σ^+ OP light. (b)π-polarized transition dipole strength (dimensionless) for the $X^2\Sigma^+(N = 1) \rightarrow B^2\Sigma^+(N' = 0)$ transition in CaF. The plotted quantity is the $|\langle B_i(B)|d_{q=0}|X_j(B)\rangle|^2$, in units of the body-frame $X - B$ transition dipole moment squared.

Once molecules get inadvertently excited into $|m_N = 0\rangle$ of $(m'_S = -\frac{1}{2}, m'_I = +\frac{1}{2})$ spin manifold of $B(N' = 1)$ state, they can spontaneously decay and distribute over all three m_N of lower spin manifold of $X(N = 1)$, as indicated by the arrows in Fig. 6.12 (a). Of these three states, the population $|m_N = -1\rangle$ state can be affected by the σ^+ OP light, as it is close to resonance and contains the right polarization, and get de-pumped, leaving the molecules to pile up in the other remaining two states $|m_N = 0, +1\rangle$ $(m_S = -\frac{1}{2}, m_I = +\frac{1}{2})$.The corresponding coupled states in low field $|F, m_F\rangle$ basis is shown in Fig. 6.13. We experimentally confirmed this with state-resolved microwave spectroscopy. After preparing molecules in the original $m_N = +1$ dark state, we applied only the π-polarized OP light for a variable duration and then shelved population in the leakage state $|m_N = -1\rangle$ $(m_S = -\frac{1}{2}, m_I = +\frac{1}{2})$ for detection. The observed population transfer into the leakage state indeed increases with the π OP duration, and population is reduced when the full σ^+, π optical-pumping sequence was applied, consistent with the picture that the π beam was weakly coupling molecules out of the OP dark state while

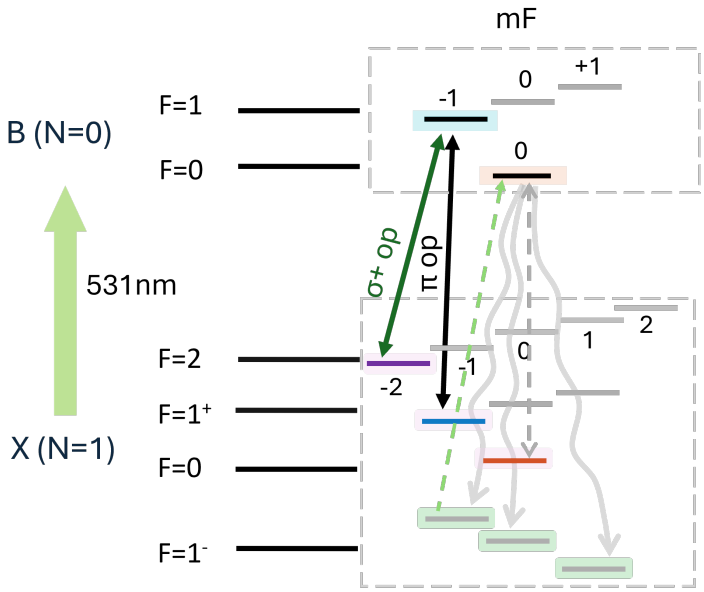


Figure 6.13: The corresponding connected states and coupling involved in higher-field RSC scheme shown in low-field basis regime.

the σ^+ beam partially repumped the leaked population.

To mitigate this loss, we interchange the roles of the two Raman states for cooling and optical pumping, and designate the $|m_N = -1\rangle$ state as the optical-pumping dark state. We begin in $|m_N = +1\rangle$ after state preparation, optically pump population into $|m_N = -1\rangle$, which is cleaner coupling at high fields. After cooling, a high-fidelity Raman carrier π pulse transfers the population back to $|m_N = +1\rangle$ for the subsequent dipolar interaction.

With this modified state choice, we re-calibrate the optical pumping frequencies and optimize the polarization purity of both OP beams. With a typical 50 μs per OP pulse and 280 total pulses applied during entire RSC sequence (i.e. 14 ms of total optical pumping light), we find there is negligible leakage out of the dark state. The measured survival probability for our modified sequence after full cooling is $\sim 65\%$ (in addition to vibrational loss), compared with 50% in the initial implementation.

6.4.3.1 Partial Raman Sideband Cooling

In our improved RSC implementation that prioritizes having higher number of surviving molecules, we do not require the full ground state optimized cooling sequence. In fact, it is more important for us to reduce the motional width relevant for dipolar dephasing, rather than increasing the ground state fraction as it could result in a broader, non-thermal distribution. Therefore we use a partial cooling sequence that balances reducing the motional width and preserving molecule number.

Since the CaF molecules trapped in tweezers are far outside the Lamb–Dicke regime, a fixed-order sideband-cooling sequence can leave population in motional states that are only weakly coupled to the selected Raman transitions. This can be seen from Eq. 6.9, where coupling of motional states with the first red sideband scales as $\eta\sqrt{n}$ at low temperature regime. But outside the Lamb-Dicke regime, the sideband matrix elements and detunings vary strongly across the distribution, passing through nodes once $\eta\sqrt{n} \gtrsim 1$ (as the form contains a generalized Laguerre polynomial). Therefore some high-n states are only weakly or off-resonantly coupled by a given pulse. These motional dark states can continue to scatter photons during later optical pumping steps, producing a non-thermal high-n tail even as population accumulates near low n.

This is particularly apparent for partial sideband cooling sequences. Simulations (see Fig. 6.14 for one example), show that such sequences can accumulate substantial population at low n while leaving a long high-n tail from weakly coupled motional states. In this regime, the mean occupation $\bar{n}$ can be strongly influenced by the tail, and can even increase despite a clear growth of the low-n population. In other words, Raman sideband cooling is state-selective and non-thermal process: it transfers population between specific motional states and then applies optical pumping, without any mechanism that rethermalizes the distribution. The resulting distribution is generically non-thermal, the more so for sequences containing many pulses with high-order-sideband, such as the one used here, and for motion outside the Lamb–Dicke regime [231, 235].

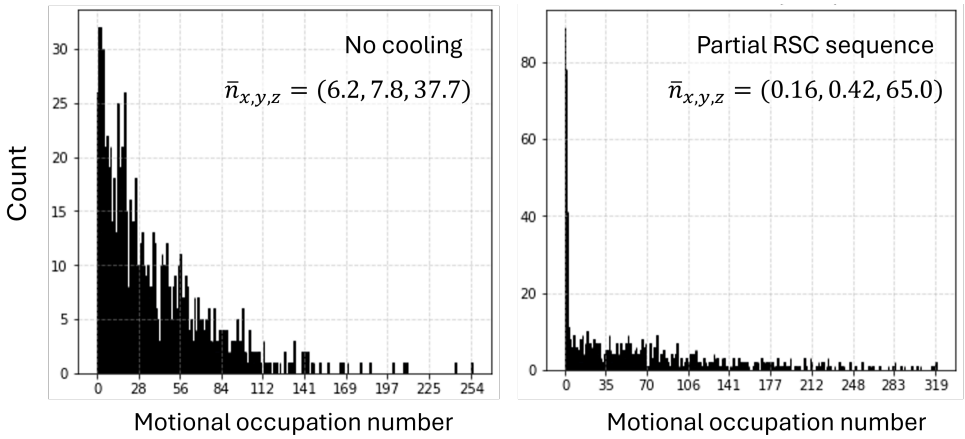


Figure 6.14: Histogram of simulated axial (z) motional distributions before (left) and after (right) a partial Raman sideband cooling sequence. The sequence transfers substantial population into low-lying motional states, especially in the radial directions, but also produces a long high-n_z axial tail from weakly cooled states and optical pumping recoil. Of 1000 simulated molecules, 839 survive the sequence.

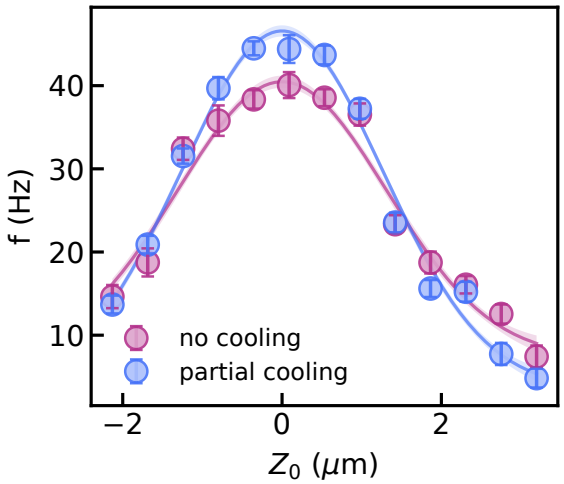


Figure 6.15: Signatures of reduced motional excitation after Raman sideband cooling Interaction frequency as a function of axial displacement, with and without partial sideband cooling applied.

We therefore employ a modified partial cooling sequence where we begin with higher-order axial sideband cooling pulses to remove a large number of motional quanta, $\Delta n_z = 10$, along the weakly confined z axis, efficiently reducing the energy of the initially broad axial distribution. As the distribution narrows, we progressively reduce the axial sideband order Δn_z, while sparsely interspersing radial cooling pulses for x and y axes. Finally, we terminate the sequence at $\Delta n_z = 5$ and $\Delta n_{x,y} = 2$. We estimate the final motional occupation using Monte Carlo

simulations of the cooling sequence. For the axial direction, the simulated distribution peaks at $n_z = 6$, with 72% of the population occupying states with $n_z < 12$.

To more directly probe the effect of sideband cooling, we measure the dipolar interaction frequency as a function of relative axial displacement z_0 between two molecules at an angle of $\theta = 0$. We observe the population $P(z_0) \sim \cos(\phi(z_0))$ and convert the fitted phase to interaction frequency through $f(z_0) = \phi(z_0)/2\pi t_{\text{int}}$. The data in Fig. 6.15 show two clear signatures of reduced motional excitations: partial Raman sideband cooling increases the interaction frequency and narrows the axial response profile. This measurement also provides intuition for the magic condition, which occurs roughly at the point where the two curves intersect. At this point the interaction rate has reduced sensitivity to the underlying motional distribution.

In theory, there is no difference between practice
and theory. In practice, there is.

Benjamin Brewster

7

Geometric Engineering of Dipolar Interactions

Work in this Chapter, including portions of the text and figures, has been distributed as publications [9], [60], and as a preprint [80] undergoing peer review as of the time of submission.

7.1 Overview

A central requirement for using polar molecules for quantum simulation and quantum information processing is the ability to generate coherent entangling interactions between molecules. This capability complements the other basic ingredients of a quantum platform: state preparation, single-qubit control, and state-resolved readout. Having established these single-qubit controls for individual CaF molecules in Chapter 6, this chapter turns to the interaction between molecules.

The intrinsic electric dipole-dipole interaction in molecules was first observed with KRb molecules in optical lattices [19] and has since been extended to lower-dimensional gases, molecular quantum gas microscopes, and tweezer arrays of individually controlled molecules [9–11, 22, 56]. In chapter 2.1, we introduced the origin of the electric dipole-dipole interaction between two molecules, and the diverse range of quantum simulation and quantum information processing enabled by it. In this chapter, we begin by describing how we measure dipolar dynamics between pairs of CaF molecules in our 1D tweezer apparatus, which was the first experimental observation of dipolar spin exchange between individual CaF molecules. This experiment established the defining signatures of the interaction, including its distance and angular dependence, but also revealed the limitation that the coherence time of dipolar interactions is limited by the finite temperature of the molecules in the optical traps.

In sections 7.4- 7.7, we investigate this thermal dephasing mechanism in greater detail and develop experimental techniques of both static and dynamic geometrical control in 3D to control and improve dipolar coherence. This includes: 1) static geometry engineering to suppress thermal dephasing by realizing interaction configurations that minimize sensitivity to motional fluctuations, and 2) a dynamic geometric echo protocol that can refocus dephasing arising from relative trap-position fluctuations. In the process, we upgraded our tweezer architecture to a hybrid 2D array generated using both SLM and AOD (described in Chapter 4.2) to access control of the interaction geometry in three dimensions.

7.2 Dipolar Spin-Exchange in 1D Array of CaF

7.2.1 Procedure and Experimental Sequence

With rotating-wave approximation, the resonant part of the dipole-dipole interaction is:

$$H_{\mathrm{dd}} = \frac{J}{2}(\hat{S}_1^+ \hat{S}_2^- + \hat{S}_1^- \hat{S}_2^+) = J(\hat{S}_1^x \hat{S}_2^x + \hat{S}_1^y \hat{S}_2^y) \tag{7.1}$$

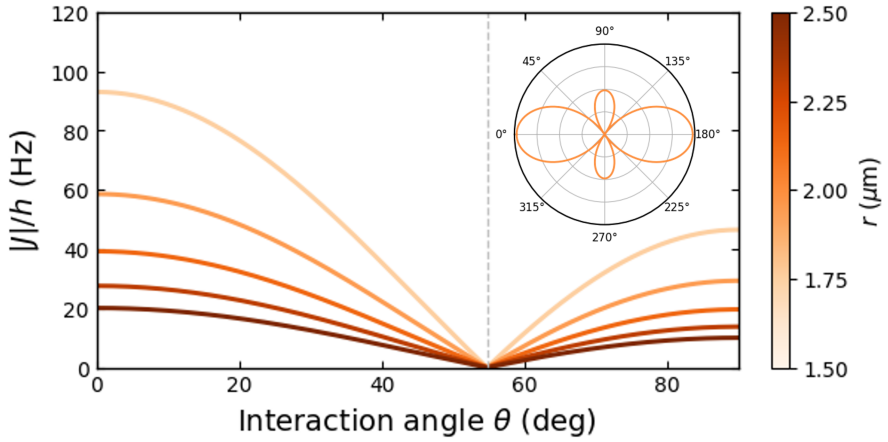


Figure 7.1: Theoretical distance and angular scaling of dipolar coupling strength for CaF molecules plotted for a range of experimentally relevant spacings. Inset: the same coupling strength shown in polar coordinates for $|\vec{r}| = 1.75\,\mu$m.

which is a spin-exchange, or a spin-1/2 XX, Hamiltonian. The coupling strength is $J = \frac{d_{\uparrow\downarrow}^2}{4\pi\epsilon_0 r^3}(1 - 3\cos^2\theta)$, as defined in Eq. 2.4. Equivalently, in the two-molecule basis $\{|\uparrow\uparrow\rangle, |\uparrow\downarrow\rangle, |\downarrow\uparrow\rangle, |\downarrow\downarrow\rangle\}$, the dipolar spin-exchange Hamiltonian in matrix form is:

$$H_{\mathrm{dd}} = \begin{pmatrix} 0 & 0 & 0 & 0 \\ 0 & 0 & J/2 & 0 \\ 0 & J/2 & 0 & 0 \\ 0 & 0 & 0 & 0 \end{pmatrix}, \tag{7.2}$$

which clearly shows that the total number of rotational excitations is conserved as only single-excitation states are coupled. We encode a qubit in two rotational states $|\uparrow\rangle \equiv |X; \nu = 0, N = 1, F = 0, m_F = 0\rangle$ and $|\downarrow\rangle \equiv |X; \nu = 0, N = 0, F = 1, m_F = 0\rangle$ within the electronic and vibrational ground state $X^2\Sigma^+$.

For the rotational transition used here is $d_{\uparrow\downarrow} = \langle\uparrow| d_0 |\downarrow\rangle = d_0/3 \simeq 1.02$ D, with $d_0 = 3.07$ D for CaF [156], which is saturated on stretched state. Figure 7.1 shows a plot of the distance and angular scaling of $|J|$ (in unit of h) for CaF molecules.

The best way to experimentally measure the electric dipole-dipole interaction is through a Ramsey sequence. We start by initializing all the molecules in the re-arranged 1D array in $|\downarrow\rangle$

(see 6.2 for state preparation procedure), so each site is either occupied by a single molecules in $|\downarrow\rangle$ or is empty. A trap being empty is due to imperfect state preparation and detection. In the data analysis, we condition the shots where both sites in a tweezer pair are initially loaded with single molecules.

The initial site spacing is $5\,\mu m$, for which the coupling rate is $|J|/2h \approx 1.26\,\text{Hz}$ (for $\theta = 90°$) is negligibly small when compared with the timescale of the experiment. To "turn on" the interaction, we sweep the AOD frequency tones of the even-numbered tweezer sites, moving them toward their neighboring odd sites and reducing the pair separation.

Starting with an initial two-molecule state $|\downarrow\downarrow\rangle$, we apply a global Ramsey sequence consisting of two global $\frac{\pi}{2}$ pulses separated by a wait time (interaction time), during which an XY8 dynamical decoupling sequence of microwave π pulses are applied. The sequence is schematically shown in Figure 7.2.

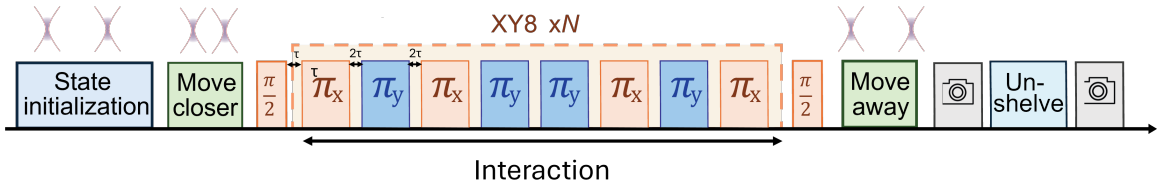


Figure 7.2: Schematic of experimental procedure used for observing dipolar interaction in 1D tweezer array of CaF molecules. The procedure for state initialization is described in Chapter 6.2. We apply a global Ramsey sequence with XY8 dynamical decoupling during the interaction. $\frac{\pi_x}{2}$ denotes a $\frac{\pi}{2}$-pulse, which rotates the quantum state around x-axis of the Bloch sphere by $90°$. Similarly, π_x (π_y) denotes a $180°$ rotation around x-axis (y-axis) on the Bloch sphere. "$\times N$" means the block of XY8 pulses is repeated multiple times during the evolution time.

For a single molecule (basis $\{|\uparrow\rangle, |\downarrow\rangle\}$), a $\frac{\pi}{2}$-pulse applies a $90°$ rotation about the x-axis:

$$R_x\left(\frac{\pi}{2}\right) = \frac{1}{\sqrt{2}}\begin{pmatrix} 1 & -i \\ -i & 1 \end{pmatrix}, \tag{7.3}$$

and prepares the molecule into a superposition state: $R_x\left(\frac{\pi}{2}\right)|\downarrow\rangle = \frac{1}{\sqrt{2}}(|\downarrow\rangle - i\,|\uparrow\rangle)$. So after

applying the first Ramsey $\frac{\pi}{2}$-pulse $U_{\pi/2} = R_x(\pi/2) \otimes R_x(\pi/2)$, the two-molecule state becomes:

$$|\psi_1\rangle = U_{\pi/2}|\downarrow\downarrow\rangle = \frac{1}{2}\left(|\downarrow\downarrow\rangle - i|\uparrow\downarrow\rangle - i|\downarrow\uparrow\rangle - |\uparrow\uparrow\rangle\right) \tag{7.4}$$

During the interaction time t, the symmetric exchange component $(|\uparrow_i\downarrow_j\rangle + |\downarrow_i\uparrow_j\rangle)$ acquires a dipolar exchange phase, giving

$$|\psi_2(t)\rangle = \frac{1}{2}\left[|\uparrow\uparrow\rangle + |\downarrow\downarrow\rangle + e^{-iJt/(2\hbar)}\left(|\uparrow\downarrow\rangle + |\downarrow\uparrow\rangle\right)\right]. \tag{7.5}$$

Note that the π pulses in the XY8 sequence applied during the interaction only swaps $|\uparrow\rangle$ and $|\downarrow\rangle$ on each molecule; under this transformation $|\uparrow\downarrow\rangle\langle\downarrow\uparrow| + h.c.$ is unchanged. XY8 suppresses single-particle decoherence from qubit transition fluctuations, dominantly caused by magnetic field noise in our experiment, while preserving the spin-exchange Hamiltonian, provided the pulses are fast compared with the exchange timescale and are applied identically to both molecules.

Finally, the second Ramsey $\frac{\pi}{2}$-pulse maps this interaction phase onto population:

$$|\psi_f(t)\rangle = \frac{1}{2}\left[\left(1 - e^{-iJt/(2\hbar)}\right)|\downarrow\downarrow\rangle - \left(1 + e^{-iJt/(2\hbar)}\right)|\uparrow\uparrow\rangle\right]. \tag{7.6}$$

The probability of detecting both molecules in $|\uparrow\rangle$ (bright state) is therefore

$$P_{\uparrow\uparrow}(t) = \cos^2\left(\frac{Jt}{4\hbar}\right) = \frac{1}{2}\left[1 + \cos\left(\frac{Jt}{2\hbar}\right)\right], \tag{7.7}$$

and the two-molecule $|\uparrow\uparrow\rangle$ signal oscillates at an angular frequency $\omega_{\text{osc}} = |J|/2\hbar$ because the dipole-dipole interaction accumulates a phase between the single-excitation manifold and the non-exchanging states.

After the the Ramsey sequences, we sweep the AOD frequencies again for even-numbered traps to move molecules apart to the initial spacing, and apply a Λ-imaging pulse to project the system to the N=1 manifold from which we measure $|\uparrow\rangle|\uparrow\rangle$, and thus our measurement

yields the probability $P_{\uparrow\uparrow}$ of detecting both molecules being in the $|\uparrow\rangle$ bright state.

To summarize, we start with each pair of the molecules in $|\downarrow\downarrow\rangle$, and with the applied Ramsey sequence $(U_{\pi/2}e^{-iH_{\mathrm{dd}}t/\hbar}U_{\pi/2})\,|\downarrow\downarrow\rangle$, the state evolves as $\psi_f(t)\rangle = \frac{1}{2}[\left(1-e^{-iJt/(2\hbar)}\right)|\downarrow\downarrow\rangle - \left(1+e^{-iJt/(2\hbar)}\right)|\uparrow\uparrow\rangle]$, resulting in the probability $P_{\uparrow\uparrow}$ that oscillates at an angular frequency of $\omega_J = \frac{J}{2\hbar}$, or in observed frequency unit $f_{\mathrm{osc}} = J/2h$.

In the final readout, there are two cases where a site could both appear dark: molecule is in the $|\downarrow\rangle$ state or that the trap is simply empty. To distinguish them, we add a microwave π-pulse to transfer any molecules in the $|\downarrow\rangle$ in the $N=0$ manifold to $|\uparrow\rangle$ in the $N=1$ manifold (this is shown as the "Un-shelve" step in the sequence in Figure 7.2), which are then detected by a final Λ-imaging pulse. Any empty trap will remain dark. This information is used to exclude the cases of empty traps during the final readout.

7.2.2 Experimental Characterization of Dipolar Interactions

The experimental setup and coordinate system are shown schematically in Figure 7.5 (a, b). The tweezer light at 776 nm is projected into a glass cell through the microscope objective, while fluorescence from the molecules at 606 nm is reflected by a dichroic mirror and collected into the EMCCD. A 1D array of 20 tweezers is generated from a single AOD, which allows the trap positions to be controlled by sweeping the RF drive tones. A half-wave plate is placed between the dichroic mirror and the microscope objective to rotate the linear polarization of the tweezer light for tuning the magic angle, as described in Chapter 6.3.1. A bias magnetic field $\vec{B}$ in the XY plane defines the quantization axis. The dipolar coupling angle θ is defined between $\vec{B}$ and the inter-molecular vector $\vec{r}$.

For single-molecule coherence, it is beneficial to work at lower trap depth (ramping down to tens ofμ K), since this reduces the sampled differential light-shift inhomogeneity for a longer coherence time. For observing coherent dipolar interaction, however, the relevant quantity we want to maximize is the number of spin-exchange oscillations before the exchange contrast decays. The temperature of molecules in tweezer traps after Λ-cooling is applied is estimated to be around 60-80 μK, measured with Release-Recapture or Time-of-Flight methods (see

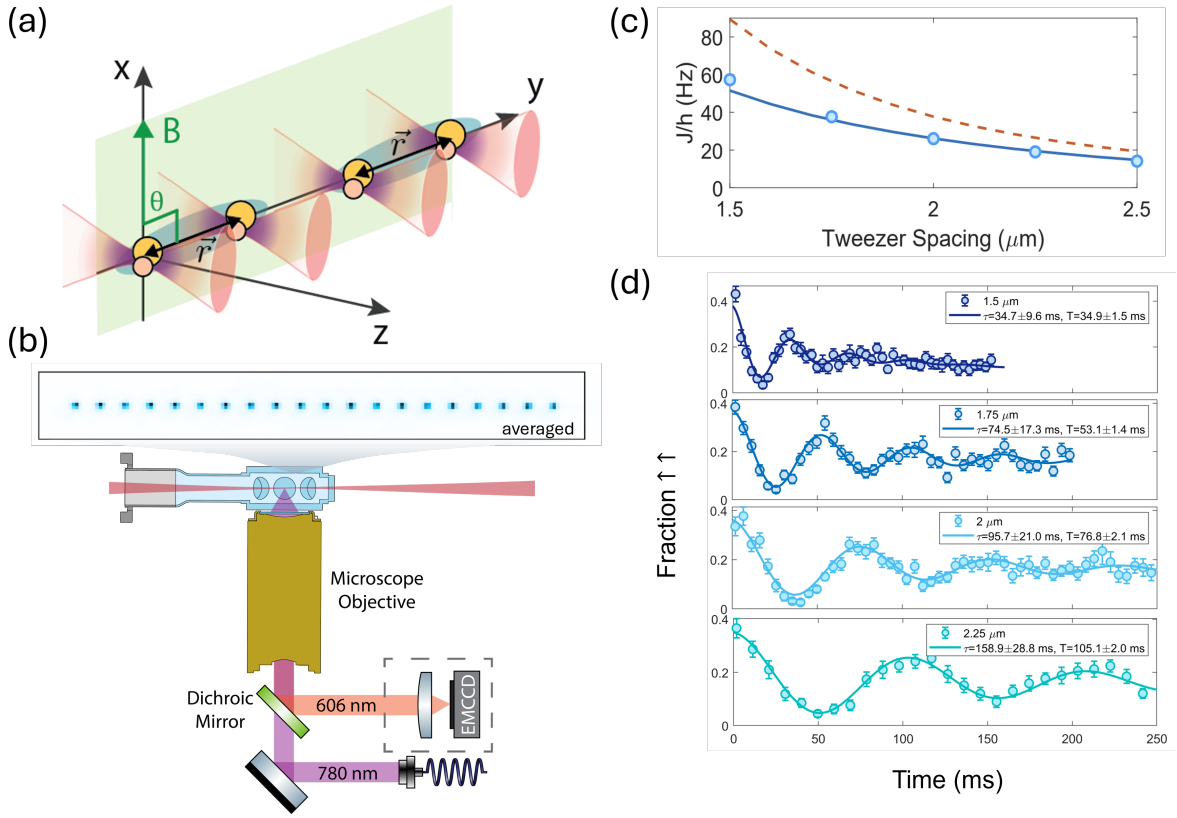


Figure 7.3: **(a)** A representative schematic of the optical tweezer and coordinate system defined in this work (For visual clarity, only four sites of the realized twenty-site array are depicted). The tweezer propagation k-vector is along z-axis. An applied magnetic field $\vec{B}$ (in the XY plane) defines the quantization axis of the spin. θ in dipolar coupling is defined between $\vec{B}$ and the inter-molecular vector $\vec{r}$. For the data shown in (c) and (d), $\mathbf{B}$ is set to be along x-axis, such that $\theta = 90°$. **(b)** Simplified schematic of the optical setup for generating the optical tweezers and an image of averaged fluorescence from a 20-site array of CaF molecules. **(c)** Dipolar coupling strength a versus the tweezer spacing $|\vec{r}|$. Orange line (dashed) shows the theoretical prediction of J assuming zero temperature. Blue line (solid) is the simulated result of J with classical thermal motion of the molecules taken into account. **(d)** Dipolar spin-exchange oscillation at various tweezer spacings, with fitted decay time constant and oscillation period shown in the legends.

5.4), meaning the molecules occupy many motional states, and the thermal motion causes molecules to sample a range of intermolecular separations and angles, producing a distribution of instantaneous coupling strengths J and hence dephasing of the spin-exchange oscillations. In a shallower trap, the molecular wave packet will have a larger spatial extent, and the thermal dephasing becomes more prominent. We therefore operate at a higher trap depth ($\sim 0.4 - 0.5\,\mathrm{mK}$) to more tightly confine the molecules. Note that is maximum trap depth that

we can work at given our field, and still maintain a magic angle configuration. To work in this higher intensity trap depth, we adjust the applied bias magnetic field strength to $\vec{B} \sim 3.2\,\mathrm{G}$ and the angle of tweezer polarization relative to it to maintain the magic condition for preserving single-body coherence; the magic angle for this is close to 90°.

With the procedure and operating condition described above, we first measure the distance dependence of the interaction frequencies by varying the tweezer separation from $1.5\,\mu$m to $2.5\,\mu$m. For each spacing, we apply the Ramsey interaction sequence and fit the oscillations in the two-molecule populations. As shown in Figure 7.3(c), as expected for a dipolar interaction, decreasing the tweezer spacing increases the oscillation frequency approximately as $1/r^3$. Figure 7.3(d) shows the corresponding dipolar oscillation of the detected $P_{\uparrow\uparrow}$ for the various tweezer spacings, from which we fit and extract the dipolar coupling rate f_{osc}. Note that the data in Figure 7.3(c) reports the interaction strength of $J/h = 2f_{\mathrm{osc}}$. For all the data in this section, unless otherwise noted, the magnetic field $\vec{B}$ is kept perpendicular to $\vec{r}$ ($\theta = 90°$.

We find that the measured J/h is slightly smaller than the theoretical prediction and deviates more as the spacing decreases. This is attributed to the finite temperature of the molecules causing the effective inter-molecular spacing $\langle|\vec{r}||\vec{r}|\rangle$ to be larger than the spacing $|\vec{R}|$ between mean trap centers. Averaging over this motion reduces the effective coupling and produces a spread of accumulated interaction phases.

We can confirm this with a Monte Carlo simulation using the measured trap frequencies and molecular temperature, modeling the dephasing effect classically, where each molecule is treated as a classical point particle moving along thermally sampled trajectories in the tweezers. Figure 7.4(a) shows the $1/e$ dipolar interaction coherence time from the simulation agrees with the increasing damping observed from the measured oscillation data. The simulation here captures the effect of classically fluctuating molecule separations, but does not use take into account the full quantum mechanical treatment with finite thermal extent as well as single-body coherence. Nonetheless, the qualitative agreement with the simulation supports the fact the dominating dephasing mechanism is the non-zero temperature of the molecules.

Next, we probe anisotropy of the dipolar Hamiltonian by rotating the applied magnetic field

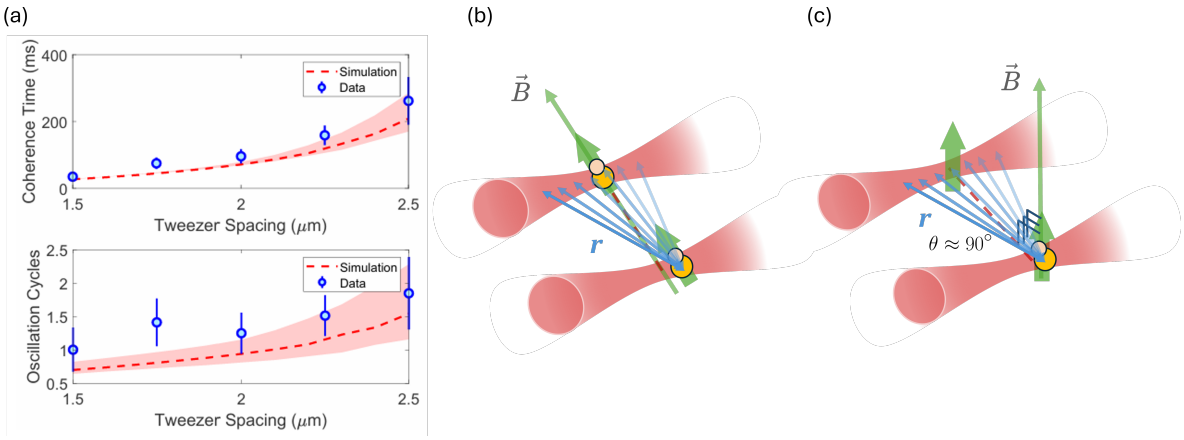


Figure 7.4: (a) Measured and Simulated $1/e$ dipolar coherence times (Top) and number of dipolar oscillation cycles (contrast decayed to $1/e$) (Bottom) at different tweezer spacings. **(b) and (d)** Simple physical picture of molecules displaced from trap center during interactions, sampling the spread of θ and separations $\vec{r}$. In (b), the magnetic field $\vec{B}$ is at small angle relative to inter-molecular separations $\vec{r}$, rendering the spins interaction closer to head-to-tail configuration. In (c), since $\vec{B}$ is perpendicular to $\vec{r}$, $\theta \approx 90°$ despite the fluctuations in $\vec{r}$.

$\vec{B}$ in the XY plane, thereby changing the θ-dependent term of the interaction, as illustrated in Figure 7.5(a). Experimentally, this is done by adjusting the currents in the x- and y-directions, while simultaneously rotating the tweezer light polarization to maintain the magic condition. We measure the corresponding dipolar interaction. In Figure 7.5(b), we show the $P_{\uparrow\uparrow}$ at three characteristic angles $\theta = 0°$, $54.7°$ and $90°$, all taken with a $|\vec{R}| = 2\,\mu$m tweezer spacing. We observe coherent spin-exchange oscillations at both $\theta = 0°$ and $\theta = 90°$, with the $0°$ oscillation occurring at approximately twice the frequency of the $90°$ oscillation, as expected from $|1 - 3\cos^2\theta|$. At $\theta = 54.7°$, the angular factor vanishes, and no clear oscillation is observed. These results agree with the absolute value of the magnitude of the anisotropic term in each configuration.

In addition, the contrast also persists for more oscillation cycles at $90°$ than at $0°$. These two limiting geometries provide a simple physical picture of the anisotropy of thermal sensitivity. As illustrated schematically in Fig. 7.4(b, c), at $\theta = 0°$, the transition dipoles are in the head-to-tail configuration, the larger motional wavefunction spread in the more weakly trapped axial direction of the optical tweezers results in a large fluctuation of the instantaneous value of θ. At $\theta = 90°$, the spins are in parallel and less affected due to the tight confinement of the

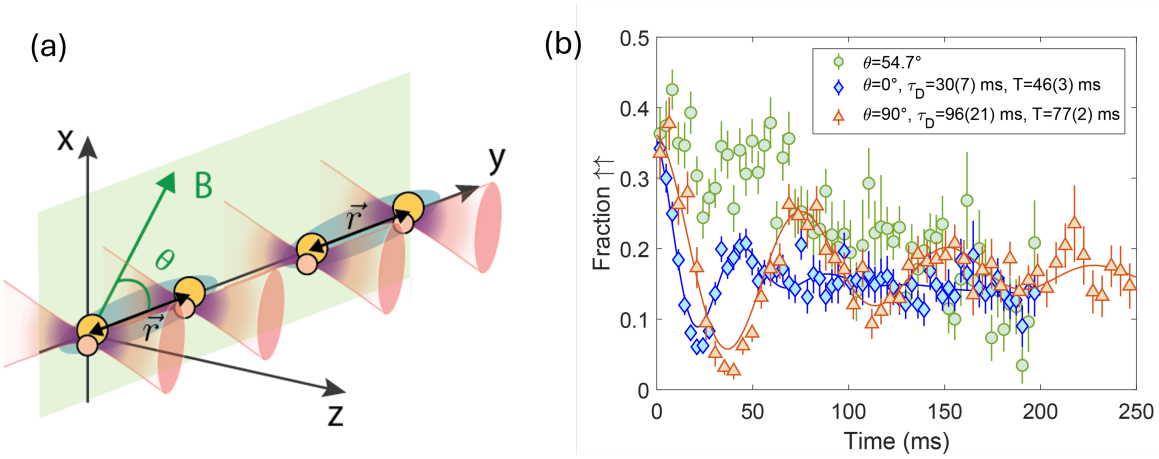


Figure 7.5: (a) Schematic of interaction geometry used for angular measurements. The applied magnetic field $\vec{B}$ can be tuned in the XY plane, varying θ from 0° to 90°. **(b)** Dipolar spin-exchange interaction at different angles $\theta = 0°$, 54.7° and 90°. The $\theta = 0°$ and 90° data is fitted to an exponentially decaying sinusoidal model with decay time constant τ_D and oscillation cycle time T, shown in solid lines.

optical tweezers in the radial direction.

7.2.3 Site-Resolved Initial-State Preparation

Lastly, the same spin-exchange Hamiltonian can be probed from an arbitrary initial state by individually addressing the molecules. As a demonstration, here we prepare an anti-aligned (or antiferromagnetic) initial state $|\uparrow\rangle|\downarrow\rangle$. Experimentally this is achieved by inducing ac Stark shifts for a subset of molecules, causing their qubit transition to be detuned from the addressing microwave pulses. To do so, instead of using a single AOD, the array is generated with a dual-AOD setup with two independent beam paths, one forming the odd-numbered sites and the other forming the even-numbered sites. This dual-AOD geometry gives independent control of the two sub-arrays and allows neighboring traps to be brought close together without the beatnote heating that can occur when closely spaced tweezers are produced by a single multi-tone AOD [88, 92]. The two tweezer beams are offset by ±100 MHz, giving a 200 MHz detuning between neighboring traps to avoid beat-note.

Starting from molecules initialized in $|\downarrow\downarrow\rangle$, the trap depth of one set of sites is adiabatically ramped to be seven times larger than that of the other, inducing a differential AC Stark shift such that molecules in higher-intensity traps are away from resonance of the $|\uparrow\rangle \rightarrow |\downarrow\rangle$ microwave

transition. A global microwave π pulse then flips only the molecules in the sub-array that are on-resonant, preparing $|\uparrow\rangle|\downarrow\rangle$ across each pair. We can confirm this by applying a microwave pulse with variable length of time and detecting molecules in the $|\uparrow\rangle$ state. Figure 7.6(a) shows clear Rabi oscillations in both even and odd sites with opposite phase.

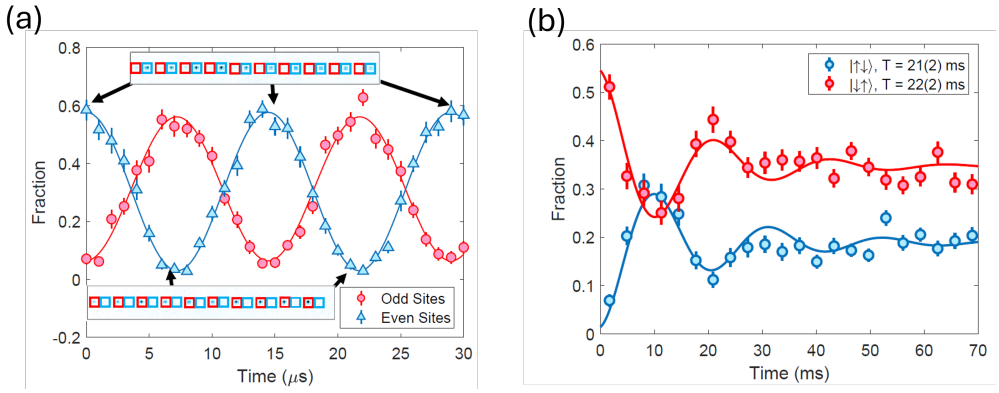


Figure 7.6: (a) Rabi oscillation of molecules initialized in $|\downarrow\uparrow\rangle$ state. (b) Dipolar spin-exchange oscillation with a initial $|\uparrow\downarrow\rangle$ state at $\theta = 90°$. Shown here are the outcomes of $|\downarrow\uparrow\rangle$ and $|\uparrow\downarrow\rangle$

Subsequently the traps are brought to an interaction spacing of $2\,\mu$m, the XY8 sequence is applied during the exchange time, and the pairs are separated again for state-resolved detection. The resultant outcome probabilities are shown in Figure 7.6(b) with a clear display of spin exchange. This preparation gives a more direct view of the exchange process. Under $H_{\mathrm{dd}} = \frac{J}{2}(|\uparrow\downarrow\rangle\langle\downarrow\uparrow| + h.c.)$, an initial $|\uparrow\downarrow\rangle$ state evolves into a coherent superposition of $|\uparrow\downarrow\rangle$ and $|\downarrow\uparrow\rangle$. The population oscillates between the two anti-aligned configurations, with

$$P_{\uparrow\downarrow} = \cos^2(Jt/2\hbar), \quad P_{\downarrow\uparrow} = \sin^2(Jt/2\hbar) \tag{7.8}$$

This oscillation occurs at angular frequency $J/\hbar$, twice of that obtained with initially symmetric state $|\downarrow\downarrow\rangle$. This is because the measured phase is between the symmetric and antisymmetric single-excitation eigenstates, whose energy splitting is J. In the previous measurement with $|\downarrow\downarrow\rangle$ initial state, the the measured phase is instead between the non-exchanging states and the symmetric single-excitation state, separated by $J/2$.

7.3 Limitation on Dipolar Coherence

As shown in the section above, the major limitation for coherent dipolar driven entanglement is dephasing induced by thermal motion of molecules. Thermal motion of molecules broadens the distribution of the dipolar interaction J across the thermal ensemble by modifying both the intermolecular separation r and the angle θ. This effect is especially severe for molecules trapped in optical tweezers, because the the weak confinement along the longer tweezer beam axis makes the molecular positional wave packet strongly anisotropic. This axial thermal motion has been attributed to be the common dominant contribution to dephasing for previous demonstrations of entanglement in polar molecules [9–12].

Naturally, one could try to further cool the molecules close to the motional ground state of the tweezer taps. But even with a large fraction of molecules cooled to or close to the ground motional state of the tweezer trap, any residual motional excitation remains limiting – a few quanta of motional excitation already put a fundamental limit on interaction coherence [11]. All this motivates finding new strategies to suppress sensitivity of J to thermal fluctuations [28, 60, 67].

7.4 Tuning Motional Sensitivity of Dipolar Coupling in 3D

7.4.1 2D Case: "Magic" Angle

Let us elucidate the sensitivity of J more clearly by expanding it about the mean inter-molecular separation. Following the theoretical analysis developed in Ref. [60], we start by considering a molecular pair with mean separation $\vec{r}_0$ and a small relative displacements $\delta\vec{r} = (\delta x, \delta y, \delta z)$ where $\delta x, \delta y, \delta z \ll |\vec{r}_0| \equiv r_0$. Taking the quantization axis to be in $\hat{x}$, the leading terms of the

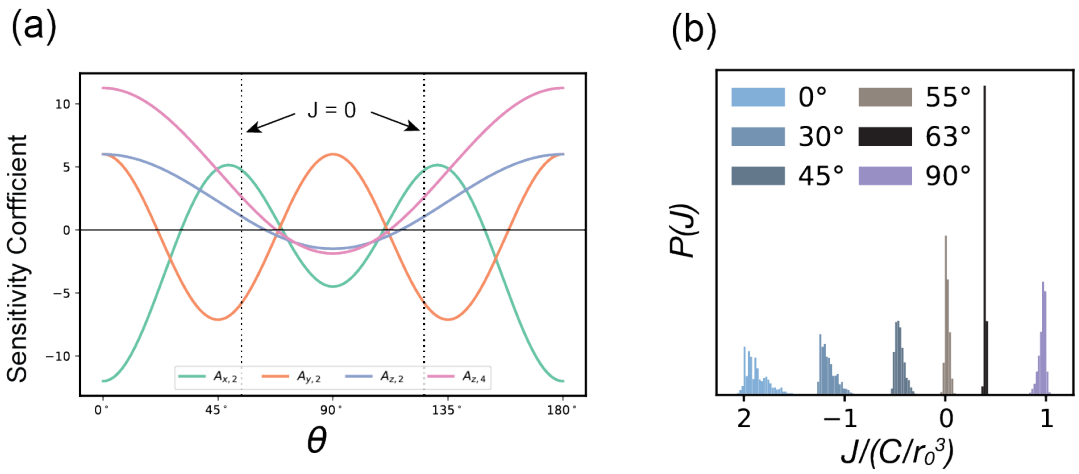


Figure 7.7: (a) Sensitivity coefficients $A_{i,2}(\theta)$ in expansion of J, showing the angular dependence. The dashed vertical lines indicate angles at which $J \propto 1 - 3\cos^2\theta = 0$. **(b)** Simulated distributions of dipolar coupling strengths $P(J)$ for different angles θ, showing a narrow distribution near $\theta \simeq 63°$, where leading-order sensitivity to axial motion vanishes. Adapted from [60].

expansion are

$$J(\vec{r}_0 + \delta\vec{r}) \approx J(\vec{r}_0) + \nabla J|_{\vec{r}_0} \cdot \delta\vec{r} + \frac{1}{2}\delta r_i \delta r_j \left.\frac{\partial^2 J}{\partial r_i \partial r_j}\right|_{\vec{r}_0} + \cdots \tag{7.9}$$

$$\approx \frac{C}{r_0^3}\left[1 - 3\cos^2\theta_0 + \sum_i A_{i,1}(\theta_0)\frac{\delta r_i}{r_0} + A_{x,2}(\theta_0)\frac{\delta x^2}{r_0^2} + A_{y,2}(\theta_0)\frac{\delta y^2}{r_0^2} + A_{z,2}(\theta_0)\frac{\delta z^2}{r_0^2} + \cdots\right], \tag{7.10}$$

where $\theta_0 = \theta(\vec{r}_0)$ and $C \equiv d_{\uparrow\downarrow}^2/4\pi\epsilon_0$. The expansion coefficients $A_{i,j}(\theta_0)$ are dimensionless factors that quantify j-th order sensitivity of J for motion along the $\hat{i}$ axis and the angle $\theta(\vec{r})$ dependence.

In all the current molecular tweezer experiments [9, 10, 12, 95], the trap frequencies are typically tens to hundreds of kilohertz, much larger than the dipolar exchange dynamics, which is at most hundreds of hertz to few kilohertz. This means that for fast thermal motion in an approximately harmonic tweezer: $\omega_r, \omega_z \gg |J|/\hbar$, the displacement is then symmetric about the trap center so linear terms average away over many trap orbits as $\langle\delta\vec{r}\rangle = 0$. This leaves the leading-order sensitivity of J to be the quadratic terms, set by the curvature coefficients $A_{i,2}(\theta)$. If one plots these coefficients over θ, shown in Figure 7.7(a), one can see that $A_{z,2}$

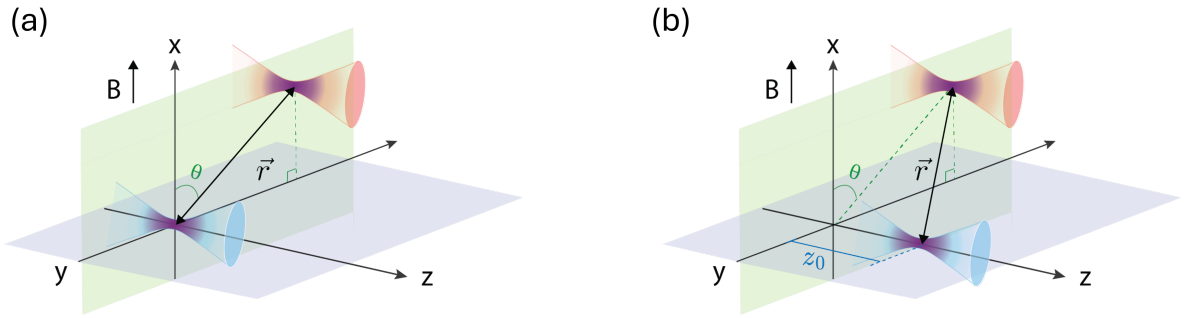


Figure 7.8: (a) Planar interaction configuration for a pair of molecules where both traps are in the same focal plane. The relative interaction vector is fully specified by $\vec{r} = (r_\perp, \theta)$. **(b)** 3D interaction configuration where the two traps have relative axial displacement z_0, and the separation vector is fully specified by $\vec{r} = (r_\perp, \theta, z_0)$

vanishes near $\theta \approx 63.4°$, suggesting that at this angle the sensitivity of J to motion along $\hat{z}$ is minimized. And note that this is different from the $\theta \approx 54.7°$, where there is no dipolar interaction $J \propto 1 - 3\cos^2\theta$.

To further check this, one can plot the distribution of dipolar couplings, $P(J)$ across the thermal ensemble at a few different angles θ. Here, $P(J)$ is obtained by sampling thermal motional states from a Boltzmann distribution in the trap and evaluating the corresponding dipolar exchange matrix element. Repeating this gives a histogram in Figure 7.7(b) (details of the simulation model and more analysis can be found in supplementary material of Ref. [60]). As expected, at the special $\theta \approx 63.4°$ "magic" dipolar angle, the distribution width becomes the most narrow, while the mean interaction rate remains finite.

This magic angle above is illuminating but limited. For all the interactions considered so far, we have assumed the two trap centers of an interacting molecule pair are constrained to the same focal plane, such that angular dependence is solely set by a single in-plane angle θ, illustrated in Figure 7.8(a). In fact, this planar magic-angle condition is only one slice of a more general three-dimensional geometry dependence, as it suppresses the leading-order axial sensitivity in the coplanar geometry, and does not generally eliminate sensitivity to radial motion or to higher-order axial terms.

This motivates one to ask more generally: Are there conditions that reduce the sensitivity of J along *all* motional directions?

7.4.2 3D case: "Magic" Configuration

To address this, let us extend the control of interaction beyond the planar configuration. Introducing a finite axial displacement z_0 between the two molecules, as shown in Figure 7.8(b), adds an additional degree of freedom, allowing sensitivities of J to thermal motion along different spatial directions to be tuned simultaneously. To better characterize the 3D geometry dependence, we define a dimensionless weighted relative sensitivity

$$\mathcal{S} \equiv \sum_i w_i |A_{i,2}| \tag{7.11}$$

where $A_{i,2} \equiv \frac{r^2}{2J}\partial_i^2 J$ is the dimensionless coefficient that quantifies the change in J under small displacement along direction $i = x, y, z$, and the weights $\propto \omega_i^{-2}$ (normalized) account for trap anisotropy and are defined as $w_i \equiv \frac{\omega_i^{-2}}{\omega_x^{-2}+\omega_y^{-2}+\omega_z^{-2}}$; since the tweezer is weakly confined along z, axial motion receives a large weight.

Figure 7.9 shows the plot of $\mathcal{S}(\theta, z_0)$ (evaluated at an in-plane spacing $r_\perp = 1.75\,\mu\,\mathrm{m}$). The horizontal axis is the in-plane angle θ. The vertical axis z_0/r is the relative axial displacement normalized by the in-plane separation. The color map essentially indicates a weighted curvature of J, telling us where the dipolar interaction is least sensitive to thermal motion. Regions with brighter regions correspond to geometries with reduced overall sensitivity of J to thermal motion. Along $z_0 = 0$, we recover the 2D planar case, with a low-sensitivity point near 63°. But once we add axial displacement, we gain another degree of freedom to let us reduce the motional sensitivity along multiple directions simultaneously, giving a 3D magic region away from the zero-interaction line.

7.5 Experimental Control of Interaction Geometry

Guided by this geometric dependence, in this section, we describe the experiment procedure and results of tuning the interaction geometry and characterizing the corresponding dipolar coherence.

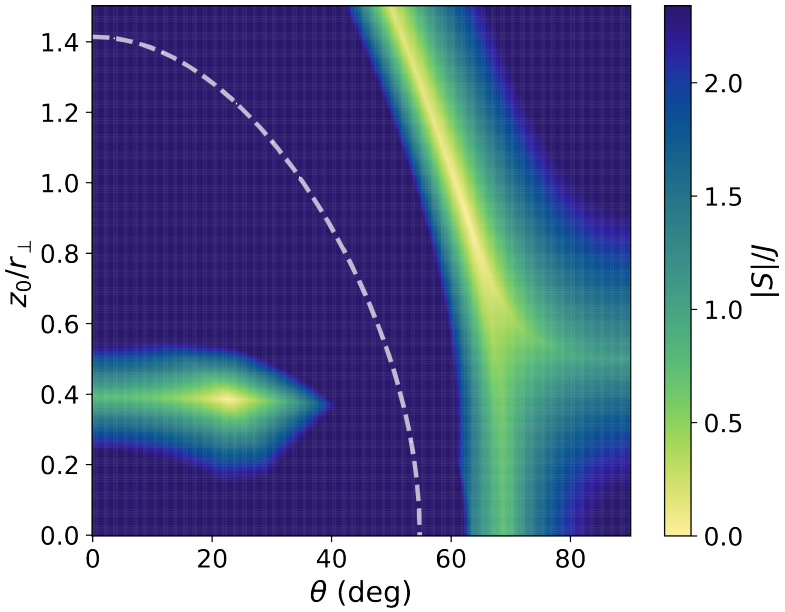


Figure 7.9: Dipolar motional sensitivity in experimentally accessible three-dimensional geometry. Color shows the dimensionless weighted relative sensitivity $\mathcal{S}$, defined in main text, of the interaction strength to thermally-induced dephasing. The dashed curve marks $J = 0$; brighter regimes indicate reduced leading-order sensitivity to thermal motion.

7.5.1 Experimental Control and Coordinates

Experimentally, three-dimensional control of the relative molecular geometry is enabled by a hybrid SLM-AOD tweezer architecture, illustrated in Fig. 7.10. The relative geometry of a molecular pair is specified in cylindrical coordinates by $(r_\perp, \theta, z_0)$, where $r_\perp$ and θ describe the in-plane separation (in transverse x-y plane) and orientation relative to $\hat{x}$, and z_0 is the relative axial displacement. Each pair of molecules then interacts with a dipolar coupling strength of

$$J = \frac{d^2}{4\pi\epsilon_0 r^3}(1 - 3\cos^2\alpha). \tag{7.12}$$

Notice now α is defined as the angle between $\vec{r}$ and the quantization axis. In most implementations, this coupling is only tuned by changing r and, when angular control of α is needed, by reorienting the pair either in the transverse plane or by rotating the quantization field itself. In our apparatus, the 2D-AODs can provide rapid lateral positioning to set the in-plane $(r_\perp, \theta)$ for each pair, while the SLM hologram defines a static tweezer array and can

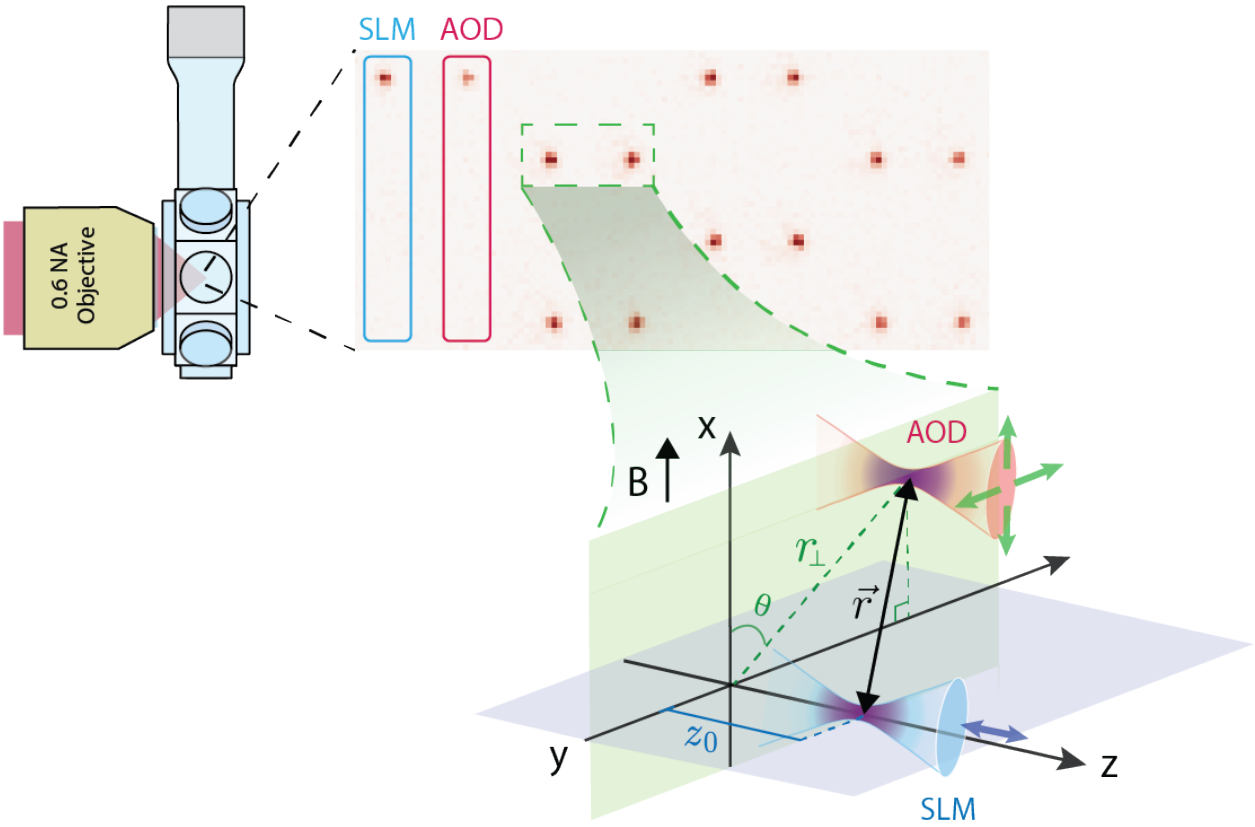


Figure 7.10: Illustration of the optical tweezer array and geometric coordinates used in this work. CaF molecules are loaded into 775 nm optical tweezers projected through a 0.6 NA microscope objective into a vacuum glass cell. Inset: Geometry and coordinates between one pair of interacting molecules. The tweezer propagation is along $\hat{z}$. The relative separation vector between two molecules is $\vec{r} = \vec{r}_\perp + z_0\hat{z}$, where $\vec{r}_\perp$ is the in-plane separation and z_0 is their relative axial displacement. The angle θ is defined between $\vec{r}_\perp$ and the quantization axis, which is set by a small applied magnetic field along $\hat{x}$. One trap (shown in red) is generated from crossed 2D-AODs, which provide lateral positioning to set $(r_\perp, \theta)$, while the other trap (shown in blue) is projected from an SLM phase mask, which can independently impose z_0.

independently impose z_0.

7.5.2 Measurement Procedure

In an experimental sequence, molecules are initially loaded into a 2D array in the SLM tweezers with 14 μm spacing. We then take a nondestructive image using Λ-imaging [160] to identify the loaded traps. This is followed by re-arrangement using a set of dynamic AOD tweezers generated by crossed acousto-optic deflectors (AODs), where we move each AOD-trapped molecule toward its neighboring SLM molecule, forming a set of spatially alternating pairs in the SLM array. An

example shot of rearranged array is shown in Fig. 7.10. Note that we alternate pairs in order to minimize any many-body effects, such that any pair-to-pair interaction rate is geometrically suppressed.

After rearrangement, all molecules in the SLM array and we initialize the molecules in the qubit state $|\uparrow\rangle$ (see Sec. 6.2 for state preparation procedure). The rotational qubit states are defined as $|\uparrow\rangle \equiv |X; \nu = 0, N = 1, F = 0, m_F = 0\rangle$ and $|\downarrow\rangle \equiv |X; \nu = 0, N = 0, F = 1, m_F = 0\rangle$. A magnetic field of $\sim 3\,\mathrm{G}$ applied along $\hat{x}$ defines the quantization axis.

Next we transfer half of the molecules in each pair from SLM to AOD traps. This is done by ramping on a 4×4 array of dynamic AOD tweezers in 250 μs, which are overlapped with every other site of the SLM array. The AOD tweezers are 3–4 times deeper than the SLM traps ($U_{\mathrm{SLM}} = k_B \times 400\,\mu\mathrm{K}$) to ensure high transfer fidelity, even with a large axial displacement between the two generated potentials. The transfer fidelity between the AOD and SLM traps is $> 99.9\%$ when the two tweezers share the same focal plane, and decreases to 95% when their relative shift in the focal plane is larger than $2.5\,\mu\mathrm{m}$. However, we find that this infidelity primarily results in heating and loss as the AOD tweezer leaves the SLM tweezer, rather than a molecule remaining in the SLM tweezer.

To probe the dipolar interaction dynamics, we use a similar microwave Ramsey sequence on the $|\uparrow\rangle - |\downarrow\rangle$ transition as described in the earlier section of this chapter but with some modifications. Briefly, during the interaction time, we apply an XY8 dynamical decoupling sequence, with an interpulse time of $200\,\mu\mathrm{s}$, and a π pulse duration of $8.5\,\mu\mathrm{s}$. The XY8 decoupling sequence mitigates dephasing from magnetic field fluctuations, measured to be $70\,\mu\mathrm{G}$, and from differential light shifts induced by the tweezer light [3]. With this decoupling sequence, we measure a single-body coherence time T_2 of $\tau_{sb} = 0.981(23)\,\mathrm{s}$. This time is comparable for both the AOD and SLM tweezers. Furthermore, we find that the optimal XY8 parameters and the measured single-particle coherence do not depend appreciably on the interaction geometry.

After the final microwave pulse, we move the AOD tweezers back to their original positions, so that they overlap the SLM traps, and ramp them down, thus returning all molecules to

the SLM-generated tweezers. The Λ-imaging light addresses molecules in $|\uparrow\rangle$. We first image molecules in the $N = 1$ rotational state, then apply a resonant heating pulse to remove all molecules remaining in $N = 1$. Finally, we apply a composite microwave π pulse to transfer population from $|\downarrow\rangle$ to $|\uparrow\rangle$ and image again [9]. All data are conditioned on retaining both molecules of an interacting pair.

7.6 Static Geometric Engineering of Motional Sensitivity

To visualize and convert sensitivity of measured dipolar coherence to the experimentally accessible parameters, we plot the predicted Q for pairs of CaF molecules with an in-plane separation of $r_\perp = 2.5\ \mu$m, shown in Fig. 7.11(a). Here, the quality factor $Q \equiv |J|\tau/h$ is our observable that quantifies the dipolar coherence, where τ is the effective $1/e$ decay time of the spin-exchange oscillation contrast, including finite single-body coherence.

We begin by measuring coherence in the planar configuration, with $z_0 = 0$. We vary the position of the AOD tweezers with respect to the static SLM tweezers, while maintaining a fixed magnetic field direction. The measured Q for a pair of molecules is shown in Figure 7.11(c) and exhibits a slight optimum near $\theta^* \approx 63°$, consistent with the previously proposed 2D magic angle [60]. The lack of a sharply peaked feature reflects the trade-off between enhanced coherence and reduced interaction strength J; $|J(\theta = 63.4°)|$ is about 40% of $|J(\theta = 90°)|$. The corresponding two-qubit population dynamics $P_{\uparrow\uparrow}$ and $P_{\downarrow\downarrow}$ measured at $(z_0 = 0, \theta^*)$, from which we extract the associated τ, is shown in Figure 7.11(b). All the reported dipolar measurements performed in the 2D array here are taken from a single representative molecule pair to avoid axial disorder in the SLM array [189], which we control to $\lesssim 100\,$nm across the array (see Chapter 5.5).

Having identified the optimal configuration within the planar geometry, we then vary the relative axial displacement z_0 at fixed θ^* by applying a variable offset of the defocus Zernike polynomial Z_2^0 on top of the base SLM phase hologram. Fig. 7.11(d) shows a peak in Q at finite offset $z_0^* \approx 1.42\,\mu$m. At this 3D "magic" configuration, we measure a maximum

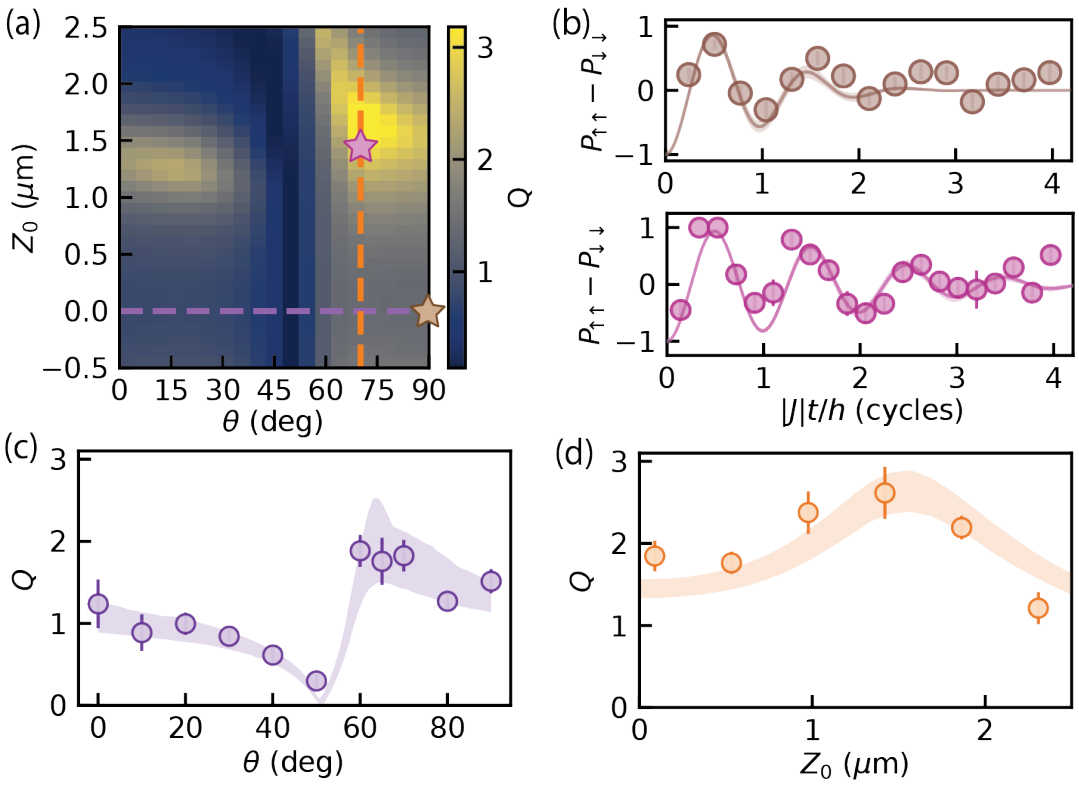


Figure 7.11: Static geometric engineering of dipolar interactions. (**a**) Predicted interaction quality factor $Q = |J|\tau/h$ over geometry space parameterized by (θ, z_0). The stars mark the geometries used for the dipolar oscillation measurements shown in B, while the horizontal (vertical) dashed lines mark the cuts depicted in c (d). (**b**) Comparison of dipolar oscillations at a reference point $(\theta, z_0) = (90°, 0)$ and an optimal configuration $(\theta^*, z_0^*) = (70°, 1.42\,\mu\text{m})$. Solid lines are fit to a damped dipolar-exchange oscillation; corresponding fitted decay times are $\tau = 40(6)$ ms and 103(12) ms, respectively. (**c**) Dipolar interaction quality factor Q as a function of angle θ at $z_0 = 0$. (**d**) Dipolar quality factor Q as a function of z_0, at a fixed angle $\theta^* = 70°$. Shaded bands in (c, d) show the two-body dipolar model simulations, with widths indicating uncertainty from finite numerical sampling.

$Q = 2.61(31)$. The 3D magic configuration improves by approximately a factor of 1.4 relative to the 2D magic-angle case, demonstrating that the additional geometric degree of freedom can substantially enhance interaction coherence by reducing the motional sensitivity of J along all three axes. Representative dipolar spin-exchange dynamics measured at (θ^*, z_0^*) are shown in Fig. 7.11(b).

7.7 Dynamic Geometric Engineering: Position Noise and Positional Echo

While the interleaved SLM-AOD array allows for precise and flexible control of the pairwise geometry, it also introduces positional fluctuations of the relative trap positions, which becomes a dephasing channel in the coherent dipolar interactions. In our setup, the two molecules of an interacting pair are held in tweezers generated from two independently propagated beam paths: one for the SLM and one for the AOD tweezer arrays. Any differential drift between these paths perturbs the mean trap positions of an interacting pair. The time scale of these positional fluctuations are slow compared to the dipolar interaction but can differ between experimental realizations producing first-order change to the intermolecular spacings and hence the interaction strength.

We reduce this technical noise by imaging the leaked light of two sets of traps on a pickoff-camera and extract the mean relative displacement between them. We then compensate this average relative offset on the SLM traps by applying a global grating to the SLM hologram, which is updated every two minutes, or whenever an experimental parameter, such as the interaction time, is changed. With the calibration and feedback, the residual radial offset noise is approximately 50 nm rms over 24 hours. Nevertheless, once we operating at the magic configurations described above, these these fluctuations become the dominant source of dipolar decoherence, since the sensitivity to *thermal fluctuations* is greatly reduced. In this regime, noise in relative position on the order of 10s of nanometers can substantially limit the interaction coherence, which is sensitive at the few nanometer scale. The ability to dynamically tune the geometry of the interacting molecules, on timescales faster than their entanglement rate, therefore provides a route to mitigating the effects of positional disorder.

This motivates the introduction of a positional echo protocol to suppress sensitivity to any static radial offsets.

Figure 7.12 (a,b) illustrates the idea of the two-step positional echo protocol, in which

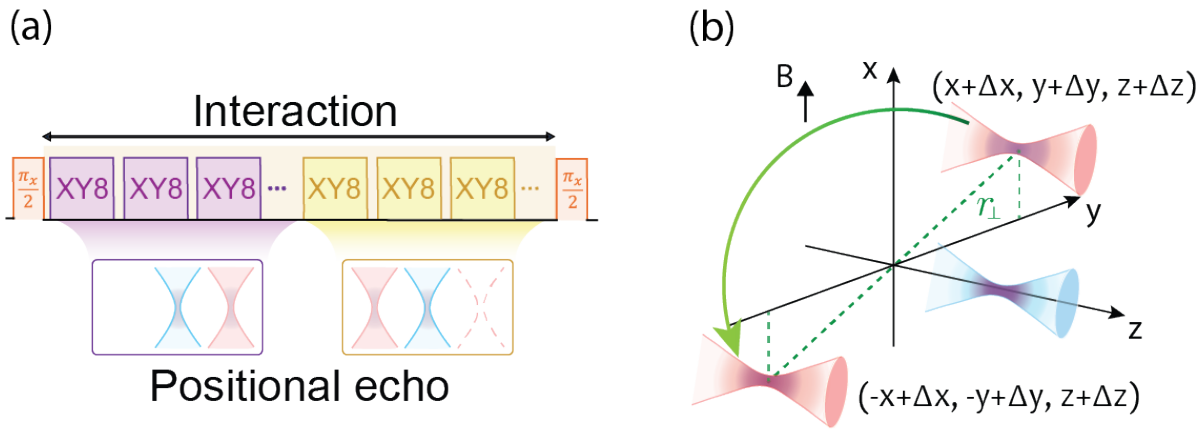


Figure 7.12: Positional Echo Protocol. (a) Timing of positional echo during the interaction. The interacting pair evolves for equal durations at two geometries, realized by rapidly moving one molecule midway through the interaction duration. The XY8 dynamical decoupling sequence is applied throughout the interaction. (b) Schematics of the positional echo protocol.

the interaction geometry is inverted during the evolution so that first-order shifts from slow position shifts cancel. Since the relative position noise during the interaction is effectively static, it can be represented as a set of fixed offsets $(\Delta x, \Delta y, \Delta z)$. As illustrated in Fig. 7.12(a), during the interaction sequence, one molecule evolves for half of the sequence at position $(x + \Delta x, y + \Delta y, z + \Delta z)$ relative to the other molecule, and is then rapidly moved by the AODs to a symmetric geometry around $\hat{z}$ at $(-x + \Delta x, -y + \Delta y, z + \Delta z)$ for the second half of the interaction. In this way, the same positional disorder shifts the interaction strength in the opposite direction during the two equal segments, so any disorder-induced phase shifts cancel to first order while the desired interaction is preserved.

Experimentally, to implement the positional echo protocol, we move the molecules in AOD tweezers along a three-segment trajectory. First, with an AOD tweezer at interaction position (x, y, z), we move the tweezer away from the SLM-trapped molecule to minimize any effects of the dipolar interaction, moving to $(x + 2y, y - 2x, z)$. We then move to $(-x + 2y, -y - 2x, z)$, and finally finish the echo by moving to $(-x, -y, z)$. We make each one of these moves with a constant-jerk trajectory over the course of 800 μs, so that the total echo takes 2.4 ms. This timing aligns the move around the π pulses in the dynamical decoupling sequence, and we

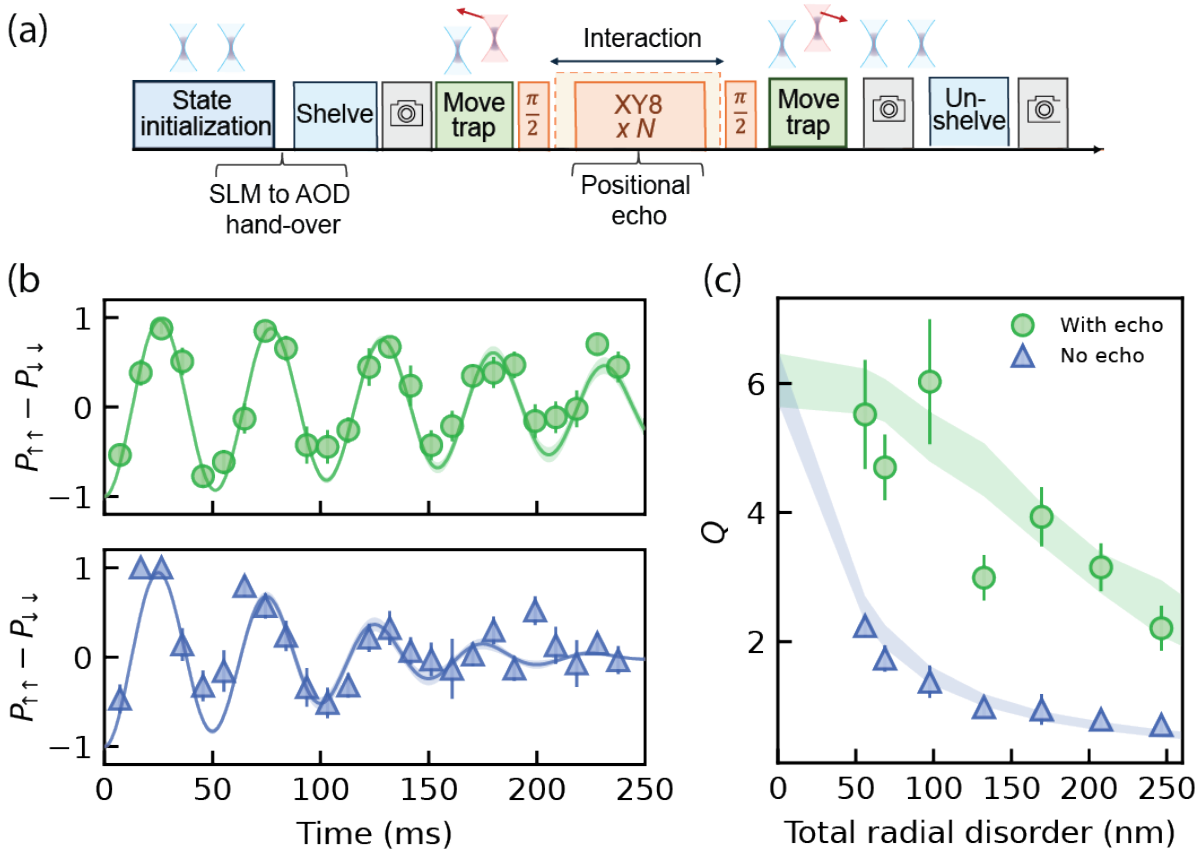


Figure 7.13: (a) Experimental sequence for probing dipolar interaction with applied positional echo protocol. **(b)** Comparison of optimal dipolar oscillations with the motional echo (top, green) and without the motional echo (bottom, blue). **(c)** We characterize the performance of the echo protocol by injecting additional disorder into the SLM trap position. The total radial disorder is obtained by adding the injected disorder in quadrature with the uncorrected baseline radial disorder ($\simeq$ 50 nm); the first data points correspond to zero injected disorder. The echo protocol improves the dipolar coherence by a factor of 3.

observe no loss in single-body coherence with and without the echo protocol. Furthermore, these moves happen on length scales of a few microns, and we find no molecule loss even at reduced echo durations of 100 μs.

In Fig. 7.13(b), we compare dipolar oscillations taken at the separately optimized geometries with and without the echo protocol. Applying the echo protocol during dipolar interaction at the optimized 3D geometry ($\theta^* = 70°, z_0^* = 1.8$ μm) yields a dipolar coherence with $Q = 6.03(97)$.

Additionally, we quantify the robustness of this geometric echo protocol by injecting random radial offsets to the SLM trap positions and comparing the interaction Q factor with and without the geometric echo. This is done by applying a different random grating on top of

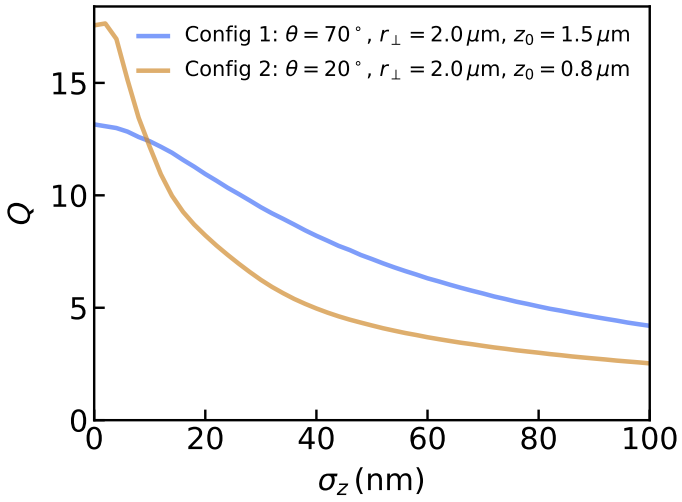


Figure 7.14: Simulated effect of reducing axial disorder. Simulated quality factor Q versus axial position disorder σ_z for two interaction geometries at $\bar{n}_z = 10$. The $\theta = 70°$, $r_\perp = 2$ μm, $z_0 = 1.8$ μm geometry is more robust to large axial disorder, while the $\theta = 20°$, $r_\perp = 2$ μm, $z_0 = 0.8$ μm geometry gives a larger Q when $\sigma_z \lesssim 20$ nm because of its stronger dipolar interaction. Adapted from [80].

the SLM pattern every 10 seconds. Figure 7.13(c) shows the measured Q as a function of the magnitude of the injected disorder. At any scale of disorder the echo performs dramatically better than without the echo. At sufficiently large displacements, the echo protocol does not cancel out higher-order effects, such as angle changes, and we see a degradation of the enhancement. This could be mitigated by using more complicated positional sequences [60].

In our present implementation, the positional echo protocol only targets transverse positional disorder. We estimate the uncanceled relative motion along the axial direction to be on the order of $\sigma_z \sim 40$ nm and attribute it mainly to thermally induced drift in the differential beam path. Implementing the echo with a three-dimensional AOD setup [236, 237] would allow σ_z to be refocused as well, suppressing this contribution. Improved passive stabilization of the tweezer optics is a simpler intermediate step that can be pursued in parallel.

The optimal interaction geometry also depends strongly on the residual axial disorder. Simulations at $\bar{n}_z = 10$ show that the present $\theta = 70°$, $r_\perp = 2$ μm, $z_0 = 1.8$ μm configuration is more robust when σ_z is large. Once effective axial fluctuations are reduced, either through passive stability or a three-dimensional echo, it becomes possible to work at another magic-angle

condition, near $\theta = 20°$ (see Fig. 7.9), which has a larger interaction strength. For the same single-particle coherence, we expect this condition to increase Q by a factor of two compared to what we report here (see Fig. 7.14).

7.8 Two-molecule Dipolar Interaction Model

In this section, we describe the quantum mechanical modelling approach used in simulating the dipolar interaction.

At the temperatures relevant to the experiment, the spatial extent of the trapped molecular wavefunctions is not negligible compared with the length scale over which the dipole-dipole interaction varies. We therefore evaluate the dipolar exchange matrix element using the quantized motional wavefunctions of the two molecules, and then average over the thermal and static positional distributions sampled in the experiment. For a pair of molecules with motional states $\mathbf{n}_i = (n_{ix}, n_{iy}, n_{iz})$, we write the dipolar spin-exchange matrix element as

$$\frac{J(\mathbf{n_1}, \mathbf{n_2}; \mathbf{r})}{2} = -\frac{d_{\downarrow\uparrow}^2}{4\pi\epsilon_0} \left\langle \mathbf{n_1 n_2} \middle| \frac{1 - 3(\hat{B} \cdot \mathbf{r})^2/\mathbf{r^2}}{r^3} \middle| \mathbf{n_1 n_2} \right\rangle, \tag{7.13}$$

where $d_{\downarrow\uparrow}$ is the transition dipole moment, $\hat{B}$ is the quantization-axis direction, and $\mathbf{r} = \mathbf{r_1} - \mathbf{r_2} + \mathbf{r_0}$ is the molecular separation including the nominal tweezer displacement $\mathbf{r_0}$ (i.e., trap positions without shot-to-shot position disorder, as discussed below). Each $|\mathbf{n_i}\rangle$ is taken to be a product of one-dimensional harmonic oscillator eigenstates with the measured trap frequencies $(\omega_x, \omega_y, \omega_z)$. We parameterize the nominal relative displacement $\mathbf{r_0}$ by the in-plane angle θ and axial offset z_0 as

$$\mathbf{r}_0 = (r_\perp \cos\theta,\, r_\perp \sin\theta,\, z_0), \tag{7.14}$$

To obtain the predicted dipolar coherence time and interaction strength for a given geometry, we perform a Monte Carlo average over motional occupation and static relative-position disorder. The motional quantum numbers for the two molecules are drawn independently along each axis

$\alpha \in \{x, y, z\}$ from Boltzmann thermal distributions $p_\alpha(n) \propto e^{\frac{-n\hbar\omega_\alpha}{k_B T}}$, where the temperature T is specified by the mean occupation $\bar{n}$: $k_B T = \hbar\omega_z / \ln(1 + 1/\bar{n})$.

In addition to motional spread, we include shot-to-shot relative position noise between the AOD and SLM trap centers, arising from fluctuations in the differential beam paths. We model this noise as a static displacement drawn from

$$(\delta x, \delta y, \delta z) \sim \mathcal{N}(0, \sigma_x^2) \times \mathcal{N}(0, \sigma_y^2) \times \mathcal{N}(0, \sigma_z^2), \tag{7.15}$$

with $\sigma_x = \sigma_y = \sigma_\perp$. The sampled relative displacement is therefore $\mathbf{r}_s = (x_0 + \delta x, y_0 + \delta y, z_0 + \delta z)$.

For each Monte Carlo sample s, the exchange matrix element is numerically evaluated and converted to an exchange frequency $f_s = J_s/h$. Repeating over N_{samples} draws of $(\mathbf{n}_1, \mathbf{n}_2)$ and $(\delta x, \delta y, \delta z)$ yields the coupling distribution $P(f)$ for that geometry. The Fourier transform of $P(f)$ gives the ensemble-averaged two-body contrast $C(t) = \left| \langle e^{i2\pi f_s t} \rangle_s \right|$.

We extract the simulated coherence time τ as the time at which the envelope, including the same single-molecule decay $e^{-t/\tau_{sb}}$, first decays to $1/e$. The simulated quality factor is then

$$Q = |\bar{f}|\, \tau, \qquad \bar{f} = \frac{1}{N_{\text{samples}}} \sum_s f_s. \tag{7.16}$$

To implement the positional echo protocol, the configuration during the second half of the interaction reverses the in-plane displacement $\mathbf{r}_\perp \to -\mathbf{r}_\perp$. The effective coupling for each sample is the time-weighted average of the couplings in the different geometric configurations.

The shaded simulation bands shown in the data quantify the simulation numerical sampling uncertainty. At each plotted geometry, we bootstrap-resample the coupling ensemble $\{f_s\}$ with replacement, recompute Q for each resampled ensemble, and plot the central 68% interval.

For the experimental data and simulation results, the quality factor Q reported in the main text is calculated from the fitted oscillation frequency f and effective $1/e$ decay time τ of the oscillation envelope. The fit model used for the experimental oscillation envelope is $D(t) = e^{-t/\tau_{sb}} e^{-(t/\tau_{tb})^2}$, where τ_{tb} is the two-body coherence. Thus, τ is defined by $D(\tau) = 1/e$,

or equivalently $(\tau/\tau_{sb}) + (\tau/\tau_{tb})^2 = 1$.

All [entangled pairs] are alike; every [unentangled pair] is [unentangled] in its own way.

Leo Tolstoy, *Anna Karenina*; altered

8

High-Fidelity Two-Molecule Entanglement Generation

Work in this Chapter, including portions of the text and figures, has been distributed as a preprint [80] undergoing peer review as of the time of submission.

In this chapter, we combine the geometric engineering techniques developed in Chapter 7, with the partial Raman sideband cooling sequence described in Sec. 6.4 and Ref [194] to benchmark the fidelity of a generated Bell state.

In Sec. 8.3, we discuss some near- and long-term technical improvements and extensions of geometric control to improve the fidelity.

8.1 Bell State Fidelity Theory

8.1.1 From Spin-exchange to Bell State Generation

In this section we show how dipolar spin-exchange can be used in a two-qubit iSWAP gate to generate entanglement between molecules in neighboring tweezers [28]. As outlined in Sec. 7.2.1, the resonant dipolar interaction between two molecules in the two-molecule basis $\{|\uparrow\uparrow\rangle, |\uparrow\downarrow\rangle, |\downarrow\uparrow\rangle, |\downarrow\downarrow\rangle\}$, has a Hamiltonian of form

$$H_{\mathrm{dd}} = \frac{J}{2}\begin{pmatrix} 0 & 0 & 0 & 0 \\ 0 & 0 & 1 & 0 \\ 0 & 1 & 0 & 0 \\ 0 & 0 & 0 & 0 \end{pmatrix}, \tag{8.1}$$

where J/h is the angular spin-exchange rate. The corresponding unitary time-evolution is

$$U(t) = \begin{pmatrix} 1 & 0 & 0 & 0 \\ 0 & \cos\varphi(t) & -i\sin\varphi(t) & 0 \\ 0 & -i\sin\varphi(t) & \cos\varphi(t) & 0 \\ 0 & 0 & 0 & 1 \end{pmatrix}. \tag{8.2}$$

where $\varphi(t) \equiv \frac{Jt}{2\hbar}$. This form helps us see the physics of dipolar oscillation more explicitly, showing an excitation can coherently oscillate between the two molecules: $|\uparrow\downarrow\rangle \to \cos\left(\frac{Jt}{2}\right)|\uparrow\downarrow\rangle - i\sin\left(\frac{Jt}{2}\right)|\downarrow\uparrow\rangle$. At time $t_{\mathrm{iSWAP}} = \frac{\pi\hbar}{|J|} = \frac{1}{2|J/h|}$, the opposite-parity states' population is fully exchanged: $|\uparrow\downarrow\rangle \to -i|\downarrow\uparrow\rangle, |\downarrow\uparrow\rangle \to -i|\uparrow\downarrow\rangle$ (assuming $J > 0$, without loss of generality), while $|\downarrow\downarrow\rangle$ and $|\uparrow\uparrow\rangle$ are unchanged. The dipolar exchange evolution therefore implements an iSWAP operation. If a molecule starts in $|\uparrow\downarrow\rangle$ and we stop the state evolution halfway at $t_{\mathrm{iSWAP}}/2$, the state becomes

$$|\uparrow\downarrow\rangle \to \frac{1}{\sqrt{2}}\left(|\uparrow\downarrow\rangle - i|\downarrow\uparrow\rangle\right), \tag{8.3}$$

which is a maximally entangled state (a Bell state).

In our experiment, however, the molecules begin in the $|\downarrow\downarrow\rangle$ (or $|\uparrow\uparrow\rangle$) state, and the exchange interaction occurs between microwave Ramsey pulses. We initialize both molecules in $|\psi_0\rangle = |\downarrow\downarrow\rangle$. The first microwave $\pi/2$ pulse prepares a product superposition state:

$$|\psi_1\rangle = R_x(\pi/2)\,|\downarrow\downarrow\rangle = \frac{1}{2}(|\downarrow\downarrow\rangle - i\,|\downarrow\uparrow\rangle - i\,|\uparrow\downarrow\rangle - |\uparrow\uparrow\rangle). \tag{8.4}$$

The Hamiltonian $H_{\mathbf{dd}}$ only acts on the single-excitation part of the $|\psi_1\rangle$. As the symmetric single-excitation state $|S\rangle = \frac{1}{\sqrt{2}}(|\downarrow\uparrow\rangle + |\uparrow\downarrow\rangle)$ is an eigenstate of H_{dd} with eigenenergy $J/2$, it acquires a phase $e^{-iJt/(2\hbar)}$ after interaction time t. After interaction time t is therefore $|\psi_2(t)\rangle = \frac{1}{2}\,|\downarrow\downarrow\rangle - \frac{1}{2}\,|\uparrow\uparrow\rangle - \frac{ie^{-iJt/2}}{2}(|\downarrow\uparrow\rangle\,|\uparrow\downarrow\rangle)$. The second $\pi/2$ pulse converts this exchange phase into an even-parity superposition:

$$|\psi_{\mathrm{f}}(t)\rangle = \frac{1 - e^{-iJt/2}}{2}\,|\downarrow\downarrow\rangle - \frac{1 + e^{-iJt/2}}{2}\,|\uparrow\uparrow\rangle\,. \tag{8.5}$$

This form makes the condition for Bell state clear: a maximally entangled state is produced when the two even-parity amplitudes have equal magnitude: $\left|1 - e^{-iJt/(2\hbar)}\right| = \left|1 + e^{-iJt/(2\hbar)}\right|$, which occurs when $\frac{|J|t}{2\hbar} = \frac{\pi}{2} \quad \Rightarrow t_{\mathrm{B}} = \frac{\pi\hbar}{|J|} = \frac{1}{2(|J|/h)}$. Experimentally, the time t_B is determined from the period T of the measured dipolar oscillation $\propto \cos(Jt/2\hbar)$, whose period is $T = \frac{4\pi\hbar}{|J|}$. That is, we generate Bell state by choosing the interaction time to be $t_{\mathrm{B}} = \frac{T}{4} + nT, n \in \mathbb{Z}$.

Substituting this time into Eq. (8.5), we get the the generated Bell state $|\psi_{\mathrm{f}}(t_{\mathrm{B}})\rangle = \frac{1+i}{2}\,|\downarrow\downarrow\rangle - \frac{1-i}{2}\,|\uparrow\uparrow\rangle\,$. Factoring out the unobservable global phase $e^{i\pi/4}$, the physical state is

$$|\Phi_B\rangle = \frac{1}{\sqrt{2}}(|\downarrow\downarrow\rangle + i\,|\uparrow\uparrow\rangle). \tag{8.6}$$

More generally, we write the even-parity Bell state as

$$|\Phi_\psi\rangle = \frac{1}{\sqrt{2}}\left(|\downarrow\downarrow\rangle + e^{i\varphi}\,|\uparrow\uparrow\rangle\right), \tag{8.7}$$

where φ is determined by the interaction sign and the microwave phase convention. In short, the first pulse in the Ramsey sequence puts part of the wavefunction into the single-excitation component, the dipolar interaction gives that component an iSWAP exchange phase, and the final Ramsey pulse maps that phase into coherence between $|\downarrow\downarrow\rangle$ and $|\uparrow\uparrow\rangle$.

8.1.2 Bell State Fidelity

The Ramsey sequence used to generate the target Bell state alone is not sufficient to identify a Bell state. For example, the Bell state in Eq. 8.7 and the incoherent mixture $\rho_{\text{mix}} = \frac{1}{2}(|\downarrow\downarrow\rangle\langle\downarrow\downarrow| + |\uparrow\uparrow\rangle\langle\uparrow\uparrow|)$ have the same populations in $|\downarrow\downarrow\rangle$ and $|\uparrow\uparrow\rangle$, and they differ only in the phase coherence between them. Therefore, what one is interested in extracting is this coherence.

This is quantitatively captured by the Bell state fidelity, which measures the closeness of an experimentally prepared state, represented by a density matrix ρ, to a target pure Bell state $|\Phi_\psi\rangle$ via the state overlap function [238–245]

$$\mathcal{F}_\psi = \langle\Phi_\psi|\,\rho\,|\Phi_\psi\rangle\,. \tag{8.8}$$

In the two-molecule basis $(|\uparrow\uparrow\rangle, |\uparrow\downarrow\rangle, |\downarrow\uparrow\rangle, |\downarrow\downarrow\rangle)$, we denote its matrix elements by $\rho_{ij,kl} = \langle ij|\,\rho\,|kl\rangle$. Expanding this expression gives

$$\mathcal{F}_\psi = \frac{1}{2}\left(P_{\downarrow\downarrow} + P_{\uparrow\uparrow}\right) + \text{Re}\left[e^{-i\varphi}\rho_{\uparrow\uparrow,\downarrow\downarrow}\right]. \tag{8.9}$$

where $P_{ij} \equiv \rho_{ij,ij}$. The first term measures population in the $\{|\uparrow\uparrow\rangle, |\downarrow\downarrow\rangle\}$ subspace. The second term $\langle\uparrow\uparrow|\,\rho\,|\downarrow\downarrow\rangle \equiv \rho_{\uparrow\uparrow,\downarrow\downarrow} = |\rho_{\uparrow\uparrow,\downarrow\downarrow}|e^{-i\varphi}$, measures the phase between these two components of the Bell state. So to measure the fidelity, we need to determine both the population and phase. In principle, one could determine this coherence by full two-qubit tomography. In practice, because the target state occupies only the same-parity manifold, it is sufficient to measure the populations and extract the coherence using a parity oscillation, explained below.

8.1.3 Parity Oscillation Signal

To extract the phase (coherence), we turn to our trusted friend again: a Ramsey-type readout, where a final $\pi/2$ pulse maps the phase of a superposition onto a population difference. Applying the same idea here, after Bell state generation, we simply add a $\pi/2$ "analysis pulse" with variable phase ϕ. Without this pulse, if we do direct detection of the entangled state in the computational basis measures, we would just get populations $P_{\downarrow\downarrow} = 1/2$ and $P_{\uparrow\uparrow} = 1/2$ without any phase information. The role of the analysis pulse is to map the relative phase into the computational basis.

More explicitly, a $\pi/2$ pulse with phase ϕ rotates the measurement basis onto the equatorial plane of the Bloch sphere. Equivalently, detecting $|\downarrow\rangle$ or $|\uparrow\rangle$ after this pulse corresponds to projecting the molecule, before the pulse, onto the phase-dependent basis

$$|\pm_\phi\rangle = \frac{1}{\sqrt{2}}(|\downarrow\rangle \pm e^{-i\phi}|\uparrow\rangle). \tag{8.10}$$

For the Bell state in Eqn. 8.7, we can rewrite the state in this analysis basis as

$$\begin{aligned}|\Phi_\psi\rangle = \frac{1}{2\sqrt{2}}\Big[&(1+e^{i(\varphi+2\phi)})(|+_\phi+_\phi\rangle + |-_\phi-_\phi\rangle) \\ &+(1-e^{i(\varphi+2\phi)})(|+_\phi-_\phi\rangle + |-_\phi+_\phi\rangle)\Big].\end{aligned} \tag{8.11}$$

The terms in the first line contain same-parity outcomes in the analysis basis, which are mapped by the analysis pulse onto even-parity population outcomes, and vice versa for terms in the second bracket. Thus the relative phase φ controls whether interference is constructive in the even-parity part or in the odd-parity part. From Eq. (8.11),

$$P_{\text{even}} = \frac{1+\cos(\varphi+2\phi)}{2}, \qquad P_{\text{odd}} = \frac{1-\cos(\varphi+2\phi)}{2}. \tag{8.12}$$

Therefore the parity signal is

$$\Pi(\phi) = P_{\text{even}} - P_{\text{odd}} = \cos(\varphi + 2\phi). \tag{8.13}$$

If the phase φ evolves in time, the even- and odd-parity probabilities oscillate in time. Note that the Bell coherence φ appears to be oscillating at twice the analysis-pulse phase ϕ. The factor of two comes from the fact that the analysis phase is applied to both molecules: a coherence between $|\downarrow\downarrow\rangle$ and $|\uparrow\uparrow\rangle$ carries two single-particle phase factors.

In our measurement, the interaction time is fixed and the analysis phase ϕ is scanned, so the same two-molecule coherence appears as a parity oscillation versus ϕ. The parity signal is fit to

$$\Pi(\phi) = \Pi_0 + A_\Pi \cos(2\phi + \phi_0), \tag{8.14}$$

where

$$A_\Pi = 2|\rho_{\uparrow\uparrow,\downarrow\downarrow}|. \tag{8.15}$$

The amplitude A_Π gives the magnitude of the Bell state coherence, while the fitted phase ϕ_0 identifies the relative phase of the generated Bell state.

8.2 Experimental Generation of High-Fidelity Bell State

In Chapter 7, we focused on using static and dynamic control over interaction geometry to suppress position fluctuations and reduce sensitivity to thermal motion. It is important to distinguish that static engineering of the geometry of the interacting molecules is aimed at minimizing the quadratic sensitivity to the spatial extent of the molecular wave packet, while shifts of the mean trap positions enter through the linear term and are a first-order source of interaction dephasing. That is, these techniques mitigate the first- and second-order sensitivities of the dipolar interaction to positional fluctuations. Meanwhile, further cooling reduces the extent itself and can still improve coherence by reducing sensitivity to higher-order

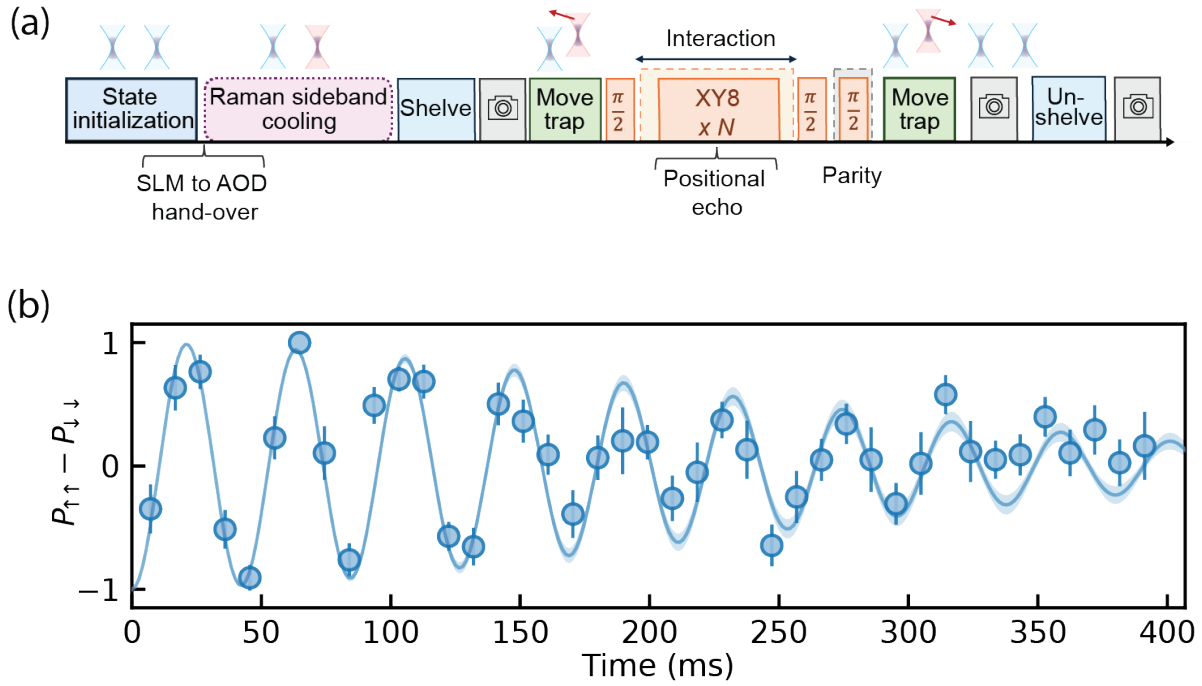


Figure 8.1: (a) Illustration of the experimental sequence. Molecules in the SLM and AOD traps are simultaneously Raman-sideband cooled and then moved to the interaction geometry. After the interaction, a $\pi/2$ analysis pulse with variable phase ϕ is used for parity measurement, followed by detection of both the $|\downarrow\rangle$ and $|\uparrow\rangle$ states. **(b)** A representative dipolar oscillation with $Q = 7.23(81)$.

perturbations [60].

The experimental sequence is summarized schematically in Fig. 8.1 (a). After initializing all the molecules in $|\uparrow\rangle$, we apply partial Raman sideband cooling with the molecules already arranged and transferred to the interleaved array, as SLM-to-AOD trap handover after cooling can introduce substantial heating, especially at large axial displacements. To narrow the motional distribution while minimizing loss into weakly coupled motional states, we apply only a partial sideband cooling sequence, which we characterized in Sec. 6.4, after which we estimate an axial occupation number of $\overline{n}_z \sim 10$.

As the final step of the cooling sequence also prepares the molecules in the $|\downarrow\rangle$ state, molecules are then directly moved to the target interaction geometry, where they evolve under dipolar exchange with the geometric echo applied. In Fig. 8.1B, we show the resulting dipolar spin-exchange dynamics of partially cooled molecules at $(\theta = 70°, z_0 = 1.42\ \mu\text{m}, r_\perp = 1.9\ \mu\text{m})$, yielding an interaction quality factor $Q = 7.23(81)$, a 17% improvement relative to without

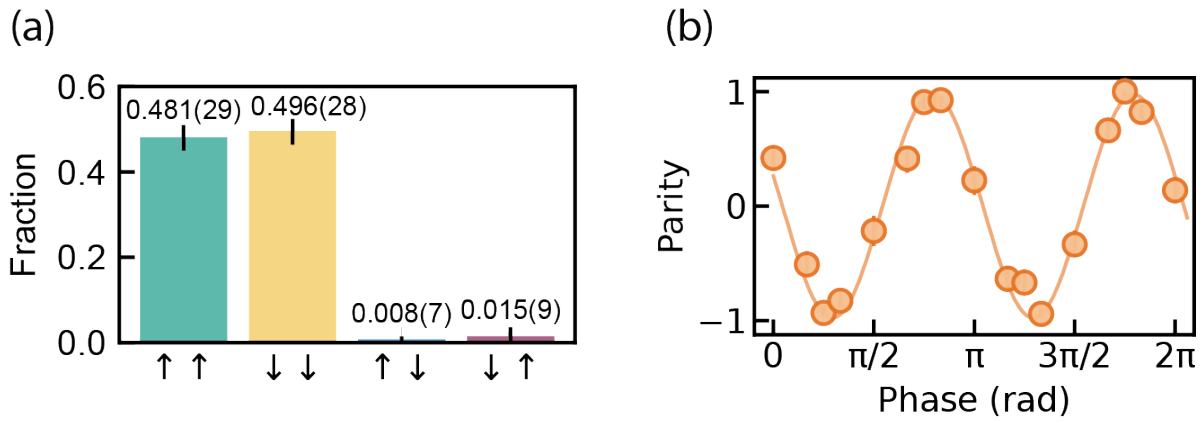


Figure 8.2: (**a**) Pair population statistics, measured in the computational basis at $t = 11.2$ ms of dipolar exchange evolution, corresponding to the $\pi/2$ point of the two-particle population oscillation. (**b**) Parity oscillations for a two-particle Bell state measured at the same evolution time. The fitted parity amplitude is $A_\Pi = 0.974^{+0.013}_{-0.018}$. Combining this with the pair populations in (a), we infer a Bell state fidelity of $\mathcal{F} = 0.976^{+0.008}_{-0.011}$.

sideband cooling.

Since the magic geometry is fundamentally insensitive to temperature, further cooling to the motional ground state is only expected to provide a modest gain in dipolar coherence. Remaining decoherence is dominated by uncorrected axial position noise, while additional cooling cycles incur additional population loss.

Using these experimental parameters, we generate a maximally entangled two-molecule Bell state by evolving the system for 1/4 of the oscillation period, as outlined in Sec. 8.1. The state is characterized by the measured two-qubit populations and by a parity measurement, shown in Fig. 8.2 (a, b).

After applying a $\pi/2$ pulse with variable phase ϕ, we measure the parity $\Pi(\phi) = P_{\uparrow\uparrow} + P_{\downarrow\downarrow} - P_{\uparrow\downarrow} - P_{\downarrow\uparrow}$. A sinusoidal fit yields the parity oscillation amplitude $A_\Pi = 0.974^{+0.013}_{-0.018}$, see Figure 8.2 (b). Combining this with the measured populations $P_{\uparrow\uparrow} + P_{\downarrow\downarrow}$ (Fig. 8.2 (a)), we infer a fidelity of $\mathcal{F} = 0.976^{+0.008}_{-0.011}$, conditioned on molecules surviving through state preparation and partial sideband cooling.

This fidelity is comparable to previous exemplary demonstrations of entanglement with assembled polar molecules near their motional ground state ($\overline{n}_z < 1$) [11, 12] (Fig. 8.3, despite the molecules here having an axial occupation of $\overline{n}_z \sim 10$. The primary further limitations to

improving dipolar coherence are threefold. First, the single-body coherence time is limited, partially due to black-body excitation between different vibrational states. Second, our current echo protocol does not cancel axial position disorder, which we estimate to be on the order of $\sim$ 50 nm over the timescale of this measurement. Dynamic tweezers in three dimensions [236, 237], a cryogenic environment [246, 247], and magic-wavelength trapping [5] provide clear avenues for improvement. Third, improved cooling to $\overline{n}_z < 1$ would further reduce higher-order thermal effects. Each of these improvements compounds, and all three of these in conjunction would result in Bell state fidelities of $\mathcal{F} \geq 0.999$.

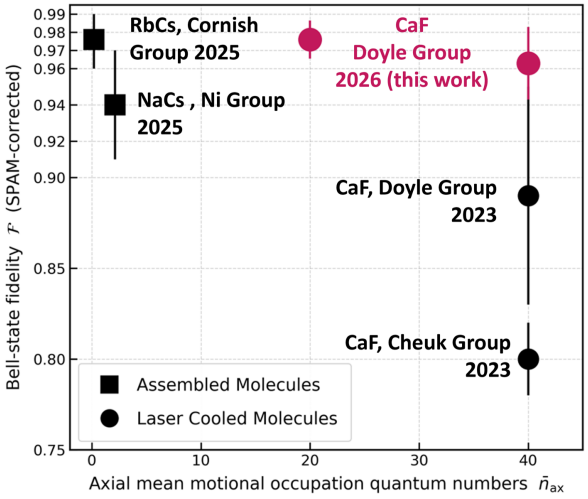


Figure 8.3: Reported SPAM-corrected Bell state fidelity in molecular tweezer platforms, plotted against reported mean motional occupation.

8.3 Future Avenues for Improving Fidelity

The Bell-state fidelity reported in this work ($\mathcal{F} = 0.976^{+0.007}_{-0.013}$, oscillation quality factor $Q \approx 7$) is limited by a combination of single-body decoherence, residual thermal motion, and tweezer position disorder. Here we outline a sequence of upgrades, each addressing a distinct one of these limitations.

Axial position disorder. As mentioned in Sec. 7.7, one of the remaining dominate sources of inhomogeneity in dipolar interaction strength is the shot-to-shot relative position disorder

in axial direction of tweezer traps. The current geometric echo we implement is only in 2D, targeting only position noise in radial direction. If one can the lower effective axial fluctuations, either through passive stability or 3D echo, then one can choose to operate the dipolar interaction at a second magic angle condition, near $\theta = 20°$, which has a larger interaction strength and would give a factor of 2 increase in Q for a fixed T_2.

Reduced thermal occupation. Once positional disorder is suppressed below the thermal extent of the molecular wave packet, the residual thermal occupation of the motional modes becomes the leading source of J-disorder. This remains true even at the magic configuration, since the static magic-angle condition cancels sensitivity to thermal motion only to leading order.

Figure 8.4 shows the simulated effect of reducing thermal occupation on dipolar quality factor Q, as defined in Chapter 7. From this, is clear that reducing $\bar{n}_z$ through Raman sideband cooling increases Q only when axial disorder is sufficiently well controlled. For larger σ_z, the spread in the mean relative axial position dominates the disorder in J, so further cooling gives a smaller improvement.

Therefore, with additional cooling toward the motional ground state [194], we expect one to be able further improve Q and to push the achievable Bell-state fidelity across the 99% threshold.

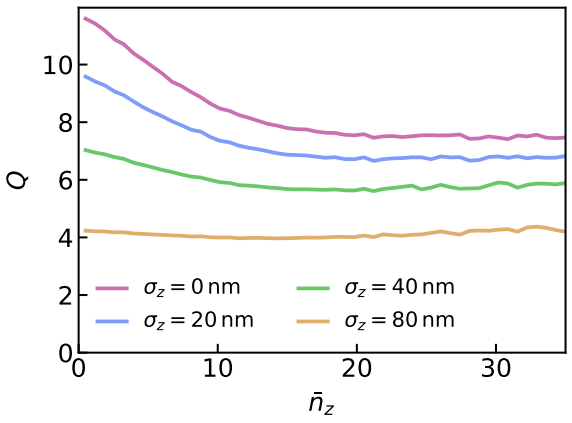


Figure 8.4: Simulated interaction quality factor Q as a function of mean motional occupation $\bar{n}$ for different rms axial position disorders σ_z. The simulation uses the two-step geometric echo configuration $(r_\perp, \theta, z_0) = (2\,\mu\text{m}, 70°, 1.8\,\mu\text{m})$.

Tighter interaction geometries. Tighter interaction geometries increase the dipolar coupling, but at the same time amplify sensitivity to positional disorder. Once both tweezer position disorder and thermal motion are sufficiently suppressed, reducing the interparticle spacing offers a further improvement in fidelity by enabling faster entangling operations relative to the single-body coherence time. Placing molecules in an optical lattice would allow spacings well below the diffraction limit of our objective, and would further mitigate site-to-site fluctuations.

Magic-wavelength trapping. Operating the array at a magic wavelength, where the differential AC Stark shift between the qubit states vanishes, would extend T_2 toward the black-body radiation (BBR) limit and provide a further improvement in Q [12]. This upgrade is particularly synergistic with tighter interaction geometries, since it decouples the trap depth from the single-body coherence time.

Black-body radiation correction. Single-body coherence in the present experiment is partially limited by black-body excitation between vibrational states, with a $1/e$ lifetime of $\tau_{\mathrm{BBR}} \approx 3.4$ s at room temperature. Of the total experimental sequence, the dipolar gate itself occupies ≈ 12 ms, while the remaining overhead from shelving, tweezer rearrangement, and imaging preparation amounts to ~ 100 ms, contributing a population-loss floor to the measured fidelity. This contribution can be corrected at the state-preparation-and-measurement (SPAM) level by shelving $|\uparrow\rangle$ into a long-lived rotational manifold (e.g. $|N = 0, F = 1, m_F = 1\rangle$) and resonantly clearing thermally repopulated vibrationally excited states prior to readout [248]. A cryogenic enclosure [246, 247] or a suitable conducting enclosure [249] could suppress the relevant black-body photon density and extend τ_{BBR} by orders of magnitude, removing BBR as a relevant limit on the timescales considered here.

The future ain't what it used to be.

Yogi Berra, probably

9

Conclusion and Outlook

9.1 Concluding Remarks

Polar molecules have been a tantalizing resource for quantum science, with the idea using molecules as qubit dating back more then two decades ago [25]. Just over the span of last three years, progress of molecular tweezer arrays, including the work described here, have started to turn proposals for molecular qubits into experiments with high-fidelity two-molecule entanglement. In this dissertation work, we identify the central limitation across these molecular tweezer systems: dipolar interactions are highly sensitive to the relative position of the molecules, so any motion of molecules in optical traps degrades the interaction coherence and limits the entanglement fidelity. A key idea developed here is geometric control can be used to reduce its sensitivity to thermal motion by controlling its geometry. We further show that a molecule can be moved during the interaction while preserving the coherence of ongoing entangling operations.

Looking more broadly, this newly demonstrated capability means that in molecular tweezer arrays, motion is not only a tool for assembly and rearrangement, but can also be a part of the entangling operation. As dipolar interaction depends on both the relative molecular distance and angle, we can use dynamic control of molecular positions to change Hamiltonian during coherent evolution, making spatial control complementary to microwave dressing Floquet engineering, and digital gate sequences. This can also open the paths towards molecular systems in which entangling gates are protected by geometry [66, 67], many-body dynamics can be made less sensitive to disorder [68], and the graph of effective dipolar couplings can be programmed in time [69, 70].

9.2 The Road Ahead

Besides taking advantage of the geometric control as a new fundamental resource for programming molecular entanglement, there are several technical ways to improve the geometric control in our present experiment. These include making a full three-dimensional AOD tweezer system to extend echo cancellation to axial direction. Once technical position noise is reduced, smaller intermolecular separations could be used to increase the dipolar coupling and shorten the entangling time, although this will place stronger demands on motional control, trap stability, and suppression of loss at close spacing.

As interaction errors are reduced, it is clear that single-particle coherence will also become increasingly limiting. For room-temperature tweezer experiments like ours, blackbody-radiation-induced population loss can put a significant bound on the single body coherence. Detecting and correcting such errors into erasure errors may become important as molecular arrays move toward deeper circuits and longer coherent evolution.

Scaling to larger arrays and working with many-body system will require continued improvements in loading, rearrangement, imaging survival, and state preparation.

Beyond quantum information and simulation, the molecular entanglement we have demonstrated may also be useful outside quantum information. As molecules are powerful probes of

small energy shifts, including those associated with symmetry-violating physics, and entangled molecular states could eventually improve the sensitivity of such measurements.

Finally, although CaF is considered to be significantly more complex than an atom, but in grand scheme of molecules, it is still a relatively simple diatomic. Polyatomic molecules can bring even richer internal structure and new opportunities. For example, recent progress with calcium monoamide ($CaNH_2$), has shown photon cycling and transverse laser cooling of an asymmetric-top molecule [250]. One can imagine the level of exquisite control demonstrated here for CaF can eventually be extended to more complex quantum objects.

A

High-field Coil Design and Assembly

The Raman sideband cooling scheme in our work (see Sec. 6.4) is performed at magnetic field on the order of $200 - 450$ G. At such high field, the electron spin S and nuclear spin I are roughly decoupled from the rotational angular momentum N. This helps to isolate a smaller manifold of states and suppress optical pumping transitions that can change m_S or m_I, reducing the number of photons scattered in each cooling cycle.

This chapter describes the design, construction, and characterization of the magnetic coils that are placed around the science glass cell to reach the high fields. The system consists of three different orthogonal coil pairs, designed to provide homogeneous fields from while retaining the large optical access. In practice, a single pair capable of reaching the field is sufficient, but at the initial stage, we decided to design coils in all three directions to leave some flexible of choice.

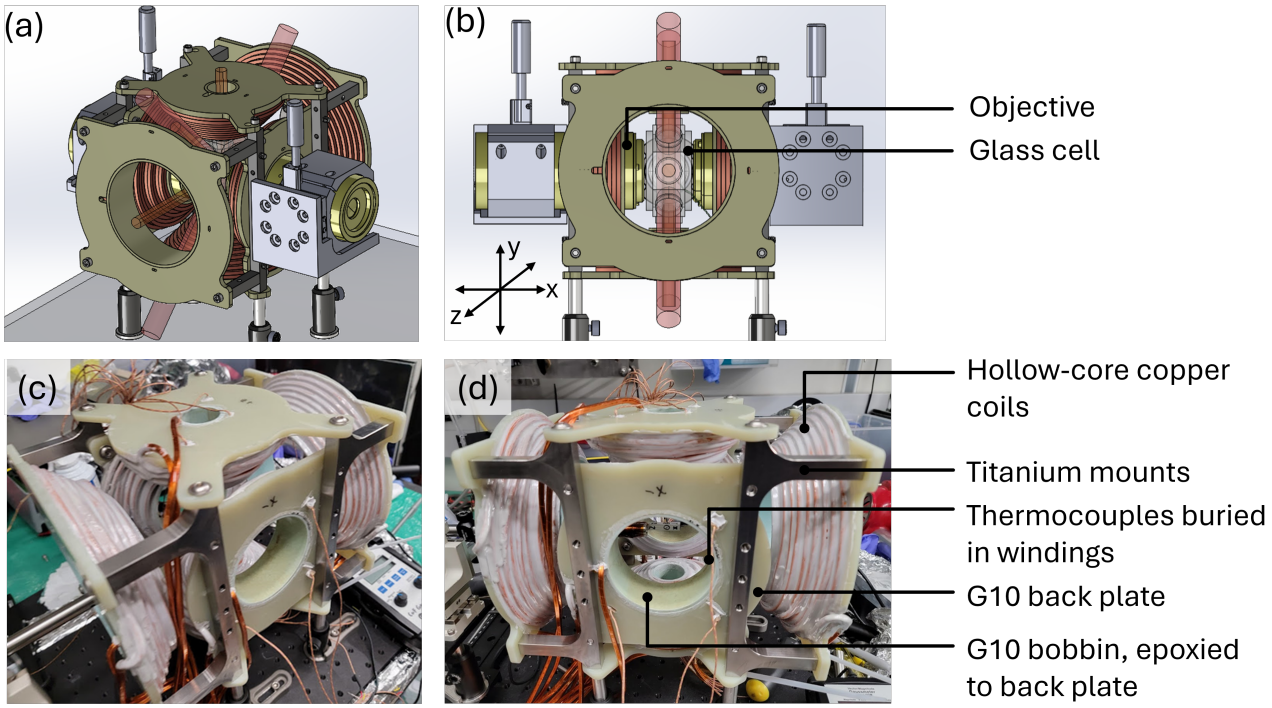


Figure A.1: High-field coils assembly surrounding the science glass cell. (a, b) CAD model views of three orthogonal coil pairs, along with objective, glass cell and laser beam; the coordinate convention used throughout this section is indicated in (b). **(c, d)** Corresponding coils as built (images shown are taken before darkening is applied). The hollow-core copper windings are supported on electrically insulating G10 structures, and mounted around the glass cell with nonmagnetic titanium supports.

A.1 Overview and Design Considerations

Design goals. The primary requirement is to generate spatially uniform magnetic field of up to 500 G across field of view of the objective (~ 100 μm) using the available Delta Elektronika SM18-220 current supply. The target is to reach 300 G at current ≤ 200 A for CW operation, with larger fields accessible with pulsed operation. At the same time, the coils must fit closely around the glass cell without obstructing the imaging, Raman, and optical pumping beams. Any water-cooling system needs to be leak-proof.

Several additional considerations also set the design principles:

- Magnetic field near coil center scales at $B \propto N \times I$, where N is the number of wire turns and I is the current. Having more windings lowers the required current to reach a given

field. But as we are contained to finite winding volume, this means the wires would need to be thinner for more windings, and consequently increasing the inductance, which scales roughly as $L \propto N^2$.

- The high field also need to settle reasonably fast on experimental timescale, when being pulsed or switched. The current dynamics is limited by by the voltage across the coils with internal winding resistance R, $V = L\frac{dI}{dt} + IR$. So large number of turns means larger inductance, which then limits the current slew rate for a fixed power-supply compliance voltage.

- Rapidly switching the magnetic field will lead to quick change of currents in the coils and can induce eddy currents in nearby objects, such as metal chambers, optics mounts, etc. The mounts for the coils should be nonmagnetic, and one needs to be careful about eliminating magnetic objects around the coils.

- For active water cooling, we want to have good thermal contact between the cooper wires and the coolant. The cooling system should ideally not have o-ring sealing, since any leaks can get onto glass cell and destroy the nano-texture coating.

Final design and materials. The available geometry is dominated by the optical access around the octagonal science glass cell, as we need to allow space for many beams enter through all 8 of the glass cell windows while placing coils are close to molecules as possible for high field. Note our the nano-textured AR-coating on our glass cell is particularly useful here, as beams can shoot through any angle, instead of being at Brewster's angle).

In the final design, we have three orthogonal coil pairs that have different shapes. The geometries and spacings for each coil pair are optimized in COMSOL. The final arrangement (without darkening paint applied) is shown in Fig. A.1.

The three field axes are X, Y, and Z, and we use them to refer the corresponding coils in that direction. The X pair surrounds the microscope objective and generates a field along the objective axis, the Z pair generates the vertical field, and Y pair is the large-diameter pair. The X pair (objective pair) is geometrically the most constrained as it goes around the microscope objective, which has an outer diameter of approximately 74 mm (2.9 in).

Other essential material and design choices are as follows:

- The conductor wires we choose are square hollow-core copper tubing, whose outer surface is wrapped with two layers of Kapton for electric insulation. The tubing has nominal

outer dimension of 4×4 mm^2 and 2×2 mm^2 core allowing for water flow, giving a nominal cross section of 12 mm^2.

- Internal water cooling is better here than, say, a cooling plate, as it allows direct thermal contact of the copper throughout the winding with the water. Additionally, because the windings are tight and stacked, the impedance of internal tubing can be quite high. So, to maintain water flow, we use home-built high-pressure water system that supplies about 150 psi at each coil inlet.

- For each coil, the copper tubing is wound on a lathe (see Sec. A.3), bonded to G10 structure that consists of a backing plate and a bobbin, and held together by filling the windings with nonmagnetic epoxy. The winding procedure and associated tooling are described in Sec. A.3.

- G10 fiberglass laminate is chosen for the backplates and bobbins because it is mechanically strong, and electrically insulating, and nonmagnetic. The G10 structures are mounted on slender machined titanium rods. Using an insulating support also suppresses large eddy-current loops close to the coils. Slots are designed on G10 for feeding in the copper tubing to the bobbin for coil winding. Additional holes made throughout the back plates to allow thermocouple wires to come out.

- During coil winding process, we embed several low-profile thermocouples at various positions throughout the windings. Temperature readings from these sensors are used to monitor and interlock the power supply in case of loss of water flow or unexpected excessive heating. Fig. A.2 shows an example of the thermal sensor.

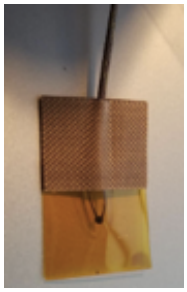


Figure A.2: Ultra-low profile K-type thermocouples (Evosensors).

- The binding epoxy (Duralco NM25) used here is specifically chosen for its non-magnetic filler and temperature compatibility. During development, we have tested other similar black high-temperature epoxies, including Duralco 4525, and they showed an appreciable magnetic response even though they are advertised to be "non-magnetic", since they contain iron oxide as a filler. Note that the there is also a "high-viscosity" variant of the

epoxy used (Duralco NM25 HV). Practically, this is much more difficult to apply during coil winding due to its high viscosity and limited working time.

- The cured epoxy finish is white and rather glossy, so we darken the coils to reduce scattered light off the surface. This is done by first sanding and cleaning the cured epoxy to prepare the surface, then using air sprayer to apply a layer of carbon-black coating (Aeroglaze Z306, diluted by 15% with Aeroglaze 9958 thinner) on top of the cured epoxy. The resultant darkend coils are shown in Fig. A.3. Strong adhesion of the coating is important because as small particulates falling onto the nano-textured glass-cell windows could be highly damaging, especially in the presence of high-power optical beams. An alternative popular black coating (MH-2200) was tested but showed substantially poorer adhesion to cured NM25 surface.



Figure A.3: Finished coils darkened with carbon-black coating (Aeroglaze Z306 diluted with Aeroglaze 9958 thinner).

- Installation: the mechanical assembly uses slide-in coil mounts and adjustable posts so that individual coils can be installed or removed without disassembling the microscope objective or glass cell.

A.2 Coil Simulations and Specs

We model each coil magneto-statically in COMSOL to determine the winding geometry compatible with the available space around the glass cell, while ensuring the required magnetic field can be reached with acceptable resistive dissipation. An example for the X pair is shown

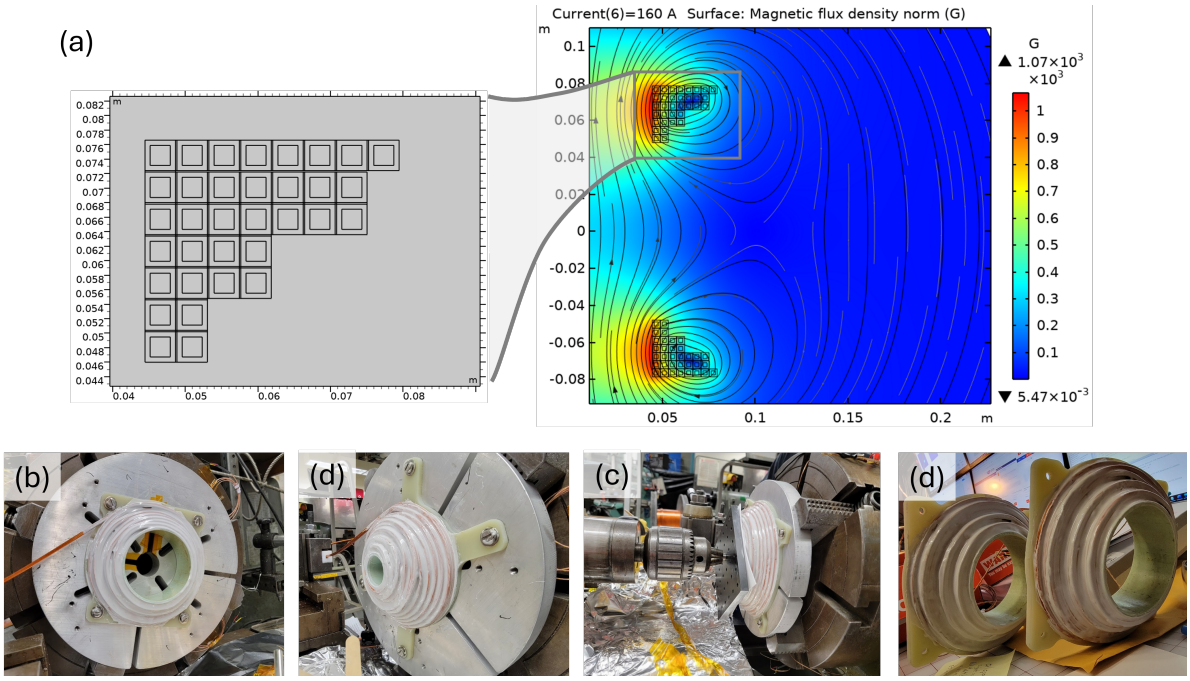


Figure A.4: (a) Simulation of generated magnetic field by the X pair at 160 A. Inset shows the cross section of the individual turns and the tapered winding profile. **(b-d)** constructed coils according to the models, showing the completed pair before blackening and assembly.

in Fig. A.4(a). Each winding is modeled using the measured copper tubing dimensions and the intended number of turns in each layer. Note that we reduce number of turns in the last two layers to taper the winding profile in order to leave a flat surface for adding a "dummy" coil for faster field switching and shimming. The completed windings are shown in Fig. A.4 (b-d), and main electrical and magnetic specs of the three coil pairs are summarized in Table A.1.

Coil pair	Num. of layers	B(200 A)	Resistance	Inductance	Simulated P(200 A)
X (objective)	7	450 G	58 mΩ	231.9 μH	1.63 kW
Y (long side)	8	277 G	62 mΩ	670 μH	2.35 kW
Z (vertical)	9	426 G	77 mΩ	267 μH	2.7 kW

Table A.1: Summary of the high-field coil specs. Listed magnetic fields are evaluated at center of coils at 200 A, Resistance and inductance are measured values, while dissipation powers are from simulation.

After fabrication, we characterize the field magnitude and spatial uniformity using a thin-head Gauss probe mounted on a translation stage and scan it through the center of each coil pair. Fig.A.5 shows the transverse scans for the X pair at 20 A, the Y pair at 20 A, and the Z pair

at 10 A. The measured profiles agree well with the COMSOL calculations. Near the center, around field maximum, each profile is fit to quadratic curve, and we find that the relative field variation over a displacement of 100 μm is below 0.006% for all three directions.

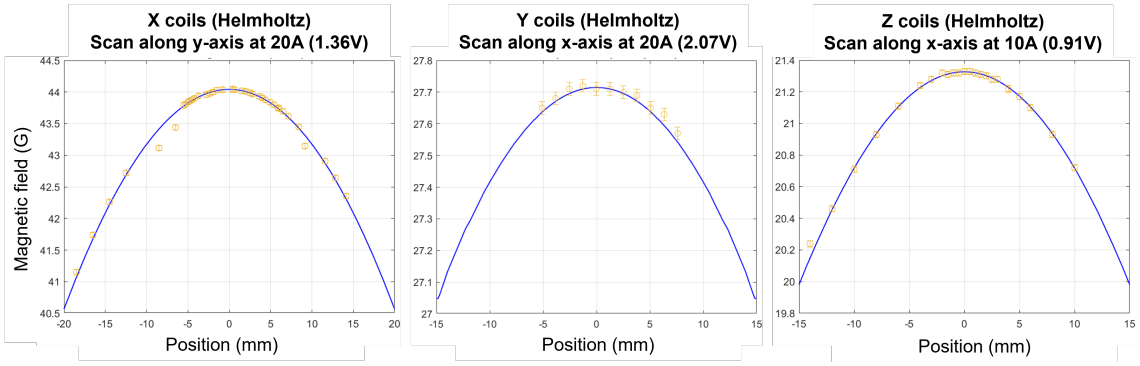


Figure A.5: Measured magnetic-field flatness of each of the three coil pairs. Points show the measured field and solid curves are quadratic fit to $B(x) = B_0 + ax^2 + bx$. The fitted curvature $2a$ around the center quantifies the field inhomogeneity over the ~ 100 μm molecular field of view.

In addition to magnetic fields, we also perform mechanical stress in COMSOL. For stress analysis, we want to ensure the G10 structures can support both the weight of the copper and the mutual magnetic force between the two coils. We estimate the attractive force in the model in two different ways: by integrating the Maxwell stress tensor around the coil and by integrating the Lorentz force density $\mathbf{J} \times \mathbf{B}$ throughout the winding. Both estimates give approximately 4.1 N at 180 A, much smaller then the gravitational load of the winding itself, which is about 20 N. Therefore, in the structural model we use and distribute a total load of 25 N over the G10 support plate. The predicted deformation is only a few tens of μm, well below the mechanical clearances around the glass cell and microscope objective.

A.3 Coil Winding and Fabrication

The copper tubing is wound layer by layer around the G10 bobbin on a lathe, using the spindle as a slowly rotating winding fixture, with epoxy applied during winding to fix the turns in place. The entire setup is shown in Fig. A.6.

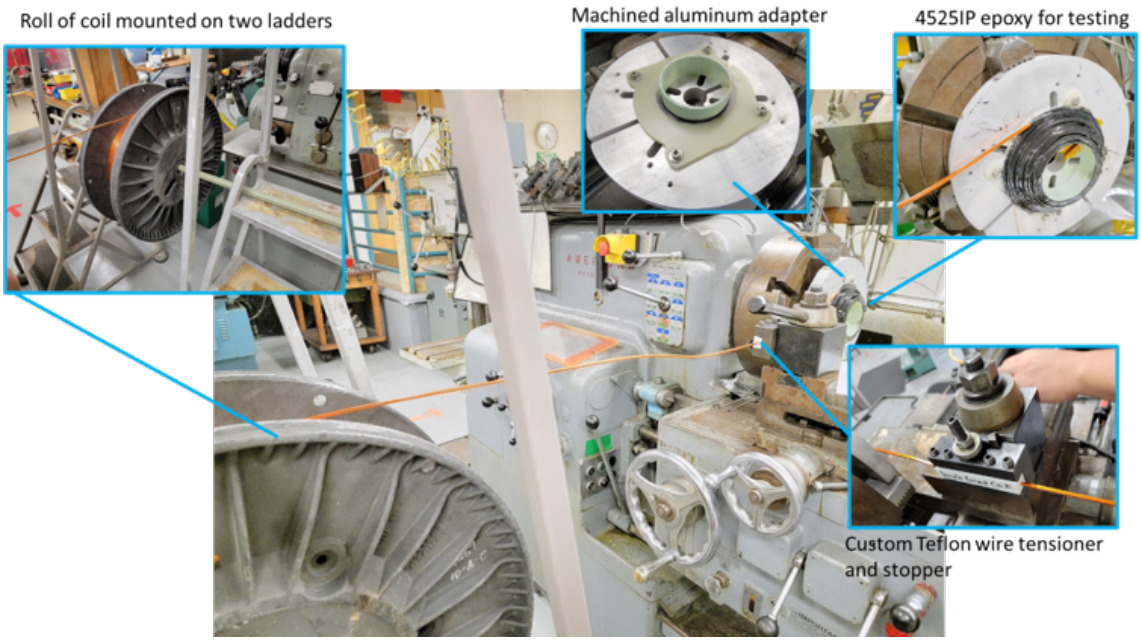


Figure A.6: Coil winding setup on the lathe. The G10 bobbin is mounted to the lathe using an aluminum adapter plate, and the hollow-core copper tubing is fed onto the bobbin as the spindle is rotated slowly. A custom Teflon guide straightens the tubing before it reaches the winding, while the individual turns are positioned by hand and bonded in place with epoxy as each layer is formed. Insets show the G10 backplate with bobbin and aluminum adapter, a partially wound coil, and the tubing-guidance tools used.

Note 2 *Safety Warning: This procedure requires two people. One person must keep a hand on the emergency stop button at all times.*

Several helpful tools and tips during fabrication are noted as follows:

- Because the lathe chuck could not reach the G10 backplate directly, a thick aluminum adapter plate is machined to hold the bobbin.
- The G10 backing plates are water-jet cut from 1/4-inch sheet. G10 material requires some care during water-jet machining, as we have found that the high-pressure piercing can force water between the fiberglass layers and delaminate the laminate. To solve this, we first cut an aluminum template, use it to pre-drill the G10 at each piercing location, and then align the part so that the water jet enters only through these pre-drilled holes.
- We cut a teflon wire tensioner to guide and straighten the copper tubing as it entered the winding.
- We guide and position individual turns by hand during winding using a plastic rod and rubber mallet, which allow small corrections without damaging the Kapton insulation.

- During the winding, we make small batches of epoxy since the working time is limited once the hardener is mixed in, and use soft brushes to apply the glue.

A.4 Thermal Performance

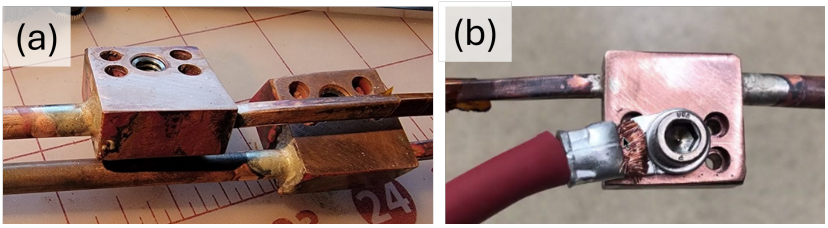


Figure A.7: Copper adapter block for water and electrical connection for the hollow-core coils. The adapter is machined with through holes for both the conductor and the 1/4-inch-OD water tube, together with a threaded electrical terminal. The copper conductor and water tube are brazed into the block.

To run water and current through the hollow-core copper conductor, we machine a copper adapter block and braze it to the end of each tubing, as shown in Fig. A.7. This copper block forms a low-resistance and leak-resistant joint, on which a Helicoil insert provides the bolted connection to the high-current cable.

We initially model the thermal design in COMSOL, using a coupled non-isothermal pipe-flow model. We choose a conservative input of 18 °C inlet water at 50 psi and assume 600 W of heat in a single coil. The model predicts a pressure drop of nearly 50 psi through the winding and a temperature difference of $3 \sim 0$ °C from inlet to outlet. In practice, we find that this substantially overestimates the temperature gradient. Testing on a prototype coil, we run continuously at 110 A for 2–3 hours using recirculating water without a chiller. After temperatures reach a steady state, the inlet water is at 29°C, while the outlet is at 33.3°C, giving only 4°C temperature difference and indicating that the internal water cooling is effectively distributed throughout the winding.

Finally, for active water cooling of the full sets of coils, we built a high-pressure water-circulation system capable of supplying about 150 psi at the each coil inlet. Note that it is

strongly recommended that proper high-pressure rated tubing and fitting are used; otherwise one might risk having a tubing burst out of some Swagelok connector one day and causing a little flood around the optical table. For a coil pair running continuously at 200 A and with water temperature at 27.9°C, we measure temperatures between 32 and 37°C from thermocouples distributed throughout the windings, demonstrating substantial thermal margin even under continuous operation.

B

Dynamic Optical Ring Trap

B.1 Motivation

Prior to the development of a conveyor MOT (see sec.5.2, the molecular cloud that gets optically transported from MOT chamber to science glass cell is spread over roughly 1 mm axially. The transported cloud is much larger than the $\sim$ 100 μm region spanned by the projected optical tweezers. This means tweezer loading only samples a small fraction of the transported cloud. Furthermore, before the development of the conveyor MOT (see Sec. 5.2), the number of molecules in the cloud was not enough to saturate and provide a stable tweezer loading. One natural way to improve the spatial overlap is to shrink the molecular cloud smaller after transport, just before loading the tweezers. An approach to achieve it is by using a blue-detuned repulsive optical potential to form barriers around molecules and one can close in the barriers. This was first proposed and demonstrated for CaF in Ref. [251], where a dynamically tunable ring-shaped repulsive trap is used and the ring size is tuned using liquid

lenses. In a blue-detuned trap, molecules are attracted to intensity minium, and so they are confined in the dark region bounded by repulsive light. The trap in principle can have very large spatial volume, and the molecules experience only minimal light shifts. Following this idea, here we describe the implementation of a compact tunable ring trap system on our apparatus.

B.2 Optical Principle and Compact Layout

The trap is formed from 531 nm light coming from a spare 1 W laser, blue-detuned from the $X - B$ main transition. The ring is generated by sending a Gaussian beam through an axicon. The axicon converts the input beam into an annular beam, with the output containing residual light in the center. This residual light is undesirable to use as extra light in the center induces ac Stark shifts and photon scattering from the molecules; i.e. we make to keep the center as dark as possible and have a sharp repulsive potential edge. To clean up the output, we add an annular aperture mask after the axicon, and all subsequent optics relay this clean ring to the molecular plane.

The key feature of the system is that the projected ring is tunable. This is realized by forming a variable telescope with two electrically tunable lenses. By changing their focal lengths together, the ring can be magnified or de-magnified while remaining focused at the molecular plane. In the end, the system will allow us to start with a large ring that overlaps the transported cloud and then compress it to a denser cloud for more efficient loading. The final optical layout is shown schematically in Fig. B.1, which was first modeled and optimized in Zemax.

The beam first passes through a 2-degree axicon (Thorlabs) to generate the annular intensity distribution. An f =30 mm lens focuses the annulus onto a 1-mm annular mask, which clips off residual light in the center of the beam. The cleaned annulus is then relayed through an $f = 75$ mm lens and then a tunable telescope made of two electrically-tunable lenses. The two tunable lenses are separated by about 240 mm and are followed by a final 100-mm imaging lens to project the ring at the plane of molecules. The ring size tuning range is set mainly by

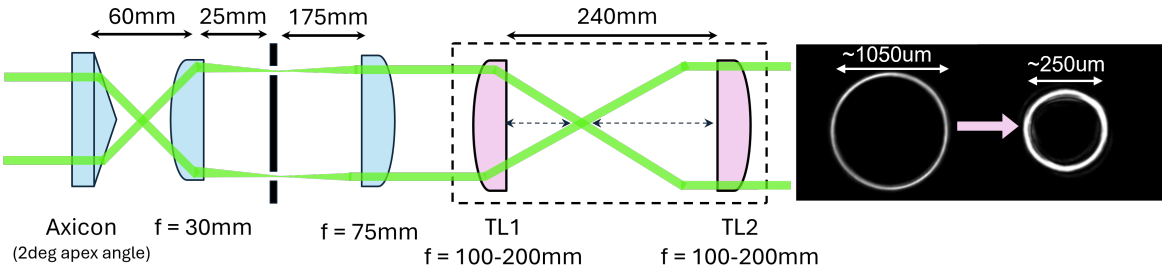


Figure B.1: Optical layout of the dynamically tunable ring trap. A 531 nm Gaussian beam is converted into an annular beam using an axicon, where a subsequent annular aperture mask the removes residual light in the center of the beam. The cleaned ring is then relayed through a tunable telescope formed by two electrically tunable lenses and projected to the molecule plane with a final imaging lens. By changing the two tunable-lens voltages together, the ring diameter can be varied dynamically from approximately 1050 μm to 250 μm.

the clear apertures of the lenses, and by the annular aperture. In our implementation, the calibrated ring diameter could be tuned from approximately 1 mm down to a 250 μm. This range is well matched to our experimental needs, where the large ring captures almost all of the transported cloud, while the compressed ring approaches the scale of the tweezer loading region.

The entire system is mounted in a vertically layout on a translational stage to fold the beam paths and keep the setup compact, since the real estate near the glass cell is quite scarce. The compact, portable assembly is shown in Fig. B.2 and Fig. B.3(b).

B.3 Ring Size Calibration

For the tunable ring trap to work, both of the tunable lenses need to be driven together. To perform the 2D calibration, We first do a coarse scan of both driving voltages applied to the lenses, and image the produced ring on a camera. For each voltage pair, we fit the projected ring to extract both the ring size and the wall width. This way, we identify and map the voltage combinations can generate a clean ring at correct image plane. Afterwards, we perform another round of finer voltage scan around the more experimentally relevant sizes and fit the resulting calibration curve and save the mapping. Finally. the control script takes as input the desired initial ring size, final ring size, and a number of compression steps, and then outputs a

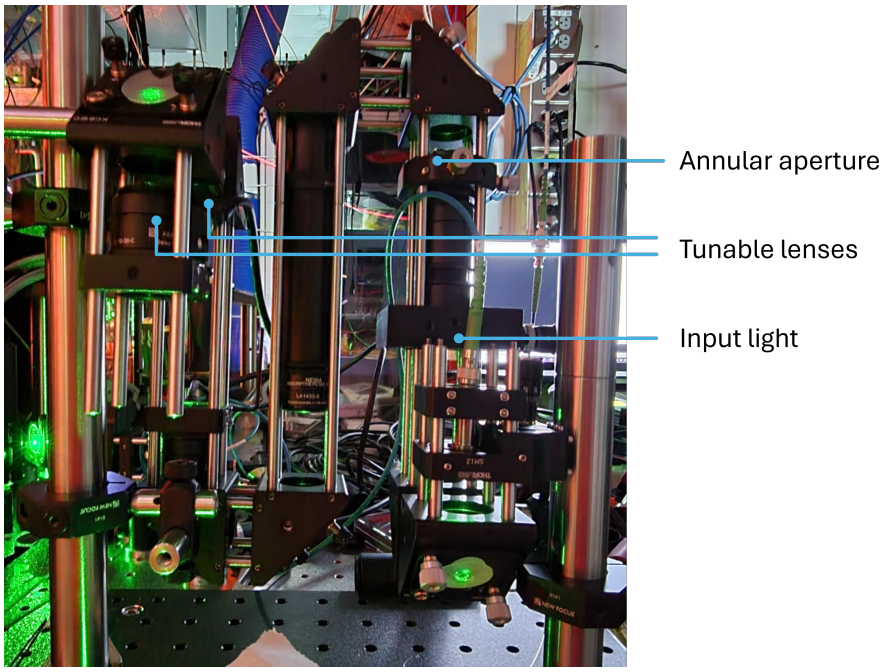


Figure B.2: Compact vertical assembly of the ring trap optics. All the optics are mounted in a vertical cage system to fold the beam path without taking up too much table space, making the setup compact enough to fit above the science glass cell.

synchronized voltage lists for the two tunable lenses. During an experimental sequence, these voltages are applied as a ramp so that the ring compresses smoothly.

B.4 In-Situ Alignment using Raman Scattering and Performance

Here we describe a useful trick to align the ring in-situ through the tweezer imaging path. The tweezer imaging optics are designed and filtered for 606 nm fluorescence and so one might expect it to be difficult to image 531 nm ring trap light on the EMCCD through the filters. In practice, the EMCCD is sensitive enough that many ordinary objects placed close to the molecular plane can produce detectable red-shifted Raman fluorescence background when illuminated by 531 nm light. The scattered light can pass through the 606-nm imaging filters and be detected by the EMCCD. Note that for less sensitive cameras, an alternative target is to put a small amount of Rhodamine 6G dye on paper and use it as a bright fluorescence target.

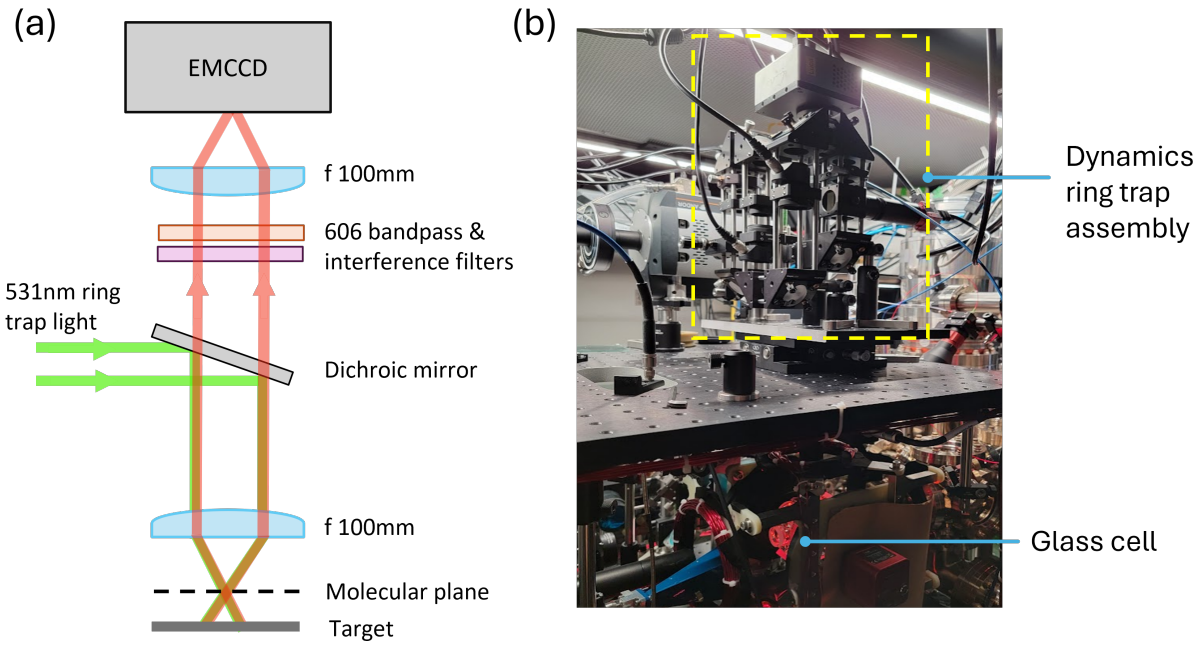


Figure B.3: (a) Schematic of the imaging path in the in-situ transverse alignment of the ring trap. Input 531 nm ring is sent through the ring-trap projection optics onto a Raman scattering fluorescent target placed below the glass cell. Red-shifted scattered light near the 606 nm is collected through the imaging path used for molecule detection and recorded on the EMCCD. **(b)** Experimental implementation. The ring trap assembly is mounted on the upper optical table above the glass cell, and the 531 nm beam is projected downward through a cutout in the table toward the molecules.

This provides us with a convenient in-situ transverse alignment method. We put a small piece of fluorescent paper with Raman shifts around 600 nm under the glass cell, send in the 531 nm ring which gets projected through the glass cell windows onto the paper and induce 600 nm ring fluorescence. The resulting annulus is imaged on the EMCCD through the tweezer objective and imaging path. With this information, we adjust the centering of the ring in-situ.

In our initial measurements, upon turning on the ring trap, we can visibility see that the ring wall cut into the molecular cloud, and after allowing the cloud to expand the ring prevents molecules from diffusing outward. By scanning the tunable lens driving voltages and the translation stage position of the ring relative to the transported cloud, we observe clear compression of the molecular distribution.

We then compare the measured loading efficient with and without the ring trap with 225 mW, compressing from ~ 1000 μm to 250 μm, corresponding to a $4\times$ compression ratio and

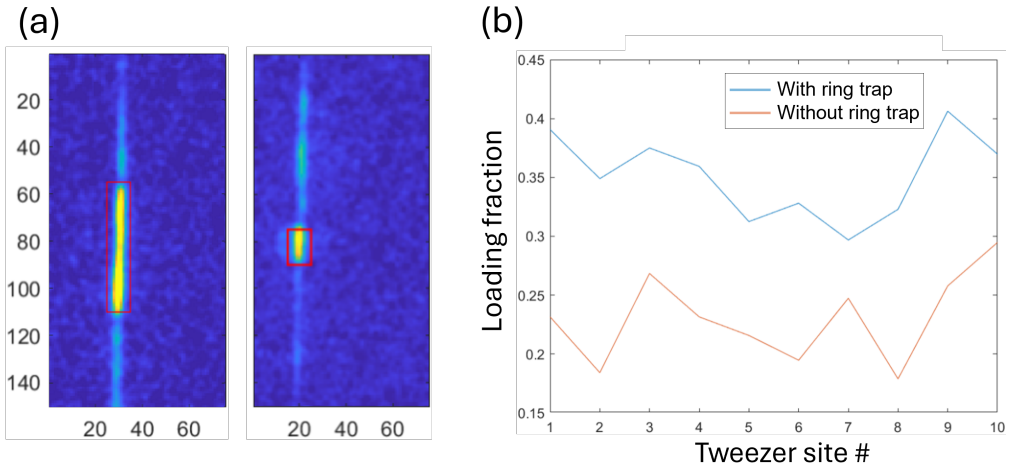


Figure B.4: Ring-trap compression and effect on tweezer loading. (a) Images of the projected 531 nm ring initially (left) and at the end of compression (right), showing dynamic tuning of the ring diameter from approximately 900 μm to 250 μm, respectively. **(b)** Tweezer loading rates with and without ring trap compression.

expected density increase of about 3.5 accounting for some loss of molecules during compression. Fig. B.4(a) shows imaged cloud with initial ring trap size (left) and the cloud with final ring size (right). The loading data is shown in Fig. B.4(b), where we see that with the spatial compression, the average loading rate improves from about 25% to a saturated 40% upper bound. Additionally, we still see the improved loading after lowering the trap power by four times to $\sim$ 57 mW. We have also observed that keeping the 531 nm ring light on during the tweezer-loading step can be detrimental, so the ring trap is only used for pre-loading compression.

With the later implementation of the conveyor MOT later, the ring trap became of no longer service to us. Although it did not become the central loading method, this is relatively simple design can be used to dynamically compress a molecular cloud.

C

Indium-Seal based Cryogenic Cell

C.1 Motivation

The CaF molecular beam in our apparatus is produced in a cryogenic cell machines from high-purity Cu101 for its excellent thermal conductivity at cryogenic temperatures of few Kelvins. The cell that we have been using is assembled from several removable copper plates, as shown in Fig. C.1 where main components are labeled. The surfaces between them are sealed using thin Kapton films coated with cryogenic grease, which then get compressed when the cell is bolted together. This technique is very simple and, for the most part, has worked well in practice, but the final sealing ultimately depends on how evenly and with how much torque the person assembling the cell tightens. Ideally, helium buffer gas exists the cell predominantly through the beam aperture. Small leak of helium gas will change the flow dynamics and molecular production, affecting the downstream MOT. So to ensure the assembled cell is leak-tight, one would check by flowing in helium while temporarily blocking the aperture with,

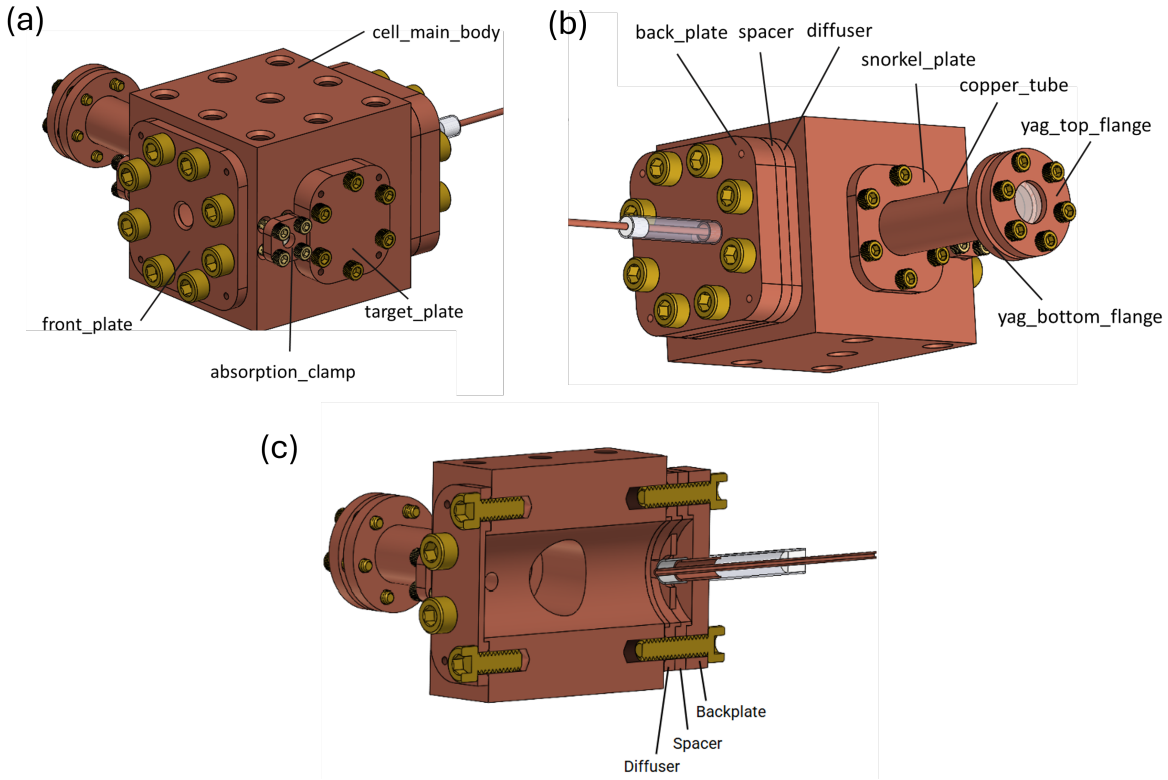


Figure C.1: CAD model of the indium-sealed cryogenic buffer-gas cell. (a,b) Exterior views of the assembled cell, showing the front plate, target plate, snorkel with YAG window, and gas inlets. **(c)** Sectioned view showing the internal cell volume, diffuser, spacer, back plate, and gas inlet.

say, a finger, to feel the pressure build-up inside the cell.

To make the sealing more reproducible, we design a cell in which sealing is done through indium wire gasket instead. The cell exterior basically looks the same except for the bolt pattern, and retains all the features of the original cell. Inside, the Kapton gaskets are replaced with groves and lips designed for indium sealing.

C.2 Indium Seals and Cell Design

Indium is widely used as a compression gasket for vacuum and cryogenic systems because it is soft and remain malleable at low temperature [252]. The sealing mechanism is essentially plastic deformation and cold welding. When indium is compressed between two mating surfaces, it can flow into to fill small gaps and imperfections, forming a conformal seal. Clean indium

surfaces cold-weld to one another, so the overlapping ends of an indium wire gasket can join by compression to form a continuous ring.

There are several precautionary notes about indium seals. Indium gasket is intended to fill small gaps, and it needs to placed centered to the sealing region and be compressed uniformly. If too little indium is used, the gap might not be completely filled; on the other hand if there is too much indium, the metal can extrude out of the sealing region [253]. With this in mind, we design shallow groove to help position the wire more accurately during assembly, as well as to define the volume into which it can flow. In standard indium seal designs, the groove cross section are typically made a bit smaller than the original wire cross section, forcing the indium to deform laterally as surfaces are compressed [252].

Our indium cell design is summarized as follows:

- The four main copper–copper sealing surfaces have annular lip machined on faces of the cell body, while a matching recess is machined on the corresponding plate. The lip and recess are toleranced in opposite directions so that any machining errors preferentially err on increasing clearance instead of creating any interference or collision. The lip is designed to have nominal 0.060 in height, while the mating recess has a depth of 0.065 in. This leaves 0.005-in (0.127-mm) gap after we mat the lip and the recess, so that 0.5-mm-diameter indium wire will be compressed to about one quarter of its original diameter. The available flat sealing width is about 2.03 mm. The sealing geometry is shown in Fig. C.2.

- For the deal on small 6.3-mm optical windows, the available area is limited to just 1 mm of sealing width between the clear aperture and the edge of the glass, just enough for the 0.5-mm-wide indium gasket.

- For the window recesses, we also have to account for differential thermal contraction. Copper contracts much more than the window's BK7 glass between room and cryogenic temperature. Using integrated contractions for estimate, we get $\Delta L/L \simeq 0.32\%$ for copper and only $\sim 0.04\%$ for the glass, so clearance at room-temperature will reduce substantially once we cool down. Thus we oversize the recess diameters so that the copper would not clamp radially onto the windows at cryogenic temperature. For the 6.3-mm (0.2480 in) and 12.5-mm (0.492 in) cell windows, the resulting recess diameters are chosen to be 0.262 in and 0.520 in, respectively, including the manufacturer's window tolerances.

- The bolt pattern is placed so that indium should be compressed uniformly and gradually

around the complete gasket. We distribute fasteners closely around each sealing surface, which are designed to be tightened incrementally in an alternating pattern.

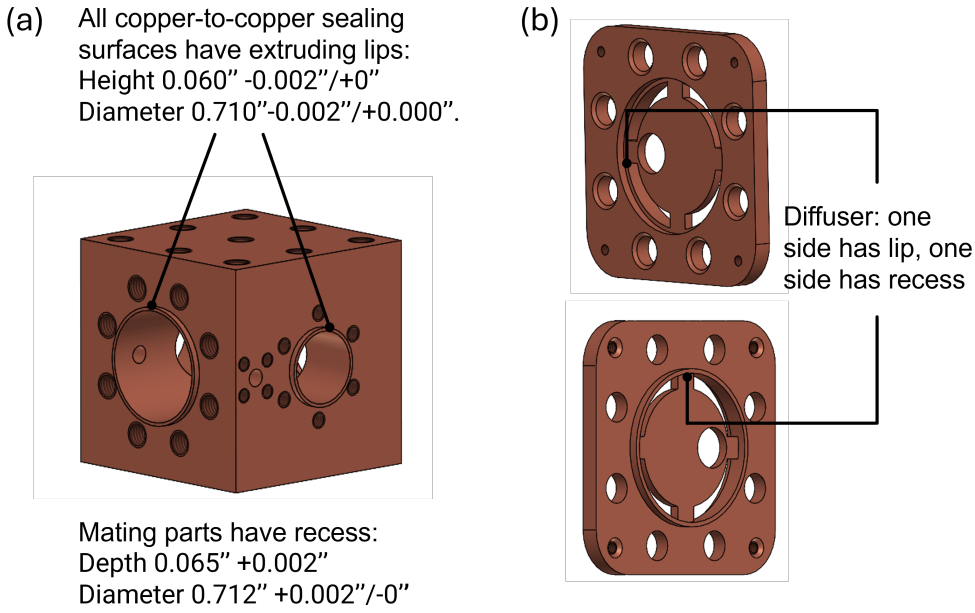


Figure C.2: Indium sealing surfaces on the cell body and mating plates. (a) Extruding lip machined on the main cell body. **(b,c)** Corresponding recessed features in the mating plates. During assembly, a 0.5-mm-diameter indium wire gasket is placed around each sealing lip and compressed as the plate is tightened.

In conclusion, the motivation of this design is reproducibility, and in principle, should make how leak-tight the cell is less sensitive to who happens to assemble the cell. In this indium version, the gasket diameter, locating groove, sealing lip's height, and flange spacing set the amount of indium material. The downside here is that this will create a considerably more laborious and time-consuming assembly procedure: one needs to position small-diameter indium wires in several narrow grooves, ensure the wire ends overlap properly, and tighten the screws evenly without accidentally moving the indium gasket. For full disclosure, although the cell described here was fully designed and machined, it has never been installed or tested on the experiment.

References

[1] WJ Childs, GL Goodman, and LS Goodman. Precise determination of the v and n dependence of the spin-rotation and hyperfine interactions in the caf x2σ12 ground state. *Journal of Molecular Spectroscopy*, 86(2):365–392, 1981.

[2] L Caldwell, JA Devlin, HJ Williams, NJ Fitch, EA Hinds, BE Sauer, and MR Tarbutt. Deep laser cooling and efficient magnetic compression of molecules. *Physical Review Letters*, 123(3):033202, 2019.

[3] Sean Burchesky, Loïc Anderegg, Yicheng Bao, Scarlett S Yu, Eunmi Chae, Wolfgang Ketterle, Kang-Kuen Ni, and John M Doyle. Rotational coherence times of polar molecules in optical tweezers. *Physical Review Letters*, 127(12):123202, 2021.

[4] Annie J Park, Lewis RB Picard, Gabriel E Patenotte, Jessie T Zhang, Till Rosenband, and Kang-Kuen Ni. Extended rotational coherence of polar molecules in an elliptically polarized trap. *Physical Review Letters*, 131(18):183401, 2023.

[5] Philip D Gregory, Luke M Fernley, Albert Li Tao, Sarah L Bromley, Jonathan Stepp, Zewen Zhang, Svetlana Kotochigova, Kaden RA Hazzard, and Simon L Cornish. Second-scale rotational coherence and dipolar interactions in a gas of ultracold polar molecules. *Nature Physics*, 20(3):415–421, 2024.

[6] Tom R Hepworth, Daniel K Ruttley, Fritz von Gierke, Philip D Gregory, Alexander Guttridge, and Simon L Cornish. Long-lived multilevel coherences and spin-1 dynamics encoded in the rotational states of ultracold molecules. *Nature Communications*, 16(1): 7131, 2025.

[7] Rahul Sawant, Jacob A Blackmore, Philip D Gregory, Jordi Mur-Petit, Dieter Jaksch, Jesús Aldegunde, Jeremy M Hutson, MR Tarbutt, and Simon L Cornish. Ultracold polar molecules as qudits. *New Journal of Physics*, 22(1):013027, 2020.

[8] Bhuvanesh Sundar, Bryce Gadway, and Kaden RA Hazzard. Synthetic dimensions in ultracold polar molecules. *Scientific reports*, 8(1):3422, 2018.

[9] Yicheng Bao, Scarlett S Yu, Loïc Anderegg, Eunmi Chae, Wolfgang Ketterle, Kang-Kuen Ni, and John M Doyle. Dipolar spin-exchange and entanglement between molecules in an optical tweezer array. *Science*, 382(6675):1138–1143, 2023.

[10] Connor M Holland, Yukai Lu, and Lawrence W Cheuk. On-demand entanglement of molecules in a reconfigurable optical tweezer array. *Science*, 382(6675):1143–1147, 2023.

[11] Lewis RB Picard, Annie J Park, Gabriel E Patenotte, Samuel Gebretsadkan, David Wellnitz, Ana Maria Rey, and Kang-Kuen Ni. Entanglement and iswap gate between molecular qubits. *Nature*, 637(8047):821–826, 2025.

[12] Daniel K Ruttley, Tom R Hepworth, Alexander Guttridge, and Simon L Cornish. Long-lived entanglement of molecules in magic-wavelength optical tweezers. *Nature*, 637(8047): 827–832, 2025.

[13] Jun-Ru Li, William G Tobias, Kyle Matsuda, Calder Miller, Giacomo Valtolina, Luigi De Marco, Reuben RW Wang, Lucas Lassablière, Goulven Quéméner, John L Bohn, et al. Tuning of dipolar interactions and evaporative cooling in a three-dimensional molecular quantum gas. *Nature Physics*, 17(10):1144–1148, 2021.

[14] Jun-Ru Li, Kyle Matsuda, Calder Miller, Annette N Carroll, William G Tobias, Jacob S Higgins, and Jun Ye. Tunable itinerant spin dynamics with polar molecules. *Nature*, 614 (7946):70–74, 2023.

[15] Calder Miller, Annette N Carroll, Junyu Lin, Henrik Hirzler, Haoyang Gao, Hengyun Zhou, Mikhail D Lukin, and Jun Ye. Two-axis twisting using floquet-engineered xyz spin models with polar molecules. *Nature*, 633(8029):332–337, 2024.

[16] Yukai Lu, Connor M Holland, Callum L Welsh, Xing-Yan Chen, and Lawrence W Cheuk. Probing coherent many-body spin dynamics in a molecular tweezer array quantum simulator. *arXiv preprint arXiv:2603.19090*, 2026.

[17] Andrea Micheli, Gavin K Brennen, and Peter Zoller. A toolbox for lattice-spin models with polar molecules. *Nature Physics*, 2(5):341–347, 2006.

[18] Alexey V Gorshkov, Salvatore R Manmana, Gang Chen, Jun Ye, Eugene Demler, Mikhail D Lukin, and Ana Maria Rey. Tunable superfluidity and quantum magnetism with ultracold polar molecules. *Physical review letters*, 107(11):115301, 2011.

[19] Bo Yan, Steven A Moses, Bryce Gadway, Jacob P Covey, Kaden RA Hazzard, Ana Maria Rey, Deborah S Jin, and Jun Ye. Observation of dipolar spin-exchange interactions with lattice-confined polar molecules. *Nature*, 501(7468):521–525, 2013.

[20] Kaden RA Hazzard, Bryce Gadway, Michael Foss-Feig, Bo Yan, Steven A Moses, Jacob P Covey, Norman Y Yao, Mikhail D Lukin, Jun Ye, Deborah S Jin, et al. Many-body dynamics of dipolar molecules in an optical lattice. *Physical review letters*, 113(19):195302, 2014.

[21] Bryce Gadway and Bo Yan. Strongly interacting ultracold polar molecules. *Journal of Physics B: Atomic, Molecular and Optical Physics*, 49(15):152002, 2016.

[22] Lysander Christakis, Jason S Rosenberg, Ravin Raj, Sungjae Chi, Alan Morningstar, David A Huse, Zoe Z Yan, and Waseem S Bakr. Probing site-resolved correlations in a spin system of ultracold molecules. *Nature*, 614(7946):64–69, 2023.

[23] Annette N Carroll, Henrik Hirzler, Calder Miller, David Wellnitz, Sean R Muleady, Junyu Lin, Krzysztof P Zamarski, Reuben RW Wang, John L Bohn, Ana Maria Rey, et al. Observation of generalized tj spin dynamics with tunable dipolar interactions. *Science*, 388(6745):381–386, 2025.

[24] Thomas Bilitewski, Luigi De Marco, Jun-Ru Li, Kyle Matsuda, William G Tobias, Giacomo Valtolina, Jun Ye, and Ana Maria Rey. Dynamical generation of spin squeezing in ultracold dipolar molecules. *Physical Review Letters*, 126(11):113401, 2021.

[25] David DeMille. Quantum computation with trapped polar molecules. *Physical Review Letters*, 88(6):067901, 2002.

[26] SF Yelin, K Kirby, and Robin Côté. Schemes for robust quantum computation with polar molecules. *Physical Review A*, 74(5):050301, 2006.

[27] Mallikarjun Karra, Ketan Sharma, Bretislav Friedrich, Sabre Kais, and Dudley Herschbach. Prospects for quantum computing with an array of ultracold polar paramagnetic molecules. *The Journal of chemical physics*, 144(9), 2016.

[28] Kang-Kuen Ni, Till Rosenband, and David D Grimes. Dipolar exchange quantum logic gate with polar molecules. *Chemical science*, 9(33):6830–6838, 2018.

[29] Simon L Cornish, Michael R Tarbutt, and Kaden RA Hazzard. Quantum computation and quantum simulation with ultracold molecules. *Nature Physics*, 20:730–740, 2024.

[30] Ivan Kozyryev, Zack Lasner, and John M Doyle. Enhanced sensitivity to ultralight bosonic dark matter in the spectra of the linear radical sroh. *Physical Review A*, 103(4): 043313, 2021.

[31] David DeMille, Nicholas R Hutzler, Ana Maria Rey, and Tanya Zelevinsky. Quantum sensing and metrology for fundamental physics with molecules. *Nature Physics*, 20(5): 741–749, 2024.

[32] TE Chupp, Peter Fierlinger, MJ Ramsey-Musolf, and JT Singh. Electric dipole moments of atoms, molecules, nuclei, and particles. *Reviews of Modern Physics*, 91(1):015001, 2019.

[33] William B Cairncross and Jun Ye. Atoms and molecules in the search for time-reversal symmetry violation. *Nature Reviews Physics*, 1(8):510–521, 2019.

[34] Ivan Kozyryev and Nicholas R. Hutzler. Precision measurement of time-reversal symmetry violation with laser-cooled polyatomic molecules. *Phys. Rev. Lett.*, 119:133002, Sep 2017. doi: 10.1103/PhysRevLett.119.133002. URL https://link.aps.org/doi/10.1103/PhysRevLett.119.133002.

[35] Nicholas R Hutzler. Polyatomic molecules as quantum sensors for fundamental physics. *Quantum Science and Technology*, 5(4):044011, 2020.

[36] Thorsten Köhler, Krzysztof Góral, and Paul S Julienne. Production of cold molecules via magnetically tunable feshbach resonances. *Reviews of modern physics*, 78(4):1311–1361, 2006.

[37] Cheng Chin, Rudolf Grimm, Paul Julienne, and Eite Tiesinga. Feshbach resonances in ultracold gases. *Reviews of Modern Physics*, 82(2):1225–1286, 2010.

[38] K-K Ni, S Ospelkaus, MHG De Miranda, A Pe'Er, B Neyenhuis, JJ Zirbel, S Kotochigova, PS Julienne, DS Jin, and Jun Ye. A high phase-space-density gas of polar molecules. *science*, 322(5899):231–235, 2008.

[39] Edward S Shuman, John F Barry, and David DeMille. Laser cooling of a diatomic molecule. *Nature*, 467(7317):820–823, 2010.

[40] JF Barry, DJ McCarron, EB Norrgard, MH Steinecker, and D DeMille. Magneto-optical trapping of a diatomic molecule. *Nature*, 512(7514):286–289, 2014.

[41] Loïc Anderegg, Benjamin L Augenbraun, Eunmi Chae, Boerge Hemmerling, Nicholas R Hutzler, Aakash Ravi, Alejandra Collopy, Jun Ye, Wolfgang Ketterle, and John M Doyle. Radio frequency magneto-optical trapping of caf with high density. *Physical Review Letters*, 119(10):103201, 2017.

[42] MD Di Rosa. Laser-cooling molecules: Concept, candidates, and supporting hyperfine-resolved measurements of rotational lines in the ax (0, 0) band of cah. *The European Physical Journal D-Atomic, Molecular, Optical and Plasma Physics*, 31(2):395–402, 2004.

[43] Alejandra L Collopy, Shiqian Ding, Yewei Wu, Ian A Finneran, Loïc Anderegg, Benjamin L Augenbraun, John M Doyle, and Jun Ye. 3d magneto-optical trap of yttrium monoxide. *Physical Review Letters*, 121(21):213201, 2018.

[44] Zixuan Zeng, Shuhua Deng, Shoukang Yang, and Bo Yan. Three-dimensional magneto-optical trapping of barium monofluoride. *arXiv preprint arXiv:2405.17883*, 2024.

[45] Jinyu Dai, Benjamin Riley, Qi Sun, Debayan Mitra, and Tanya Zelevinsky. Magneto-optical trapping of a metal hydride molecule. *Physical Review Letters*, 136(23):233403, 2026.

[46] Nathaniel B Vilas, Christian Hallas, Loïc Anderegg, Paige Robichaud, Andrew Winnicki, Debayan Mitra, and John M Doyle. Magneto-optical trapping and sub-doppler cooling of a polyatomic molecule. *Nature*, 606(7912):70–74, 2022.

[47] Zack D. Lasner, Alexander Frenett, Hiromitsu Sawaoka, Loïc Anderegg, Benjamin Augenbraun, Hana Lampson, Mingda Li, Annika Lunstad, Jack Mango, Abdullah Nasir, Tasuku Ono, Takashi Sakamoto, and John M. Doyle. Magneto-optical trapping of a heavy polyatomic molecule for precision measurement. *Physical Review Letters*, 134:083401, Feb 2025. doi: 10.1103/PhysRevLett.134.083401.

[48] Loïc Anderegg, Benjamin L Augenbraun, Yicheng Bao, Sean Burchesky, Lawrence W Cheuk, Wolfgang Ketterle, and John M Doyle. Laser cooling of optically trapped molecules. *Nature Physics*, 14(9):890–893, 2018.

[49] Loïc Anderegg, Lawrence W Cheuk, Yicheng Bao, Sean Burchesky, Wolfgang Ketterle, Kang-Kuen Ni, and John M Doyle. An optical tweezer array of ultracold molecules. *Science*, 365(6458):1156–1158, 2019.

[50] Daniel Barredo, Henning Labuhn, Sylvain Ravets, Thierry Lahaye, Antoine Browaeys, and Charles S Adams. Coherent excitation transfer in a spin chain of three rydberg atoms. *Physical review letters*, 114(11):113002, 2015.

[51] Gabriel Emperauger, Mu Qiao, Guillaume Bornet, Cheng Chen, Romain Martin, Yuki Torii Chew, Bastien Gély, Lukas Klein, Daniel Barredo, Antoine Browaeys, et al. Benchmarking direct and indirect dipolar spin-exchange interactions between two rydberg atoms. *Physical Review A*, 111(6):062806, 2025.

[52] DM Zajac, AJ Sigillito, M Russ, F Borjans, JM Taylor, G Burkard, and JR Petta. Quantum cnot gate for spins in silicon. *arXiv preprint arXiv:1708.03530*, 2017.

[53] Sylvain de Léséleuc, Daniel Barredo, Vincent Lienhard, Antoine Browaeys, and Thierry Lahaye. Optical control of the resonant dipole-dipole interaction between rydberg atoms. *Physical Review Letters*, 119(5):053202, 2017.

[54] Guillaume Bornet, Gabriel Emperauger, Cheng Chen, Bingtian Ye, Maxwell Block, Marcus Bintz, Jamie A Boyd, Daniel Barredo, Tommaso Comparin, Fabio Mezzacapo, et al. Scalable spin squeezing in a dipolar rydberg atom array. *Nature*, 621(7980):728–733, 2023.

[55] Paul Niklas Jepsen, Jesse Amato-Grill, Ivana Dimitrova, Wen Wei Ho, Eugene Demler, and Wolfgang Ketterle. Spin transport in a tunable heisenberg model realized with ultracold atoms. *Nature*, 588(7838):403–407, 2020.

[56] William G Tobias, Kyle Matsuda, Jun-Ru Li, Calder Miller, Annette N Carroll, Thomas Bilitewski, Ana Maria Rey, and Jun Ye. Reactions between layer-resolved molecules mediated by dipolar spin exchange. *Science*, 375(6586):1299–1303, 2022.

[57] Dolev Bluvstein, Harry Levine, Giulia Semeghini, Tout T Wang, Sepehr Ebadi, Marcin Kalinowski, Alexander Keesling, Nishad Maskara, Hannes Pichler, Markus Greiner, et al. A quantum processor based on coherent transport of entangled atom arrays. *Nature*, 604 (7906):451–456, 2022.

[58] Juan M Pino, Jennifer M Dreiling, Caroline Figgatt, John P Gaebler, Steven A Moses, MS Allman, CH Baldwin, Michael Foss-Feig, David Hayes, Karl Mayer, et al. Demonstration of the trapped-ion quantum ccd computer architecture. *Nature*, 592(7853): 209–213, 2021.

[59] Steven A Moses, Charles H Baldwin, Michael S Allman, R Ancona, L Ascarrunz, C Barnes, J Bartolotta, B Bjork, P Blanchard, M Bohn, et al. A race-track trapped-ion quantum processor. *Physical Review X*, 13(4):041052, 2023.

[60] Jiaqi You, John M. Doyle, Zirui Liu, Scarlett S. Yu, and Avikar Periwal. Control of dipolar dynamics by geometrical programming. *Phys. Rev. Lett.*, 135:253002, Dec 2025. doi: 10.1103/k22t-xgcy. URL https://link.aps.org/doi/10.1103/k22t-xgcy.

[61] Emily J Davis, Bingtian Ye, Francisco Machado, Simon A Meynell, Weijie Wu, Thomas Mittiga, William Schenken, Maxime Joos, Bryce Kobrin, Yuanqi Lyu, et al. Probing many-body dynamics in a two-dimensional dipolar spin ensemble. *Nature physics*, 19(6): 836–844, 2023.

[62] Antoine Browaeys and Thierry Lahaye. Many-body physics with individually controlled rydberg atoms. *Nature Physics*, 16(2):132–142, 2020.

[63] Lin Su, Alexander Douglas, Michal Szurek, Robin Groth, S Furkan Ozturk, Aaron Krahn, Anne H Hébert, Gregory A Phelps, Sepehr Ebadi, Susannah Dickerson, et al. Dipolar quantum solids emerging in a hubbard quantum simulator. *Nature*, 622(7984):724–729, 2023.

[64] Sadegh Raeisi, Nathan Wiebe, and Barry C Sanders. Quantum-circuit design for efficient simulations of many-body quantum dynamics. *New Journal of Physics*, 14(10):103017, 2012.

[65] Dolev Bluvstein, Simon J Evered, Alexandra A Geim, Sophie H Li, Hengyun Zhou, Tom Manovitz, Sepehr Ebadi, Madelyn Cain, Marcin Kalinowski, Dominik Hangleiter, et al. Logical quantum processor based on reconfigurable atom arrays. *Nature*, 626(7997):58–65, 2024.

[66] Anna E Webb, Simon C Webster, S Collingbourne, David Bretaud, Adam M Lawrence, Sebastian Weidt, Florian Mintert, and Winfried K Hensinger. Resilient entangling gates for trapped ions. *Physical review letters*, 121(18):180501, 2018.

[67] Matteo Bergonzoni, Sven Jandura, and Guido Pupillo. iswap gate with polar molecules: Robustness criteria for entangling operations. *Physical Review A*, 112(3):032621, 2025.

[68] Joonhee Choi, Hengyun Zhou, Helena S Knowles, Renate Landig, Soonwon Choi, and Mikhail D Lukin. Robust dynamic hamiltonian engineering of many-body spin systems. *Physical Review X*, 10(3):031002, 2020.

[69] Thomas Bilitewski and Ana Maria Rey. Manipulating growth and propagation of correlations in dipolar multilayers: From pair production to bosonic kitaev models. *Physical Review Letters*, 131(5):053001, 2023.

[70] Or Katz, Lei Feng, Diego Porras, and Christopher Monroe. Floquet control of interactions and edge states in a programmable quantum simulator. *Nature Communications*, 16(1): 8815, 2025.

[71] John David Jackson and Ronald F Fox. Classical electrodynamics, 1999.

[72] Alan Robert Edmonds. *Angular momentum in quantum mechanics*, volume 4. Princeton university press, 1996.

[73] D. A. Varshalovich, A. N. Moskalev, and V. K. Khersonskii. *Quantum theory of angular momentum*. World Scientific, 1988.

[74] John M Brown and Alan Carrington. *Rotational spectroscopy of diatomic molecules*. Cambridge university press, 2003.

[75] David Parker Craig and Thiru Thirunamachandran. *Molecular quantum electrodynamics*. Courier Corporation, 2012.

[76] A Salam. The unified theory of resonance energy transfer according to molecular quantum electrodynamics. *Atoms*, 6(4):56, 2018.

[77] Mikhail A Baranov. Theoretical progress in many-body physics with ultracold dipolar gases. *Physics Reports*, 464(3):71–111, 2008.

[78] Alexey V Gorshkov, Salvatore R Manmana, Gang Chen, Eugene Demler, Mikhail D Lukin, and Ana Maria Rey. Quantum magnetism with polar alkali-metal dimers. *Physical Review A—Atomic, Molecular, and Optical Physics*, 84(3):033619, 2011.

[79] William B Cairncross, Jessie T Zhang, Lewis RB Picard, Yichao Yu, Kenneth Wang, and Kang-Kuen Ni. Assembly of a rovibrational ground state molecule in an optical tweezer. *Physical Review Letters*, 126(12):123402, 2021.

[80] Scarlett S. Yu, Avikar Periwal, Jiaqi You, Zirui Liu, Qinshu Lyu, Youngju Cho, Loïc Anderegg, Eunmi Chae, and John M. Doyle. High-fidelity entanglement of polar molecules by dynamic geometric control. *arXiv preprint arXiv:2607.13008*, 2026.

[81] Thaddeus D Ladd, Fedor Jelezko, Raymond Laflamme, Yasunobu Nakamura, Christopher Monroe, and Jeremy Lloyd O'Brien. Quantum computers. *nature*, 464(7285):45–53, 2010.

[82] Austin G Fowler, Matteo Mariantoni, John M Martinis, and Andrew N Cleland. Surface codes: Towards practical large-scale quantum computation. *Physical Review A—Atomic, Molecular, and Optical Physics*, 86(3):032324, 2012.

[83] John Preskill. Quantum computing in the nisq era and beyond. *Quantum*, 2:79, 2018.

[84] David P DiVincenzo. The physical implementation of quantum computation. *Fortschritte der Physik: Progress of Physics*, 48(9-11):771–783, 2000.

[85] Adam M Kaufman and Kang-Kuen Ni. Quantum science with optical tweezer arrays of ultracold atoms and molecules. *Nature Physics*, 17(12):1324–1333, 2021.

[86] Phelan Yu, Lawrence W Cheuk, Ivan Kozyryev, and John M Doyle. A scalable quantum computing platform using symmetric-top molecules. *New Journal of Physics*, 21(9): 093049, 2019.

[87] Nathaniel B Vilas, Paige Robichaud, Christian Hallas, Junheng Tao, Loïc Anderegg, Grace K Li, Hana Lampson, Lucie D Augustovičová, John L Bohn, and John M Doyle. Quantum-state-controlled collisions of ultracold polyatomic molecules. *Physical Review X*, 16(2):021001, 2026.

[88] Manuel Endres, Hannes Bernien, Alexander Keesling, Harry Levine, Eric R Anschuetz, Alexandre Krajenbrink, Crystal Senko, Vladan Vuletic, Markus Greiner, and Mikhail D Lukin. Atom-by-atom assembly of defect-free one-dimensional cold atom arrays. *Science*, 354(6315):1024–1027, 2016.

[89] Daniel Barredo, Sylvain De Léséleuc, Vincent Lienhard, Thierry Lahaye, and Antoine Browaeys. An atom-by-atom assembler of defect-free arbitrary two-dimensional atomic arrays. *Science*, 354(6315):1021–1023, 2016.

[90] Hannes Bernien, Sylvain Schwartz, Alexander Keesling, Harry Levine, Ahmed Omran, Hannes Pichler, Soonwon Choi, Alexander S Zibrov, Manuel Endres, Markus Greiner, et al. Probing many-body dynamics on a 51-atom quantum simulator. *Nature*, 551(7682): 579–584, 2017.

[91] LR Liu, JD Hood, Yichao Yu, JT Zhang, NR Hutzler, Till Rosenband, and K-K Ni. Building one molecule from a reservoir of two atoms. *Science*, 360(6391):900–903, 2018.

[92] Jessie T Zhang, Lewis RB Picard, William B Cairncross, Kenneth Wang, Yichao Yu, Fang Fang, and Kang-Kuen Ni. An optical tweezer array of ground-state polar molecules. *Quantum Science and Technology*, 7(3):035006, 2022.

[93] Yuchen Wang, Zixuan Hu, Barry C Sanders, and Sabre Kais. Qudits and high-dimensional quantum computing. *Frontiers in Physics*, 8:589504, 2020.

[94] Xiaoqin Gao, Paul Appel, Nicolai Friis, Martin Ringbauer, and Marcus Huber. On the role of entanglement in qudit-based circuit compression. *Quantum*, 7:1141, 2023.

[95] Lewis Russell Bartos Picard. *Control, Readout, and Entanglement of Molecular Qubits*. Harvard University, 2024.

[96] Victor V Albert, Jacob P Covey, and John Preskill. Robust encoding of a qubit in a molecule. *Physical Review X*, 10(3):031050, 2020.

[97] Arda Aydin, Max A Alekseyev, and Alexander Barg. A family of permutationally invariant quantum codes. *Quantum*, 8:1321, 2024.

[98] Brandon J Furey, Zhenlin Wu, Mariano Isaza-Monsalve, Stefan Walser, Elyas Mattivi, René Nardi, and Philipp Schindler. Strategies for implementing quantum error correction in molecular rotation. *Quantum*, 8:1578, 2024.

[99] Roman V Krems. Cold controlled chemistry. *Physical Chemistry Chemical Physics*, 10 (28):4079–4092, 2008.

[100] N Balakrishnan and A Dalgarno. Chemistry at ultracold temperatures. *Chemical physics letters*, 341(5-6):652–656, 2001.

[101] S Ospelkaus, K-K Ni, D Wang, MHG De Miranda, B Neyenhuis, 1 G Quéméner, PS Julienne, JL Bohn, DS Jin, and J Ye. Quantum-state controlled chemical reactions of ultracold potassium-rubidium molecules. *Science*, 327(5967):853–857, 2010.

[102] Zbigniew Idziaszek, Goulven Quéméner, John L Bohn, and Paul S Julienne. Simple quantum model of ultracold polar molecule collisions. *Physical Review A—Atomic, Molecular, and Optical Physics*, 82(2):020703, 2010.

[103] M-G Hu, Yu Liu, David D Grimes, Y-W Lin, Andrei H Gheorghe, Romain Vexiau, Nadia Bouloufa-Maafa, Olivier Dulieu, Till Rosenband, and K-K Ni. Direct observation of bimolecular reactions of ultracold krb molecules. *Science*, 366(6469):1111–1115, 2019.

[104] Ming-Guang Hu, Yu Liu, Matthew A Nichols, Lingbang Zhu, Goulven Quéméner, Olivier Dulieu, and Kang-Kuen Ni. Nuclear spin conservation enables state-to-state control of ultracold molecular reactions. *Nature Chemistry*, 13(5):435–440, 2021.

[105] Yu Liu, Ming-Guang Hu, Matthew A Nichols, Dongzheng Yang, Daiqian Xie, Hua Guo, and Kang-Kuen Ni. Precision test of statistical dynamics with state-to-state ultracold chemistry. *Nature*, 593(7859):379–384, 2021.

[106] Lawrence W Cheuk, Loïc Anderegg, Yicheng Bao, Sean Burchesky, Scarlett S Yu, Wolfgang Ketterle, Kang-Kuen Ni, and John M Doyle. Observation of collisions between two ultracold ground-state caf molecules. *Physical review letters*, 125(4):043401, 2020.

[107] Matthew A Nichols, Yi-Xiang Liu, Lingbang Zhu, Ming-Guang Hu, Yu Liu, and Kang-Kuen Ni. Detection of long-lived complexes in ultracold atom-molecule collisions. *Physical Review X*, 12(1):011049, 2022.

[108] Luigi De Marco, Giacomo Valtolina, Kyle Matsuda, William G Tobias, Jacob P Covey, and Jun Ye. A degenerate fermi gas of polar molecules. *Science*, 363(6429):853–856, 2019.

[109] Giacomo Valtolina, Kyle Matsuda, William G Tobias, Jun-Ru Li, Luigi De Marco, and Jun Ye. Dipolar evaporation of reactive molecules to below the fermi temperature. *Nature*, 588(7837):239–243, 2020.

[110] Michael Mayle, Goulven Quéméner, Brandon P Ruzic, and John L Bohn. Scattering of ultracold molecules in the highly resonant regime. *Physical Review A—Atomic, Molecular, and Optical Physics*, 87(1):012709, 2013.

[111] Philip D Gregory, Matthew D Frye, Jacob A Blackmore, Elizabeth M Bridge, Rahul Sawant, Jeremy M Hutson, and Simon L Cornish. Sticky collisions of ultracold rbcs molecules. *Nature communications*, 10(1):3104, 2019.

[112] AV Gorshkov, P Rabl, G Pupillo, A Micheli, P Zoller, MD Lukin, and HP Büchler. Suppression of inelastic collisions between polar molecules with a repulsive shield. *Physical review letters*, 101(7):073201, 2008.

[113] Goulven Quéméner and John L Bohn. Shielding σ 2 ultracold dipolar molecular collisions with electric fields. *Physical Review A*, 93(1):012704, 2016.

[114] Maykel L González-Martínez, John L Bohn, and Goulven Quéméner. Adimensional theory of shielding in ultracold collisions of dipolar rotors. *Physical Review A*, 96(3):032718, 2017.

[115] Kyle Matsuda, Luigi De Marco, Jun-Ru Li, William G Tobias, Giacomo Valtolina, Goulven Quéméner, and Jun Ye. Resonant collisional shielding of reactive molecules using electric fields. *Science*, 370(6522):1324–1327, 2020.

[116] Loïc Anderegg, Sean Burchesky, Yicheng Bao, Scarlett S Yu, Tijs Karman, Eunmi Chae, Kang-Kuen Ni, Wolfgang Ketterle, and John M Doyle. Observation of microwave shielding of ultracold molecules. *Science*, 373(6556):779–782, 2021.

[117] Andreas Schindewolf, Roman Bause, Xing-Yan Chen, Marcel Duda, Tijs Karman, Immanuel Bloch, and Xin-Yu Luo. Evaporation of microwave-shielded polar molecules to quantum degeneracy. *Nature*, 607(7920):677–681, 2022.

[118] Niccolo Bigagli, Claire Warner, Weijun Yuan, Siwei Zhang, Ian Stevenson, Tijs Karman, and Sebastian Will. Collisionally stable gas of bosonic dipolar ground-state molecules. *Nature Physics*, 19(11):1579–1584, 2023.

[119] Siwei Zhang, Weijun Yuan, Niccolò Bigagli, Haneul Kwak, Tijs Karman, Ian Stevenson, and Sebastian Will. Observation of self-bound droplets of ultracold dipolar molecules. *Nature*, 651(8106):601–606, 2026.

[120] MA Baranov, MS Mar'enko, Val S Rychkov, and GV Shlyapnikov. Superfluid pairing in a polarized dipolar fermi gas. *Physical Review A*, 66(1):013606, 2002.

[121] MA Baranov, C Lobo, and GV Shlyapnikov. Superfluid pairing between fermions with unequal masses. *Physical Review A—Atomic, Molecular, and Optical Physics*, 78(3): 033620, 2008.

[122] J Levinsen, Nigel R Cooper, and Georgy V Shlyapnikov. Topological $p_x + ip_y$ superfluid phase of fermionic polar molecules. *Physical Review A—Atomic, Molecular, and Optical Physics*, 84(1):013603, 2011.

[123] Krzysztof Góral, Luis Santos, and Maciej Lewenstein. Quantum phases of dipolar bosons in optical lattices. *Physical Review Letters*, 88(17):170406, 2002.

[124] Hans Peter Büchler, Eugene Demler, Mikhail Lukin, Andrea Micheli, N Prokof'Ev, Guido Pupillo, and Peter Zoller. Strongly correlated 2d quantum phases with cold polar molecules: Controlling the shape of the interaction potential. *Physical Review Letters*, 98 (6):060404, 2007.

[125] MS Safronova, D Budker, D DeMille, Derek F Jackson Kimball, A Derevianko, and Charles W Clark. Search for new physics with atoms and molecules. *Reviews of Modern Physics*, 90(2):025008, 2018.

[126] David DeMille, John M Doyle, and Alexander O Sushkov. Probing the frontiers of particle physics with tabletop-scale experiments. *Science*, 357(6355):990–994, 2017.

[127] Nicholas R Hutzler, A Borschevsky, D Budker, D DeMille, VV Flambaum, G Gabrielse, RF Ruiz, AM Jayich, LA Orozco, M Ramsey-Musolf, et al. Searches for new sources of cp violation using molecules as quantum sensors. *arXiv preprint arXiv:2010.08709*, 2020.

[128] PGH Sandars. The electric-dipole moments of an atom i. some general considerations. *Journal of Physics B: Atomic and Molecular Physics*, 1(3):499–510, 1968.

[129] Tanya S Roussy, Luke Caldwell, Trevor Wright, William B Cairncross, Yuval Shagam, Kia Boon Ng, Noah Schlossberger, Sun Yool Park, Anzhou Wang, Jun Ye, et al. An improved bound on the electron's electric dipole moment. *Science*, 381(6653):46–50, 2023.

[130] ACME Collaboration Andreev V. 1 5 5 Ang DG 1 DeMille D. acme@ physics. harvard. edu 2 d Doyle JM 1 Gabrielse G. 1 3 Haefner J. 1 Hutzler NR 1 4 Lasner Z. 2 Meisenhelder C. 1 O'Leary BR 2 Panda CD 1 West AD 2 6 6 West EP 1 6 6 Wu X. 1 2. Improved limit on the electric dipole moment of the electron. *Nature*, 562(7727):355–360, 2018.

[131] Loïc Anderegg, Nathaniel B Vilas, Christian Hallas, Paige Robichaud, Arian Jadbabaie, John M Doyle, and Nicholas R Hutzler. Quantum control of trapped polyatomic molecules for eedm searches. *Science*, 382(6671):665–668, 2023.

[132] Benjamin L Augenbraun, Zack D Lasner, Alexander Frenett, Hiromitsu Sawaoka, Calder Miller, Timothy C Steimle, and John M Doyle. Laser-cooled polyatomic molecules for improved electron electric dipole moment searches. *New Journal of Physics*, 22(2):022003, 2020.

[133] Malika Denis, Yongliang Hao, Ephraim Eliav, Nicholas R Hutzler, Malaya K Nayak, Rob GE Timmermans, and Anastasia Borschesvky. Enhanced p, t-violating nuclear magnetic quadrupole moment effects in laser-coolable molecules. *The Journal of Chemical Physics*, 152(8), 2020.

[134] Roman Bause, Nithesh Balasubramanian, Ties Fikkers, Eifion H Prinsen, Kees Steinebach, Arian Jadbabaie, Nicholas R Hutzler, I Agustín Aucar, Lukáš F Pašteka, Anastasia Borschevsky, et al. Prospects for measuring the electron's electric dipole moment with polyatomic molecules in an optical lattice. *Physical Review A*, 111(6):062815, 2025.

[135] TA Isaev, AV Zaitsevskii, and E Eliav. Laser-coolable polyatomic molecules with heavy nuclei. *Journal of Physics B: Atomic, Molecular and Optical Physics*, 50(22):225101, 2017.

[136] Victor V Flambaum. Enhanced nuclear schiff moment and time-reversal violation in th 229-containing molecules. *Physical Review C*, 99(3):035501, 2019.

[137] VV Flambaum and MG Kozlov. Studying variation of fundamental constants with molecules. *arXiv preprint arXiv:0711.4536*, 2007.

[138] D DeMille, S Sainis, J Sage, T Bergeman, S Kotochigova, and E Tiesinga. Enhanced sensitivity to variation of me/mp in molecular spectra. *Physical review letters*, 100(4): 043202, 2008.

[139] David DeMille, Sidney B Cahn, Dennis Murphree, David A Rahmlow, and Mikhail G Kozlov. Using molecules to measure nuclear spin-dependent parity violation. *Physical review letters*, 100(2):023003, 2008.

[140] Eunmi Chae. *Laser slowing of CaF molecules and progress towards a dual-MOT for Li and CaF*. PhD thesis, Harvard University.

[141] Loic Gregory Anderegg. *Ultracold molecules in optical arrays: from laser cooling to molecular collisions*. Harvard University, 2020.

[142] Luke Caldwell. *Deep laser cooling and coherent control of molecules*. PhD thesis, Imperial College London, 2020.

[143] NJ Fitch and MR Tarbutt. Laser-cooled molecules. *Advances in Atomic, molecular, and Optical Physics*, 70:157–262, 2021.

[144] Michael Dulick, Peter F Bernath, and Robert W Field. Rotational and vibrational analysis of the caf b2σ+–x 2σ+ system. *Canadian Journal of Physics*, 58(5):703–712, 1980.

[145] S Truppe, HJ Williams, M Hambach, L Caldwell, NJ Fitch, EA Hinds, BE Sauer, and MR Tarbutt. Molecules cooled below the doppler limit. *Nature Physics*, 13(12):1173–1176, 2017.

[146] TE Wall, JF Kanem, JJ Hudson, BE Sauer, D Cho, MG Boshier, EA Hinds, and MR Tarbutt. Lifetime of the a (v= 0) state and franck-condon factor of the a-x (0-0) transition of caf measured by the saturation of laser-induced fluorescence. *Physical Review A—Atomic, Molecular, and Optical Physics*, 78(6):062509, 2008.

[147] P. J. Dagdigian, H. W. Cruse, and R. N. Zare. Radiative lifetimes of the alkaline earth monohalides. *The Journal of Chemical Physics*, 60:2330–2339, 1974.

[148] Léo Lavy, Peter F Bernath, and Adam Pastorek. Line list for the a 2π- x 2σ+ and the b 2σ+- x 2σ+ band systems of caf. *The Astrophysical Journal*, 979(1):19, 2025.

[149] Yongliang Hao, Lukáš F Pašteka, Lucas Visscher, Parul Aggarwal, Hendrick L Bethlem, Alexander Boeschoten, Anastasia Borschevsky, Malika Denis, Kevin Esajas, Steven Hoekstra, et al. High accuracy theoretical investigations of caf, srf, and baf and implications for laser-cooling. *The Journal of chemical physics*, 151(3), 2019.

[150] Valentina Zhelyazkova, Anne Cournol, Thomas E Wall, Aki Matsushima, Jonathan J Hudson, EA Hinds, MR Tarbutt, and BE Sauer. Laser cooling and slowing of caf molecules. *Physical Review A*, 89(5):053416, 2014.

[151] S. Truppe, H. J. Williams, N. J. Fitch, M. Hambach, T. E. Wall, E. A. Hinds, B. E. Sauer, and M. R. Tarbutt. An intense, cold, velocity-controlled molecular beam by frequency-chirped laser slowing. *New Journal of Physics*, 19:022001, 2017. doi: 10.1088/1367-2630/aa5ca2.

[152] Ebram Youssef, Kaiya Wilson, Jiahe Cao, Reilly Brislawn, Avani Lakkireddy, Kun Liu, Aaron Teo, Phoebe Turner, and Loïc Anderegg. Enhanced loading of a molecular magneto-optical trap. *arXiv preprint arXiv:2605.30296*, 2026.

[153] H. J. Williams, L. Caldwell, N. J. Fitch, S. Truppe, J. Rodewald, E. A. Hinds, B. E. Sauer, and M. R. Tarbutt. Magnetic trapping and coherent control of laser-cooled molecules. *Physical Review Letters*, 120:163201, 2018. doi: 10.1103/PhysRevLett.120.163201.

[154] MR Tarbutt and TC Steimle. Modeling magneto-optical trapping of caf molecules. *Physical Review A*, 92(5):053401, 2015.

[155] Supeng Xu, Paul Kaebert, Mariia Stepanova, Timo Poll, Mirco Siercke, and Silke Ospelkaus. Maximizing the capture velocity of molecular magneto-optical traps with bayesian optimization. *New Journal of Physics*, 23(6):063062, 2021.

[156] WJ Childs, LS Goodman, U Nielsen, and V Pfeufer. Electric-dipole moment of CaF (X $^2\sigma^+$) by molecular beam, laser-rf, double-resonance study of Stark splittings. *The Journal of chemical physics*, 80(6):2283–2287, 1984.

[157] Eric B Norrgard, Stephen P Eckel, Christopher L Holloway, and Eric L Shirley. Quantum blackbody thermometry. *New Journal of Physics*, 23(3):033037, 2021.

[158] Shilin Hou and Peter F Bernath. Line list for the ground state of caf. *Journal of Quantitative Spectroscopy and Radiative Transfer*, 210:44–51, 2018.

[159] Yicheng Bao. Ultracold molecules in an optical tweezer array: From dipolar interaction to ground state cooling. *Thesis, Harvard University*, 2024.

[160] Lawrence W Cheuk, Loïc Anderegg, Benjamin L Augenbraun, Yicheng Bao, Sean Burchesky, Wolfgang Ketterle, and John M Doyle. Λ-enhanced imaging of molecules in an optical trap. *Physical review letters*, 121(8):083201, 2018.

[161] Scarlett S Yu, Jiaqi You, Yicheng Bao, Loïc Anderegg, Christian Hallas, Grace K Li, Dongkyu Lim, Eunmi Chae, Wolfgang Ketterle, Kang-Kuen Ni, et al. A conveyor-belt magneto-optical trap of caf. *arXiv preprint arXiv:2409.15262*, 2024.

[162] Kevin Singh, Shraddha Anand, Andrew Pocklington, Jordan T Kemp, and Hannes Bernien. Dual-element, two-dimensional atom array with continuous-mode operation. *Physical Review X*, 12(1):011040, 2022.

[163] Donggyu Kim, Alexander Keesling, Ahmed Omran, Harry Levine, Hannes Bernien, Markus Greiner, Mikhail D Lukin, and Dirk R Englund. Large-scale uniform optical focus array generation with a phase spatial light modulator. *Optics letters*, 44(12):3178–3181, 2019.

[164] Florence Nogrette, Henning Labuhn, Sylvain Ravets, Daniel Barredo, Lucas Béguin, Aline Vernier, Thierry Lahaye, and Antoine Browaeys. Single-atom trapping in holographic 2d arrays of microtraps with arbitrary geometries. *Physical Review X*, 4(2):021034, 2014.

[165] Bahtiyar Mamat, Cheng Sheng, Yi-Qing Zhang, Jia-Yi Hou, Peng Xu, Kun-Peng Wang, Jun Zhuang, Ming-Rui Wei, Min Liu, Jin Wang, et al. Mitigating the noise of residual electric fields for single rydberg atoms with electron photodesorption. *Physical Review Applied*, 22(6):064021, 2024.

[166] Carsten Klempt, T Van Zoest, T Henninger, O Topic, E Rasel, W Ertmer, and J Arlt. Ultraviolet light-induced atom desorption for large rubidium and potassium magneto-optical traps. *Physical Review A—Atomic, Molecular, and Optical Physics*, 73(1):013410, 2006.

[167] Connor M Holland, Yukai Lu, and Lawrence W Cheuk. Synthesizing optical spectra using computer-generated holography techniques. *New Journal of Physics*, 23(3):033028, 2021.

[168] EB Norrgard, DJ McCarron, MH Steinecker, MR Tarbutt, and D DeMille. Submillikelvin dipolar molecules in a radio-frequency magneto-optical trap. *Physical Review Letters*, 116(6):063004, 2016.

[169] Christian Hallas, Nathaniel B Vilas, Loïc Anderegg, Paige Robichaud, Andrew Winnicki, Chaoqun Zhang, Lan Cheng, and John M Doyle. Optical trapping of a polyatomic molecule in an ℓ-type parity doublet state. *Physical Review Letters*, 130(15):153202, 2023.

[170] MR Tarbutt. Laser cooling of molecules. *Contemporary Physics*, 2018.

[171] Shiqian Ding, Yewei Wu, Ian A Finneran, Justin J Burau, and Jun Ye. Sub-doppler cooling and compressed trapping of yo molecules at μ k temperatures. *Physical Review X*, 10(2):021049, 2020.

[172] Thomas K Langin and David DeMille. Toward improved loading, cooling, and trapping of molecules in magneto-optical traps. *New Journal of Physics*, 25(4):043005, 2023.

[173] JA Devlin and MR Tarbutt. Three-dimensional doppler, polarization-gradient, and magneto-optical forces for atoms and molecules with dark states. *New Journal of Physics*, 18(12):123017, 2016.

[174] JA Devlin and MR Tarbutt. Laser cooling and magneto-optical trapping of molecules analyzed using optical bloch equations and the fokker-planck-kramers equation. *Physical Review A*, 98(6):063415, 2018.

[175] MR Tarbutt. Magneto-optical trapping forces for atoms and molecules with complex level structures. *New Journal of Physics*, 17(1):015007, 2015.

[176] Thomas K Langin, Varun Jorapur, Yuqi Zhu, Qian Wang, and David DeMille. Polarization enhanced deep optical dipole trapping of λ-cooled polar molecules. *Physical Review Letters*, 127(16):163201, 2021.

[177] Kyle N Jarvis, JA Devlin, TE Wall, BE Sauer, and MR Tarbutt. Blue-detuned magneto-optical trap. *Physical Review letters*, 120(8):083201, 2018.

[178] Varun Jorapur, Thomas K Langin, Qian Wang, Geoffrey Zheng, and David DeMille. High density loading and collisional loss of laser-cooled molecules in an optical trap. *Physical Review Letters*, 132(16):163403, 2024.

[179] Justin J Burau, Parul Aggarwal, Kameron Mehling, and Jun Ye. Blue-detuned magneto-optical trap of molecules. *Physical Review Letters*, 130(19):193401, 2023.

[180] Samuel J Li, Connor M Holland, Yukai Lu, and Lawrence W Cheuk. Blue-detuned magneto-optical trap of caf molecules. *Physical Review Letters*, 132(23):233402, 2024.

[181] Christian Hallas, Grace K Li, Nathaniel B Vilas, Paige Robichaud, Loïc Anderegg, and John M Doyle. High compression blue-detuned magneto-optical trap of polyatomic molecules. *arXiv preprint arXiv:2404.03636*, 2024.

[182] Grace K. Li, Christian Hallas, and John M Doyle. Conveyor-belt magneto-optical trapping of molecules. *New Journal of Physics*, 27(4):043002, apr 2025. doi: 10.1088/1367-2630/adc032. URL https://dx.doi.org/10.1088/1367-2630/adc032.

[183] S. J. M. Kuppens, K. L. Corwin, K. W. Miller, T. E. Chupp, and C. E. Wieman. Loading an optical dipole trap. *Phys. Rev. A*, 62:013406, Jun 2000. doi: 10.1103/PhysRevA.62.013406. URL https://link.aps.org/doi/10.1103/PhysRevA.62.013406.

[184] Nicolas Schlosser, Georges Reymond, Igor Protsenko, and Philippe Grangier. Sub-poissonian loading of single atoms in a microscopic dipole trap. *Nature*, 411(6841): 1024–1027, 2001. doi: 10.1038/35082512.

[185] N. Schlosser, G. Reymond, and P. Grangier. Collisional blockade in microscopic optical dipole traps. *Phys. Rev. Lett.*, 89:023005, Jun 2002. doi: 10.1103/PhysRevLett.89.023005. URL https://link.aps.org/doi/10.1103/PhysRevLett.89.023005.

[186] Brianna R Heazlewood and Timothy P Softley. Towards chemistry at absolute zero. *Nature Reviews Chemistry*, 5(2):125–140, 2021.

[187] Kai-Niklas Schymik, Bruno Ximenez, Etienne Bloch, Davide Dreon, Adrien Signoles, Florence Nogrette, Daniel Barredo, Antoine Browaeys, and Thierry Lahaye. In situ equalization of single-atom loading in large-scale optical tweezer arrays. *Physical Review A*, 106(2):022611, 2022.

[188] Alexandre Cooper, Jacob P Covey, Ivaylo S Madjarov, Sergey G Porsev, Marianna S Safronova, and Manuel Endres. Alkaline-earth atoms in optical tweezers. *Physical Review X*, 8(4):041055, 2018.

[189] Y Torii Chew, Martin Poitrinal, Takafumi Tomita, Sota Kitade, Jorge Mauricio, Kenji Ohmori, and Sylvain de Léséleuc. Ultraprecise holographic optical tweezer array. *Physical Review A*, 110(5):053518, 2024.

[190] Ian Christen, Christopher Panuski, Thomas Propson, and Dirk Englund. Full-volume aberration-space holography. *arXiv preprint arXiv:2505.08777*, 2025.

[191] Yohann Machu, Gautier Creutzer, Clément Sayrin, and Michel Brune. Full-field-of-view aberration correction for large arrays of focused beams. *arXiv preprint arXiv:2512.15967*, 2025.

[192] GT Hickman and M Saffman. Speed, retention loss, and motional heating of atoms in an optical conveyor belt. *Physical Review A*, 101(6):063411, 2020.

[193] E Torrontegui, S Ibáñez, Xi Chen, A Ruschhaupt, D Guéry-Odelin, and JG Muga. Fast atomic transport without vibrational heating. *Physical Review A—Atomic, Molecular, and Optical Physics*, 83(1):013415, 2011.

[194] Yicheng Bao, Scarlett S Yu, Jiaqi You, Loïc Anderegg, Eunmi Chae, Wolfgang Ketterle, Kang-Kuen Ni, and John M Doyle. Raman sideband cooling of molecules in an optical tweezer array to the 3d motional ground state. *Physical Review X*, 14(3):031002, 2024.

[195] Eunmi Chae. Entanglement via rotational blockade of mgf molecules in a magic potential. *Physical Chemistry Chemical Physics*, 23(2):1215–1220, 2021.

[196] Bernhard Albrecht, Yijian Meng, Christoph Clausen, Alexandre Dareau, Philipp Schneeweiss, and Arno Rauschenbeutel. Fictitious magnetic-field gradients in optical microtraps as an experimental tool for interrogating and manipulating cold atoms. *Physical Review A*, 94(6):061401, 2016.

[197] L Caldwell and MR Tarbutt. General approach to state-dependent optical-tweezer traps for polar molecules. *Physical Review Research*, 3(1):013291, 2021.

[198] Rory W Speirs and Paul D Lett. Pseudo-arbitrary sideband generation by phase modulation calculated with iterative phase retrieval. *Optics Express*, 31(13):21093–21106, 2023.

[199] CE Rogers III, JL Carini, JA Pechkis, and PL Gould. Creation of arbitrary spectra with an electro-optical modulator. In *APS Division of Atomic, Molecular and Optical Physics Meeting Abstracts*, volume 55, pages OPT–11, 2010.

[200] Colm A Ryan, Jonathan S Hodges, and David G Cory. Robust decoupling techniques to extend quantum coherence in diamond. *Physical Review Letters*, 105(20):200402, 2010.

[201] Alexandre M Souza, Gonzalo A Alvarez, and Dieter Suter. Robust dynamical decoupling for quantum computing and quantum memory. *Physical review letters*, 106(24):240501, 2011.

[202] Holly K Cummins and JA Jones. Use of composite rotations to correct systematic errors in nmr quantum computation. *New Journal of Physics*, 2(1):6–6, 2000.

[203] Jee Woo Park, Zoe Z Yan, Huanqian Loh, Sebastian A Will, and Martin W Zwierlein. Second-scale nuclear spin coherence time of ultracold 23na40k molecules. *Science*, 357 (6349):372–375, 2017.

[204] Frauke Seeßelberg, Xin-Yu Luo, Ming Li, Roman Bause, Svetlana Kotochigova, Immanuel Bloch, and Christoph Gohle. Extending rotational coherence of interacting polar molecules in a spin-decoupled magic trap. *Physical Review Letters*, 121(25):253401, 2018.

[205] Philip D Gregory, Jacob A Blackmore, Sarah L Bromley, Jeremy M Hutson, and Simon L Cornish. Robust storage qubits in ultracold polar molecules. *Nature Physics*, 17(10): 1149–1153, 2021.

[206] Jacob A Blackmore, Rahul Sawant, Philip D Gregory, Sarah L Bromley, Jesús Aldegunde, Jeremy M Hutson, and Simon L Cornish. Controlling the ac stark effect of rbcs with dc electric and magnetic fields. *Physical Review A*, 102(5):053316, 2020.

[207] SS Kondov, C-H Lee, KH Leung, C Liedl, I Majewska, R Moszynski, and T Zelevinsky. Molecular lattice clock with long vibrational coherence. *Nature Physics*, 15(11):1118–1122, 2019.

[208] Till Rosenband, David D Grimes, and Kang-Kuen Ni. Elliptical polarization for molecular stark shift compensation in deep optical traps. *Optics Express*, 26(16):19821–19825, 2018.

[209] Roman Bause, Ming Li, Andreas Schindewolf, Xing-Yan Chen, Marcel Duda, Svetlana Kotochigova, Immanuel Bloch, and Xin-Yu Luo. Tune-out and magic wavelengths for ground-state na 23 k 40 molecules. *Physical Review Letters*, 125(2):023201, 2020.

[210] Erwin L Hahn. Spin echoes. *Physical review*, 80(4):580, 1950.

[211] Herman Y Carr and Edward M Purcell. Effects of diffusion on free precession in nuclear magnetic resonance experiments. *Phys. Rev.*, 94(3):630, 1954.

[212] Lorenza Viola and Seth Lloyd. Dynamical suppression of decoherence in two-state quantum systems. *Physical Review A*, 58(4):2733, 1998.

[213] Lorenza Viola, Emanuel Knill, and Seth Lloyd. Dynamical decoupling of open quantum systems. *Physical Review Letters*, 82(12):2417, 1999.

[214] Terry Gullion, David B Baker, and Mark S Conradi. New, compensated carr-ourcell sequences. *Journal of Magnetic Resonance (1969)*, 89(3):479–484, 1990.

[215] Gijs De Lange, Zhi-Hui Wang, D Riste, VV Dobrovitski, and R Hanson. Universal dynamical decoupling of a single solid-state spin from a spin bath. *Science*, 330(6000): 60–63, 2010.

[216] LS Theis, F Motzoi, FK Wilhelm, and M Saffman. High-fidelity rydberg-blockade entangling gate using shaped, analytic pulses. *Physical Review A*, 94(3):032306, 2016.

[217] Michael H Goerz, Mark A Kasevich, and Vladimir S Malinovsky. Robust optimized pulse schemes for atomic fountain interferometry. *Atoms*, 11(2):36, 2023.

[218] Nicolas Vanhaecke and Olivier Dulieu. Precision measurements with polar molecules: the role of the black body radiation. *Molecular Physics*, 105(11-12):1723–1731, 2007.

[219] L. Caldwell, H. J. Williams, N. J. Fitch, J. Aldegunde, J. M. Hutson, B. E. Sauer, and M. R. Tarbutt. Long rotational coherence times of molecules in a magnetic trap. *Physical Review Letters*, 124:063001, 2020. doi: 10.1103/PhysRevLett.124.063001.

[220] Ch Monroe, DM Meekhof, BE King, Steven R Jefferts, Wayne M Itano, David J Wineland, and P Gould. Resolved-sideband raman cooling of a bound atom to the 3d zero-point energy. *Physical review letters*, 75(22):4011, 1995.

[221] Vladan Vuletić, Cheng Chin, Andrew J Kerman, and Steven Chu. Degenerate raman sideband cooling of trapped cesium atoms at very high atomic densities. *Physical Review Letters*, 81(26):5768, 1998.

[222] SE Hamann, DL Haycock, G Klose, PH Pax, IH Deutsch, and Poul S Jessen. Resolved-sideband raman cooling to the ground state of an optical lattice. *Physical Review Letters*, 80(19):4149, 1998.

[223] Helene Perrin, Axel Kuhn, Isabelle Bouchoule, and Christophe Salomon. Sideband cooling of neutral atoms in a far-detuned optical lattice. *Europhysics Letters*, 42(4):395, 1998.

[224] Jeffrey Douglas Thompson, TG Tiecke, Alexander S Zibrov, V Vuletić, and Mikhail D Lukin. Coherence and raman sideband cooling of a single atom in an optical tweezer. *Physical review letters*, 110(13):133001, 2013.

[225] Adam M Kaufman, Brian J Lester, and Cindy A Regal. Cooling a single atom in an optical tweezer to its quantum ground state. *Physical Review X*, 2(4):041014, 2012.

[226] Yewei Wu, Justin J Burau, Kameron Mehling, Jun Ye, and Shiqian Ding. High phase-space density of laser-cooled molecules in an optical lattice. *Physical review letters*, 127(26): 263201, 2021.

[227] Dietrich Leibfried, Rainer Blatt, Christopher Monroe, and David Wineland. Quantum dynamics of single trapped ions. *Reviews of Modern Physics*, 75(1):281, 2003.

[228] Mark Kasevich and Steven Chu. Laser cooling below a photon recoil with three-level atoms. *Physical review letters*, 69(12):1741, 1992.

[229] A Aspect, Ennio Arimondo, R e a1 Kaiser, N Vansteenkiste, and C Cohen-Tannoudji. Laser cooling below the one-photon recoil energy by velocity-selective coherent population trapping. *Physical Review Letters*, 61(7):826, 1988.

[230] David J Wineland, Christopher Monroe, Wayne M Itano, Dietrich Leibfried, Brian E King, and Dawn M Meekhof. Experimental issues in coherent quantum-state manipulation of trapped atomic ions. *Journal of research of the National Institute of Standards and Technology*, 103(3):259, 1998.

[231] Giovanna Morigi, JI Cirac, M Lewenstein, and P Zoller. Ground-state laser cooling beyond the lamb-dicke limit. *EPL (Europhysics Letters)*, 39(1):13–18, 1997.

[232] MK Joshi, P Hrmo, V Jarlaud, F Oehl, and RC Thompson. Population dynamics in sideband cooling of trapped ions outside the lamb-dicke regime. *Physical Review A*, 99 (1):013423, 2019.

[233] F Diedrich, JC Bergquist, Wayne M Itano, and DJ Wineland. Laser cooling to the zero-point energy of motion. *Physical review letters*, 62(4):403, 1989.

[234] Luke Caldwell and MR Tarbutt. Sideband cooling of molecules in optical traps. *Physical Review Research*, 2(1):013251, 2020.

[235] AJ Rasmusson, Marissa D'Onofrio, Yuanheng Xie, Jiafeng Cui, and Philip Richerme. Optimized pulsed sideband cooling and enhanced thermometry of trapped ions. *Physical Review A*, 104(4):043108, 2021.

[236] Yue-Hui Lu, Nathan Song, Tai Xiang, Jacquelyn Ho, Tsai-Chen Lee, Zhenjie Yan, and Dan M Stamper-Kurn. Astigmatism-free 3d optical tweezer control for rapid atom rearrangement. *arXiv preprint arXiv:2510.11451*, 2025.

[237] Lewis RB Picard and Manuel Endres. A three-dimensional acousto-optic deflector. *arXiv preprint arXiv:2510.07633*, 2025.

[238] QA Turchette, CS Wood, BE King, CJ Myatt, D Leibfried, WM Itano, C Monroe, and DJ Wineland. Deterministic entanglement of two trapped ions. *Physical Review Letters*, 81(17):3631, 1998.

[239] Rainer Blatt and David Wineland. Entangled states of trapped atomic ions. *Nature*, 453 (7198):1008–1015, 2008.

[240] Cass A Sackett, David Kielpinski, Brian E King, Christopher Langer, Volker Meyer, Christopher J Myatt, M Rowe, QA Turchette, Wayne M Itano, David J Wineland, et al. Experimental entanglement of four particles. *Nature*, 404(6775):256–259, 2000.

[241] Harry Levine, Alexander Keesling, Giulia Semeghini, Ahmed Omran, Tout T Wang, Sepehr Ebadi, Hannes Bernien, Markus Greiner, Vladan Vuletić, Hannes Pichler, et al. Parallel implementation of high-fidelity multiqubit gates with neutral atoms. *Physical review letters*, 123(17):170503, 2019.

[242] Ivaylo S Madjarov, Jacob P Covey, Adam L Shaw, Joonhee Choi, Anant Kale, Alexandre Cooper, Hannes Pichler, Vladimir Schkolnik, Jason R Williams, and Manuel Endres. High-fidelity entanglement and detection of alkaline-earth rydberg atoms. *Nature Physics*, 16(8):857–861, 2020.

[243] Thaned Pruttivarasin. Spectroscopy, fundamental symmetry tests and quantum simulation with trapped ions. 2014.

[244] Nathan Schine, Aaron W Young, William J Eckner, Michael J Martin, and Adam M Kaufman. Long-lived bell states in an array of optical clock qubits. *Nature Physics*, 18 (9):1067–1073, 2022.

[245] Shuo Ma, Alex P Burgers, Genyue Liu, Jack Wilson, Bichen Zhang, and Jeff D Thompson. Universal gate operations on nuclear spin qubits in an optical tweezer array of yb 171 atoms. *Physical Review X*, 12(2):021028, 2022.

[246] Kai-Niklas Schymik, Sara Pancaldi, Florence Nogrette, Daniel Barredo, Julien Paris, Antoine Browaeys, and Thierry Lahaye. Single atoms with 6000-second trapping lifetimes in optical-tweezer arrays at cryogenic temperatures. *Physical Review Applied*, 16(3): 034013, 2021.

[247] Zhenpu Zhang, Ting-Wei Hsu, Ting You Tan, Daniel H Slichter, Adam M Kaufman, Matteo Marinelli, and Cindy A Regal. High optical access cryogenic system for rydberg atom arrays with a 3000-second trap lifetime. *PRX Quantum*, 6(2):020337, 2025.

[248] Connor M Holland, Yukai Lu, Samuel J Li, Callum L Welsh, and Lawrence W Cheuk. Demonstration of erasure conversion in a molecular tweezer array. *arXiv preprint arXiv:2406.02391*, 2024.

[249] Haiteng Wu, Rémi Richaud, J-M Raimond, Michel Brune, and Sébastien Gleyzes. Millisecond-lived circular rydberg atoms in a room-temperature experiment. *Physical Review Letters*, 130(2):023202, 2023.

[250] Grace K Li, Giseok Lee, Jack Mango, Hana Lampson, YongWoong Lee, Winston Wang, Avikar Periwal, Nathaniel B Vilas, Alexander Frenett, LoÃƉc Anderegg, et al. Photon cycling and laser cooling of an asymmetric top molecule. *arXiv preprint arXiv:2606.12323*, 2026.

[251] Yukai Lu, Connor M Holland, and Lawrence W Cheuk. Molecular laser cooling in a dynamically tunable repulsive optical trap. *Physical review letters*, 128(21):213201, 2022.

[252] N. H. Balshaw. *Practical Cryogenics: An Introduction to Laboratory Cryogenics*. Oxford Instruments, Scientific Research Division, 1996. ISBN 0952759403. URL https://andor.oxinst.com/downloads/uploads/practical-cryogenics.pdf.

[253] Indium Corporation. Indium vacuum, hermetic and cryogenic seals, October 2012. URL https://www.indium.com/blog/indium-vacuum-hermetic-and-cryogenic-seals/.